UTS UNIVERSITY OF TECHNOLOGY SYDNEY

Nano/microcharacterization on mechanical properties and structures of geopolymeric matrices and interfacial transition zones

by Zhiyu Luo

Thesis submitted in fulfilment of the requirements for the degree of

Doctor of Philosophy

under the supervision of
Dr. Wengui Li (Principal supervisor)
Prof. Surendra P Shah (Co-supervisor)
Prof. John Zhou (Co-supervisor)

University of Technology Sydney
Faculty of Engineering and Information Technology

February 2021

CERTIFICATE OF ORIGINAL AUTHORSHIP

I, Zhiyu Luo declare that this thesis, is submitted in fulfilment of the requirements for the award of Doctor of Philosophy in the Faculty of Engineering and Information Technology at the University of Technology Sydney.

This thesis is wholly my own work unless otherwise referenced or acknowledged. In addition, I certify that all information sources and literature used are indicated in the thesis.

This document has not been submitted for qualifications at any other academic institution.

This research is supported by the Australian Government Research Training Program.

Production Note:
Signature: Signature removed prior to publication.

Date: 17/02/2021

ACKNOWLEDGEMENT

I wish to express my deep appreciation to my principal supervisor, Dr. Wengui Li for his continuous support, encouragement and valuable guidance throughout my whole Ph.D research. Frequent communication and his excellent insights helped me solve many problems and ensured that my research was in the right direction. I would also like to express my sincere gratitude to Prof. Surendra P. Shah and Prof. John Zhou, my co-supervisors. Their constructive comments and suggestions have significantly improved the quality of my research.

I greatly appreciate the financial support from the Australian Government Research Training Program and the equipment supports from UTS Tech Lab, UTS MAU labs, UTS material lab, and USYD Particles and Grains Lab. The training and assistance provided by technical staff and friends are heartily acknowledged, especially the help from Herbert Yuan, Alexander Angeloski, Muller Hailu, Peiran Li, Yongmei Zhang, Yanyao Bao and Linxiao Zhou. Special thanks are given to A/Prof. Yixiang Gan and Prof. Kejin Wang, who have provided important resources and training/guidance to help me complete my experiment and research. I am also very grateful to group members and friends such as Zhuo Tang, Fulin Qu, Caihong Xue, Wenkui Dong, Peiran Li and Yipu Guo etc, for their care and help, and also their comfort when I was frustrated in research. The suggestions on writing, format and analysis from Prof. Arnaud Castel, Dr. Xuzhen He, Prof. Daichao Shen and Kavya Mendu, etc., are highly appreciated as well.

Finally, I wish to extend my sincere thanks to my family, especially my father and mother. Their support, understanding and encouragement have always been my motivation and the source of confidence to meet the challenges.

LIST OF PUBLICATIONS

Published journal papers:

1. Luo, Z., Li, W., Wang, K. and Shah, S.P., 2018. Research progress in advanced nanomechanical characterization of cement-based materials. *Cement and Concrete Composites*, *94*, pp.277-295.

2. Luo, Z., Li, W., Tam, V.W., Xiao, J. and Shah, S.P., 2019. Current progress on nanotechnology application in recycled aggregate concrete. *Journal of Sustainable Cement-Based Materials*, *8*(2), pp.79-96.

3. Luo, Z., Li, W., Gan, Y., Mendu, K. and Shah, S.P., 2020. Applying grid nanoindentation and maximum likelihood estimation for NASH gel in geopolymer paste: Investigation and discussion. *Cement and Concrete Research*, *135*, p.106112.

4. Luo, Z., Li, W., Gan, Y., Mendu, K. and Shah, S.P., 2020. Maximum likelihood estimation for nanoindentation on sodium aluminosilicate hydrate gel of geopolymer under different silica modulus and curing conditions. *Composites Part B: Engineering*, *198*, p.108185.

5. Luo, Z., Li, W., Gan, Y., He, X., Castel, A. and Sheng, D., 2020. Nanoindentation on micromechanical properties and microstructure of geopolymer with nano-SiO_2 and nano-TiO_2. *Cement and Concrete Composites*, p.103883.

6. Luo, Z., Li, W., Wang, K., Castel, A. and Shah, S.P., 2021. Comparison on the properties of ITZs in fly ash-based geopolymer and Portland cement concretes with equivalent flowability. *Cement and Concrete Research*, *143*, p.106392.

7. Luo, Z., Li, W., Li, P., Wang, K. and Shah, S.P., 2021. Investigation on effect of nanosilica dispersion on the properties and microstructures of fly ash-based geopolymer composite. *Construction and Building Materials*, *282*, p.122690.

Under review:

1. Nanoscratch on mechanical properties of interfacial transition zone (ITZ) in fly ash-based geopolymer composites (*Composites science and technology*)

2. Nanomechanical characterization and image analysis of the properties and heterogeneity of ITZs in geopolymer concrete (*Cement and Concrete Research*)

TABLE OF CONTENTS

LIST OF ACRONYMS

AAFA	Alkali-activated fly ash
AFM	Atomic force microscopy
ASTM	American Society for Testing and Materials
BIC	Bayesian Information Criterion
BSE	Backscattered scanning electron
CDF	Cumulative distribution function
CH	Calcium hydroxide
DMT model	Derjaguin-Muller-Toporov model
EDS	Energy-dispersive spectrometry
ER	Elastic recovery
FIB	Focussed ion beam
FTIR	Fourier transform infrared spectroscopy
GMM	Gaussian mixture model
H	Hardness
HD C-S-H	High-density calcium silicate hydrate
ITZ	Interfacial transition zone
LD C-S-H	Low-density calcium silicate hydrate
LSE	Least-Square Estimation
M	Elastic modulus
MLE	Maximum likelihood estimation
Ms	Silica modulus
N-A-S-H	Sodium aluminosilicate hydrate

NMR	Nuclear magnetic resonance
NS	Nano-SiO_2
NT	Nano-TiO_2
PC	Portland cement
PD	Penetration depth
PDF	Probability density function
PeakForce QNM	PeakForce quantitative nanomechanical mapping
RD	Residual depth
SE	Secondary electrons
SEM	Scanning electron microscope
SNT	Statistical indentation technique
SPM	Scanning probe microscope
SSD	Saturated surface dry
TGA	Thermogravimetric analysis
UHD phase	Ultra-high density phase
XPM	Accelerated property mapping
XRD	X-ray diffraction

LIST OF FIGURES

LIST OF TABLES

ABSTRACT

This study aims to promote the fundamental understanding of fly ash-based geopolymer through micro and nanoscale mechanical and structural characterization. Geopolymer concrete is studied from two aspects of paste and interfacial transition zone (ITZ). In addition to properties investigation and related mechanism analysis, new insights and methods are provided for the nano/micromechanical testing and analysis of highly heterogeneous materials.

Prior to research, several typical nanomechanical testing techniques are introduced and compared. The review provides the current research trend, advantages/disadvantages and suitable application of these techniques in cement-based materials. Then, based on the study of geopolymer paste, some critical questions of the statistical nanoindentation technique (SNT) are discussed. The study reveals the disadvantages of using the least-square estimation (LSE) for deconvolution of data in some highly heterogeneous materials such as geopolymers and proposes a "compromise approach" using maximum likelihood estimation (MLE) for deconvolution. Correlation and difference of different statistical techniques are analyzed to clarify the rationality of the proposed method. Thereafter, the effects of the general design parameters such as silica modulus, alkali concentration, and curing condition on the properties of N-A-S-H gel and its association with the performance of geopolymer are investigated and discussed. The properties of geopolymer are further modified by nano-SiO_2 and nano-TiO_2. The effects of different nanoparticles on microstructure, gel proportion and gel micromechanical properties are discussed to reveal the macro-strength reinforcement mechanism.

For ITZ research, a method based on modelled ITZ samples is proposed to facilitate comparison research and nanomechanical testing. This part starts with the comparison of

ITZ in geopolymer concrete and Portland cement (PC) concrete. The mechanism of the better ITZ performance in geopolymer than PC is revealed. Afterwards, scratch technique coupled with Gaussian mixture model (GMM) is introduced on the modelled ITZ samples as a quick method for interfacial properties evaluation. The statistical results indicate that silica modulus is an important factor governing the interfacial properties of geopolymer. In the last section of ITZ research, the heterogeneity of ITZ in section concrete is categorized into three levels. The study promotes the heterogeneity of the investigated ITZ to the second level for a deeper understanding of ITZ in geopolymer. Echoing the beginning of the thesis, scratch and indentation techniques are combined used, which clearly shows some of their different advantages for nanomechanical properties investigation. Strategies are proposed to overcome the higher level of heterogeneity to realize ITZ properties investigation with feasible workload and accuracy.

CHAPTER 1. INTRODUCTION

1.1 Background

More than 10 billion tons of concrete are produced globally each year, making it one of the most used commodities in the world (Andrew 2019; Provis & Bernal 2014). As a critical raw material of current concrete, Portland cement owing to prominent properties and low cost has made a significant contribution to meeting human construction needs. Despite these benefits, the application of Portland cement is accompanied by increasing concern about its environmental impact. The recent statistical result (Andrew 2019) showed that up to 8% of global carbon dioxide emissions are related to the Portland cement industry. It is necessary to develop green binders with a low carbon footprint for the sustainable development of mankind. In addition, the accumulation of large amounts of industrial wastes is another environmental issue that has received increasing attention. The wastes are sometimes hard to be efficiently treated and cause serious pollution. If industrial wastes can be reused to replace Portland cement, there will be great environmental benefits.

This idea is realized by alumina and silica-rich industrial by-products such as fly ash and ground granulated blast furnace slag. The addition of fly ash and slag can not only bring environmental benefits, but also improve the long-term strength and durability of concrete (Juenger & Siddique 2015; Lothenbach, Scrivener & Hooton 2011). Nevertheless, fly ash and slag as supplementary cementitious materials are just used to partially replace Portland cement with replacing ratio generally lower than 30% ~ 40% (Gholampour & Ozbakkaloglu 2017; Rashad 2015). A large amount of fly ash and slag still have not been properly treated. The reuse of slag is 60-70% of the total production in Australia and is

less than 25% in some developing countries (Dhoble & Ahmed 2018; Gao et al. 2020). Coal ash was reported to be one of Australia's most severe waste problems, accounting for 18% of the entire waste stream (Millington 2019). The global utilization rate of fly ash is around 25% (Bhatt et al. 2019), and the utilization rate in countries like Australia is even lower than this value, only around 22% (Millington 2019). One of the most anticipated solutions for Australia's fly ash is still to use it in the concrete industry (Millington 2019).

As a matter of fact, applying a high amount of fly ash would bring adverse effects on the strengths of concrete (Hemalatha & Ramaswamy 2017; Herath et al. 2020). Additives (Herath et al. 2020) are sometimes incorporated to make up for strength loss. However, this method is not to improve concrete performance by giving full play to the role of fly ash and still needs a considerable amount of Portland cement. In addition to adjusting solids, the properties of fly ash-based cementitious material can be improved by adjusting aqueous media. Fly ash can be activated by alkali solution to unleash its potential. Alkali activated fly ash or called "geopolymer" (Davidovits 2002), is a promising construction material that can maximize the use of fly ash and develop concrete that is truly clinker-free. Proper design of fly ash-based geopolymer can make its mechanical properties and durability comparable to Portland cement materials (Zhuang et al. 2016). Despite the great advantages and potential of geopolymer, the understanding and application of geopolymer is far less than that of Portland cement concrete. In addition to general engineering properties, great efforts are needed in basic research to gain more scientific insights into geopolymer.

In recent decades, the rapid development and popularization of cutting-edge technology have brought new horizons to the research of cement-based materials. One of the very noticeable advances is understanding and modifying of cement-based materials from

small scales of micro and nanoscale. Micro and nanoscale characterization techniques such as nanomechanical test techniques and microstructure observation technique can reveal the inner mechanisms of materials' macro behaviours. Mechanisms analysis is an important means of finding out engineering problems in various cases and providing strategies for improving materials. Scientific understanding and theory are the essential basis for the wide application of materials, especially the construction materials closely related to life and property safety. Currently, studies such as micro and nanoscale mechanical properties testing and modification are still insufficient for geopolymer.

1.2 Research objectives

The main research objective is to understand fly ash-based geopolymer via micro and nanoscale techniques to lay a basis for the better application of geopolymer in engineering. However, there are controversial academic questions on these techniques such as the rationality of using Least-Square Estimation (LSE) and grid nanoindentation in heterogeneous cement-based materials. This thesis is thereby also devoted to promoting the more proper and innovative use of these techniques. This is not only of great significance to the research of this thesis, but also beneficial to various studies in related fields.

From the perspective of raw materials, geopolymer concrete is prepared from aggregates, alkali solutions and alumina and silica-rich precursor materials such as fly ash and metakaolin. After the reaction, the latter two became geopolymer binder, which bonds to aggregate and form geopolymer concrete with three components of aggregate, paste and ITZ between them. Paste and ITZ as shown in Figure 1.1 are the dominant parts that control the properties of geopolymer, and hence the focus of the research. The study on geopolymer was accompanied by comparisons with Portland cement concrete to deepen

the understanding. The research objectives of this thesis are detailed in the following three aspects.

1. Understanding the micro and nanoscale properties of geopolymer paste. At the microscopic scale, geopolymer paste is mainly composed of sodium aluminosilicate hydrate (N-A-S-H) gel, unreacted fly ash, partially reacted fly ash, crystalline phases and defects. The N-A-S-H gel is the most crucial component linked to the performance of geopolymer. The basic properties, nanoscale reinforcement of N-A-S-H gel and related mechanisms are the main focuses of this part.

2. Understanding the micro and nanoscale properties of the interfacial transition zone (ITZ). Owing to the wall effect, ITZ displays different properties from the bulk paste. Based on the comparative study with ITZ in Portland cement concrete, this part aims to understand the features of heterogeneous ITZ in geopolymer, reveal the mechanism that governs the properties of ITZ, and propose reinforcement methods.

3. Improving and developing nanomechanical testing methods for some highly heterogeneous materials like geopolymer. The techniques used are decisive in the testing results. This work was dedicated to re-discuss previous questions on statistical nanoindentation technique and provide new understanding and strategy. ITZ in concrete is highly heterogeneous. The local ITZ properties investigated by micro and nanoscale techniques are hard to reflect the overall situation in concrete and may lead to unreliable conclusion for some research. Efforts were made to establish a simplified test method for the properties investigation and comparative study of ITZs.

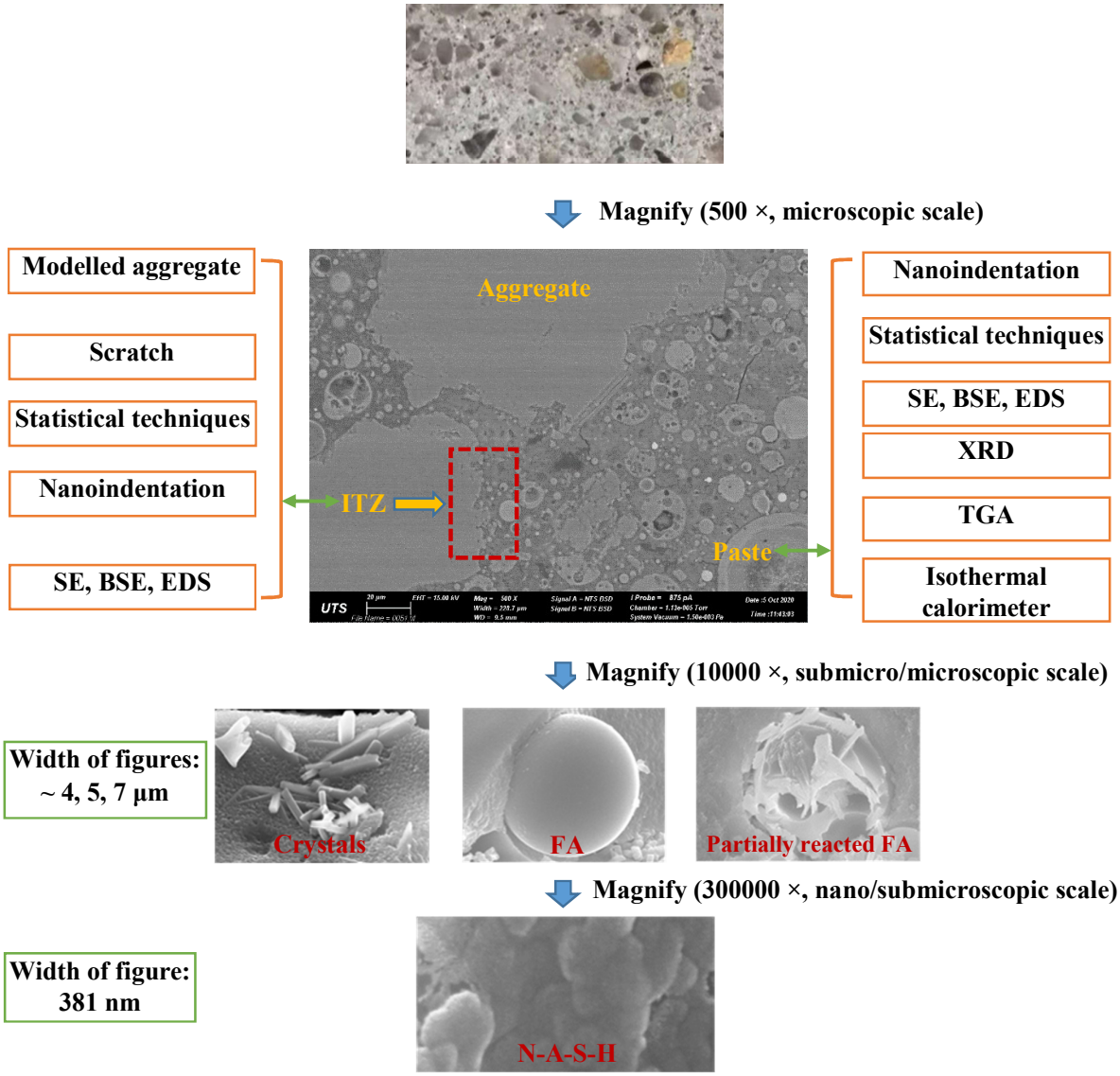

Figure 1.1 Structure of geopolymer concrete and research techniques

1.3 Thesis outline

The thesis consists of ten chapters. The studies on paste are mainly given in Chapter 4 to Chapter 6, and the study on ITZ are presented in Chapter 7 to Chapter 9. The discussions on nanomechanical testing techniques run through these studies. The structure of the thesis is shown as follows:

Chapter 1 introduces the background, significance and objectives of this study.

Chapter 2 provides a literature review of nanomechanical testing techniques as well as nano/microscale study and knowledge related to geopolymer.

Chapter 3 presents the information regarding raw materials and testing techniques used in this work.

Chapter 4 investigates and discusses questions on statistical nanoindentation technique.

Chapter 5 investigates and discusses whether the elastic modulus is an intrinsic materials invariant properties of N-A-S-H gel; understands the effects of general design parameters on the properties of N-A-S-H gel and its association with the performance of geopolymer.

Chapter 6 reinforces of geopolymer with nanoparticles and reveals the microscale modification mechanisms of macro behaviour.

Chapter 7 compares ITZ between Portland cement concrete and geopolymer concrete to reveal properties difference and mechanisms; illustrates the idea and significance of modelled ITZ samples.

Chapter 8 investigates the effects of silica modulus on the micromechanical properties of ITZ and paste; introduces nanoscratch technique on modelled ITZ to improve test efficiency.

Chapter 9 studies the properties of ITZ at different locations surrounding an aggregate particle; proposes testing strategies for ITZ with higher heterogeneity.

Chapter 10 presents key conclusions drawn from this study and suggestions for future research.

CHAPTER 2. LITERATURE REVIEW

At present, advanced characterization and simulation techniques allow the study of materials from small scales such as micro and nanoscales. The introduction of these techniques (Dolado & Van Breugel 2011; Provis, Palomo & Shi 2015; Sanchez & Sobolev 2010; Scrivener, Juilland & Monteiro 2015) has greatly promoted the understanding of cement-based materials. Some techniques such as scanning electron microscope (SEM) and X-ray diffraction (XRD) are already well known and widely used, while the application of nanomechanical characterization techniques is still very few. In this chapter, the research progress in advanced nanomechanical characterization techniques and their related studies for geopolymer are reviewed.

2.1 Nanomechanical testing techniques and their applications in cement-based materials

The early concept of nanotechnology originated from Feynman's classic lecture in 1959, who considered the possibility of manipulating matter at the atomic level (Feynman 1959). The rapid development of science and technology has turned this idea into reality. Nanotechnology has successfully promoted the development of various fields. Its application in concrete was classified into two categories of nanoscience and nano-engineering (Sanchez & Sobolev 2010). Nanoscience refers to the type of research that aims to understand the nano/microscale structure and properties of materials, whereas nano-engineering means the study of manipulating the nanoscale structure of materials to achieve improved performance. Nanomechanical testing techniques is a representative method to gain scientific understanding of material, which typically include nanoindentation, nanoscratch, modulus mapping and PeakForce quantitative

nanomechanical mapping. Currently, most of the related studies for cement-based materials are conducted by using nanoindentation. Other techniques are rarely understood and used. For this topic, considering the research purpose and objects, indentation and scratch techniques were selected for investigation. Nevertheless, in the review chapter, other two techniques that can reflect the current research trend were also briefly introduced. These techniques were compared to reveal their respective advantages. This chapter provides a basic understanding of these advanced techniques, comments on existing studies and suggestions on selecting techniques properly for research.

2.1.1 **Nanoindentation technique**

2.1.1.1 Basis of nanoindentation technique

Nanoindentation is the most commonly used technique to measure nano/microscale elastic modulus and hardness of materials. It can also be used for other investigations such as creep (Jones & Grasley 2011; Vandamme & Ulm 2013), fracture (Soliman, Aboubakr & Taha 2017; Zhang et al. 2016) and tensile strength (Němeček et al. 2016).

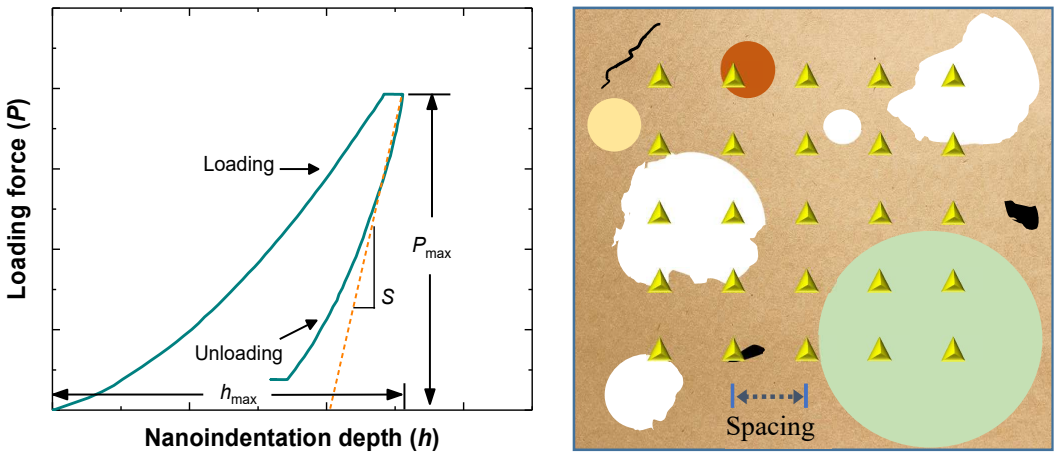

(a) Load-depth curve in a test (b) Grid nanoindentation

Figure 2.1 Nanoindentation test technique

$$H = \frac{P_{\max}}{A} \tag{2.1}$$

$$S = \frac{dP}{dh}\Big|_{h=h_{\max}} = \frac{2}{\sqrt{\pi}} E_r \sqrt{A} \tag{2.2}$$

$$\frac{1}{E_r} = \frac{1-\nu^2}{E} + \frac{1-\nu_i^2}{E_i} \tag{2.3}$$

$$A(h_c) = m_0 h_c^{\,2} + m_1 h_c + m_2 h_c^{\,(1/2)} + \ldots + m_n h_c^{\,(1/2^{(n-1)})} \tag{2.4}$$

$$h_c = h - (\varepsilon P)/S \tag{2.5}$$

where P and h are the indentation load and indentation depth, respectively. A is the projected contact area. S is the initial unloading stiffness. E_r is the reduced elastic modulus, which contains the elastic response of both indenter tip and tested material. E_i and ν_i are the elastic modulus and Poisson's ratio of the indenter, respectively. E and ν are the corresponding parameters for sample. The projected contact area A is determined by the contact depth h_c and tip area function (Oliver & Pharr 1992). For Berkovich tip, ε is 0.75. Coefficient m_0, m_1… m_n can be obtained by doing calibration on reference material such as fused silica.

Nanoindentation test can be performed in different models such as load control model and depth control model. Load control is generally adopted for the test of cementitious materials. In a test, an indenter with known geometry and mechanical parameters is pressed into the tested material under a continuously increasing load. After reaching the pre-set value, the load is generally kept constant for a while to eliminate creep and then removed gradually. A diagram of load depth curve during a test is shown in Figure 2.1 (a). Based on it, the elastic modulus E and hardness H of tested material can be determined by Equations (2.1)-(2.3) (Oliver & Pharr 1992). Although this technique is called as "nanoindentation", for cement-based material research, the test depth, tip radius, and involved range is sometimes more than 100 nanometre. A typical radius of curvature for

the commonly used Berkovich probe is 150 nm (COOPER 2007). Tip with large size like 600 nm was also reported for the study of Portland cement paste (Li et al. 2015b; Xu, Corr & Shah 2015b). The suitable maximum indentation depth used for studying C-S-H of cement-based materials frequently ranges from 100 nm to 300 nm (Constantinides & Ulm 2007). Research has also shown that the actual interaction range is 3-4 times the penetration depth (Chen et al. 2010c), and the typical interaction volume would be up to 1 μm^3 (Lura, Trtik & Münch 2011). Nevertheless, this term can help distinguish it from the microindentation technique. Because of these factors, different terms such as 'nanomechanical properties', 'micromechanical properties' and 'nano/micromechanical properties' are found to describe the properties of gel phase tested by nanoindentation.

Initially, the application of nanoindentation was mainly for homogeneous materials. However, lots of materials are composed of more than one component. There are some challenges in applying this advanced technique directly to obtain the mechanical properties of each micro-constituent. When the microstructure of the target components has a large characteristic length size, the investigation could be conducted on each specified component with the aid of microscope. However, when the material is still heterogeneity at the scale of several microns, it becomes very difficult to identify and locate the components. To solve the problem, the method of using grid nanoindentation shown in Figure 2.1 (b) coupled with statistical deconvolution techniques has been developed and widely used for many heterogeneous materials such as concrete, bone, shale, and ceramic composites (Roa et al. 2015; Ulm et al. 2007). It is called as statistical indentation technique (SNT). During the course of development, some studies clarified the principles of SNT and established test criteria (Constantinides et al. 2006; Constantinides & Ulm 2007; Miller et al. 2008). These works can be understood from two parts: the test part and the deconvolution part.

2.1.1.2 Principles and criteria for statistical nanoindentation techniques

The nanoindentation testing theory is based on the infinite half-space model and assumes that the surface is perfectly flat and smooth. Surface roughness criteria were proposed for the nanoindentation study of cement-based materials (Miller et al. 2008). Another study pointed out that there would be intrinsic porosity, so a low limit should be specified to avoid the filling of pores caused by over-polishing artefacts (Trtik et al. 2008).

To determine the critical indentation depth that could generate a homogeneous mechanical response of a component, studies were conducted on a binary layered system (Constantinides et al. 2006). The thin films-substrates model was considered to represent the most uncomplicated but most severe geometric condition the nanoindentation test would experience in a two-component material. Depending on the test parameters, the test results on this system may come from the corresponding single-phase response, or from different degrees of composite response. As given in Equation (2.6) (Constantinides et al. 2006), the composite modulus E_{eff} is related to E_{f} and E_{s}, the elastic modulus of the film and substrate, respectively. The weight coefficient Ψ reflects the contribution of different components of the binary layered system. When Ψ is 0, it means that the elastic modulus obtained is totally tested from the film. The increase of the weight coefficient indicates that the role of the substrate becomes more and more significant. The influence of film is negligible for the case that the coefficient is close to 1.

The weight coefficient is considered to be highly relevant to test and material parameters such as the size and shape of indenter, the test depth, the thickness of the film and the stiffness difference between film and substrate. The quantitative relationship of them was established and developed by many researchers (Barthel & Perriot 2004; Chen & Vlassak 2001; Huajian, Cheng-Hsin & Jin 1992). The typical evaluation equations are given in Equations (2.7)-(2.8) (Barthel & Perriot 2004; Constantinides et al. 2006), where the

allowed modulus ratio E_s/ E_f for analysis is in the wide range of 10^{-2} ~10^2, and the empirical constant n is around 1.27. It is clear that for a given coated substrate material, the weight coefficient Ψ decreases with the increase of the ratio of film thickness t to contact radius a. The summary study (Constantinides et al. 2006) indicated that these studies could draw a consistent conclusion: if the modulus ratio E_s/E_f is in the range of 0.2-5, indentation tests with a depth to film thickness ratio h/t less than 10% can ensure that the results come from the individual response of the film without being affected by the substrate. Thus, a scale separability condition shown in Equation (2.9) was proposed (Constantinides et al. 2006). An indentation test was considered to be able to assess the homogeneous mechanical properties of a micro-component once the contact depth satisfies this rule of thumb. One thing to note is that this widely used criterion is based on depth h. At the same depth, indenter with different sizes and shapes may result in different responses.

$$E_{\text{eff}} = E_f + \Psi\left(E_s - E_f\right) \tag{2.6}$$

$$\Psi = \left[1 + (kt/a)^n\right]^{-1} \tag{2.7}$$

$$\log(k) = -0.093 + 0.792\log(E_s/E_f) + 0.05\left(\log(E_s/E_f)\right)^2 \tag{2.8}$$

$$d << h_{\max} < D/10 \tag{2.9}$$

where D and d are the characteristic length size of the micro-constituents, and the largest microstructural heterogeneity within the micro-constituents, respectively.

The above principles and criteria were for a single test point. Due to the heterogeneous of composites materials, nanoindentation testing is usually performed in the form of grids to collect massive test points, as shown in Figure 2.1 (b). Therefore, it is necessary to specify a proper grid spacing. Based on the analysis of two-component materials, the

spacing was suggested to be greater than the characteristic size of the residual indentation mark to avoid the interference of adjacent test points (Constantinides et al. 2006; Constantinides & Ulm 2007). Besides, in order to reflect the spatial distribution of components, the spacing s was specified to be much larger than the characteristic size of the two components ($s\sqrt{N} >> D$) (Constantinides et al. 2006; Constantinides & Ulm 2007). In fact, it is better to specify the spacing more strictly than these criteria. For the microindentation hardness test (ASTM E384-2017), the minimum spacing recommended for Knoop and Vickers indentations are 2 or 2.5 times of the impression diagonals. Although the degree of plastic damage may decrease for the smaller scale nanoindentation test, it cannot be ignored that the residual impression is much smaller than the contact region and the contact region is much smaller than the involved range. The involved range was reported to be around 3-4 times the test depth (Chen et al. 2010c). In addition, it is a fact that the properties of the micro-constituents themselves sometimes show local heterogeneous, which also calls for large spacing. Thus, it is recommended that for indentation test, especially the large depth test, the minimum spacing could be determined by considering both the 2-2.5 times of the impression diagonals and 3-4 times of depth criteria. Besides, for comparative study, sufficient test data set in the form of different random grids is suggested to avoid the influence of local heterogeneity of the material.

For the deconvolution part, the initial studies (Constantinides et al. 2006; Constantinides & Ulm 2007; DeJong & Ulm 2007) assumed the mechanical property distribution (e.g. elastic modulus) of the heterogeneous material tested from SNT a one-dimensional Gaussian mixture model as given in Equation (2.10). The experiment data were constructed into frequency density histogram with a specified bin size, where each bar provides the frequency observation of the range of property value in the bin. The unknown parameters of theoretical probability density function (PDF), namely, the mean value,

standard deviation and proportion of each component can be obtained by minimizing the sum of squared errors between the observed values and the theoretical values. However, the results may vary with the bin size specified. Then, this method was developed to use the cumulative distribution function (CDF) given in Equation (2.12)-(2.13) (Ulm et al. 2007). Nevertheless, the PDF based method can intuitively present the peak of components, making it the most used deconvolution technique. The same point of these two methods is that the least-square estimation (LSE) method is used for fitting.

$$P(x) = \sum_{j=1}^{n} f_j p_j(x) \tag{2.10}$$

$$\min \sum_{i=1}^{m} \frac{(P^i - P(x_i))^2}{m} \tag{2.11}$$

$$D_X(X_i) = \frac{i}{N} - \frac{1}{2N} \qquad \text{for } i \in [1, N], \quad X=(M, H) \tag{2.12}$$

$$\min \sum_{i=1}^{N} \sum_{X=(M,H)} \left(D_X(X_i) - \sum_{j=1}^{n} f_j D_j(X_i) \right)^2 \tag{2.13}$$

$$\sum_{j=1}^{n} f_j = 1 \tag{2.14}$$

where n and f is the number of the components of the material and their proportion, respectively. P_j (x) and D_j (X_i) are the normal distribution function to describe the mechanical distribution of the j-th component. P^i is the frequency value of the i-th bin. $D_X(X_i)$ indicates the experimental cumulative distribution function for the sorted test data X_i. m is the number of bins specified in the frequency histogram, while N is the number of the indentation test points. Details can be found in references (Constantinides et al. 2006; Ulm et al. 2007).

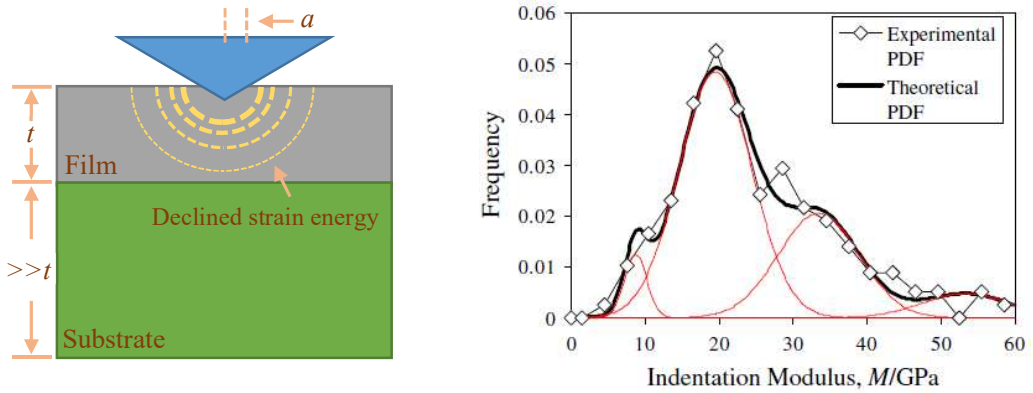

(a) Indentation on thin film model (Constantinides et al. 2006)

(b) Fitting of PDF by using LSE method (Ulm et al. 2007)

Figure 2.2 Principles of statistical nanoindentation technique

The above studies are a major breakthrough in the application of nanomechanical testing in heterogeneous materials. These techniques and related approaches such as micromechanics (Ulm et al. 2007; Vandamme, Ulm & Fonollosa 2010) have promoted the understanding of the mechanical properties and structure of micro-constituents in materials. However, limitations were sometimes found for the application of the statistical nanoindentation technique.

2.1.1.3 Examinations on statistical nanoindentation technique

Based on the proposed scale separability criterion and deconvolution technique, tests were conducted on Ti–TiB composites to verify the validity of the SNT method (Constantinides et al. 2006). The elastic modulus of components obtained by SNT was found to agree fairly well with the values reported in the literature. The packing density of C-S-H determined by SNT and micromechanics was also in line with the results calculated based on the mass density and particle density values measured by experiment (Ulm et al. 2007). However, some studies questioned the validity of using of SNT in Portland cement paste, especially for the identification of both low-density (LD) C-S-H

and high-density (HD) C-S-H from the peaks of probability density function (Lura, Trtik & Münch 2011; Trtik, Münch & Lura 2009). These works were conducted by virtual statistical indentation experiments, as displayed in Figure 2.3. According to the results (Lura, Trtik & Münch 2011), the main problems of SNT lies in the characteristic of microstructure and the numerical instability of the LSE method to fit the experimental curve. Figure 2.3 (b) provides the statistical results for distribution densities of phases detected by 1 μm^3 involved volume, which indicate that not all of the phases have an apparent peak. Besides, for deconvolution technique, the global optimum is hard to be found while significantly different results would be generated from different local optimum; the fewer number of phases of 2 and 3 are even found to better fit the frequency distribution histogram than 4 in Portland cement paste. These issues could also affect the investigation of geopolymer. They are discussed in a separate chapter, Chapter 4.

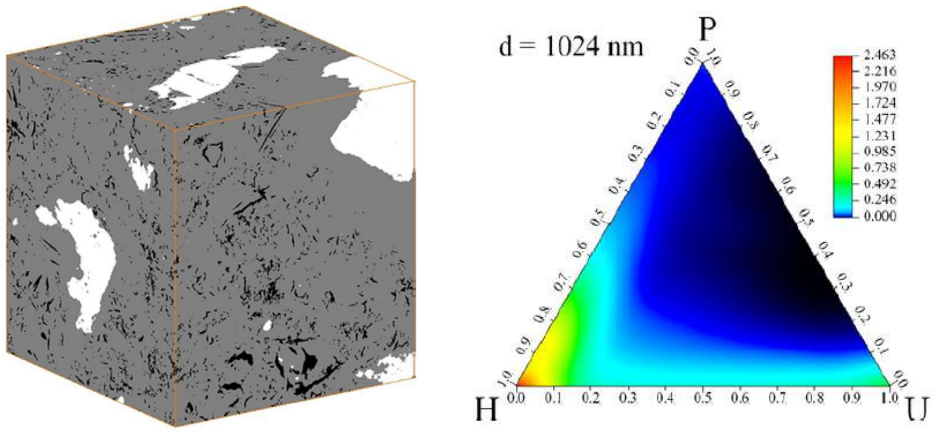

(a) A FIB-nt sample of cement paste with a size of 14.0 × 14.2 × 13.1 μm^3

(b) Ternary plot of Gaussian-filtered phase distribution densities

Figure 2.3 Virtual experiment for statistical indentation on Portland cement paste (Lura, Trtik & Münch 2011)

2.1.1.4 Progress of nanoindentation technique

In summary, the disadvantages of nanoindentation technique mainly include the time-consuming testing procedure, large involved volume, and numerical instability when applied in the form of SNT. Some efforts have been made to improve the nanoindentation technique. It was reported that conventionally, typical one point indentation test could cost 7-8 minutes to complete (Howind, Hughes & Zhu 2014). Some sophisticated nanoindentation equipment has developed the "Express test", where a single point test takes only about one seconds to complete (Howind, Hughes & Zhu 2014; Sebastiani et al. 2016). New breakthrough, accelerated property mapping (XPM) was reported to achieve an ultrahigh speed of six measurements per second. Several preliminary attempts for the ultra-high-speed nanoindentation have been found since 2017 (Guo et al. 2018; Hintsala et al. 2017; Hintsala, Hangen & Stauffer 2018; North et al. 2017; Zhang, Patel & Ren 2017). This technique is also recently introduced for the cement-based materials research (Němeček & Lukeš 2020). Despite the significant progress, there are some concerns. The high speed is realized by ignoring thermal drifts and creep, and the maximum scan area was reported to be only 90 μm × 90 μm (Němeček & Lukeš 2020). Besides, the test needs to consider the strain rate effect (Hintsala, Hangen & Stauffer 2018; Němeček & Lukeš 2020).

In addition to statistical analysis, efforts have been made on finding new methods for distinguishing different phases in a composite material. A "manual" method was adopted by Davydov, Jirásek & Kopecký (2011), to identify specified phases using a backscattered scanning electron (BSE) detector and then to navigate and select testing points on the specified phases using AFM. Currently, there are increasing interests to combine nanoindentation with other research techniques like backscatter electron (BSE) (Gao, Wei & Huang 2017b; Hrbek, Petráňová & Němeček 2017; Hu, Hou & Li 2017;

Long et al. 2018; Shen, Pan & Zhan 2017), Energy-dispersive spectrometry (EDS) (Brown, Allison & Sanchez 2018; Hrbek, Petráňová & Němeček 2017; Hu, Hou & Li 2017; Li, Wang & Wang 2017; Wilson et al. 2017; Zhu et al. 2017), and X-ray diffraction (XRD) (Hu, Hou & Li 2017; Li, Wang & Wang 2017; Shaikh, Supit & Barbhuiya 2017; Wang et al. 2017).

For the relatively large indenter tip and interaction volume of nanoindentation, it would make the results not pure individual phases and limit some delicate research at very small scale. While some researchers were trying to solve these problems by using advanced analysis methods, such as micromechanics, to evaluate the influence of embedded phases on the modulus of C-S-H at the indentation scale (Chen et al. 2010b; Hu et al. 2016; Hu et al. 2014), others have introduced new research techniques, such as modulus mapping (Gao, Wei & Huang 2017a; Li, Kawashima, et al. 2016; Li et al. 2015b; Wei, Gao & Liang 2018a; Wei, Liang & Gao 2017; Xu, Corr & Shah 2015a; Xu, Corr & Shah 2015b), PeakForce QNM (Asgari, Ramezanianpour & Butt 2016; Horszczaruk et al. 2015; Howind, Hughes & Zhu 2014; Li, Kawashima, et al. 2016; Li et al. 2015b; Trtik, Kaufmann & Volz 2012; Zhu et al. 2018) and nanoscratch test (Barbhuiya & Chow 2017; Mao, Yao & Xu 2013; Palin et al. 2015; Stynoski 2015; Xu, Corr & Shah 2017; Xu & Yao 2011, 2012; Zhao et al. 2016).

2.1.2 **Modulus mapping technique**

The modulus mapping technique incorporates the nanoscale dynamical mechanical analysis (nanoDMA) with in-situ scanning probe microscope (SPM) imaging, which can quantitatively map the nanomechanical properties of a material surface. In a modulus mapping test, the indenter scans the surface of the tested materials with a tiny high frequency sinusoidal oscillation, which is superimposed by a pre-set sinusoidal force and quasi-static force. Two key parameters, storage modulus E' and loss modulus E'', can be

obtained by analyzing the recorded displacement amplitude and phase lag in the scanning process. The storage modulus and loss modulus represent the materials' capacity to store energy (elastic portion) and dissipate energy as heat (viscous portion) of the viscoelastic material, respectively (Chawla & Meyers 1999). The mechanism of modulus mapping was summarized in the literature (Balooch et al. 2004; Li et al. 2015a). This technique is available on Hysitron Triboindenter when the Modulus Mapping module is equipped. As shown in some typical studies, the tip radius of the indenter used for a modulus mapping test is often large (e. g., 400 nm (Gao, Wei & Huang 2017a; Wei, Liang & Gao 2017), 600 nm (Xu, Corr & Shah 2015a; Xu, Corr & Shah 2015b)). Even if the same size of indenter tip is used for nanoindentation and modulus mapping tests, a significant increase in resolution has been observed in modulus mapping test (Xu, Corr & Shah 2015c), due to the smaller force and more precise tip control. For some materials, only several nanometres of contact depth (Zlotnikov, Zolotoyabko & Fratzl 2017) and nanoscale influence radius of tip (Gao, Wei & Huang 2018) were achieved, which allows a nearly non-destructive testing with very small test spacing. Each image of the modulus mapping has 256 × 256 test points. These massive test points can be obtained in just 10 minutes (Balooch et al. 2004). However, large scanning area would have increased time consumption (Balooch et al. 2004; Xu, Corr & Shah 2015a), and the maximum scanning area of this technique is only 50 μm × 50 μm (Balooch et al. 2004; Xu, Corr & Shah 2015a).

$$E' = \frac{K_s \sqrt{\pi}}{2\sqrt{A_c}} \tag{2.15}$$

$$E'' = \frac{\omega D_s \sqrt{\pi}}{2\sqrt{A_c}} \tag{2.16}$$

where A_c is the contact area; K_s and D_s are the contact stiffness and damping coefficient, respectively; ω is the angular frequency.

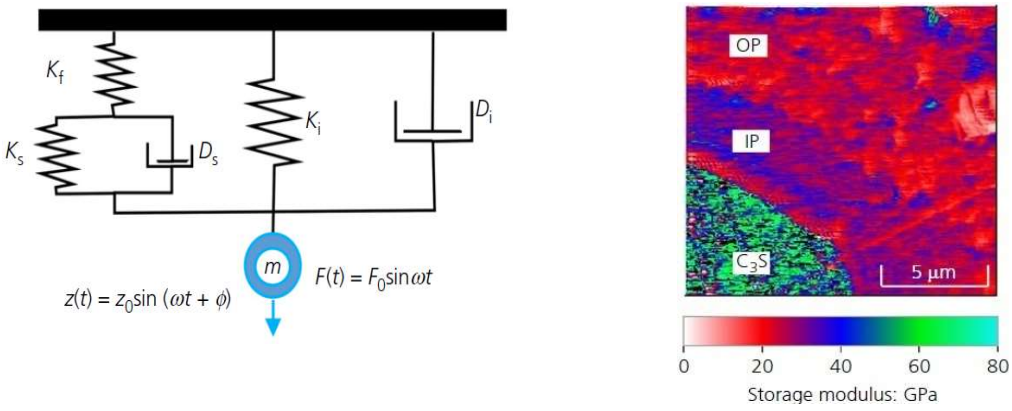

(a) Physical model (Gao, Wei & Huang 2017a)

(b) Storage modulus map (Gao, Wei & Huang 2017a)

Figure 2.4 Basic principle and results of the modulus mapping technique

2.1.3 **Atomic force microscopy-based nanomechanical mapping techniques**

The typical atomic force microscopy (AFM)-based nanomechanical mapping technique is PeakForce quantitative nanomechanical mapping (PeakForce QNM). The AFM mainly has three operating modes: contact mode, tapping mode and non-contact mode, in which tapping mode is a very widely used mode for study in ambient conditions or aqueous medium (Chatterjee, Gadad & Kundu 2010; Giessibl & Quate 2006). Presently, some new operating modes have been developed, for instance, the PeakForce Tapping mode. Different from the conventional tapping mode, where the vibration amplitude of the cantilever is kept constant and force curve is not available during the scanning process, the PeakForce QNM operates with PeakForce Tapping, which is characterized by accurately controlling of the maximum force during the acquisition of the force curves (Voss et al. 2015). This control method can protect the tip and sample from damage, and minimize the contact area between them. Therefore, a noticeable improvement in

resolution is achieved. By this technique, materials properties such as elastic modulus, adhesion, deformation and dissipation can be mapped with nanoscale resolution. Besides, high-resolution sample topography can be provided simultaneously.

The force versus tip-sample separation curve for a single cycle PeakForce tapping test is shown in Figure 2.5 (a). Mechanical parameters can be extracted from this curve (Pittenger, Erina & Su 2010; Smolyakov et al. 2016). The Derjaguin-Muller-Toporov (DMT) model given in Equation (2.17) is used to fit the retract curve (blue line) to obtain the reduced modulus E^*. Then, the elastic modulus of the sample E_s can be acquired by Equation (2.18). The typical elastic modulus contour map obtained by PeakForce QNM is revealed in Figure 2.5 (b).

$$F_{tip} - F_{adh} = \frac{4}{3} E^* \sqrt{R d^3} \tag{2.17}$$

$$E_s = (1-\nu_S^2)\left[\frac{1}{E^*} - \frac{1-\nu_{tip}^2}{E_{tip}}\right]^{-1} \tag{2.18}$$

where F_{tip} is the force on the AFM tip; the F_{adh} is the adhesion force between the tip and sample; R is the tip radius and d is sample deformation; E_{s} and ν_{s} are the Young's modulus and Poisson's ratio of the sample, respectively; E_{tip} and ν_{tip} are the corresponding parameters of the tip, respectively.

The spring constant for available cantilevers in PeakForce QNM range from 0.3 to 300 N/m, which enables force control from pN to μN (Pittenger, Erina & Su 2010). The detectable elastic modulus of the testing materials was in the range of 700 KPa to 70 GPa (Pittenger, Erina & Su 2010; Voss et al. 2015) or 1.0 kPa to 100 GPa (Lee et al. 2016) depending on instruments. In terms of indenter tip, the tip adopted in PeakForce QNM technique is smaller than that used in traditional nanoindentation and modulus mapping,

which helps to realize unprecedented high-resolution. Tip radius of 8 nm (Li, Kawashima, et al. 2016), 5 nm (Smolyakov et al. 2016), and even 2 nm (Smolyakov et al. 2016) were reported. Typical contact depth in cement-paste materials research was only 2-10 nm (Howind, Hughes & Zhu 2014; Li, Kawashima, et al. 2016). A test for 512 × 512 points on a 20 μm × 20 μm area was reported to take 17 minutes (Trtik, Kaufmann & Volz 2012). The test area is possible to reach 90 μm × 90 μm (5000 × 5000 points), but the test time would also rise to around one day (Trtik, Kaufmann & Volz 2012).

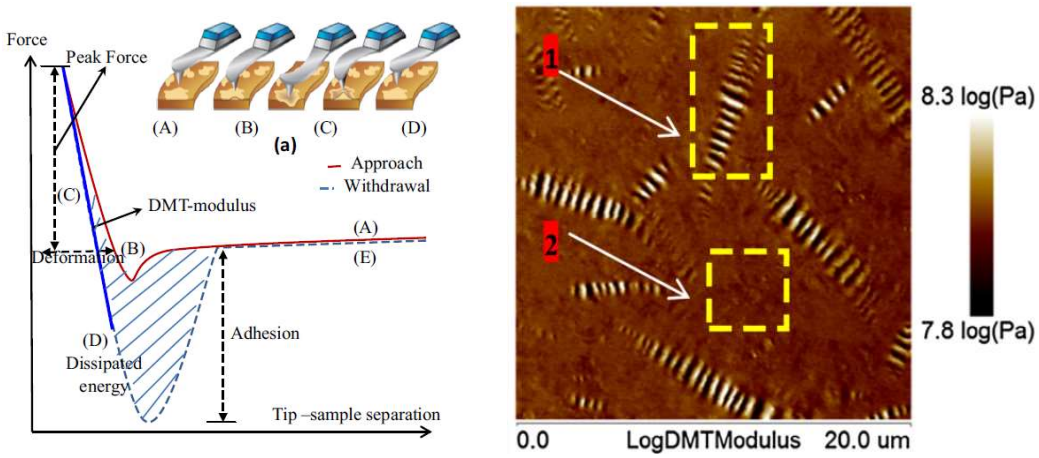

(a) Approach and withdrawal of AFM-tip in a single tapping cycle

(b) Elastic modulus contour map

Figure 2.5 Basic principle and results of the PeakForce QNM technique (Wang & Liu 2017)

2.1.4 **Nanoscratch technique**

Nanoscratch has become an increasingly used technique for nanoscale analysis and characterization of thin films, coatings and bulk materials, which can be used to detect the adhesion strength, scratch hardness and wear resistant, etc. (Beake, Harris & Liskiewicz 2013; Geetha et al. 2017; Mallikarjunachari & Ghosh 2016). Similar to indentation test, scratch is a traditional test method, but it is not frequently used for cement-based materials, especially for nanoscale scratch. The parameters specified in a

scratch test mainly include the maximum normal force, lateral scratch length and speed. As shown in Figure 2.6, during a nanoscratch test, an indenter is pressed into the specimen. Then it is pulled straight over the surface of the tested specimen at a given speed. There are two transducers in the scratch testing system. One acquires control force (normal force P) and displacement in the press-in direction, and the other records the force (lateral force F_{scr}) and the displacement in the movement direction (Xu, Corr & Shah 2017). Prescan and postscan under low loads are usually combined with the scratch test to provide surface topography before and after the scratch (Xu, Corr & Shah 2017; Xu & Yao 2011; Zhao et al. 2016). The penetration depth value (PD) can be calculated by subtracting the prescan displacement from the scratch displacement, which consists of the residual depth (RD) part and the elastic recovery (ER) part, as displayed in Figure 2.6 (b).

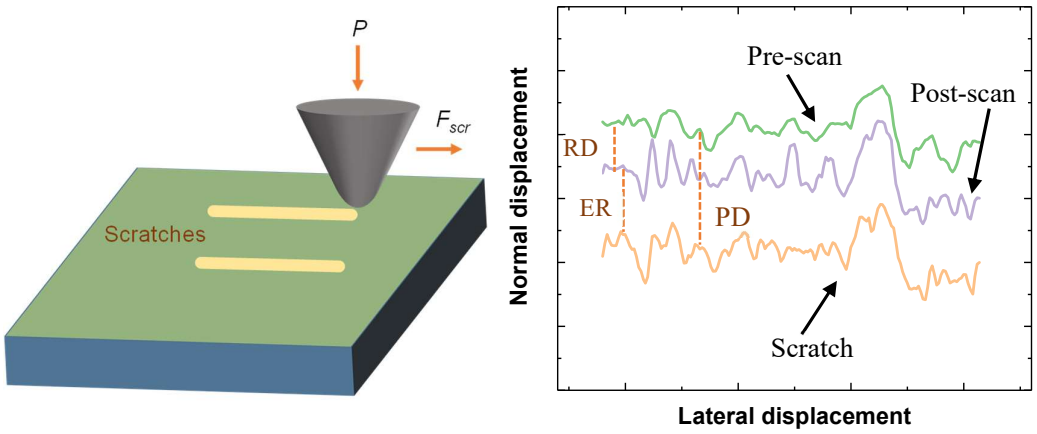

(a) Scratch tests (b) Scratch displacement

Figure 2.6 Basic principle and results of the nanoscratch technique (constant load model)

Based on the displacement, force and residue impressions acquired, scratch test can provide various information to reflect the elastic, plastic, fracture, etc. of materials, as described in below standards and literature (Liu, Zeng & Xu 2020; Wang et al. 2019). In a test, there are different modes to choose from. The main modes contain constant load

scratch tests, ramped load scratch tests and wear tests. Progressively increasing normal force is generally used for the study of coatings (ASTM C1624 − 05, ASTM D7187 – 20) and fracture toughness of bulk materials (Akono 2016; Akono, Chen & Kaewunruen 2018), while constant force model can be used for the test of scratch hardness of both coated surfaces and some bulk materials (ASTM G171 - 03). In the above three standards, the tip's geometry is specified as spherical or hemispherical, different from the three-sided pyramid of the generally used Berkovich tip in the indentation test. According to ASTM G171 – 03, the hardness HS_P and stylus drag coefficient D_{sc} can be determined by Equations (2.19) - (2.20). Currently, the scratch study of fracture toughness of cement-based materials are almost all microscopic scratch (Akono 2016; Akono, Chen & Kaewunruen 2018; Akono, Reis & Ulm 2011; Johnson et al. 2017; Ulm & James 2011), where the tip radius is 200 μm. The lack of nanoscratch tests may be due to the increased heterogeneity. Components would affect the nanoscale fracture results significantly. Besides, nanoscratch tests may sometimes not be severe enough to cause a fracture of some materials/phases. However, the tiny tip of nanoscratch technique makes it possible to test very small size objects, such as ITZs.

$$HS_P = \frac{kP}{w^2} \tag{2.19}$$

$$D_{sc} = \frac{F_{scr}}{P} \tag{2.20}$$

The current nanoscratch studies of the cement-based materials are mainly using the constant load nanoscratch, with the load applied commonly ranges from 2 to 8 mN and a scratch length ranges from 10 μm to 200 μm (Mao, Yao & Xu 2013; Xu, Corr & Shah 2017; Xu & Yao 2011, 2012; Zhao et al. 2016). The nanoscratch technique is characterized by continuous testing. Therefore, it can be expected to acquire more

intensive data than discrete point measurement methods. For instance, the data acquisition rate was reported to achieve as high as 192 kHz in NST³ nano scratch tester. Nanoscratch was found to have some advantages over AFM on measurement stability and less tip wear on hard materials (Beake, Harris & Liskiewicz 2013). It acts as a powerful tool in simulating single asperity contact in tribological experiments (Beake, Harris & Liskiewicz 2013). However, similar to the nanoindentation, there are usually large applied force and penetration depth in nanoscratch test. For instance, a 600 nm radius Berkovich indenter was reported for nanoscratch test (Xu, Corr & Shah 2017). Under the normal force of 4 mN, the average penetration depth in the C-S-H phase achieved about 466 nm. Thus, the large depth also leads to a large spacing between each scratch test. The spacing for microscope scratch hardness testing is no less than five scratch widths (ASTM G171 - 03).

2.1.5 **Applications and comparisons**

Nanoindentation has been widely used for the mechanical properties investigation of micro-constituents in Portland cement pastes, blended cementitious composites and alkali-activated cementitious materials, as well as properties investigation of ITZs in aggregate and fibre reinforced cementitious composites (Hu & Li 2015b). Numerical model (Gautham, Sindu & Sasmal 2017; Jingjing et al. 2015; Li et al. 2018; Luković, Schlangen & Ye 2015; Soliman, Aboubakr & Taha 2017; Xiao et al. 2012, 2013), micromechanical models (Constantinides & Ulm 2004a; Hu et al. 2014; Hughes & Trtik 2004; Jennings et al. 2007) and corresponding theories have also been developed based on the nanoindentation mechanical tests. In addition to the usual elastic properties, this versatile technique has also been used for other investigations such as strength (Němeček et al. 2016), fracture performance (Soliman, Aboubakr & Taha 2017; Zhang et al. 2016) and creep (Jones & Grasley 2011; Vandamme & Ulm 2013). Compared with the great

achievements acquired by nanoindentation, the research results obtained by the other techniques such as modulus mapping, PeakForce QNM and nanoscratch are far less. In fact, these powerful techniques have their own advantages, which can be displayed by comparing their testing characteristics and current applications.

The significant difference of these techniques shows in testing speed, testing spatial resolution, testing area, material damage, etc. For the testing speed, XPM improves the nanoindentation testing speed from the conventional one testing point in a few minutes to six testing points in a second. However, modulus mapping can achieve 109 points per second (256 ×256 points /10 min (Balooch et al. 2004)), and PeakForce QNM can achieve 257 points per second (512 ×512 points/17 min (Trtik, Kaufmann & Volz 2012)). The testing speed in nanoscratch depends on the specified scratch speed and data acquisition rate. Typically, for Agilent G200 Nano Indenter, the allowed maximum scratch speed is 2.5 mm/s, even if the data density is just 1 point/micron, it could reach 250 points per second. Thus, the maximum test speed of nanoscratch would be even far higher than PeakForce QNM. The test speed for this comparison is only the speed at which the test officially started. Other factors such as waiting time of thermal drift would also significantly increase the real testing time. Besides, small depth tests result in high requirements on surface roughness, parameters settings and tip calibration, which was reported to causes high preparation time for of modulus mapping (Němeček & Lukeš 2020) and PeakForce QNM (Howind, Hughes & Zhu 2014).

For the testing spatial resolution (spacing between test points), compared with nanoindentation, modulus mapping technique decrease the applied force and depth, which results in high resolution. In addition to the applied force, PeakForce QNM also decreases the tip radius to several nanometres, which realizes further improvement in resolution. Any discrete points testing method above would have a spacing, while scratch test

transformed the test into a continuous manner. For an instrument with high data acquisition rate, scratch testing could obtain more intensive data than the above techniques. However, it should be noted that the scratch technique only achieves high spatial resolution in the scratch direction, whereas modulus mapping and PeakForce QNM allow very small spacing in both *x* and *y* directions. Besides, the spacing in the discrete testing method is to avoid the influence of adjacent test points. There may be mutual interference between adjacent points in the continuous scratch tests.

For the testing area, there is almost no restriction for the grid size of conventional nanoindentation. For scratch, typically, the scratch length in Agilent G200 Nano Indenter can also reach up to 500 mm. However, the maximum scan area was decreased to 90 μm × 90 μm for XPM (Němeček & Lukeš 2020) and PeakForce QNM (Trtik, Kaufmann & Volz 2012), and 50 μm × 50 μm for modulus mapping (Balooch et al. 2004; Xu, Corr & Shah 2015a). Compared with XPM, modulus mapping and especially PeakForce QNM have smaller test depth, much denser data. As a consequence, the abundant test data significantly increased testing time for a given scan area. Therefore, modulus mapping and PeakForce QNM are mainly for very detailed local investigation, which are non-destructive test methods. As shown in Table 2.1, the test parameters set in some current studies can also clearly reveal the test characteristics of different techniques.

The current applications of these techniques were briefly summarized in Table 2.2. More details can be found in the author's published paper (Luo et al. 2018). The different advantages of techniques can be displayed by comparing their applications in the research of ITZ. It is evident that the aggregate, fibre and reinforcing steel/mortar ITZs investigated by nanoindentation all have a large size, for instance, 50 μm for aggregate/mortar interfaces (Mondal, Shah & Marks 2009) and approximately 200 μm for RPEC coated steel/mortar ITZs (Allison et al. 2015). The modulus mapping and

nanoscratch techniques were applied for small scale ITZ, the ITZ between unhydrated cement grain and C-S-H, which was detected to have sizes in the range of 155 nm to 3.3 μm (Mao, Yao & Xu 2013; Wei, Gao & Liang 2018b; Xu, Corr & Shah 2015a; Xu, Corr & Shah 2015b; Xu, Corr & Shah 2017). The PeakForce QNM was used to test the ITZ between C-S-H colonies in early stages of cement hydration, which was found to have a width less than 10 nm (Asgari, Ramezanianpour & Butt 2016). It is obvious that, due to the ability to set large grid, nanoindentation has advantages in properties investigation of large ITZs, while modulus mapping and PeakForce QNM techniques can reveal very detailed local mechanical information at decreased scales. Nanoscratch shows similar advantages as modulus mapping in testing small scale objects. In fact, it can also investigate large size ITZ as that of nanoindentation.

The advantages of these mechanical mapping techniques have also been played in other aspects. Due to the feature of non-destructive test with dense test points, modulus mapping has been used for identification and then size measurement of phases, such as for inner product and outer product C-S-H in cement paste (Wei, Liang & Gao 2017). Similarly, PeakForce QNM also has the potential to identify phases (Trtik, Kaufmann & Volz 2012). Besides, the ultra-high-speed scanning capability of PeakForce QNM was used to test the early age properties of cement paste (Asgari, Ramezanianpour & Butt 2016), where the topography and Young's Modulus of cement paste after 10 min, 14 min and 18 min of hydration were investigated. Considering the different advantages, these techniques can be combined used so as to extend the information to be obtained from the nanomechanical characterization. For instance, modulus mapping was helped to identify different phases, which was followed by traditional nanoindentation test on the target individual phase (Wei, Gao & Liang 2018b). In addition to using multiple nanocharacterization techniques, there is a growing trend for the combination of

nanoscience and nano-engineering approaches (Luo et al. 2018). A typical case is the application of nanomechanical characterization to the study of nanomaterial modified cement-based materials. The combination could lead to potential breakthroughs for developing next generation of multifunctional and high performance cementitious materials.

Table 2.1 Typical parameters set in nanomechanical testing techniques

Literatures	Applied force (μN)	Pixel spacing (μm)	Testing area/length (μm)	Testing methods
Li et al. (2016)	1200	3 ×3	100 ×100	NI
Howind, Hughes & Zhu (2014)	1000	3 ×3	87 ×87	NI
Xu, Corr & Shah (2015b)	1200	3 ×5	30 ×10	NI
Wei, Liang & Gao (2017)	4 ±3.5	0.137 ×0.059	35 ×35	MM
Xu, Corr & Shah (2015b)	8 ±3.5	0.059 ×0.059	15 ×15	MM
Wei, Liang & Gao (2017)	4 ±3.5	0.028 ×0.028	7.0 ×7.0	MM
Trtik, Kaufmann & Volz (2012)	3.0	0.039 ×0.039	20 ×20	PF QNM
Howind, Hughes & Zhu (2014)	—	0.010 ×0.020	5.0 ×5.0	PF QNM
Li et al. (2016)	0.05	0.010 ×0.010	5.0 ×5.0	PF QNM
Zhao et al. (2016)	2000	—	10	NS
Xu, Corr & Shah (2017)	4000	—	12	NS
Xu & Yao (2012)	8000	—	200	NS

Note: NI is nanoindentation; MM is Modulus mapping; PF QNM is PeakForce QNM; NS is nanoscratch.

Table 2.2 Summary of the advanced nanomechanical characterization techniques for the study of cement-based materials

Techniques	Commonly used testing parameters	Current common applications	Main advantages/concerns
NI	Young's modulus; Hardness; Indentation load; Indentation depth	Mechanical study of phases; Various tests at micro- and nano-scale (fracture, etc.) ITZs: aggregate, fibre and reinforcing steel/mortar.	Measure in a large area; Relatively mature theory for testing cement paste Multiphase interaction; Large spacing restricts precise measurement
MM	Storage modulus; Loss Modulus; Contact force; Displacement amplitude	Identification and then mechanical/size measurement of phases; ITZs: unhydrated cement grain/C-S-H	Non-destructive, quick and high resolution mapping; Phase identification and relevant small scale research Local test; Test results may be more easily affected by the sample surface, tip and microstructural heterogeneity
PF QNM	Young's modulus; Adhesion force; Energy dissipation; Maximum deformation	Properties investigation of phases and small scale research like mechanical/size measurement of C-S-H colonies; ITZs: aggregate/cement paste; C-S-H colonies/ C-S-H colonies	Non-destructive; Higher resolution and faster mapping than nanoindentation and modulus mapping; Phase identification; Extremely small scale research; Local test; Limited modulus test range; Test results may be more easily affected by the sample surface, tip and microstructural heterogeneity
NS	Deformation; Friction coefficient; Loads/critical loads; Displacement	Mechanical properties study of phases; ITZs: unhydrated cement grain/C-S-H; bond strength	Quick and continuous test; Adhesion strength/wear resistant/fracture No direct elastic modulus; Multiphase interaction

2.2 Nano/microscale mechanical characterization of geopolymer concrete

Due to the environmental benefit of fly ash-based geopolymer, it has attracted extensive studies covering both macro properties (Ling et al. 2019; Rashad 2014; Reddy, Dinakar & Rao 2016; Tang et al. 2019), microstructure characterization and mechanisms analysis (Khale & Chaudhary 2007; Provis, Palomo & Shi 2015). Even books were published to guide academic research and engineering application of this kind of material (Provis & Van Deventer 2013; Shi, Roy & Krivenko 2003). Although there is progress in the understanding of geopolymer from micro and nanoscale resorting new model, as well as advanced characterization techniques such as Fourier transform infrared (FTIR), nuclear magnetic resonance (NMR) spectroscopy and X-ray microtomography (Provis et al. 2012; Provis, Palomo & Shi 2015), no sufficient work was reported to investigate the nano/micromechanical properties of geopolymer.

2.2.1 **Geopolymer matrix**

The microstructure of geopolymer matrix can be typically observed in Figure 2.7. The gel phase is the most crucial component of cementitious binders. The calcium silicate hydrate C-S-H gel in Portland cement paste and blended cement pastes has been widely studied by various nanomechanical testing techniques. For the counterpart N-A-S-H gel, although there are nanoindentation studies for the elastic modulus (Chanda et al. 2018; Das et al. 2015; Lee, Vimonsatit & Chindaprasirt 2016; Ma, Ye & Hu 2017; Nedeljković et al. 2018; Němeček, Šmilauer & Kopecký 2011), hardness (Chanda et al. 2018; Lee, Vimonsatit & Chindaprasirt 2016), creep (Lee et al. 2018), and fracture toughness (Lyngdoh et al. 2020), the amount and scope of research is far less than that of C-S-H. The insufficient studies not only leave gaps but also lead to inconsistent results. Typically,

based on the investigation on heat-cured alkali-activated fly ash (AAFA), ambient cured AAFA and heat-cured alkali-activated metakaolin, study (Němeček, Šmilauer & Kopecký 2011) found that the mature N-A-S-H gels (6 months) show almost the constant intrinsic Young's modulus of 17-18 GPa, which is independent of the precursor material and the temperature curing regime. In other studies, the elastic modulus of N-A-S-H gel was reported to be 16.3 GPa (Das et al. 2015), 4.44-16.78 GPa (after 28-day) (Lee, Vimonsatit & Chindaprasirt 2016) and 11-25 GPa (at 28 days) (Ma, Ye & Hu 2017). Thus, the results are different in these studies and also varied in a large range in the same study. This phenomenon is similar to nanomechanical investigation for Portland cement paste. There are a plenty number of studies indicating that the elastic modulus of C-S-H is one of intrinsic material properties and does not depend on water to cement ratio, type of cement, admixtures, heat curing, etc. (Bernard, Ulm & Lemarchand 2003; Constantinides & Ulm 2004b; Jennings et al. 2007; Sorelli et al. 2008). Besides, when comparing cement paste with different curing age, tests at 28 d (DeJong & Ulm 2007; Jennings et al. 2007) reveal similar modulus results as those at longer time of curing of 5 months and even 1 year (DeJong & Ulm 2007). However, some other studies found that the elastic modulus of cement paste is influenced by the water to cement ratio (Hu et al. 2014), fly ash (Hu 2014). Besides, a review paper indicates that discrepancy was found among results reported by different researchers (Hu & Li 2015b).

The different phenomenon above for geopolymer may be attributed to the difference between mature and immature gel. However, it shall also be noticed that different testing, analysis methods and different parameters were adopted in the above studies. For the statistical analysis of geopolymer, the LSE method is normally adopted while different bin sizes such as 2 GPa (Ma, Ye & Hu 2017) and 1 GPa (Das et al. 2015; Němeček, Šmilauer & Kopecký 2011) and different phase numbers of 3 (Ma, Ye & Hu 2017) or 4

(Lee, Vimonsatit & Chindaprasirt 2016; Němeček, Šmilauer & Kopecký 2011) were used. The different parameters also possibly affect the results. Therefore, further studies are necessary on the microstructure composition and micromechanical properties of AAFA paste, and also the nanoindentation testing and data analysis method themselves. After all, the correct understanding of the elastic modulus of N-A-S-H should be based on the premise that the test and data deconvolution analysis method are consistent and reliable to eliminate errors caused by the analysis process.

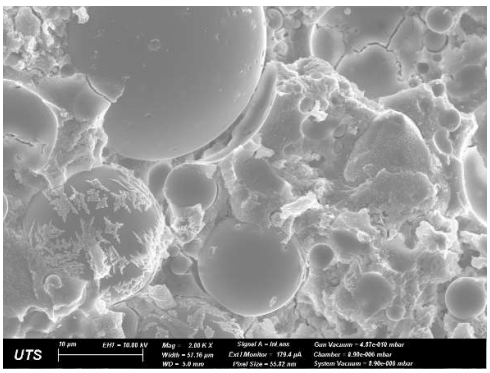

Figure 2.7 Geopolymer matrix

The investigation of the effects of design parameters such as silica modulus on the properties of N-A-S-H gels is vital since it is closely linked to the engineering performance of geopolymer. In addition to optimizing the general design parameters, some studies modified geopolymer with nano-engineering approaches. Typically, geopolymer strength was improved by the addition of nano-SiO_2 (Çevik et al. 2018; Deb, Sarker & Barbhuiya 2016; Riahi & Nazari 2012), nano-Al_2O_3 (Alomayri 2019), nano-TiO_2 (Duan et al. 2016), nano-clay (Assaedi, Shaikh & Low 2016) and carbon nanotubes (Abbasi et al. 2016). Higher durability such as enhanced sulphuric acid attack resistance (Deb, Sarker & Barbhuiya 2016), and lower water absorption (Assaedi, Shaikh & Low 2016) were realized by incorporating nano-SiO_2 and nano-clay, respectively. However,

there is no nanomechanical testing to help understand the changes in the micro- and nanoscale properties of the modified geopolymer.

Considering the above aspects, in this study, chapter 4 focuses on the statistical nanoindentation technique. In chapter 5, whether the N-A-S-H gel is an intrinsic material property are investigated and discussed. In chapter 6, the effects of the most commonly used nanomaterials nano-SiO_2 and nano-TiO_2 on micromechanical properties and microstructure of geopolymer are studied. In chapter 5 and 6, some aspects of the SNT are further discussed.

2.2.2 **Interface transition zone in geopolymer concrete**

The research on the interface transition zone between aggregate and paste of geopolymer is limited. The limited studies seem to indicate that the ITZ in geopolymer concrete is not a distinct weak region as the ITZ in Portland cement concrete. A pull-out study showed that for most fibres, the bond strength in fly ash based-geopolymer mortars is stronger than that in Portland cement mortar (Bhutta et al. 2017). Similarly, fly ash based-geopolymer paste (Khedmati et al. 2018) and metakaolin/GGBFS-based geopolymer paste (Peng et al. 2019) were found to have better bond with aggregate than that of Portland cement paste. At the micro scale, scanning electron microscope (SEM) observation revealed that no significant ITZ was identified between the siliceous aggregates and fly ash-based geopolymer (Lee & Van Deventer 2004). The strong interface could be attributed to the alkali solution used, especially the presence of soluble silicates (Lee & Van Deventer 2004, 2007). By using SEM, the ITZ in sodium silicate-activated slag was also reported to be more homogeneous (San Nicolas et al. 2014) and have less porosity (Shi & Xie 1998) than that in Portland cement mortars.

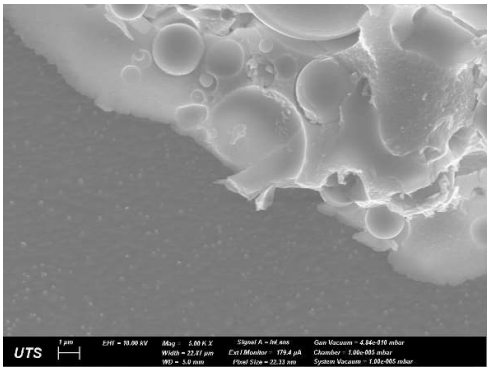

Figure 2.8 The interface between aggregate and geopolymer matrix

One of the most important aspects to understand ITZ is its mechanical properties. Owing to the small width of ITZ, micro- and nanomechanical test techniques are important tools to quantitatively evaluate interfacial properties. At present, microindentation and nanoindentation (Allison et al. 2015; Khedmati, Kim & Turner 2019; Khedmati et al. 2018) have been used to investigate the properties of ITZ in geopolymer (Allison et al. 2015; Khedmati, Kim & Turner 2019; Khedmati et al. 2018; Liu et al. 2016; Peng et al. 2019) and alkali-activated slag (Ding, Dai & Shi 2018; Ji et al. 2017; Shi & Xie 1998). Nanoindentation studies on fly ash-based geopolymeric recycled aggregate concrete show that the new ITZ formed between geopolymer and old cement paste is not an obvious weak region (Khedmati, Kim & Turner 2019; Liu et al. 2016). Geopolymer even makes the pre-existing old ITZ achieve similar micromechanical properties as surrounded paste (Khedmati, Kim & Turner 2019). However, the ITZ in metakaolin/GGBFS-based geopolymer was found to have lower microhardness than paste (Peng et al. 2019). For alkali-activated slag, a study indicated that the average Vickers micro-hardness of ITZ was 76.8% of bulk paste (Ding, Dai & Shi 2018), while another study found that, the microhardness of ITZ could be either higher or lower than paste, which depends on the alkali solution used (Ji et al. 2017).

There are comparison studies between ITZs in geopolymer and Portland cement concretes by using grid nanoindentation (Khedmati, Kim & Turner 2019; Khedmati et al. 2018; Liu et al. 2016). Grid nanoindentation tests revealed that for concrete made with nature aggregate (Khedmati et al. 2018), the well-bonded ITZ in PC paste does not significantly differ in elastic modulus and hardness compared to the bulk paste. The modulus and hardness of ITZ in geopolymer were more heterogeneous than that in Portland cement concrete. When recycled aggregate was used, one study indicated that the ITZ between new paste and old mortar coated recycled aggregate in Portland cement concrete was about 20 μm according to the micromechanical distribution, but no obvious weak ITZs were found in geopolymer concrete (Khedmati, Kim & Turner 2019), whereas another study found no distinct new ITZ in both Portland cement concrete and geopolymer concrete (Liu et al. 2016).

When applying grid nanoindentation in the study of ITZ, the ITZ sample is generally randomly selected from one or several local areas of a real concrete sample. It is known that the ITZ is highly heterogeneous in Portland cement concrete. In Portland cement concrete, ITZs are different depending on the aggregate investigated and are also heterogeneous around the same aggregate (Scrivener, Crumbie & Laugesen 2004). For instance, internal bleeding beneath an aggregate would lead to different water to cement ratio and then different properties of ITZ when compared with ITZ in other locations surrounding the aggregate. Moreover, the degree of internal bleeding is different for aggregates in PC concrete with different shape and size (Elsharief, Cohen & Olek 2003; Mehta & Monteiro 2017). Mixture process would also lead to heterogeneous of ITZs. The complex nature of ITZ causes great difficulties in quantitative testing.

It is a very time-consuming and challenging task to determine an “average” property of ITZ even by doing BSE image statistical analysis in a real concrete (Scrivener 2004;

Scrivener, Crumbie & Laugesen 2004). Therefore, most of quantitative ITZ research is conducted using fine aggregate with small size in mortar samples. Even for mortars (Diamond 2001), when the whole ITZ surrounding a sand particle was characterized by BSE analysis, the number of sand grains used for test would be few due to the large test workload. Alternatively, if too many sand particles were selected for analysis, only few regions around the sand particle with certain long could be taken for BSE analysis. The workload levels increase dramatically for a similar study of ITZ in coarse aggregate by BSE. Therefore, comparative studies of ITZ between different concrete samples by BSE would be either not reliable enough or involved too much workload. Different from BSE technique where an image captures information from a several hundred microns by several hundred microns area, the indentation test obtains just one point from a several minutes test. It is impossible for nanoindentation to face the challenge that can't even be solved by BSE.

Although the heterogeneous in geopolymer may be lower than Portland cement concrete when the alkali silicate solution is used, there is no doubt that the ITZ of geopolymer concrete would still show high heterogeneity. Therefore, the ITZ part of this thesis aims to understand the ITZ properties in geopolymer and also to promote the appropriate application of nanomechanical testing techniques in interface research. For the ITZ properties, the properties differences of ITZ between geopolymer and Portland cement concrete were investigated in Chapter 7. The effects of the critical design parameter silica modulus on the ITZ micromechanical properties were studied in Chapter 8. The heterogeneous of ITZ at different location of an aggregate particle was analyzed in Chapter 9. For the test method, in Chapter 7, modelled ITZ was prepared, which greatly decreased the heterogeneity of the ITZ. In addition, large force nanoindentation was used to activate a large involved range and more homogeneous material response. In Chapter

8, based on the neat ITZ provided in modelled ITZ sample, the nanoscratch technique with the capabilities of quick testing a very long linear range was introduced. In Chapter 9, nanoscratch and nanoindentation are combined used for investigation. Nanoscratch provides a rapid evaluation and comparison of different ITZs, while nanoindentation provides the important elastic modulus information. The test bias and test strategies for complex ITZ is proposed.

2.2.3 **Brief summary**

Only limited studies have been conducted to investigate the nano/micromechanical properties of geopolymer. Although elastic modulus, hardness, fracture toughness, etc., of N-A-S-H gel were reported for geopolymer matrix and comparison of ITZ and matrix were performed, the outcomes are too few to be used for the thorough understanding of geopolymer. In addition, test techniques need to be improved to allow more scientific characterization of geopolymer concrete.

CHAPTER 3. MATERIALS AND TESTING METHODS

3.1 Raw materials

Geopolymer was synthesized by alkali-silica activation of low calcium fly ash. Alkali silicate solution used is the mixture of sodium silicate and sodium hydroxide solution. The composition of sodium silicate is 14.7% of Na_2O, 29.4% of SiO_2 and 55.9% of H_2O (Ms=2.07). The sodium hydroxide solution was prepared by dissolving sodium hydroxide pellets into water. After cooled down, sodium hydroxide solution was incorporated into sodium silicate solution to adjust the silica modulus to the designed value. The chemical composition of fly ash is shown in Table 3.1. In Chapter 7, the Portland cement used for comparative study has the chemical composition given in Table 3.2. Mortar samples were prepared based on river sand with a fineness modulus of 2.1. For modelled concrete samples, the coarse aggregate used was from a limestone rock contained mainly calcite as shown in Figure 3.1. Several small ϕ 25 mm cylinders were drilled out from the rock and then cut into slices.

Table 3.1 Chemical composition of fly ash

Oxide	Al_2O_3	CaO	SiO_2	Fe_2O_3	K_2O	MgO	Na_2O	MnO	P_2O_5	TiO_2	LOI
Weight (%)	25.21	1.73	64.55	2.85	1.47	0.41	0.48	0.07	0.19	0.91	1.54

Table 3.2 Chemical composition of Portland cement

Oxide	Al_2O_3	CaO	SiO_2	Fe_2O_3	K_2O	MgO	Na_2O	SiO3	LOI
Weight (%)	4.78	64.18	19.67	3.10	1.11	0.91	0.11	2.37	3.77

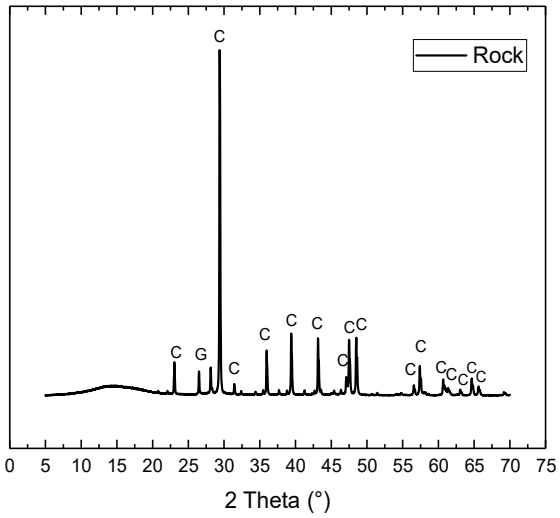

Figure 3.1 X-ray diffraction patterns of rock. C: calcite, G: graphite.

3.2 Testing techniques

3.2.1 **Nanoindentation and nanoscratch**

The nanomechanical testing instrument used is Agilent G200 Nano Indenter, as shown in Figure 3.2. Nanoindentation and nanoscratch tests were performed on the same instrument but with different indenter tips. A Berkovich tip with a radius of curvature of 20 nm was adopted for nanoindentation test. A hemispherically-tipped, conical stylus with a radius of 5 μm and apex angle of 120° was chosen for the nanoscratch study. One thing to note is that the tip size in the scratch test is as large as several microns. The tip size specified in a nanoscratch-based standard, ASTM D7187 − 15 (Standard Test Method for Measuring Mechanistic Aspects of Scratch/Mar Behavior of Paint Coatings by Nanoscratching), is in the range of 1 to 100 microns. Thus, scratch in this study by using 5 μm tip is still called as nanoscratch.

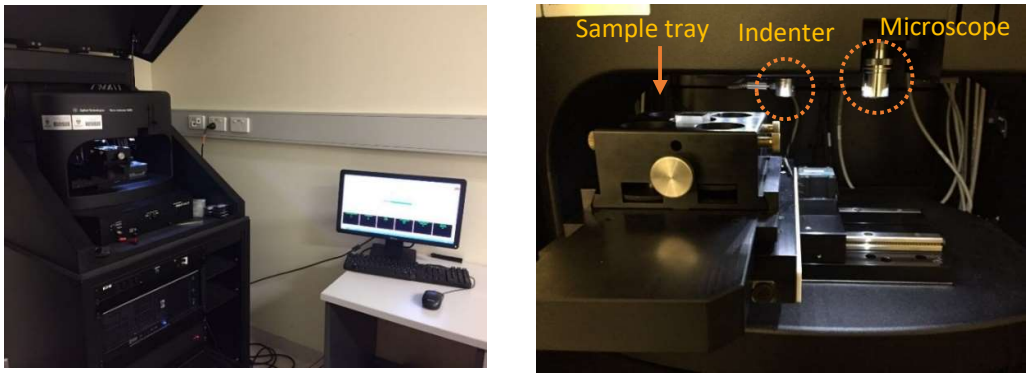

(a) Instrument (b) Test area

Figure 3.2 Agilent G200 Nano Indenter

3.2.2 **Scanning electron microscope (SEM) and X-ray diffraction (XRD)**

Zeiss EVO LS15 SEM equipped with an energy dispersive X-Ray spectroscopy (EDS) detector was used for the microstructure observation and element analysis. The scanning electron (SE) model, BSE model and EDS tests were all operated under an accelerating voltage of 15 kV.

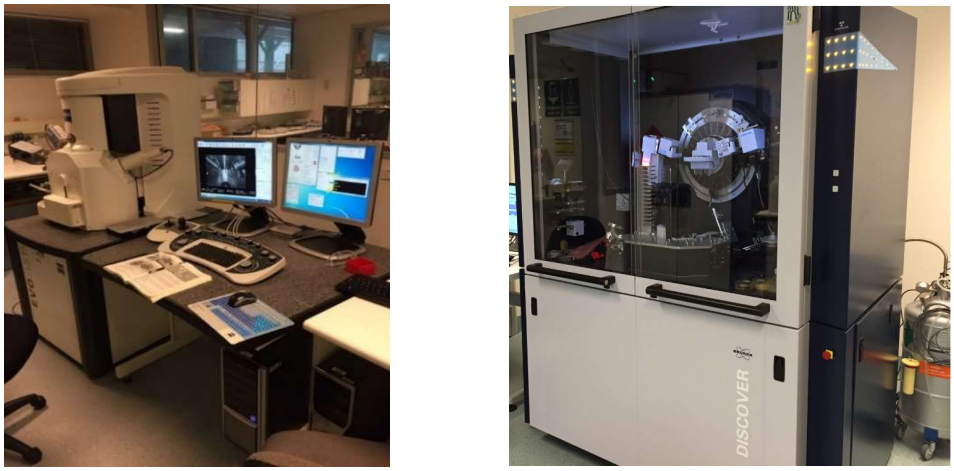

(a) Zeiss EVO LS15 (b) Bruker D8 Discover diffractometer

Figure 3.3 Scanning electron microscope (SEM) and X-ray diffraction (XRD)

Zeiss Supra 55VP with high resolution was adopted for further SE image observation of geopolymer to the nanoscale. The corresponding accelerating voltage was 5 or 10 kV. The crystals in raw material fly ash and reacted geopolymer were detected by Bruker D8 Discover diffractometer. The step size and 2θ range were 0.02° and 5-70°, respectively.

3.2.3 **Thermogravimetric analysis (TGA) and heat of reaction**

The heat of reaction was measured by TAM Air Isothermal Calorimeter. In order to simulate the heat curing of geopolymer, the temperature condition in the isothermal calorimeter was pre-set and kept at 65 °C for testing. TGA test was conducted by STA449 F5 JUPITER. Vacuum dried powder was heated from 25 °C to 1000 °C with a heating rate of 10 °C/min.

3.2.4 **Compressive testing and Workability**

For compressive strength, cubic mortar samples were tested at 28 days in accordance with the ASTM C109 (ASTM 2016). The workability of fresh geopolymer mortars was tested by flow table test as described in ASTM C1437 (ASTM 2015).

CHAPTER 4. INVESTIGATION AND DISCUSSION ON STATISTICAL NANOINDENTATION TECHNIQUE

4.1 Introduction

Although there are new techniques such as modulus mapping and PeakForce quantitative nanomechanical mapping that can avoid the large interaction volume of nanoindentation, these techniques are only available on some specific instruments. Besides, these techniques with very shallow penetration depth have high requirement on sample preparation and tip calibration. Typically, the sample for PeakForce quantitative nanomechanical mapping testing is not prepared by the regular polishing method, but by advanced focussed ion beam (FIB) milling (Trtik, Kaufmann & Volz 2012). In fact, the FIB technique is also concerned for re-deposition of sputtered materials, Ga+ ion damage and heat damage of microstructure (Chen et al. 2015; Ishitani & Kaga 1995; Němeček et al. 2016), which may affect test results, especially for surface nanomechanical testing. The small depth would also increase the risk of interference from the microstructural heterogeneity of the constituent (*d* criterion in Equation (2.9)). Additionally, the local information provided by these mapping techniques is not as good as the large size grid nanoindentation to represent the overall information of the materials for a comparative study. Thus, there is no perfect technique to determine the nano/micromechanical properties of highly heterogeneous materials. The regular statistical nanoindentation technique is currently still the most widely used method.

For SNT, the LSE method was questioned for its robustness (Lura, Trtik & Münch 2011): the global optimum is hard to be found and significantly different results would be generated from different local optimum; the fewer number of phases of 2 and 3 are even

found to better fit the frequency distribution histogram than 4 in Portland cement paste. In addition to the LSE method, maximum likelihood estimation (MLE) is another method that can be used for deconvolution analysis. However, the MLE method gains much less attention than LSE. Only limited studies used this method which can be typically found in literatures (Davydov, Jirásek & Kopecký 2011; Hu & Li 2015a; Thomas et al. 2018; Ulm et al. 2010). Besides, based on the MLE method, it was found that the results obtained were not a pure phase but a mixture of phases, particularly calcium silicate hydrate (C-S-H) and calcium hydroxide (CH) (Davydov, Jirásek & Kopecký 2011). The LSE method is still the mainstream technique used for deconvolution of statistical nanoindentation data, which is manifested in the study of geopolymer.

Based on the geopolymer sample synthesized with different alkali concentrations, the validity of the LSE method and the MLE method is examined by investigating the effect of bin size, number of phases and grid number on the results. Results indicate that the model estimated by the MLE method can effectively reflect the micromechanical distribution of alkali-activated fly ash (AAFA) geopolymer. The number of components needed to separate the N-A-S-H gel is sometimes more than the commonly used 3 or 4, depending on the sample and test factors. The gel phase does not always display as a prominent peak in the histogram and is easy to be mixed with other adjacent peaks even if the bin size is small, indicating the challenges of employing the LSE method to investigate the gel phase in highly heterogeneous materials, such as geopolymer. The MLE method is found to have significant advantages over the LSE method. Besides, the gel phase with significant inclusions removed is obtained by MLE. However, the conventional method of using MLE would not be able to obtain the gel phase. The advantages of the MLE method can only be displayed based on a premise that a "compromise approach" is adopted. In addition, following the inspirations in the

development of the high-resolution techniques mentioned, a tiny Berkovich tip with a radius of 20 nm is used in this study to decrease the involved volume.

4.2 Experimental and analysis methods

4.2.1 Sample preparation

Different samples with Na_2O to fly ash weight ratio of 6%, 8%, and 10% were prepared. For these samples, constant silica modulus of 1.0 in alkali solution, as well as constant water to solid ratio of 0.338 were adopted to keep other factors similar for each kind of sample. Fly ash was mixed with corresponding alkali solution for 5 min and cast into cubic plastic moulds with the size of 50 mm ×50 mm ×50 mm. The samples were vibrated for 3 min and sealed by plastic film. Then, they were put into an oven with heat treatment of 70 °C for 24 hr. After that, samples were taken out of the oven and put into a standard curing cabinet for further curing (temperature of 20 °C and RH of 95%).

The centre part of cubic specimens was taken out and cut into slices with the size of around 10 mm ×10 mm ×5 mm. Then, these samples were embedded in cold-mounting epoxy resin with one surface exposed to air. After the epoxy solidified, these samples were successively ground on 320, 600 and 1200 grits abrasive papers with each grade lasted for 10 min and then polished with a small force for 40 min by 0.3 μm alumina and 40 min by 0.05 μm cerium oxide slurry to obtain a smooth surface. After each grade of polishing, samples were cleaned in an ultrasonic bath with isopropanol for 3 min to remove particles on their surface. Samples were put in a vacuum oven with a temperature of 50 °C for 12 hr to dry and then stored in a vacuum desiccator until testing at 28 days.

4.2.2 Grid nanoindentation test

Nine 10×10 grid nanoindentation were performed with a grid spacing of 15 μm. The nanoindentation depth can be determined by satisfying both the scale separability

condition and roughly one-tenth rule of thumb given in Equation (2.9) (Constantinides & Ulm 2007), where d is the largest heterogeneity of geopolymer phases and D is the characteristic size of microstructure. Besides, enough depth is also necessary to avoid interference from surface roughness (Miller et al. 2008; Zhai et al. 2016). For the investigation of N-A-S-H gel, it was reported that the N-A-S-H gel consists of particles with a diameter of about 5 nm (Provis, Lukey & van Deventer 2005). As for characteristic microstructure size, more than about 4 μm can be found even just 7% Na_2O (Ms=1) is used (Lloyd et al. 2009). After several attempts, trapezoid loading with the peak force of 2 mN was adopted, with an average penetration depth of 228.21 nm. The loading procedure adopted in this test would be suitable for achieving balance to satisfy the scale separability condition and avoid the effect of surface roughness and multiple phases' responses. Similar loading procedures have also been adopted by other studies for Portland cement paste and AAFA (Allison et al. 2015; Hu & Li 2015a; Khedmati et al. 2018; Miller et al. 2008; Vandamme, Ulm & Fonollosa 2010), making it easy for comparison. In this study, the constant Poisson's ratio of 0.2 was set for testing. According to nanoindentation load-penetration curves and some basic parameters, nanoindentation modulus E and hardness H for material at each testing point can be calculated by Equations (2.1) to (2.3). All testing points with abnormal load-penetration curves were deleted before the subsequent deconvolution analysis.

4.2.3 **Deconvolution technique**

Maximum likelihood estimation (Bishop 2006) was adopted for the result analysis. The micromechanical properties distribution of AAFA was assumed as a Gaussian mixture model as in Equation (4.1). Each phase was treated as two-dimensional Gaussian distribution with probability density function shown as in Equation (4.3), where $x = (M, H)^T$ is a column vector.

$$p(\mathrm{x}) = \sum_{k=1}^{K} \pi_k \mathrm{N}\ (\mathrm{x} \mid \mu_\mathrm{k}, \Sigma_k) \tag{4.1}$$

$$\sum_{k=1}^{K} \pi_k = 1 \tag{4.2}$$

$$\mathrm{N}\ (\mathrm{x} \mid \mu, \Sigma) = \frac{1}{\sqrt{\det(2\pi\Sigma)}} \exp\left(-\frac{1}{2} (\mathrm{x} - \mu)^{\mathrm{T}}\, \Sigma^{-1} (\mathrm{x} - \mu) \right) \tag{4.3}$$

where π_k, μ_k and Σ_k are the corresponding weighting coefficient, mean value and covariance of the k[th] component, respectively.

The log-likelihood function is given by Equation (4.4) and the mean value (μ), weighting coefficient (π) and covariance matrix (Σ) that make the likelihood function achieve the maximum value for the data set of observations are the estimated parameter values.

$$\ln L = \sum_{n=1}^{N} \ln \left\{ \sum_{k=1}^{K} \pi_k \mathrm{N}\ (\mathrm{x}_n \mid \mu_k, \Sigma_k) \right\} \tag{4.4}$$

EM algorithm was used to achieve this purpose. The *E* step is shown in Equation (4.5) and *M* step shown in Equations (4.6) to (4.8), where $x_n = (M_n, H_n)$ is a row vector with the modulus and hardness data from the n^{th} nanoindentation point. In the E step, $\gamma(z_{nk})$ is a posterior probability that can be regarded as the responsibility that component *k* takes for 'explaining' the observation x_n (Bishop 2006), or understood as the probability of the given n^{th} nanoindentation point belongs to the k^{th} component in this case. In the *M* step, the parameters were re-estimated by the current responsibilities. Iteration calculation of *E* and *M* steps was made until the convergence of the log-likelihood. K-means algorithm was combined used to find the suitable initial values for parameters to decrease the time for iteration calculation. At least 1000 times of repeated calculation with random initial input values were made to find global maximum log-likelihood function value. Then the final estimated parameter values and GMM model were determined.

$$\gamma(z_{nk}) = \frac{\pi_k \mathrm{N}\,(\mathrm{x}_n \mid \mu_k, \Sigma_k)}{\sum_{j=1}^{K} \pi_j \mathrm{N}\,(\mathrm{x}_n \mid \mu_j, \Sigma_j)} \tag{4.5}$$

$$\mu_k = \frac{1}{N_k} \sum_{n=1}^{N} \gamma(z_{nk})\, \mathrm{x}_n \tag{4.6}$$

$$\Sigma_k = \frac{1}{N_k} \sum_{n=1}^{N} \gamma(z_{nk})(\mathrm{x}_n - \mu_k)(\mathrm{x}_n - \mu_k)^{\mathrm{T}} \tag{4.7}$$

$$\pi_k = \frac{N_k}{N} \tag{4.8}$$

$$N_k = \sum_{n=1}^{N} \gamma(z_{nk}) \tag{4.9}$$

$$\mathrm{BIC} = k \ln n - 2 \ln L \tag{4.10}$$

where π_k, μ_{k} and Σ_k are the corresponding weighting coefficient, mean value and covariance of the k^{th} component, respectively. N is the total number of observed data, corresponding to nanoindentation testing data here.

In theory, GMM model can fit any type of probability distribution and higher order of model tends to fit given distribution better. In order to penalize the overfitting errors, Bayesian Information Criterion (BIC) was adopted (Bishop 2006; Schwarz 1978), which is known for more heavily penalizing the model complexity than the Akaike Information Criterion especially when the amount of data N is huge. The model with minimum BIC value is the target model that has a suitable number of components. After the above calculation, the raw testing data was clustered, which was based on the estimated parameters and model by MLE. For a given nanoindentation data point, which belongs to the component where achieves the maximum posterior probability. Confidence ellipses under different confidence levels of 95%, 80% and 70% for each estimated component model were also plotted.

4.3 Deconvolution results

4.3.1 **Deconvolution for AAFA-10%**

The deconvolution results for AAFA-10% were summarized in Table 4.1, where *K* is the number of components, *M* is elastic modulus, *H* is hardness and *f* is proportion.

Table 4.1 Deconvolution of AAFA-10% (clustered blue points for *K*=2, 4, 5 and 12)

K	*M* [GPa]	*H* [GPa]	*f*	BIC	*C*	
2	20.80	1.26	44.64%	9033.55	53.86	3.33
					3.33	0.27
3	20.26	1.20	40.29%	8825.91	49.13	3.01
					3.01	0.23
4	19.83	1.16	38.04%	8762.12	46.91	2.85
					2.85	0.22
5	15.63	0.77	10.30%	8733.89	12.13	0.72
					0.72	0.06
6	15.73	0.77	10.41%	8715.35	12.29	0.73
					0.73	0.06
7	15.46	0.73	8.67%	8704.53	11.62	0.67
					0.67	0.05
8	15.53	0.74	8.77%	8690.73	11.77	0.68
					0.68	0.05
9	15.39	0.71	8.95%	8683.30	12.49	0.72
					0.72	0.05
10	15.43	0.74	9.06%	8679.30	11.72	0.68
					0.68	0.05
11	15.32	0.70	7.38%	8671.01	12.71	0.71
					0.71	0.05
12	15.21	0.70	7.57%	8662.68	11.44	0.66
					0.66	0.05
Ave-grid5-12	15.46	0.73	8.89%	—	12.02	0.70
					0.70	0.05

In Figure 4.1, some critical deconvolution processes were presented to reveal the variation of phases and corresponding micromechanical properties with the increase of components. It is clear that there is a good consistency between clustered data and the GMM model determined by the EM algorithm. The tilt of the axis of the confidence ellipses means that the covariance of modulus and hardness for phases are not zero, namely the correlation coefficients are not zero and there is a linear relationship between these two properties.

As a gel phase, N-A-S-H would have lower elastic modulus and hardness than unreacted fly ash particles. This feature acted as a criterion in the initial stage to judge whether a new phase presented in the deconvolution process is the possible N-A-S-H phase. When the number of components in the GMM model was set as 2, there is a component with the modulus of 20.80 GPa and hardness of 1.26 GPa (clustered blue points). The properties of this phase change just slightly when the number of components increases from 2 to 4. However, a new phase (clustered blue points) with a lower modulus of 15.63 GPa and hardness of 0.77 GPa emerges when the number of components in the model reaches 5. More details can be found by the magnified area in Figure 4.1 (d). The new phase even presents when the number of components for the GMM model increased to 12 as shown in Figure 4.1 (f) and Table 4.1. For this study, nine 10×10 grids were set for AAFA-10%. The total number of test points here is more than those usually used in the nanoindentation test for Portland cement paste, AAFA and alkali-activated slag paste. However, it should be noted that the BIC still has not reached the optimum value even 12 phases were assumed in the reacted AAFA system (for K=13, BIC is 8647.16). Further calculation with more components becomes more and more difficult because it takes a longer time and hard to be calculated successfully for many random initial input values. It leads to more difficult to find the real global optimal solution. What more important is when increasing the number of components, the insufficient test data for some phases

leads to greater error for estimated results. Therefore, the calculation was stopped at 12 components. For the constant phase existing from 5 components to 12 components, the average modulus and hardness are 15.46 GPa and 0.73 GPa, and the corresponding standard deviation of them are 3.47 and 0.22, respectively, which are all close to the properties of low-density (LD) C-S-H reported (Hu & Li 2015b; Vandamme, Ulm & Fonollosa 2010). It is therefore empirically regarded as the possible N-A-S-H gel phase, and subjected to further discuss in the next subsections for whether it is a pure phase, why it should be an individual phase instead of spurious phase, and the possible reasons of the small proportion of this phase.

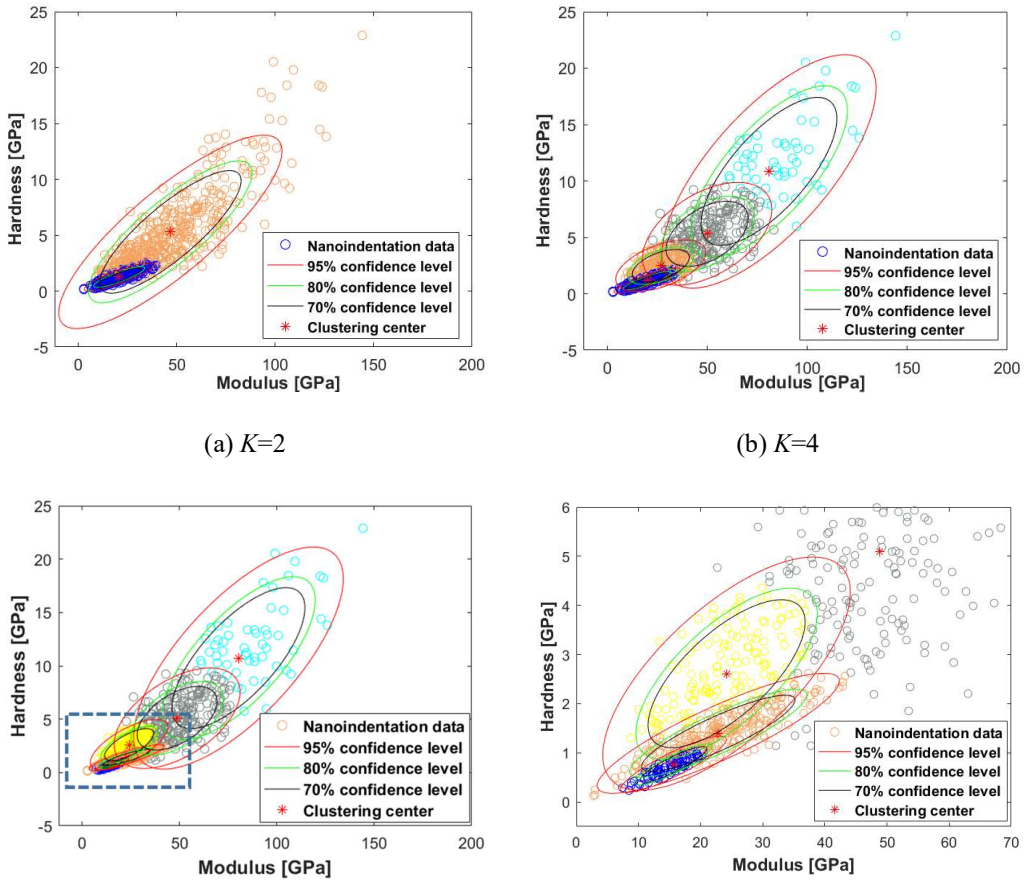

(a) K=2 (b) K=4

(c) K=5 (d) Local details for K=5 (only partial ellipses)

Figure 4.1 Deconvolution of nanoindentation data for AAFA-10%

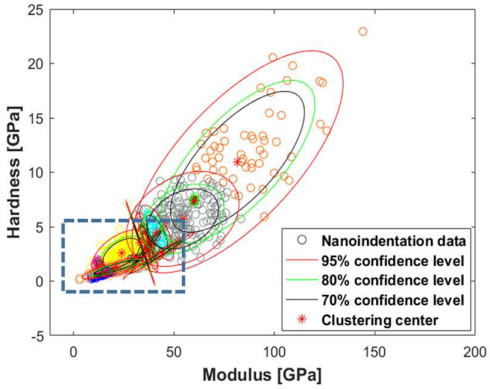

(e) K=12

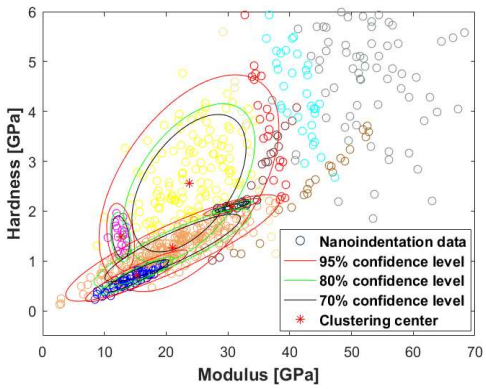

(f) Local details for K=12 (only partial ellipses)

Figure 4.1 Deconvolution of nanoindentation data for AAFA-10% (continuing)

4.3.2 **Deconvolution for AAFA-6%**

The deconvolution results of AAFA-6% are summarised in Table 4.2. For this sample, the deconvolution process is similar to AAFA-10% and the possible N-A-S-H phase appears when K is 3 earlier than that of AAFA-10%. It becomes a stable phase when K is 4 and shows almost the same value even K reaches 12. This stable phase has average modulus, hardness and fraction of (12.70, 0.62, and 10.67%). The average standard deviation for modulus and hardness are 4.06 and 0.24, respectively, which are similar to that of AAFA-10%.

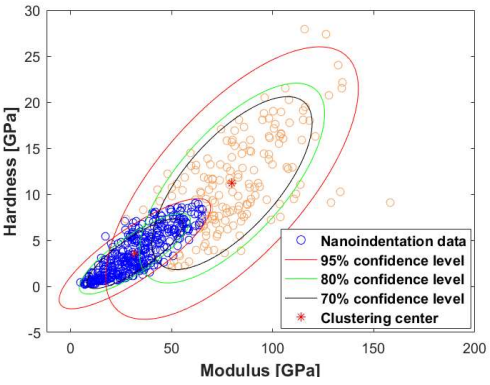

(a) K=2

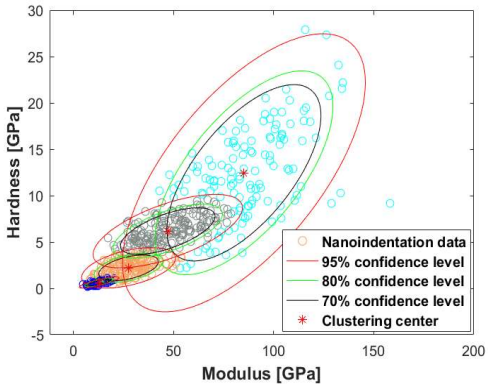

(b) K=4

Figure 4.2 Deconvolution of nanoindentation data for AAFA-6%

Table 4.2 Deconvolution results for AAFA-6% (clustered blue points for K =2 and 4)

K	M [GPa]	H [GPa]	f	BIC	C	
2	31.74	3.55	65.78%	7315.92	234.90	31.32
					31.32	5.98
3	13.42	0.68	11.66%	7158.23	21.23	1.17
					1.17	0.09
4	12.75	0.63	10.83%	7086.09	16.98	0.87
					0.87	0.06
5	12.74	0.63	10.83%	7052.31	16.95	0.87
					0.87	0.06
6	12.71	0.62	10.76%	7035.45	16.77	0.86
					0.86	0.06
7	12.73	0.62	10.81%	7014.24	16.85	0.86
					0.86	0.06
8	12.55	0.62	10.14%	7001.98	15.88	0.82
					0.82	0.06
9	12.71	0.62	10.20%	6993.97	15.95	0.84
					0.84	0.06
10	12.72	0.63	10.54%	6984.93	15.59	0.84
					0.84	0.06
11	12.54	0.61	10.60%	6979.63	15.93	0.80
					0.80	0.06
12	12.88	0.63	10.97%	6938.78	17.43	0.92
					0.92	0.07
Ave-grid 4-12	12.70	0.62	10.67%	—	16.48	0.85
					0.85	0.06

4.3.3 **Deconvolution for AAFA-8%**

For the deconvolution of AAFA-8%, the results are different from those of AAFA-10% and AAFA-6%. As shown in Table 4.3 and Figures. 4.3 (a) to 4(d), with the increase of the number of components, a phase presents when K is 3 and shows as a stable phase in

the GMM model with 8 components to the model with 12 components. However, based on the tested results for AAFA-6% and AAFA-10%, this phase is not accepted as a possible N-A-S-H gel phase. The modulus and hardness of this phase are more than normal properties found for the possible gel phase in this study. Besides, the high variance of 61.96 and 0.27 for modulus and hardness also indicate that this phase may not be a pure N-A-S-H gel phase. Typically, when comparing with the deconvolution results for AAFA-10%, there is a phase with very similar properties. This similar phase can be seen in Table 4.1 and Figures. 4.1 (a) and (b) (clustered blue points) when *K* is 2, 3 and 4. Actually, as can be seen from Figures. 4.1 (b) to (f), the possible N-A-S-H phase is separated from this phase. In order to acquire the corresponding N-A-S-H phase as AAFA-10%, further deconvolution for AAFA-8% is necessary. However, further increase of components in this model is not efficient to deal with this problem as illustrated previously, and attempts for the GMM models with 13, 14 and 15 components also failed to separate the possible N-A-S-H gel phase.

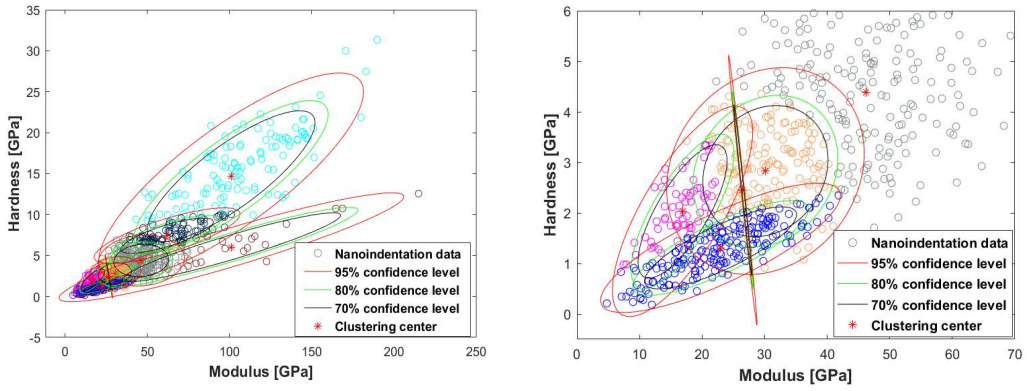

(a) *K*=8 (b) Local magnification for *K*=8

Figure 4.3 Deconvolution of nanoindentation data for AAFA-8%

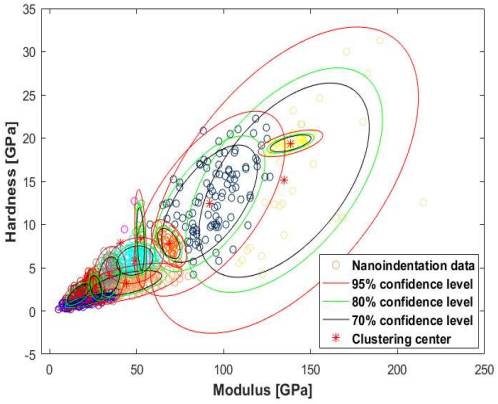

(c) K=12

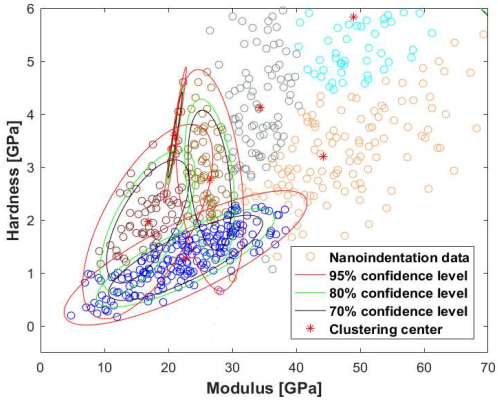

(d) Local magnification for K=12

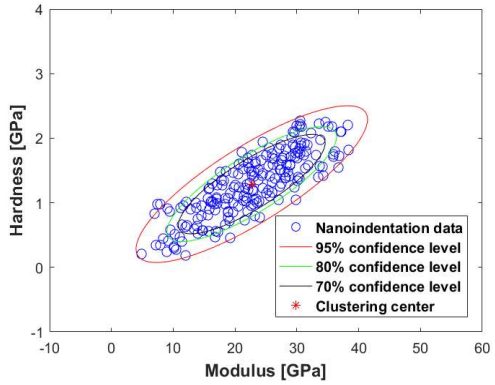

(e) 2th deconvolution with K=1 (12-1)

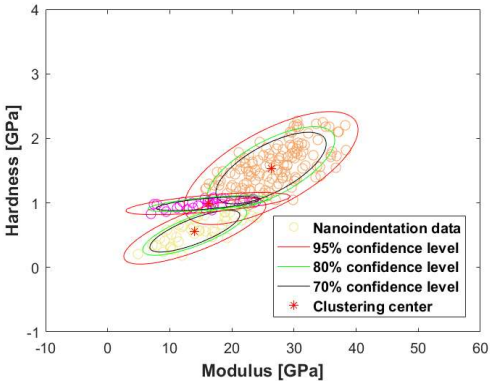

(f) 2th deconvolution with K=3 (12-3)

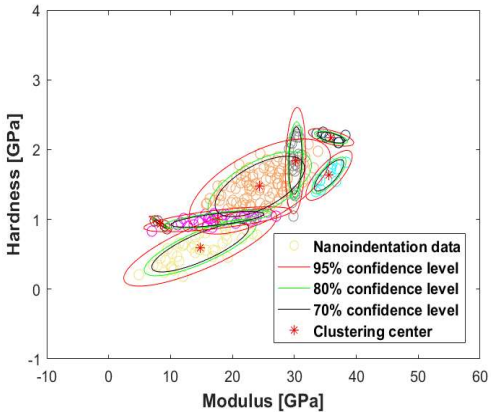

(g) 2th deconvolution with K=7 (12-7)

Figure 4.3 Deconvolution of nanoindentation data for AAFA-8% (continuing)

Table 4.3 Deconvolution results for AAFA-8% (clustered blue points for K=8 and 12)

K	M [GPa]	H [GPa]	f	BIC	C	
2	31.66	2.94	72.15%	11191.64	178.21	17.28
					17.28	3.03
3	23.39	1.66	45.36%	11004.61	65.51	3.66
					3.66	0.54
4	24.73	1.45	37.08%	10930.86	85.58	4.82
					4.82	0.39
5	24.62	1.44	36.82%	10893.79	84.00	4.72
					4.72	0.38
6	23.95	1.39	36.83%	10870.81	71.05	3.80
					3.80	0.33
7	24.09	1.40	37.34%	10864.59	73.57	3.95
					3.95	0.34
8	22.95	1.31	30.71%	10850.75	61.36	3.32
					3.32	0.27
9	23.20	1.33	33.42%	10831.49	67.43	3.53
					3.53	0.29
10	22.73	1.30	30.57%	10823.63	60.10	3.22
					3.22	0.27
11	22.96	1.31	30.84%	10819.10	60.60	3.16
					3.16	0.26
12	22.69	1.29	30.25%	10811.48	60.32	3.27
					3.27	0.27
Ave-grid 8-12	22.90	1.31	31.16%	—	61.96	3.30
					3.30	0.27

In theory, upper-level data would be better to be used as the original data of the second deconvolution. Namely, choosing the clustered data of the phase which corresponds to the lowest modulus and hardness in the GMM model with $1 \leq K <$ m. m is the number of components where the stable phase with the average modulus of 22.90 GPa and hardness of 1.31 GPa is observed for the first time. This would reduce the risk of information loss of meaningful data but didn't achieve efficient results in this case. In order to simplify the deconvolution process, the nanoindentation data that have been clustered to the phase with the average modulus of 22.90 GPa and hardness of 1.31 GPa were used as the data directly and subjected to the second deconvolution. The clustered data obtained at 12 components are adopted for this deconvolution process.

The results from the second deconvolution display in Figures. 4.3 (e) to 4.3 (g) and Table 4.4. Figure 4.3 (e) shows the clustered data that belong to the stable phase when *K* is 12 in the first deconvolution, and subjected to the second deconvolution with one component. As the results listed in Table 4.3 (*K*=12) and Table 4.4 (*K*=12-1), there is a good agreement between the previous Gaussian model for this stable phase and the second time's Gaussian model estimated based on the clustered data. This means it is reasonable to use this data to represent the original stable phase. Similar to the first deconvolution, there is also a stable phase in the second deconvolution that starts at the model with 3 components and lasts until model with 7 components. When comparing with the results of AAFA-10% and AAFA-6%, this phase was regarded as the possible N-A-S-H phase as they show similar modulus, hardness and covariance matrix value. When *K* is higher than 7, although smaller BIC value still can be obtained, there will be no more stable phase, and phases with smaller modulus, hardness and very low percentage occur. As the limited number of data here, more components for deconvolution were regarded as an excessive division.

Table 4.4 Deconvolution for clustered data belong to stable phase when *K* is 12 (AAFA-8%, clustered yellow points for *K*=12-3 and 12-7)

K	*M* [GPa]	*H* [GPa]	*f*	BIC	*C*	
12-1	22.71	1.29	100.00% (30.25%)	1473.28	58.54 3.14	3.14 0.25
12-2	22.20	1.24	93.54% (28.30%)	1460.87	58.45 2.96	2.96 0.22
12-3	14.03	0.56	19.90% (6.02%)	1446.38	16.84 0.75	0.75 0.04
12-4	14.19	0.58	21.06% (6.37%)	1435.05	16.90 0.79	0.79 0.05
12-5	14.67	0.58	20.17% (6.10%)	1425.61	19.83 0.84	0.84 0.04
12-6	15.26	0.63	19.99% (6.05%)	1419.11	19.36 0.81	0.81 0.04
12-7	14.79	0.60	22.74% (6.88%)	1416.02	19.68 0.91	0.91 0.05
Ave-grid 3-7	14.59	0.59	20.77% (6.28%)	—	18.53 0.82	0.82 0.05

Note: the fraction without brackets is the proportion of the component to all components in the second deconvolution, and the fraction within brackets is the proportion of the component to all components in original AAFA reaction system.

4.4 Results analysis and discussion

4.4.1 Pure N-A-S-H phase properties

When conducting the nanoindentation test for C-S-H or N-A-S-H in cement paste material, there are several critical issues that determine whether the micromechanical properties of gel detected are based on pure individual phase. Typically, intermix pores or other small phases in the gel phase are suspected to influence the accurate measurement

of modulus and hardness of the gel phase. Choosing the suitable indentation depth and deleting the abnormal indentation test points help partially avoid these problems but may not be all.

In order to verify these issues, Davydov, Jirásek & Kopecký (2011) conducted comparative research and pointed that part of the CH is mixed with C-S-H because the percentage of CH detected by nanoindentation is lower than that by Back-scattered Electron Detector (BSE) and X-ray powder diffraction (XRD). Besides, even test points precisely conducted on the same target phase C-S-H_{HD}, big scatter properties results were obtained and the peak corresponding to CH can even sometimes be observed directly on the frequency densify figure. The number of component *K* was set as 4 to keep it the same as the *K* usually used in the nanoindentation test (Davydov, Jirásek & Kopecký 2011). The total proportion of low-density (LD) C-S-H and high-density (HD) C-S-H reached a high level of 85% with only 10% CH. This proportion is not reasonable and means the existence of mixed phase as put forward by Davydov, Jirásek & Kopecký (2011). Actually, these facts also hint that when the nanoindentation data is sufficient, increasing the number of components may be able to separate purer gel phase since there is a difference between the micromechanical properties of gel and gel with significant inclusions. At the same time, it should be noted that the modulus and hardness of low-density (LD) C-S-H and high-density C-S-H reached a high value of (30.10, 1.25) and (36.23, 1.55), respectively in that study (Davydov, Jirásek & Kopecký 2011). For other studies (Chen et al. 2010c; Vandamme, Ulm & Fonollosa 2010) that also identified and verified a mixed phase, that phase also has high modulus and hardness and is called ultra-high density (UHD) phase. The UHD phase is considered to be an intimate nanocomposite where nanoscale CH reinforces C–S–H by partially filling the latter's gel pores. The modulus and hardness of this phase achieved a high value of 47.2 GPa and 1.6

GPa, respectively. Therefore, mixed phase is characterized by high mechanical properties (e.g. *H* reflects strength) as the reinforcing effect by inclusions. As typically shown in Figure 4.1 (d), the clustered sandy brown points span a very large range of modulus and hardness value. Some of the points reach high modulus and hardness of almost 40 GPa and 2 GPa, respectively. Besides, the similar phase does not exist in AAFA-6%. These features indicate that the phase shows high average modulus and hardness of (22.90, 1.31) in AAFA-8% as shown in Table 4.3 and exists in AAFA-10% when *K* is 2, 3 or 4 as shown in Table 4.1 is one of the mixed phases instead of a single gel phase. The final stable phases separated from mixed phase with small modulus, hardness and proportion in the range of 12.7 to 15.46 GPa, 0.59 to 0.73 GPa and 6.28% to 10.67% in this study were therefore regarded as the purer gel phases. The separation process can be seen in Figures. 4.1 to 4.3, and the variation of modulus and hardness in key separation steps is given in Figure 4.4.

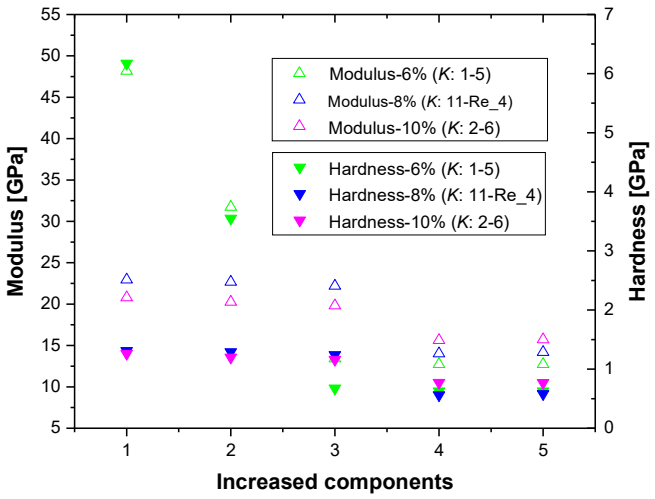

Figure 4.4 Separation of N-A-S-H from the mixed phase in AAFA

In order to verify if the possible pure phase obtained can be further divided into purer N-A-S-H phase, deconvolution analysis was conducted on the clustered data that belongs to the 'possible N-A-S-H phase', as typically for AAFA-10% with 12 components shown

in Figure 4.5 and Table 4.5. This process is conducted for a maximum of 5 components and this number is considered as more than necessary. For 2 and 3 components, the 'possible N-A-S-H phase' (K=1) is divided into a major phase and one or two phases with a small proportion. The major phases still show similar modulus and hardness as 'possible N-A-S-H phase'. When K reached 4 and 5, different results present and there are two phases with considerable proportion, the clustered blue points and the clustered sandy brown points.

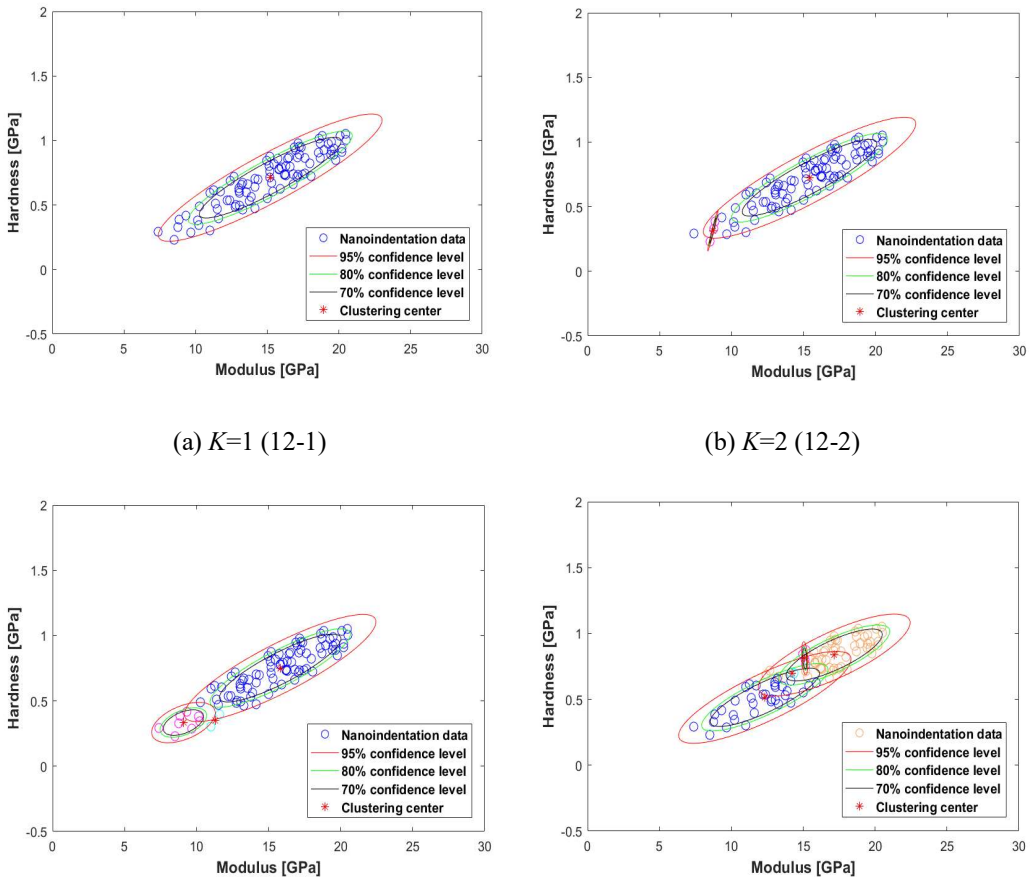

(a) K=1 (12-1)

(b) K=2 (12-2)

(c) K=3 (12-3)

(d) K=4 (12-4)

Figure 4.5 Deconvolution of clustered data belongs to possible N-A-S-H (AAFA-10%, K=12) and mixed phases (AAFA-10%, K=3)

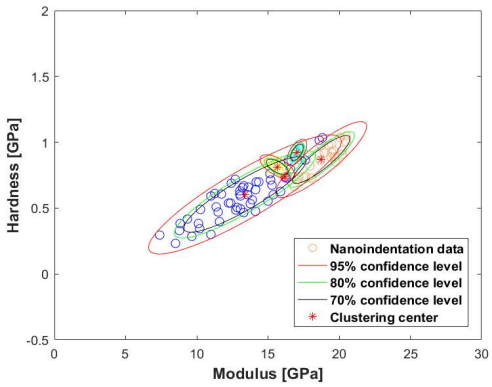

(e) K=5 (12-5)

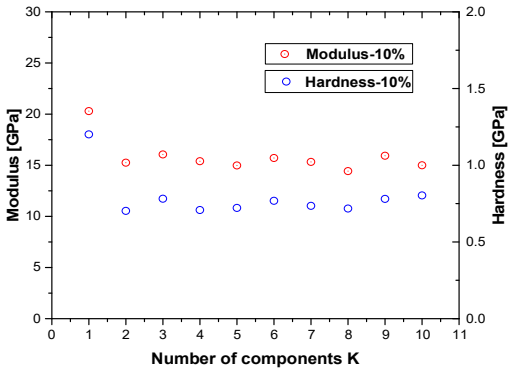

(f) Deconvolution of mixed phase (3-1 to 3-10)

Figure 4.5 Deconvolution of clustered data belongs to possible N-A-S-H (AAFA-10%, K=12) and mixed phases (AAFA-10%, K=3) (continuing)

Table 4.5 Deconvolution for clustered data belong to possible N-A-S-H phase (AAFA-10%, K=12)

K	M [GPa]	H [GPa]	f	BIC	C	
12-1	15.21	0.71	100.00%	288.04	10.19	0.60
					0.60	0.04
12-2	15.41	0.72	96.88%	280.26	8.76	0.47
					0.47	0.03
12-3	15.80	0.75	90.38%	218.08	7.40	0.39
					0.39	0.03
12-4-1	17.16	0.84	56.75%	209.82	4.66	0.22
					0.22	0.02
12-4-2	12.33	0.52	37.65%	209.82	6.01	0.29
					0.29	0.02
12-5-1	13.38	0.60	58.26%	178.59	7.65	0.46
					0.46	0.03
12-5-2	18.74	0.87	24.59%	178.59	1.70	0.13
					0.13	0.01

For this study here, even if up to nine 10×10 nanoindentation grids were tested, due to the small proportion of the 'possible N-A-S-H phase', nanoindentation testing points for this

deconvolution are still relatively sparse, especially when points away from the centre of the Normal model. The sparse data would undoubtedly influence the clustered results and result in unreliable new phases. Besides, in the deconvolution process, some new phases are generated based on only 3 tested points (e.g. K=2) or 2 tested points (e.g. K=3, 4, 5). That would not be able to be identified as a phase in a test that has near 800 valid tested points due to the negligible proportion. These phases consist of 2 or 3 points also cannot be regarded as testing errors as they are at varied locations shown in Figure 4.5 in the deconvolution process. Although there is a phase with modulus and hardness similar to the average results in AAFA-6% when K is 4 or 5, this phase does not show as a stable phase, and the fraction even increased with K. Besides, this phase shows much smaller proportion and variance than that in AAFA-6%. When conducting deconvolution for 'possible N-A-S-H phase' in AAFA-6%, the phase with the average modulus of 12.70 GPa and hardness of 0.62 GPa no more exists when reaching similar small proportion and variance, and also no stable phase appears. Therefore, the further deconvolution for the 'possible N-A-S-H phase' is regarded as an excessive division of this phase, at least for the number of available data here.

The second round of verification is conducted by deconvolution of clustered data that belongs to mixed phase for AAFA-10% with 3 components. The clustered data contain all possible data for the N-A-S-H phase but don't have lots of data that belong to unreacted fly ash. It is the upper-level data of N-A-S-H and treated as a mixed phase. This deconvolution process can more strictly separate the N-A-S-H than deconvolution of all tested data, but less strict than the deconvolution of 'possible N-A-S-H phase' directly. The results in Figure 4.5 (f) show that the 'possible N-A-S-H phase' presents when K is 2 and is always there even the number of components set as 10, although some data within the ellipses of the 'possible N-A-S-H phase' are divided into individual phases when K is

8, 9 and 10 due to excessive division. This process still proved that the N-A-S-H phase is still a stable phase at a relatively stricter extent and verified the feasibility of the way of separating N-A-S-H phase from the mixed phase for AAFA-8%.

In summary, there is a clear separation of the 'possible N-A-S-H phase' from the mixed phase. This phase behaves as a relatively stable phase in the deconvolution process and is not suitable to be separated anymore based on the available data. Therefore, it is accepted as the pure N-A-S-H phase in this study. However, this is the pure phase that can be obtained by the deconvolution technique, not necessarily the real pure phase defined by the chemical composition. The modulus, hardness and standard deviation of the N-A-S-H phase obtained in this study are similar to previous research results for the LD C-S-H gel phase in Portland cement paste.

4.4.2 **Number of phases, bin size and feasibility of PDF by MLE**

For the deconvolution of nanoindentation data, the number of phases is usually determined by empirical estimation or features of frequency distribution histogram. In this study, Bayesian Information Criterion is used for choosing the number of phases. It should be noted that the Bayesian Information Criterion aims at the whole model. Thus it is not always ideal for the investigation of the micromechanical properties of pure N-A-S-H, and it can just be used for the preliminary estimation of the number of phases.

For alkali-activated fly ash, the raw material fly ash is a highly heterogeneous material composed of amorphous phases SiO_2 glass, Si–Al glass, Si–Al [Na, K, Ca] glass, etc. and also many crystalline phases such as mullite, quartz, and iron oxides hematite, with size ranges from 0.5 μm to 300 μm (Škvára et al. 2009; Yan et al. 2018; Zhao et al. 2017). It makes the activated system more complex than the Portland cement paste. Besides, there are a considerable number of pores on the surface of fly ash particles and new pores can

be generated in the dissolution process, which further increases the divergence when testing micromechanical properties. This can be observed directly from Figures. 4.1 to 4.3 for the unreacted fly ash phases, the biggest ellipse means the biggest deviation of data. All these factors make the investigation of nanomechanical properties of pure N-A-S-H more difficult due to the presence of more kinds of partly-activated and unreacted particles and mixed phases.

For most of the cases, the number of components set for current research of modulus of Portland cement paste and AAFA is 3 or 4 and bin size is 1 or sometimes 2 GPa, based on the LSE method for deconvolution. In this study, when adopting the MLE method, the number of phases for AAFA-8% and AAFA-10% are more than the typically used number. Besides, The LSE method obtains the mechanical properties of different phases by fitting the probability density functions (PDF), or sometimes the cumulative distribution function (CDF). The former is the most commonly used one. It can display the distribution of modulus and hardness of different phases intuitively based on frequency distribution histogram, but is also questioned for the artificial choice of the bin size. In order to make some comparisons, the PDF obtained in this study by MLE is plotted with frequency distribution histograms as shown in Figures. 4.6 and 4.7.

PDF of GMM models obtained based on a different number of phases is given in Figures. 4.6 and 4.7. As listed in Table 4.1, the N-A-S-H gel appears when K is 5, which can also be observed by modulus frequency density histogram in Figures. 4.6 (a) to 4.6 (c) for the necessity of treating this phase as an individual phase. When K is 3 or 4, the model failed to include an evident phase (gel phase) displayed by ‘green’ colour in Figure 4.6 (c), which leads to worse matching between the two models and histograms in the adjacent area of this phase than that for 5 components. When increased the number of components

in the GMM model to 12, the corresponding PDF in Figure 4.6 (d) can reflect information in the modulus histogram better than the GMM model with 5 components.

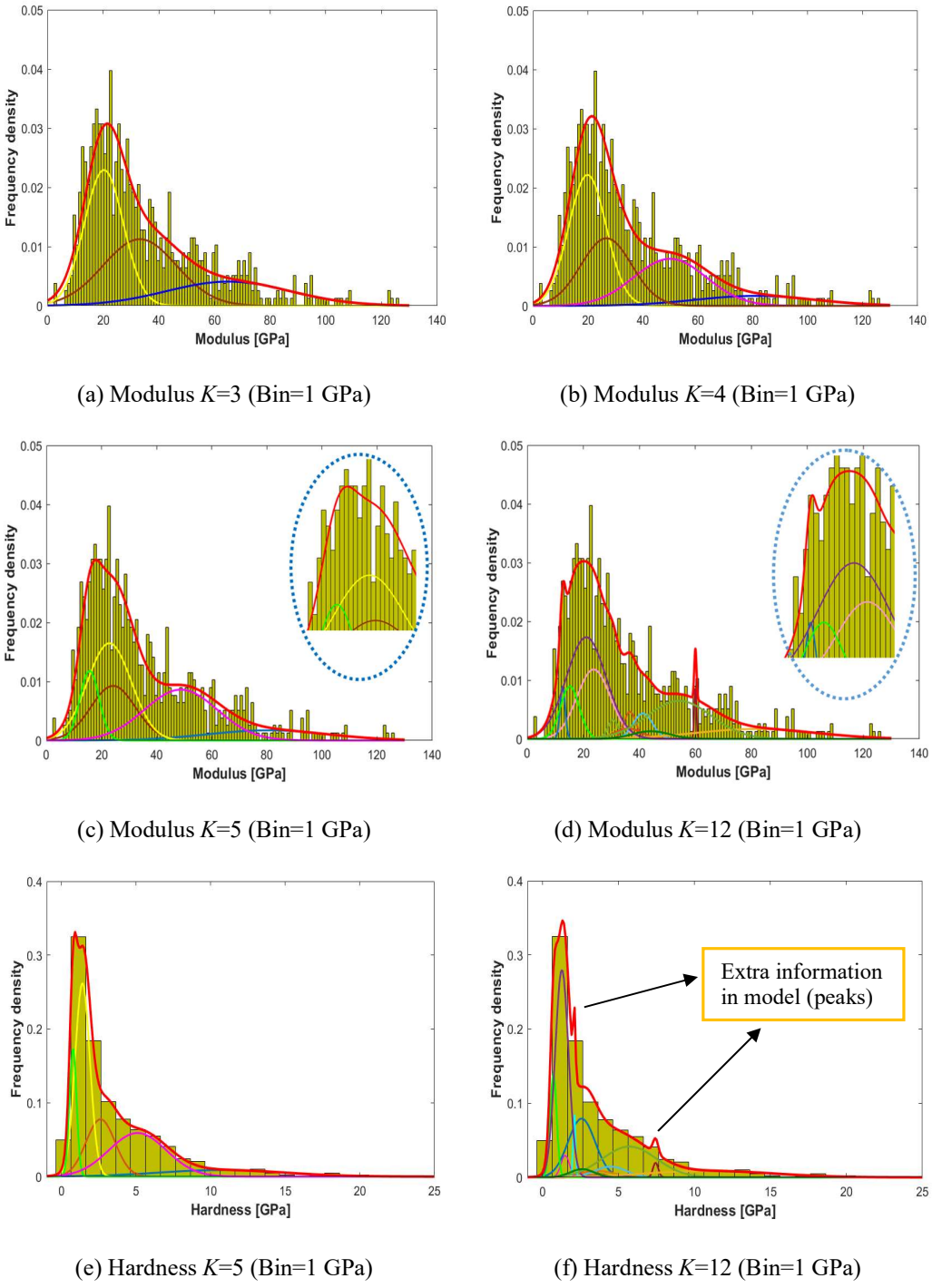

(a) Modulus K=3 (Bin=1 GPa)

(b) Modulus K=4 (Bin=1 GPa)

(c) Modulus K=5 (Bin=1 GPa)

(d) Modulus K=12 (Bin=1 GPa)

(e) Hardness K=5 (Bin=1 GPa)

(f) Hardness K=12 (Bin=1 GPa)

Figure 4.6 Comparison of PDF obtained by MLE with frequency histogram: effect of number of components

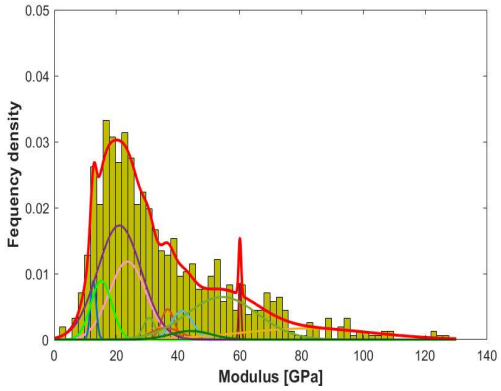

(a) Modulus K=12 (Bin=2 GPa)

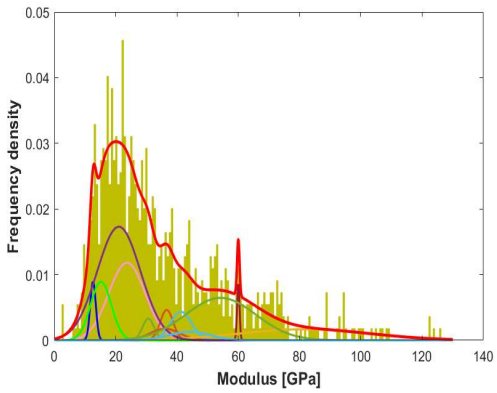

(b) Modulus K=12 (Bin=0.7 GPa)

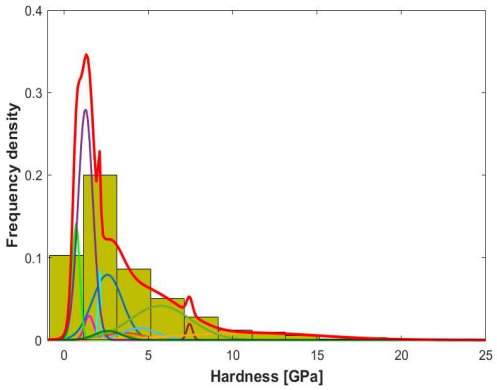

(c) Hardness K=12 (Bin=2 GPa)

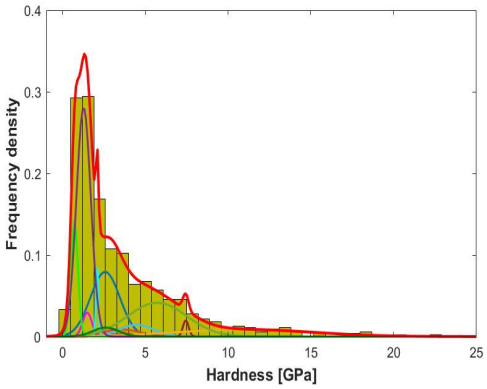

(d) Hardness K=12 (Bin=0.7 GPa)

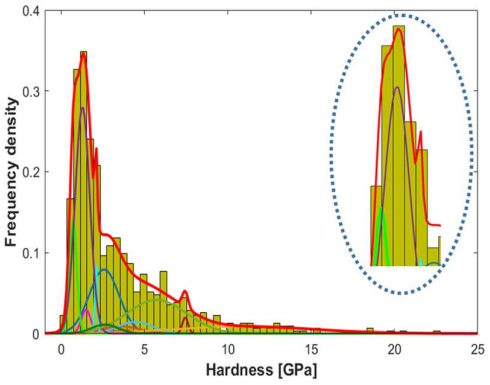

(e) Hardness K=12 (Bin=0.4 GPa)

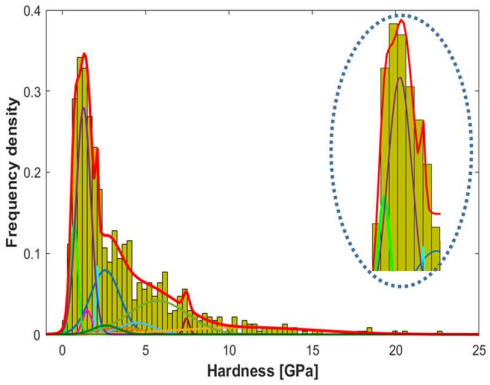

(f) Hardness K=12 (Bin=0.3 GPa)

Figure 4.7 Comparison of PDF obtained by MLE with frequency histogram: effect of different bin size

For hardness frequency density histogram, as revealed in Figures. 4.6 (e) and (f), the GMM model with 12 components is even less match histogram than the GMM model with 5 components. For this phenomenon, before questioning the estimated model, the

more important concerns should be the different bin sizes needed for modulus histogram and hardness histogram.

The effect of bin size was studied. Firstly, the normally used bin size of 1.0 or 2.0 GPa in deconvolution of modulus data was investigated as shown in Figures. 4.6 (d) and 4.7 (a). When the number of bin size only increased to 2.0 GPa, there is no distinct difference for the frequency distribution histogram. In order to reveal more information from the histogram, bin size was decreased to 0.7 GPa. Due to the large range of modulus value and corresponding low frequency density and especially the limited number of test points, the decrease of bin size leads to more discrete data instead of detailed frequency density information in Figure 4.7 (b). Due to the significantly smaller distribution range and higher frequency density, the change of bin size in hardness frequency histogram leads to a different phenomenon. For large bin size of 2.0 GPa, as shown in Figure 4.7 (c), it is difficult to identify hardness distribution information of individual phases from the histogram, and the peaks of the histogram clearly deviate from the peaks in the histogram with a bin size of 1 as shown in Figure 4.6 (f). When decreased the bin size from 1 to 0.7 GPa as shown in Figure 4.7 (d), the histogram is also markedly changed, which means the bin size adopted would influence the LSE results for hardness. Further decrease of bin size to 0.4 and 0.3 GPa is accompanied by a better match of the PDFs estimated by the MLE method with histograms. It is clear that some extra information (peaks) didn't show in the histogram in Figure 4.6 (f) has appeared. Namely, for the model that can match modulus histogram with the bin size of 1, it matches the hardness histogram well only when the bin size decreased to at least 0.4. For a given test data set, it is very difficult to specify the bin size reasonably for the LSE analysis. The needed bin size is at least determined by factors such as the nature of samples, the types of the histogram and the

number of the test data. The inappropriate bin size may either lose the real information or lead to spurious peaks and irregular histogram.

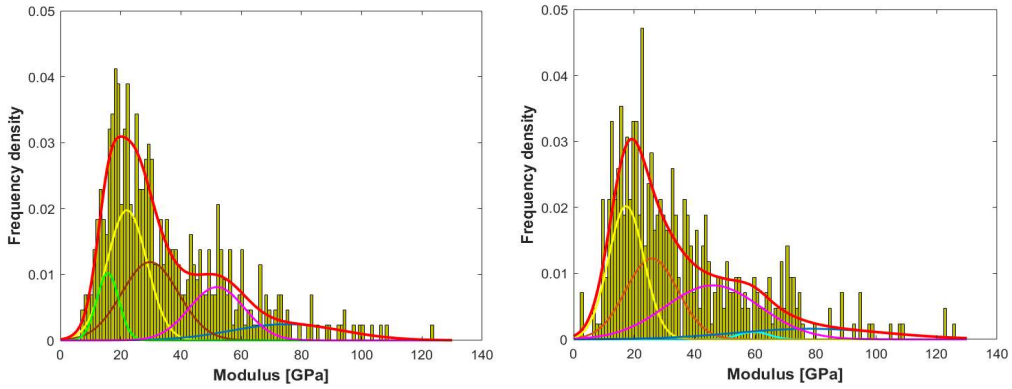

(a) 5 grids-1st (K=5, Bin=1 GPa) (b) 5 grids-2nd (K=5, Bin=1 GPa)

Figure 4.8 Comparison of modulus PDF obtained by MLE with frequency histogram: 5 grids

When using the LSE method, enough test points are needed to allow reasonably small bin size to show the details of distribution and avoid the spurious peaks and irregular histogram. This point can be observed by the histograms from 5 grids in Figure 4.8, where 5 grids-1st means 5 grids randomly chosen from 9 grids and 5 grids-2nd consists of the remaining 4 grids and 1 random grid from the 5 grids-1st. It is obvious that when the bin size is 1, the shape of the histogram of 5 grids-1st and especially the 5 grids-2nd is more discrete and irregular than the corresponding histogram of 9 grids in Figure 4.6 (c), increasing the difficulty of fitting by LSE. Besides, as shown in Figures. 4.9 (a) and 4.9(b) and Table 4.6, the deconvolution results of the 5 grids-1st based on 5 components are quite close to the results from 9 grids. It means that the PDF determined by the MLE method from 5 grids-1st still can reflect the micromechanical properties distribution of AAFA and is reliable. The mismatch of PDF and histogram in Figure 4.8 (a) implies that when the test data are not enough, specifying of small bin size forcibly for a histogram and then fitting it by the LSE method would cause deviation in results. In Figure 4.8 (b),

in the result of 5 grids-2nd, the corresponding deconvolution result with 5 components doesn't generate the gel phase. However, the gel phase occurs when the number of components specified for deconvolution is raised to 6 as can be observed in Figures. 4.9 (c) and 4.9 (d) and Table 4.6. Decrease of grid number from 9 to 5 significant increases the difficulty for LSE method as it is dependent on the histogram, while the MLE method helps to reveal the properties of gel phase and other key phases from all the three kinds of data sources and the results from 9 grids, 5 grids-1st, and 5 grids-2nd are similar to each other. It clearly displays the reliability and stability of the MLE method. In addition, the deconvolution process again indicates that the number of components needed to generate the gel phase in the model should not be a constant value of 3 or 4 and would change with both sample and test factors.

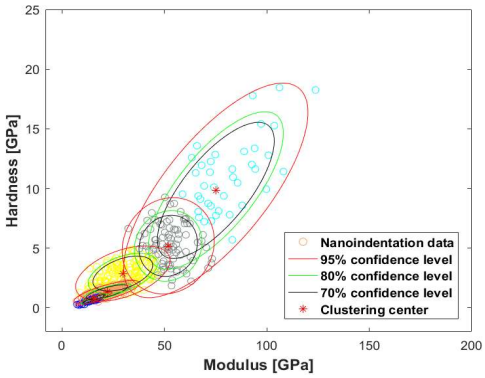

(a) K=5 (5 grids-1st)

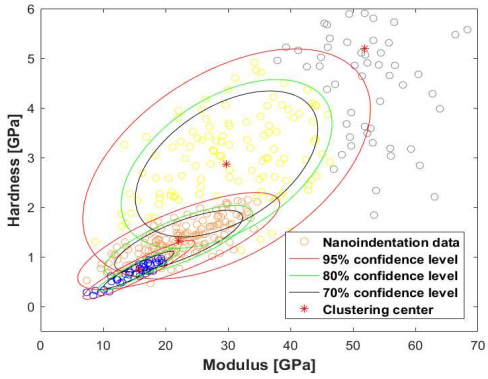

(b) Local details for K=5 (5 grids-1st)

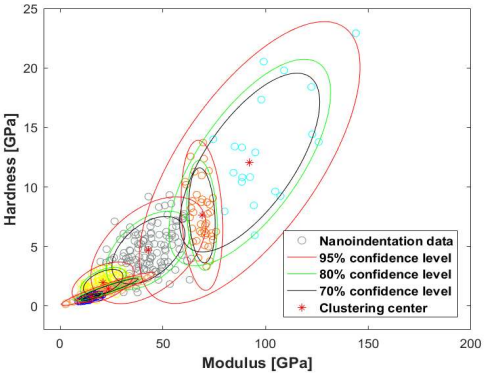

(c) K=6 (5 grids-2nd)

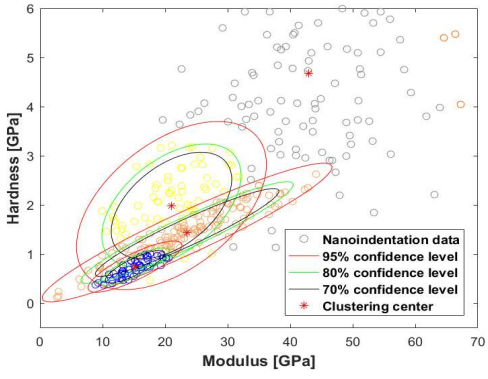

(d) Local details for K=6 (5 grids-2nd)

Figure 4.9 Deconvolution of different 5 grids nanoindentation data in AAFA-10%

Table 4.6 Deconvolution results for AAFA-10% based 5 grids (clustered blue points)

Data source	*K*	*M* [GPa]	*H* [GPa]	*f*	*C*	
9 grids	5	15.63	0.77	10.30%	12.13	0.72
					0.72	0.06
5 grids-1st	5	15.72	0.75	9.38%	13.44	0.83
					0.83	0.06
5 grids-2nd	5	17.39	0.99	29.78%	34.66	2.15
					2.15	0.16
5 grids-2nd	6	15.18	0.75	11.29%	9.43	0.54
					0.54	0.05

In fact, even the suitable bin size based on enough tested points is specified, it is still difficult to identify the N-A-S-H phase from a histogram. It may be ignored or be combined into a big peak becoming properties of a mixed phase when using the LSE method. Typically, as shown in Figures. 4.6 (c) and 4.6 (d) and 4.7 (b), the 'green' Gaussian distribution is the N-A-S-H phase, but it does not correspond to any recognizable peaks in histogram or PDF of GMM model. At the same time, the 'blue' Gaussian distribution in Figures. 4.6 (d) and 4.7 (b) under a prominent peak is easy to be considered as the gel phase. In this study, a two-dimensional GMM model is adopted, which can reveal both modulus and hardness of each phase at the same time. The 'blue' Gaussian distribution phase corresponds to clustered purple points in Figure 4.1 (f) and has modulus and hardness of 12.62 GPa and 1.48 GPa, respectively. This phase shows high hardness, small proportion (2.06%) and negative correlation coefficient between modulus and hardness. Therefore, it is not accepted as a gel phase. As for hardness histogram, even the bin size decreased to 0.4 or 0.3 GPa, in Figures. 4.7 (e) and 4.7 (f), it is still easy to include the N-A-S-H ('green' Gaussian distribution) into the big peak in the dotted ellipses rather than a single phase especially when a small number of phases is

set. The results indicate that there are challenges for using the LSE method to investigate the N-A-S-H phase.

For this study, it is highly suspected that the BIC cannot reach optimal value even for a model with 12 components is caused by disturbance from limited and discrete data. However, what undoubtedly is that at least 5 components (for AAFA-10%) are needed to obtain the pure N-A-S-H phase and more components are needed when describing the micromechanical distribution of the whole model. These are caused by the highly heterogeneous components of fly ash and the complex reacted system, and also the limited data. It should be mentioned that for the estimation method itself, better fitting of the model from the mathematical perspective should be at the cost of introducing spurious phases even if the BIC is used. Part of the analysis based on 12 components presented above aims to illustrate that the model estimated by MLE and BIC can reflect the overall micromechanical distribution of AAFA but does not mean that 12 components conform to the real situation in AAFA. The most reasonable model that can both reflect the real micromechanical distribution and also conforms to the real number of components in AAFA may have the number of components more than 5 and less than 12, but that is not the focus of this study.

4.4.3 **Small proportion of N-A-S-H gel**

The deconvolution results for AAFA with different alkali concentrations are listed in Table 4.7 and shown in Figure 4.10. All the fraction, average modulus and hardness vary in a small range. The proportion of N-A-S-H gel ranged from 6.28% to 10.67%. Even for AAFA-6%, which achieved the maximum value, the proportion of N-A-S-H gel of it is still far less than the normally reported range for C-S-H gel. Easy to mix or interact of the gel phase with other phases is considered as the main reason that largely decreases the proportion of pure N-A-S-H gel detected. The “other phases” include partly-activated or

un-activated small particles in the highly heterogeneous AAFA system. Besides, mixing of C-S-H gel with nanoscale CH crystal is the most common form of the mixed phase detected in the research of Portland cement paste (Chen et al. 2010c; Davydov, Jirásek & Kopecký 2011). CH crystal does not exist in the AAFA and nanoscale crystal is not considered in any current nanoindentation investigation of AAFA. However, the AAFA has crystal phases and some micron-sized crystals can be observed directly by SEM as in Figure 4.11.

Table 4.7 Properties of N-A-S-H in AAFA with different alkali concentration

Sample	*K*	*M* [GPa]	*H* [GPa]	*f*	*C*	
AAFA-6%	≥ 4	12.70	0.62	10.67%	16.48	0.85
					0.85	0.06
AAFA-8%	> 12	14.59	0.59	6.28%	18.53	0.82
					0.82	0.05
AAFA-10%	≥ 5	15.46	0.73	8.89%	12.02	0.70
					0.70	0.05

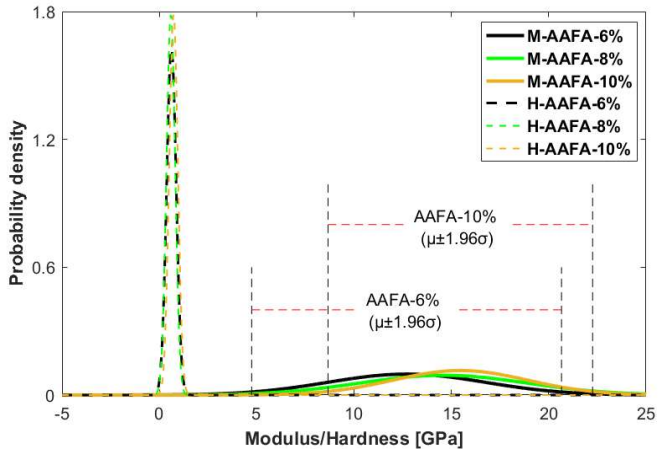

Figure 4.10 Modulus and hardness probability density distribution of N-A-S-H in AAFA with different alkali concentration

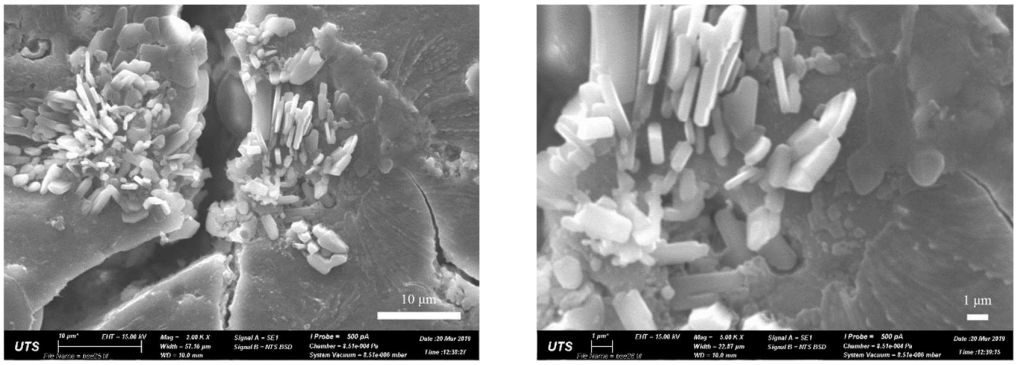

(a) Magnification of 2000 × (b) Magnification of 5000 ×

Figure 4.11 Morphology of micron-sized crystals in AAFA

Some of those crystals would also exit in smaller sizes like nano and sub-micron scale. Lots of crystals that affect the indentation results may be introduced by the raw material fly ash. The nanoindentation results in this study agree well with the phenomenon of coexistence of crystal and amorphous gel phase in binders. As given in Tables 4.1 and 4.3, the upper-level mixed phases before generating the gel phase show average modulus slightly larger than 20 GPa and hardness slightly larger than 1 in AAFA-8% and in AAFA-10% may be the mixture of crystal and gel phase, as the mechanical properties of it is similar and slightly lower than the phase mixed by low-density (LD) C-S-H with nanoscale CH crystal (Davydov, Jirásek & Kopecký 2011). Therefore, the interaction of gel with crystals in nanoindentation test are possibly important factors leading to the low proportion of pure gel detected.

The presence of crystals can then help to more reasonably explain why the N-A-S-H gel detected in this study is less than results from other techniques. Typically, when segmenting of phases based on grey value (Brough & Atkinson 2000; Hu & Li 2015a; Scrivener 2004) as shown in Figure 4.12, the statistical amount of reacted products in AAFA-8% is 50.38%. In fact, when referring to Table 4.3, for the upper-level mixed phases starting from 2 components identified by statistical nanoindentation, they all have relatively large proportions. When considering factors such as different resolutions

between techniques and easy to encounter others phases (particles & crystals) in interaction zone even if the surface is identified as N-A-S-H by BSE, the final small proportion of pure N-A-S-H obtained by statistical nanoindentation is reasonable.

For micromechanical properties results in this study, when the alkali concertation increased from 6% to 10%, the results show that there is a trend of a slight increase of modulus and hardness. The micromechanical properties probability distribution of N-A-S-H was plotted in Figure 4.10 for more intuitive observation. It shows that although there is an increasing trend, it is in a small range and distributions are similar for AAFA with different concentrations. For the study of Portland cement paste with different water to cement ratios, regarding the modulus and hardness as intrinsic material properties is also not based on fully consistent results, but on a small range of variation, such as smaller mean properties difference than the standard deviation, and so on (Vandamme, Ulm & Fonollosa 2010). This is a reasonable consideration as errors are unavoidable in any real experiments, but it also cannot eliminate the possibility that the micromechanical properties themselves just change in a very small range and the increasing trend also seems plausible. Therefore, further studies are needed for understanding whether the modulus and hardness are intrinsic material properties of N-A-S-H.

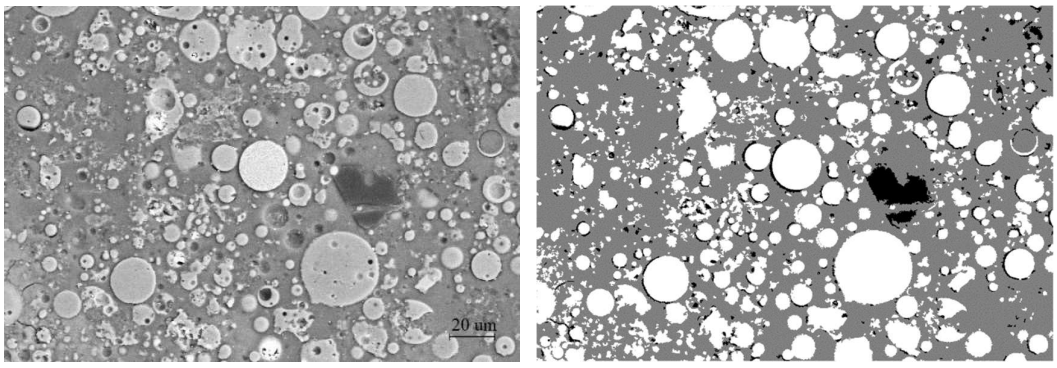

(a) BSE image (500 ×) (b) Binary image

Figure 4.12 Microstructures and phase segments of AAFA based on BSE images

4.4.4 **Classical questions on statistical nanoindentation**

As mentioned in the review, the LSE method has been questioned for several aspects (Lura, Trtik & Münch 2011). For the research of AAFA in this paper by MLE and BIC, the notion of MLE itself includes the method of searching global optimum. The constant gel properties in a model with a different number of components and varied grid numbers indicate the robustness of the results for gel phase. Besides, the statistic process does not depend on the distribution histogram, while the model obtained by the MLE method is expected to be able to match the histograms very well if there are infinite test data and then infinitely small bin size. These points indicate the reliability of the MLE method, which can avoid aspects that are questioned for the LSE method. Another key point for the validity of the statistical nanoindentation is the interaction volumes. The interaction volume of about 1 μm^3 was thought to be too large for Portland cement paste because the collected test data are not able to present a clear peak for all known phases (Lura, Trtik & Münch 2011). The two aspects of interaction volumes and statistical method constitute the main questions for using statistical nanoindentation as an experimental approach to investigate the Portland cement paste, and combining of indentation with microstructure investigation is considered as a promising alternative way for research (Lura, Trtik & Münch 2011).

Regarding the issues about interaction volumes as a restriction for using statistical nanoindentation, in fact, in some aspects, this concern is modestly exacerbated in the virtual nanoindentation. The amount of clinker is just 13.8% (Lura, Trtik & Münch 2011). The local sample adopted in the FIB-nt study (14 μm^3) contains much less linker than the real sample in the SNT test. Besides, the involved range of clinker should be much less than 1 μm^3 cube, since it has larger mechanical properties and hence smaller indentation depth than the gel phase under the constant load model. Moreover, the ternary plot in the

virtual nanoindentation is for different phases and not for mechanical properties as in SNT. The significant mechanical properties differences would magnify the peak. These factors would affect the appearance of the peak for clinker. Even for the gel phase, the effective involved volume of the gel phase would be smaller than the 1 μm^3. The 1 μm^3 homogeneous cubes used is based on 3-4 times of the indentation depth, while the strain energy density field decreases with distance significantly in this range (Ulm et al. 2010). Even so, it is still difficult to obtain the mechanical properties of all phases by SNT in the complex AAFA system with limited test points.

In this study, SNT is used in a compromise way, namely, focusing on the gel phase only. The mechanical difference (combining of modulus and hardness) between gel and other phases such as mixture phases and unreacted phases is the foundation to separate them. It is a fact that the data points are density in the location around the gel phase but sparse in the locations with larger mechanical properties. Before reaching the limit of mechanical property difference to separate the gel phase from the mixture phase, spurious phases may sometimes be introduced from discrete data location, sacrificing the accuracy of other phases. The increase in the number of components from 5 for 9 grids to 6 for 5 grids-2nd is possible an evidence. However, it should be reminded that it is the gel phase that most important and also most hard to be detected while unreacted fly ash can be investigated by target indentation under BSE or even microscope equipped for nanoindentation system with high accuracy. This idea may also be used for the investigation of Portland cement paste. Even if 1 μm^3 is used, there is still a clear peak for the gel phase in (Lura, Trtik & Münch 2011).

For the research of AAFA in this study, it is known that the Si/Al of N-A-S-H gel itself is in a range of around 1-3 (Provis, Lukey & van Deventer 2005). Then, considering the chemical formula of mullite, quartz and possible zeolite, it is hard to identify and exclude

if there are such crystals or their combination in N-A-S-H by EDS. Besides, the involved volume of EDS (Monte Carlo simulation) and nanoindentation (finite element simulation) can be matched approximately, but currently is just based on the pure phase. It may be changed for different mixed phases. The chemical composition of N-A-S-H for simulation can be determined by referring to the literature (Lloyd, Provis & van Deventer 2009) and considering the minimum amount of H_2O (y is 3) (Reddy, Dinakar & Rao 2016). As shown in Figure 4.13, based on the CASINO v2.51 (Drouin et al. 2007) software, the Monte Carlo simulation of the penetration of electrons into N-A-S-H gel indicates that both the 15 kV and 12 kV are too large to match the indentation involved range in this study. However, sufficient accelerating voltage is necessary to excite elements effectively.

Considering the above factors and possible test error, it is almost impossible to judge whether the test points are on the real pure gel. In fact, the pure phase determined by deconvolution that based on mechanical properties' differences may not be 100% pure in chemical composition. In a real test, it is highly possible that, sometimes, there are small inclusions within the 1 μm strain energy density field range of the gel phase, but do not significantly change the mechanical properties detected by nanoindentation and still clustered as the gel phase. However, the mechanical properties of the gel phases obtained by deconvolution in this study would be close to the real pure gel phase for several reasons. The content of the crystal phase is much less than the gel phase in cementitious materials and the involved volume is not too large. There must be test points hitting on the area without or with just a very small content of inclusions that not change the mechanical properties significantly. When the test point is enough, this phase can be separated in deconvolution. Similarly, pore is the phase with the smallest proportion. Large pores can be removed according to the abnormal nanoindentation curves. The very small proportion

of remaining pores would not change the properties of gel significantly, as the result obtained is the average value of many test points.

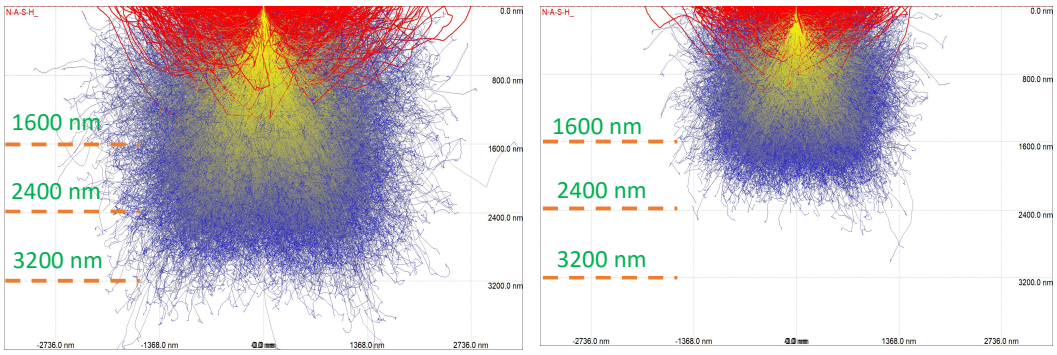

(a) 15 kV (b) 12 kV

Figure 4.13 Monte Carlo simulation of the penetration of electrons into N-A-S-H gel (The red trajectories are back-scattered electrons. The yellow and blue trajectories are high energy X-rays and low energy X-rays, respectively)

Empirically, the very small values should also be close to the properties of the pure phase. For Portland cement paste, even for 1 μm^3 of involved volume, a very significant peak can still be found for the gel phase in the virtual nanoindentation (Lura, Trtik & Münch 2011). If there is a significant peak with a large proportion in the micromechanical properties histogram, the LSE method is also expected to be able to obtain the properties of the pure LD C-S-H phase. There must be results close to the pure LD C-S-H in the summary of exiting results (Hu & Li 2015b). The smaller micromechanical properties of N-A-S-H than that of LD C-S-H (Hu & Li 2015b) and the small proportion of it also indicate it may be close to the pure N-A-S-H phase. Other test methods/techniques, for instance, testing the synthesized gel directly, are expected to be used in the future to obtain the mechanical properties of real pure N-A-S-H phase.

4.5 Conclusions

The nanomechanical properties of N-A-S-H gel in AAFAs were investigated based on the grid nanoindentation and maximum likelihood estimation method. Then, the statistical nanoindentation technique is discussed. The related conclusions can be drawn as follows:

(1) When using the MLE method, the process of separating stable N-A-S-H gel from mixed phases can be intuitively observed. Moreover, nanoindentation data can be clustered to corresponding components with a good match, which allows for further analysis. MLE also shows the advantages in independent on distribution histogram, more reasonable determination of component numbers, and less sensitive to the number of test points than LSE.

(2) Bayesian Information Criterion is not necessary to achieve the optimum value when just focusing on the N-A-S-H phase in the highly heterogeneous AAFA reaction system. When the number of components is large, sparse data in some locations leads to misidentification of new phases, which may also affect reaching the optimum value of BIC and increase the complexity of the model.

(3) The number of components needed to obtain the pure N-A-S-H phase is usually more than the typically used value of 4, and even the second deconvolution is sometimes needed. Although this is partially caused by different deconvolution method used, it is still necessary that the number of components should be enough to avoid mixed phases.

(4) A sufficiently small bin size is needed to present the actual and detailed micromechanical properties distribution of AAFA, which calls for enough testing points to construct a regular and ordered histogram when using the LSE method. The N-A-S-H phase does not always show as a distinct peak in the histogram and is easy to be mixed into identifiable large peaks, which means that even if the bin size used

is small enough it is still hard to obtain the properties of N-A-S-H phase by the LSE method.

(5) The proportion, average modulus and average hardness of pure N-A-S-H phase in AAFA with different alkali concentrations vary in small ranges of 6.28% to 10.67%, 12.70 to 15.46 GPa and 0.59 to 0.73 GPa, respectively. The main reason for the small proportion is supposed to be the presence of mixed phases, such as mixing of crystals, partly-activated and un-activated small particles with the gel phase in the highly heterogeneous AAFA system, which largely decreases the volume of pure N-A-S-H gel detected by SNT.

CHAPTER 5. NANO/MICROMECHANICAL PROPERTIES OF N-A-S-H GEL IN GEOPOLYMERS

5.1 Introduction

N-A-S-H known as the zeolite precursor gel has the most critical impact on the performance of geopolymer. The micromechanical properties of N-A-S-H have been investigated in several studies, but there are inconsistent results that if the elastic modulus is an intrinsic invariance property of N-A-S-H. The MLE-based deconvolution technique is used to fundamentally further understand this issue. Geopolymers with different silica modulus and under different curing conditions are investigated. Followed to chapter 4, the correlation and difference of different statistical techniques are further compared to clarify the rationality of the method used. In this process, the reasons and consequences for the generation two types of spurious phases, mixed phases and sub-phases in statistical nanoindentation study of some highly heterogeneous materials are pointed. After evaluated the method error, the nano/micromechanical properties of gels are compared. The effects of design parameters on the properties of gel, and its association with the performance of geopolymer are discussed.

5.2 Experimental and analysis methods

5.2.1 Sample preparation

The AAFA geopolymer samples prepared have the same Na_2O/fly ash and water to solid ratio but different silica modulus and curing conditions. The details are shown in Table 5.1. Small pieces of crushed samples were used for microstructure observation under the SE model, while polished samples were prepared for BSE imaging analysis and nanoindentation test. The sample preparation is the same as Chapter 4.

Table 5.1 Mixture ratio and curing condition of geopolymer

Samples	SiO_2/Na_2O	Na_2O/fly ash	w/s	Curing condition
AAFA-M1-S	1	8%	0.338	Standard curing
AAFA-M0-H	0 (NaOH)	8%	0.338	Heat curing at 70 °C for 24 h
AAFA-M1-H	1	8%	0.338	Heat curing at 70 °C for 24 h
AAFA-M1.5-H	1.5	8%	0.338	Heat curing at 70 °C for 24 h

Note: w/s is water to solid ratio. 'M0', 'M1' or "M1.5" behind AAFA means the silica modulus of alkali solution to make AAFA is 0, 1 or 1.5. 'H' or 'S' behind AAFA denotes the corresponding curing condition is heat curing or always standard curing.

5.2.2 **Characterization techniques**

In addition to statistical nanoindentation, multiple characterization techniques are applied for mechanism analysis. Zeiss EVO SEM equipped with an EDS detector was used for the microscale structure observation and element analysis of AAFA samples. Nanoscale observation of AAFA was conducted on Zeiss Supra 55VP. Bruker D8 Discover diffractometer was adopted to detect crystals in raw material fly ash and reacted AAFA samples.

5.3 Characterization of AAFA

The typical microstructure of AAFA is presented in Figure 5.1, which mainly consists of unreacted fly ash, partially reacted fly ash, N-A-S-H surrounding fly ash particles, crystals, and defects (pores, microcracks). From the appearance of the partially reacted particles A and B in Figure 5.1 (b), it is easy to realize that there are different kinds of fly ash particles in raw materials. Microscale crystals can be clearly found in Figure 5.1 (c). Besides, the SE image in Figure 5.1 (d) reveals that the appearance of the matrix is still very dense

even under 8000 times of magnification. In fact, the microstructure observation of AAFA can't fully show the heterogeneous nature of AAFA.

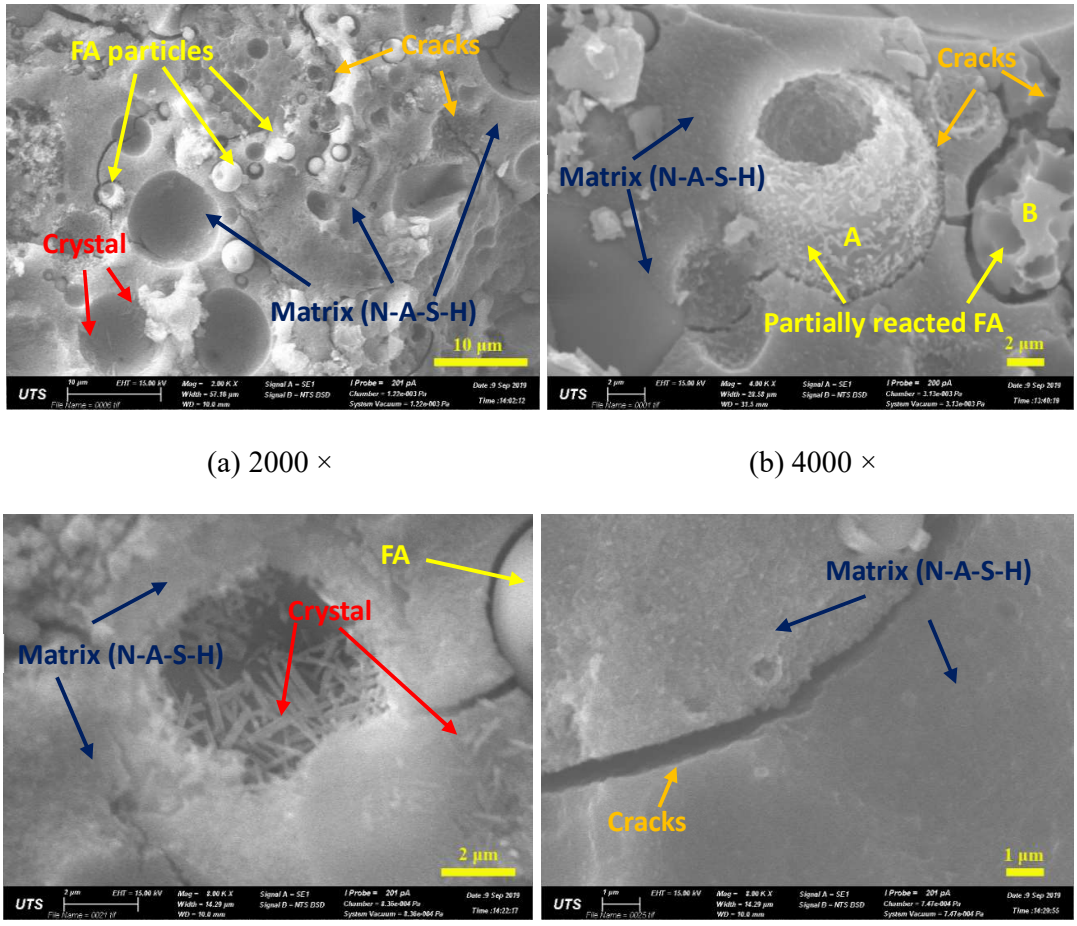

(a) 2000 ×

(b) 4000 ×

(c) 8000 ×

(d) 8000 ×

Figure 5.1 Microstructure of AAFA

The uneven distribution of elements is shown in Figure 5.2 to provide a further understanding of this issue. Diverse fly ash with different chemical compositions can be found in the second figure, which is one of the main reasons for the highly heterogeneous characteristics of AAFA. Typically, the brightest fly ash particle is rich in Fe, while other particles are normally rich in Al and Si. Even if a dense matrix is observed by SE, it may still have different chemical compositions and varied micromechanical properties in

different locations due to the mix of N-A-S-H with other phases (e.g. crystals and tiny unreacted particles).

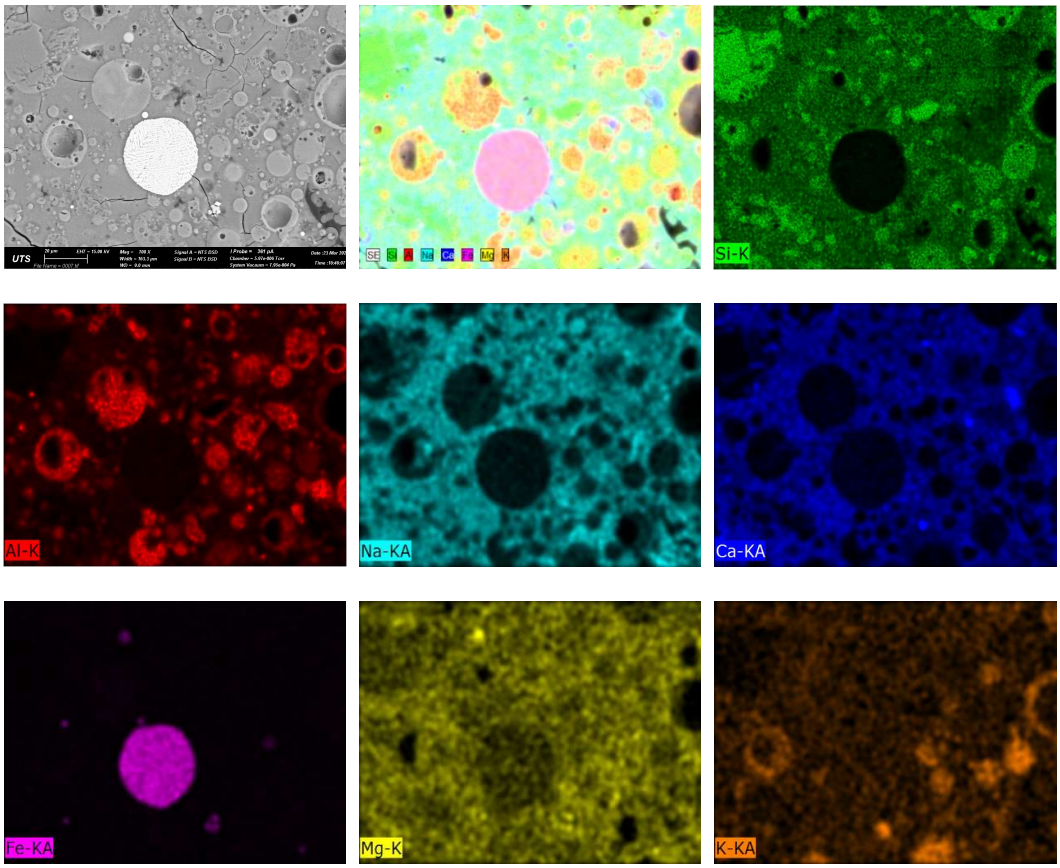

Figure 5.2 EDS element maps of AAFA

5.4 Deconvolution results

5.4.1 A compromise approach for the mismatch between the real components and micromechanical peaks

Normally, the number of phases set for the deconvolution of statistical nanoindentation data is the real number of components in the sample (Roa et al. 2015; Vandamme, Ulm & Fonollosa 2010). However, this kind of match is not always reasonable. For this study, different kinds of fly ash particles composed of different elements would have different micromechanical properties. The micromechanical distribution of fly ash may vary in a large range and overlap other phases such as crystal and mixed phase. The involved range

of gel is known as 3-4 times of the nanoindentation depth (Ulm et al. 2010). Crystals and unreacted particles at the submicron and nano-scale would be mixed with N-A-S-H gel to be identified as mixed phases. For crystal and unreacted particles at a larger scale, the interaction of the different phases (e.g. gel and unreacted FA) at the region around interface would also lead to the identification of mixed phases. Another factor that cannot be ignored is the limited test number in any real test, which would be not able to fully present the real information of micromechanical distribution. Because of very few data acquired, some real phases with a very small proportion may be mixed into other phases instead of identifying as an individual peak in the deconvolution process. In the meantime, due to discrete data, some phases with large proportion and broad distribution are possibly breakdown into several sub-phases in deconvolution. Both the mixed phases and sub-phases are spurious phases and can appear simultaneously. The difference is, when increasing the number of components for deconvolution, the sub-phases would increase while the mixed phases would decrease.

Both the nature of the sample, the test factors and the deconvolution parameters (number of components for MLE) would be responsible for the generation of mixed phases and sub-phases. It is virtually impossible to reconcile these two kinds of spurious phases to obtain the accurate micromechanical properties of all real component in geopolymer by statistical nanoindentation. The strategy of is using a “compromise approach”, focusing on the most crucial phase N-A-S-H gel merely. The micromechanical properties of some phases like crystals are not able to be obtained by statistical nanoindentation since there are intrinsic limitations from the size and proportion of the phase (nature of the sample), and the involved volume (test factors) as well. However, as a gel phase, N-A-S-H has a large proportion, suitable characterization size. In addition, the micromechanical properties (elastic modulus and hardness) of it would be significantly smaller than the

unreacted fly ash particles, crystal, and significant mixed phases. Those factors ensure that the micromechanical peak of the N-A-S-H gel can be separated from mixed phases by increasing the number of components in the deconvolution. In this process, the individual phase N-A-S-H is sometimes obtained by sacrificing the accuracy of other phases as spurious phases (sub-phases) may be introduced.

5.4.2 **Deconvolution results for AAFA-M1-S**

For AAFA cured under standard curing condition, the deconvolution results of the phase ($k \leq 9$) or the two phases ($k > 9$) which show the minimum micromechanical properties are listed in Table 5.2. Some key deconvolution results are revealed in Figure 5.3.

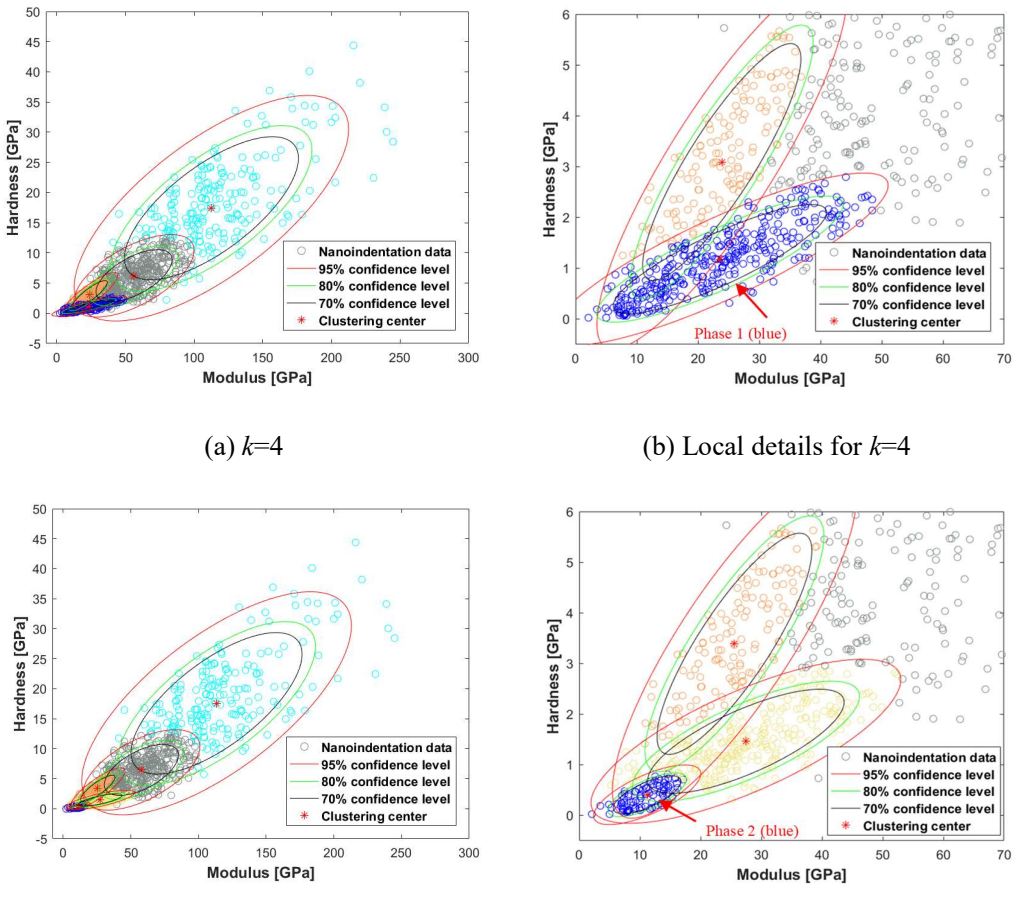

(a) k=4 (b) Local details for k=4

(c) k=5 (d) Local details for k=5

Figure 5.3 Deconvolution of nanoindentation data for AAFA-M1-S

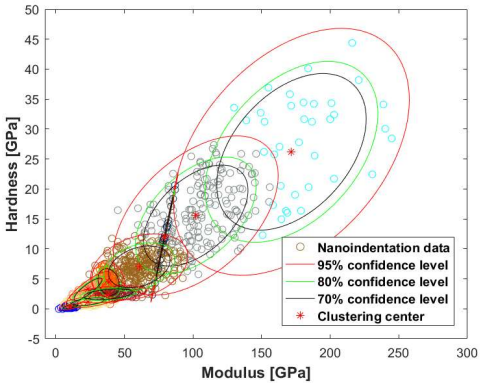

(e) k=9

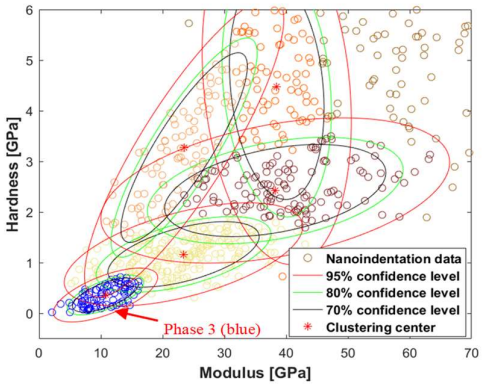

(f) Local details for k=9

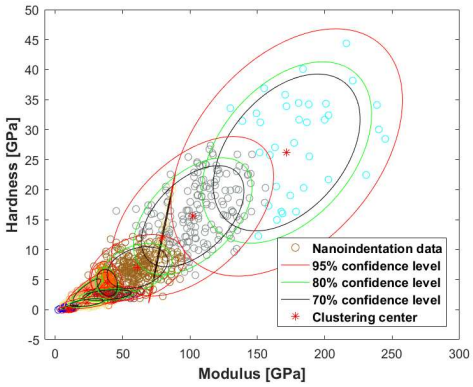

(g) k=10

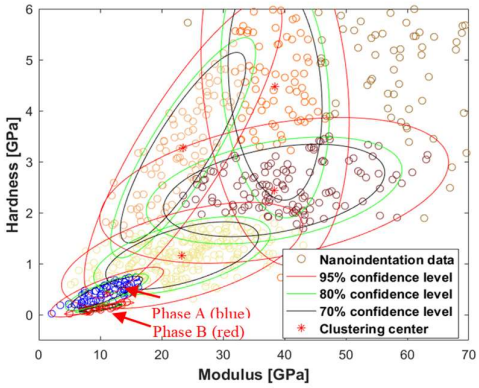

(h) Local details for k=10

Figure 5.3 Deconvolution of nanoindentation data for AAFA-M1-S (continuing)

These results indicate that when k (the number of phases) is 2 or 3 or 4, the corresponding phase has high variance values. For instance, for the model with 4 components, the elastic modulus of the "blue phase" ranges from very small values to almost 50 GPa, while the hardness of it ranges from around 0 GPa to more than 2 GPa. Besides, high average elastic modulus and hardness values are observed. When the number of components reaches 5, a new phase, phase 2 in Figure 5.3(d) with small micromechanical properties and variances is separated from the phase 1 in the model with 4 components. For this new phase, its standard deviation of elastic modulus and hardness are 3.61 and 0.25, respectively, which are similar to the value reported for the C-S-H gel in cement pastes (Hu & Li 2015b). In addition, the elastic modulus of 11.20 GPa and hardness of 0.41 GPa

of this phase are also close to lots of results reported for low-density C-S-H (Hu & Li 2015b), although a bit low. Therefore, the big phase, phase 1, in the model with 4 components should be a phase mixed by gel and other inclusions, while the phase 2 separated from it in the model with 5 components should be the gel phase. The reinforcing effect of the inclusions enhances the micromechanical properties of the mixed phase. The presence of multiple phases induces a large range of variation for both elastic modulus and hardness.

Table 5.2 Deconvolution result for AAFA-M1-S (clustered blue points and red points)

k	M [GPa]	H [GPa]	f	BIC	C		
					$C11$	$C12=C21$	$C22$
2	32.96	2.95	65.30%	16050.70	296.21	32.10	5.26
3	22.32	1.13	29.73%	15568.81	116.77	5.87	0.42
4	23.56	1.18	30.09%	15466.12	126.07	6.66	0.48
5	11.20	0.41	7.27%	15403.81	13.03	0.62	0.06
6	11.18	0.41	7.28%	15363.51	13.01	0.61	0.06
7	10.76	0.36	7.16%	15326.70	11.85	0.49	0.05
8	10.76	0.36	7.16%	15298.94	11.87	0.49	0.05
9	10.76	0.36	7.23%	15278.04	11.92	0.49	0.05
10-phase A	11.08	0.45	5.15%	15255.38	14.24	0.62	0.04
10-phase B	9.87	0.13	1.86%	15255.38	5.66	0.12	0.003
11-phase A	11.37	0.46	5.57%	15243.42	14.93	0.66	0.04
11-phase B	9.89	0.13	1.86%	15243.42	5.70	0.12	0.003
12-phase A	11.10	0.45	5.10%	15233.15	14.19	0.63	0.04
12-phase B	9.86	0.13	1.86%	15233.15	5.63	0.12	0.003
Ave_5-7	11.05	0.40	7.24%	—	12.63	0.57	0.06

Note: k is the number of phases. The numbers in the column of "M" and "H" refer to mean value of elastic modulus and hardness, respectively. f is the proportion of the phase. C is covariance matrix, where $C11$ is the variance of elastic modulus, $C22$ is the variance of hardness and $C12$ is the covariance of modulus and hardness.

As revealed in Table 5.2, there is a slight decrease in the elastic modulus and hardness of the gel phase when the number of components in the model increases from 5 to 9. A more significant change occurs when the number of components reaches 10, where the phase 3 in the model with 9 components is decomposed into two small phases, phase A and phase B shown in Figure 5.3 (h). The properties of the phase A and phase B remain stable even the number of components increases to 12. Increasing the number of components further makes the calculation difficult to converge with lots of random initial input values and hard to find the real global optimal solution. Therefore, the calculation is stopped after the model reaches 12 components, even if it does not reach the optimal Bayesian value (minimum value).

5.4.3 **Deconvolution results for AAFA-M0-H**

Table 5.3 and Figure 5.4 present the deconvolution results for the NaOH activated fly ash sample. For this sample, a phase with micromechanical properties conforming to the empirical knowledge (LD C-S-H and N-A-S-H identified in AAFA-M1-S) of the gel phase presents when k is 3. Then, the properties of the phase decrease slightly with the increase in the number of components until 6 components are given to the model. For the models with 3 to 6 components, the properties of the phase listed in Table 5.3 are similar to some results for standard cured sample AAFA-M1-S in Table 5.2. However, this phase is decomposed into two smaller phases when k is 7, which can be observed from Figures. 5.4(b), (d) and (f). These two phases persist even if there are 12 components in the model as shown in Table 5.3.

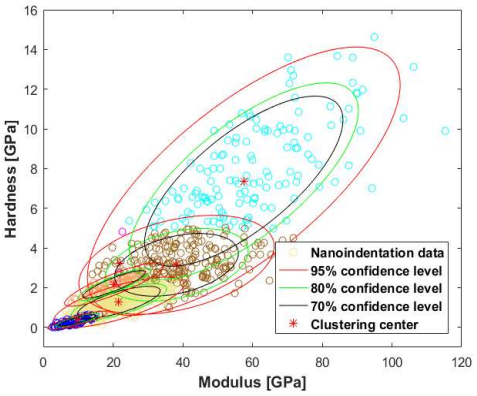

(a) k=6 (purple dots is a phase)

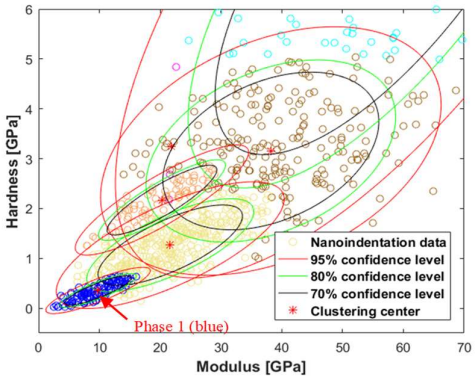

(b) Local details for k=6 (purple dots is a phase)

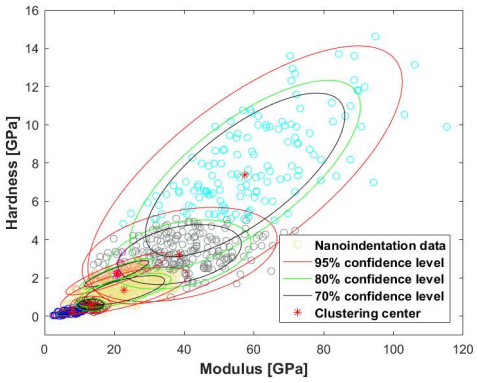

(c) k=7

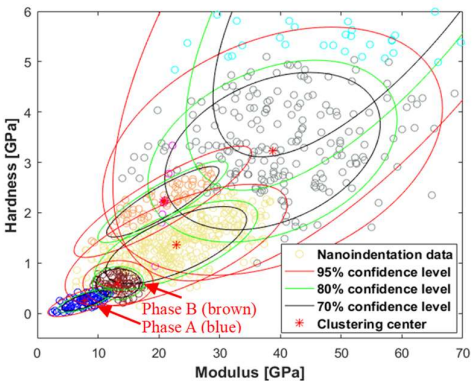

(d) Local details for k=7

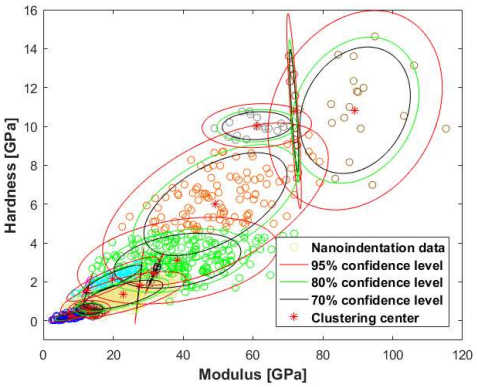

(e) k=12

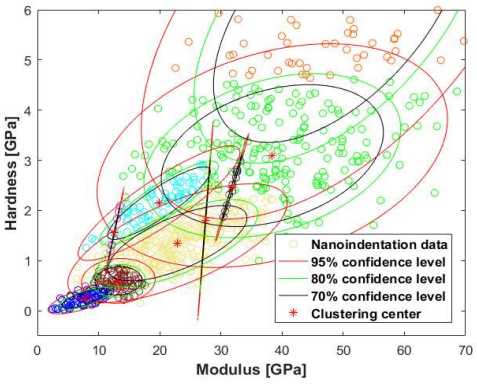

(f) Local details for k=12

Figure 5.4 Deconvolution of nanoindentation data for AAFA-M0-H

Table 5.3 Deconvolution results for AAFA-M0-H (clustered blue points and brown points)

k	M [GPa]	H [GPa]	f	BIC	C		
					$C11$	$C12=C21$	$C22$
2	20.74	1.33	65.81%	10247.74	91.06	6.07	0.64
3	11.49	0.48	17.77%	10054.60	19.84	1.04	0.07
4	10.22	0.39	14.11%	9961.75	14.01	0.67	0.05
5	9.78	0.36	12.10%	9930.88	12.40	0.57	0.04
6	9.78	0.36	12.13%	9911.21	12.41	0.57	0.04
7-phase A	7.84	0.25	8.23%	9893.07	6.26	0.24	0.02
7-phase B	13.28	0.60	8.24%	9893.07	5.58	0.01	0.03
8-phase A	7.81	0.25	8.13%	9882.40	6.32	0.24	0.02
8-phase B	13.40	0.61	9.71%	9882.40	7.11	0.08	0.04
9-phase A	7.76	0.25	7.98%	9880.84	6.14	0.23	0.02
9-phase B	13.29	0.60	8.26%	9880.84	5.77	0.05	0.03
10-phase A	7.83	0.25	8.23%	9874.01	6.25	0.24	0.02
10-phase B	13.24	0.60	8.19%	9874.01	5.59	0.01	0.03
11-phase A	7.21	0.20	5.78%	9865.82	6.17	0.19	0.01
11-phase B	12.80	0.56	10.10%	9865.82	7.46	0.11	0.03
12-phase A	7.78	0.25	8.10%	9857.43	6.14	0.23	0.02
12-phase B	13.23	0.60	8.60%	9857.43	6.05	0.03	0.03
Ave_3-5	10.50	0.41	14.66%	—	15.42	0.76	0.05

Note: k is the number of phases. The numbers in the column of "M" and "H" refer to mean value of elastic modulus and hardness, respectively. f is the proportion of the phase. $C11$ is the variance of elastic modulus, $C22$ is the variance of hardness and $C12$ is the covariance of modulus and hardness.

5.4.4 **Deconvolution results for AAFA-M1-H**

For the AAFA-M1-H sample, the deconvolution results are presented in chapter 4 and summarized in Figure 5.5. The properties of AAFA-M1-H start to vary in a small range when the number of components reaches 3, and the final stable phase is generated from the model with 8 components to the model with 12 components. However, even for the model with 12 components, the variance of elastic modulus and hardness of this phase are still large values, which are 60.32 and 0.27, respectively. Besides, the elastic modulus, hardness, and proportion of the phase in the model with 12 components are 22.69 GPa, 1.29 GPa, and 30.25%, respectively, which are similar to the mixed phase (blue phase, k=4) in AAFA-M1-S. Therefore, the final stable phase in models with 8 to 12 components is not regarded as the possible N-A-S-H gel phase. The second deconvolution is conducted for the final stable phase.

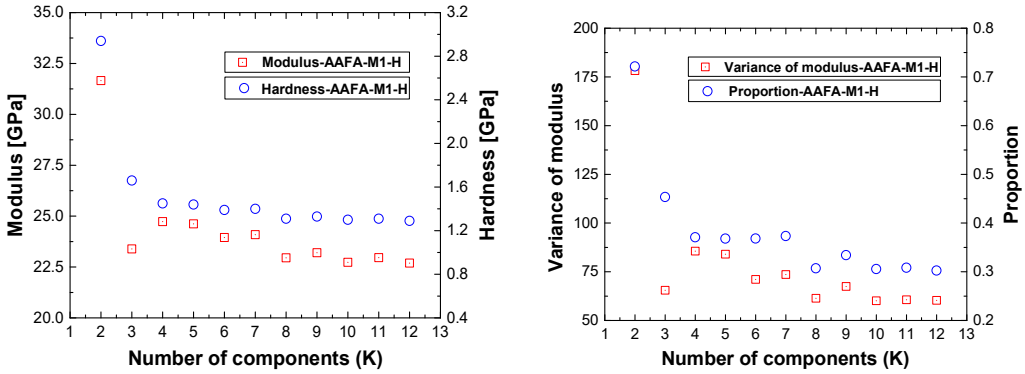

(a) Micromechanical properties of AAFA-M1-H (b) Variance and proportion of AAFA-M1-H

Figure 5.5 The first deconvolution results for AAFA-M1-H

The results for the second deconvolution are listed in Table 5.4. For the second deconvolution, a stable phase is separated from phase 1 in the model with 3 to 7 components. The properties of it are in line with empirical knowledge for the gel phase. Further deconvolution with an increased number of components would lead to no more

stable phase with reasonable proportion due to the limited data. Therefore, a maximum of 7 components is assigned to the model for deconvolution.

Table 5.4 Deconvolution result for clustered data belong to the stable phase of AAFA-M1-H when k is 12

k	M [GPa]	H [GPa]	f	BIC	C		
					$C11$	$C12=C21$	$C22$
12-1	22.71	1.29	100% (30.25%)	1473.28	58.54	3.14	0.25
12-2	22.20	1.24	93.54% (28.30%)	1460.87	58.45	2.96	0.22
12-3	14.03	0.56	19.90% (6.02%)	1446.38	16.84	0.75	0.04
12-4	14.19	0.58	21.06% (6.37%)	1435.05	16.90	0.79	0.05
12-5	14.67	0.58	20.17% (6.10%)	1425.61	19.83	0.84	0.04
12-6	15.26	0.63	19.99% (6.05%)	1419.11	19.36	0.81	0.04
12-7	14.79	0.60	22.74% (6.88%)	1416.02	19.68	0.91	0.05
Ave_12_3-5	14.30	0.57	20.38% (6.16%)	-	17.86	0.79	0.04

Note: the fraction without brackets is the proportion of the component to all components in the second time of deconvolution, and the fraction within brackets is the proportion of the component to all components in original AAFA reaction system.

5.4.5 **Deconvolution results for AAFA-M1.5-H**

The deconvolution results for the AAFA-M1.5-H sample are shown in Figure 5.6 and Table 5.5. For this sample, the variation of the properties of phases starts in a small range when the number of components reaches 3. The more stable phase presents from the model with 5 components. Afterwards, the properties of this phase do not change evidently even if the number of components reaches 12.

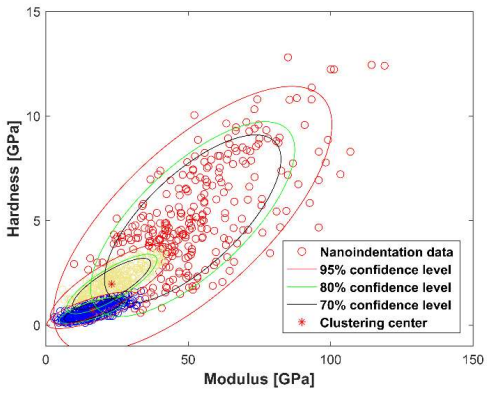

(a) k=3

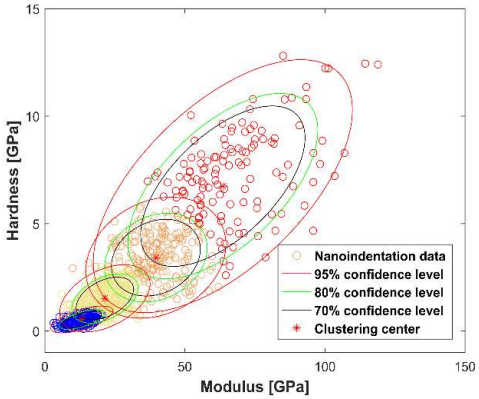

(b) k=4

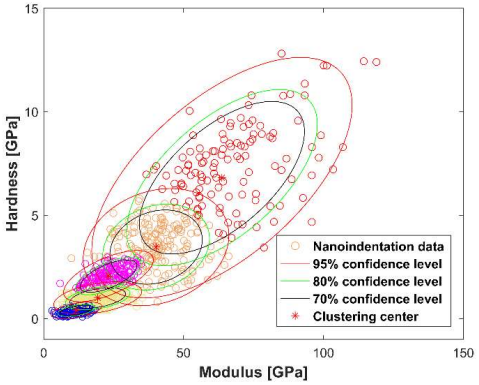

(c) k=5

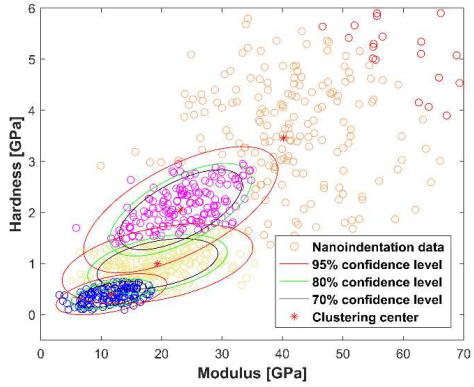

(d) Local details for k=5

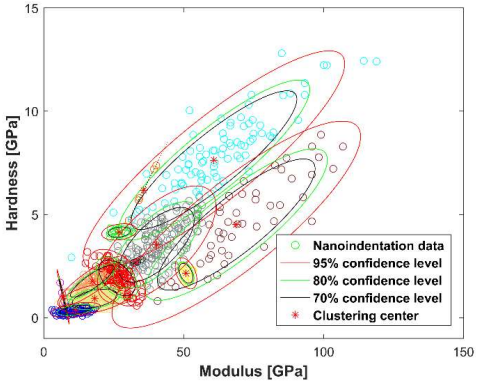

(e) k=12

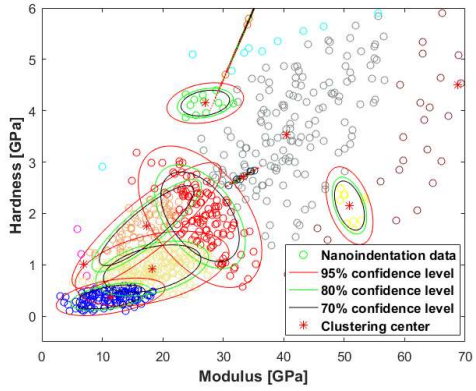

(f) Local details for k=12

Figure 5.6 Deconvolution of nanoindentation data (elastic modulus and hardness) for AAFA-M1.5-H

Table 5.5 Deconvolution result for AAFA-M1.5-H (clustered blue points)

k	M [GPa]	H [GPa]	f	BIC	C		
					$C11$	$C12=C21$	$C22$
2	18.68	1.19	60.21%	9330.89	54.53	3.96	0.55
3	16.57	0.71	33.69%	9185.27	43.51	1.79	0.13
4	13.21	0.54	22.40%	9135.45	20.70	0.76	0.07
5	11.71	0.40	15.21%	9088.36	14.02	0.31	0.03
6	11.70	0.40	15.10%	9066.53	13.98	0.31	0.03
7	11.72	0.40	15.40%	9048.99	14.02	0.31	0.03
8	11.36	0.39	14.63%	9033.79	12.81	0.27	0.03
9	11.72	0.40	15.41%	9026.87	14.00	0.31	0.03
10	11.37	0.38	13.81%	9011.51	13.50	0.26	0.02
11	11.58	0.39	13.95%	8996.77	12.14	0.26	0.02
12	11.37	0.38	13.62%	8995.79	13.53	0.26	0.02
Ave_4-6	12.21	0.45	17.57%	—	16.23	0.46	0.04

5.5 Analysis and discussion

5.5.1 **Determination of gel phase in geopolymer**

For the deconvolution results given above, one crucial step is to determine the gel phase correctly. Chapter 4 illustrated that BIC is not an ideal method to determine the gel phase. The BIC results in this chapter also fail to reach the optimum value. The presence of phases with a very small proportion in models indicates that some points are misidentified as an individual phase. The knowledge (Standard deviation, mechanical properties, etc.) of the gel phase is used for determining the N-A-S-H gel.

As typically analyzed above for AAFA-M1-S, the phase in the model with 4 components and has high modulus and hardness of 23.56 GPa and 1.18 GPa should be the mixed phase,

while the phase in 5 components model with modulus and hardness of 11.20 GPa and 0.41 GPa, respectively, is consistent with the features of gel phase. It is easy to find that there are similar mixed phase and gel phase in the other three kinds of samples. When further increasing the number of components, the micromechanical properties and proportion of the gel phase in AAFA-M1-S and especially AAFA-M0-H are decreased. In the deconvolution process, few components for a model may make the phase that has minimum micromechanical properties a mixed phase as mentioned. Actually, too many components may result in the excessive separation of the gel phase, breaking the single gel phase into sub-phases. The gel phase in 5 to 9 components models of AAFA-M1-S just has a small proportion of slightly more than 7.27%, the breakdown of the single phase into two phases with very small proportions should be more ascribed to the spurious phase generated when too much phase number assigned to the model. For the results slightly changed from the 5 components model to 9 components model, it is hard to ascertain if it is a refinement of the result by removing more inclusion or an excessive separation of the gel phase. In this study, if the possible gel phase lasts more than three models, then the final properties of the gel phase are determined by the average value of the first three results to reduce the impact of uncertainty (average all gel phases when less than 3). Considering the fact that geopolymer at least contains gel, mixed phase, and unreacted fly ash, the possible gel phase should be selected from the model by at least 3 components. For AAFA-M1-S, it is the average result from 5 components model to 7 components model as listed in the last row of Table 5.2. Correspondingly, it is the average result of 3 components model to 5 components model for AAFA-M0-H, 12-3 components model to 12-5 components model for AAFA-M1-H and 4 components model to 6 components model for AAFA-M1.5-H. The phase in the 3 components model of AAFA-M1.5-H is

not accepted as the gel phase as it has large variance and a large range of variation of both modulus and hardness.

5.5.2 **Evaluation of error**

In order to compare the micromechanical properties of N-A-S-H in different geopolymers, one of the key issues is to evaluate the errors generated from the analytical technique itself. The first error should be the average method adopted to represent the micromechanical properties of gels. Illustrated by the case of AAFA-M1-S, the possible elastic modulus of gel for it is 11.20, 11.18 or 10.76 GPa. For the average value of 11.05 GPa adopted, the corresponding deviation is 0.15, 0.13 or -0.29 GPa, as shown in Figure 5.7. For all these samples, the maximum possible deviations are 0.99 GPa for elastic modulus, 0.09 GPa for hardness and 4.83% for proportion. The average value of all those deviations (absolute value) for elastic modulus, hardness, and proportion are 0-0.2 GPa, 0.04 GPa, and 1.37%, respectively.

Another possible error can be ascribed to the test data, although the number of points (Nine grids) tested is more than conventional research. The number of grids was increased to 18 for AAFA-M0-H to check if there are significant different results for the properties obtained from 9 grids and 18 grids. Since this study aims at the gel phase only, the additional grids were intentionally put on the areas that very rich in gel to provide more data for the analysis of gel. Some typical results for AAFA-M0-H based on 18 grids are compared with the results from 9 grids and shown in Figure 5.8. The micromechanical results from models are (11.08, 0.57) for 3 components and (9.43, 0.42) for 4 components, respectively. There are close to the corresponding values obtained from the deconvolution of 9 grids as given in Table 5.3. When increasing the number of components, there will be no more similar gel phase. Namely, the average properties for N-A-S-H gel based on 18 grids are (10.26, 0.50).

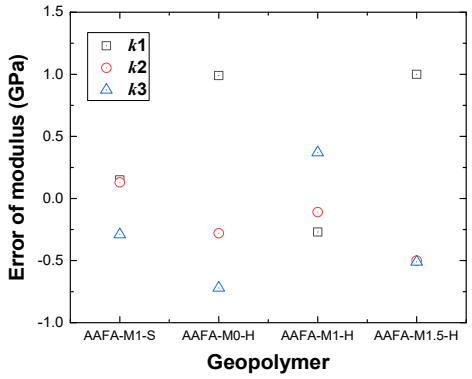

(a) Error of modulus

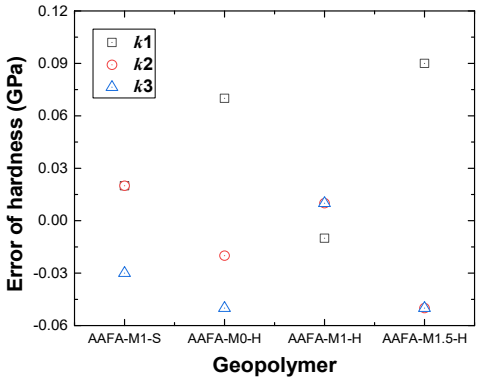

(b) Error of hardness

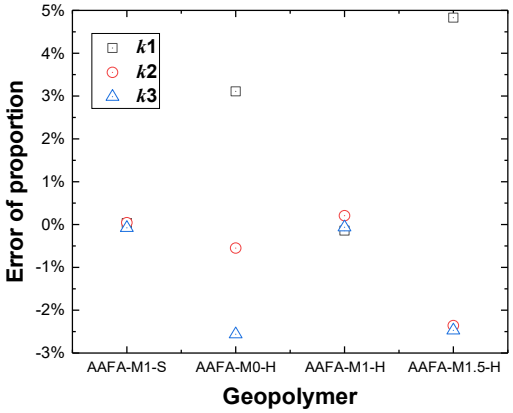

(c) Error of proportion

Figure 5.7 Errors result from average method to determine micromechanical properties of gel

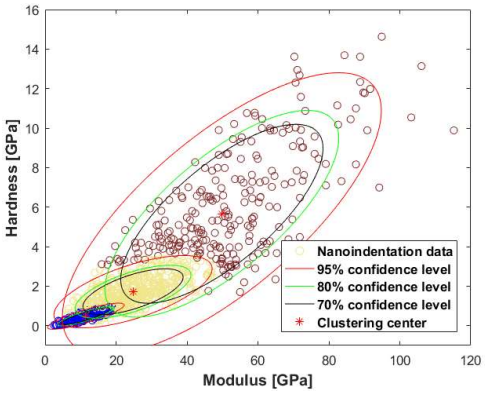

(a) k=3 (9 grids)

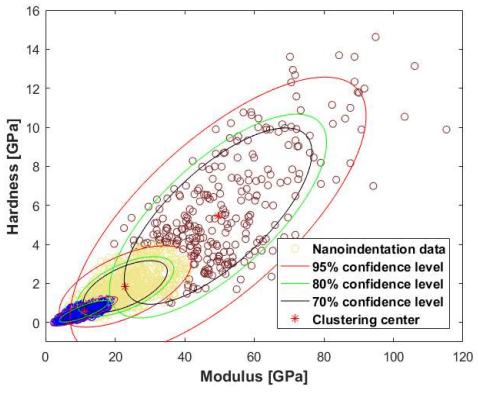

(b) k=3 (18 grids)

Figure 5.8 Errors result from limited test data of statistical nanoindentation

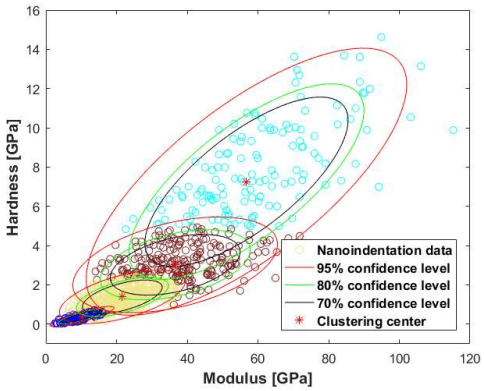

(c) k=4 (9 grids)

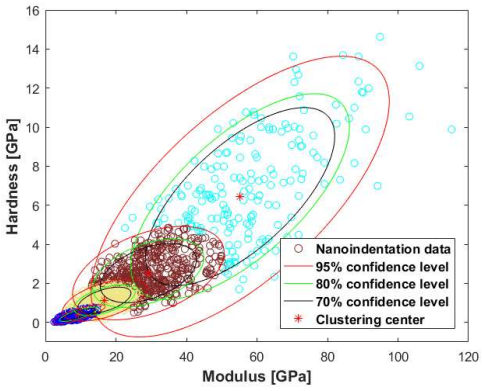

(d) k=4 (18 grids)

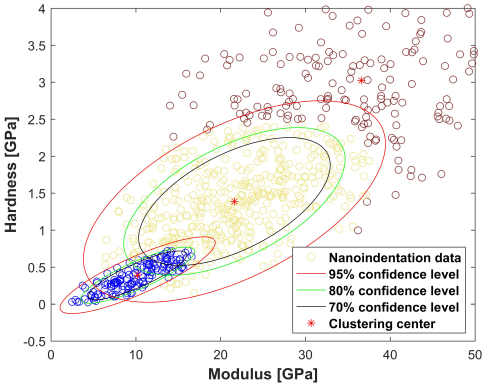

(e) Local details for k=4 (9 grids)

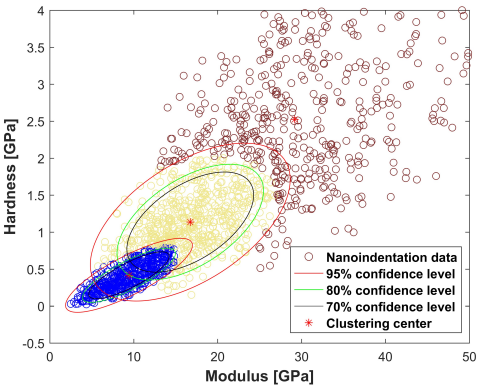

(f) Local details for k=4 (18 grids)

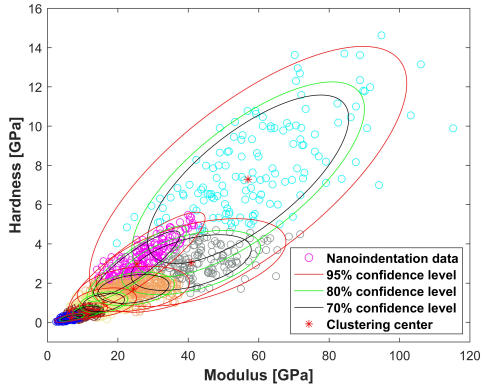

(g) k=7 (18 grids)

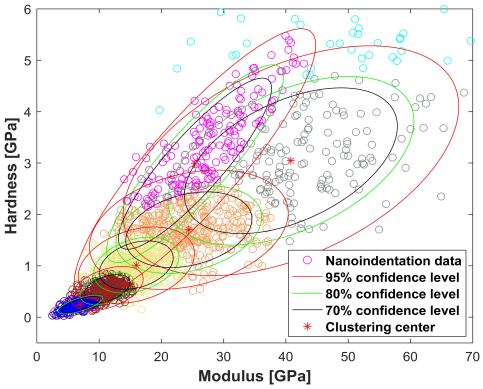

(h) Local details for k=7 (18 grids)

Figure 5.8 Errors result from limited test data of statistical nanoindentation (continuing)

One special phenomenon for AAFA-M0-H is the presence of two phases when the number of components is more than 7, while both of these two phases have a considerable proportion. For the sake of comparison, the 7 components model based on 18 grids is

provided in Figures. 5.8(g) and (h). Similar to that in Figure 5.4, there are also two phases. The blue phase and the brown phase have the properties of (6.99, 0.25) and (11.27, 0.56), respectively. It indicates that the two phases are not generated due to the limited test data. It is easy to track that these two phases are mainly decomposed by the gel phase in models that have few components, although some points are removed or included during this process. The average properties of these two phases in the 7 component model based on both 9 grids and 18 grids are obtained by the cluster of data for each phase. As shown in Figure 5.8, the nanoindentation data that belong to the phases with micromechanical properties of (6.99, 0.25) and (11.27, 0.56) are clustered into blue points and brown points according to the maximum posterior probability. The blue points and brown points are collected and plotted in Figures. 5.9(a) and (b), with their average value denoted by the clustering centre, which are (6.75, 0.23) and (11.32, 0.55), respectively. Namely, the clustered data can well represent the estimated phase in the deconvolution of AAFA-M0-H based on 18 grids. Then, the blue points and brown points are combined together. The average properties of all those points are (9.60, 0.43) as shown in Figure 5.9(c). Similarly, the average properties of all those points in AAFA-M0-H based on 9 grids are (10.66, 0.42). The average properties of blue and brown phase are similar in models with different grid numbers. Moreover, the average properties of these two phases are very close to the properties of the gel phase. It is possible that the blue phase is the gel with higher porosity than the brown phase.

The errors result from limited test data are summarized in Figure 5.9(d). For the elastic modulus and hardness of N-A-S-H we study, the deviation of results is just -0.24 and 0.09 GPa, respectively. Taking into account the above errors caused by the average method to determine the properties of the gel phase, the approximate errors for elastic modulus and hardness are 0.68 and 0.13 GPa. Meanwhile, the maximum deviations are obtained as

1.23 GPa for elastic modulus and 0.18 GPa for hardness. One thing to note is the results are based on the sum of the absolute values that would enlarge the evaluation of the errors. Namely, the positive and negative errors do not cancel each other out.

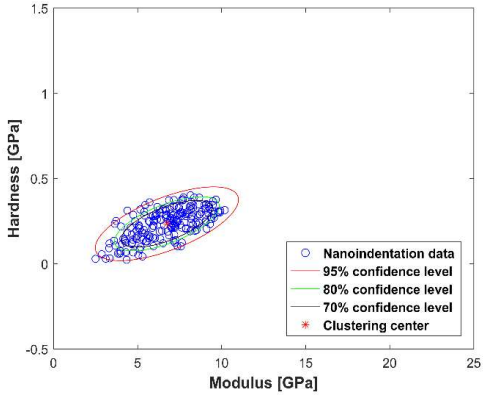

(a) Clustered data for estimated phase with M of 6.99 and H of 0.25

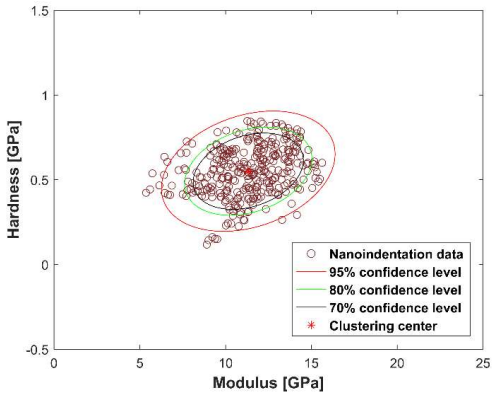

(b) Clustered data for estimated phase with M of 11.27 and H of 0.56

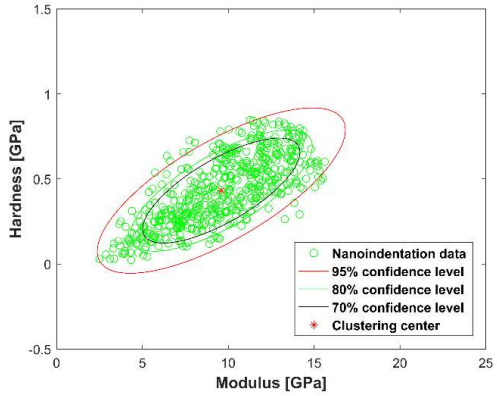

(c) Average properties of two decomposed phases

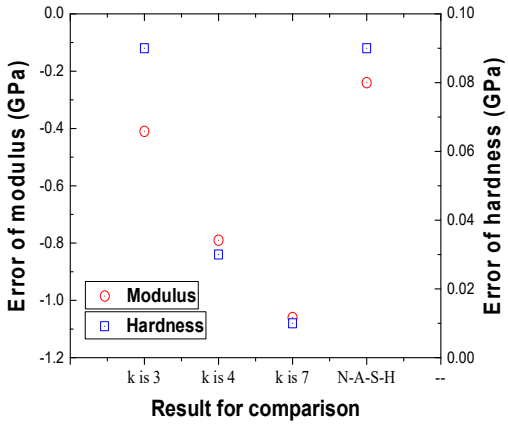

(d) Deviation of results between deconvolution of 9 grids and 18 grids data

Figure 5.9 Average properties of decomposed phases in 7 component model of AAFA-M0-H (18 grids), and results of error evaluation.

5.5.3 **Correlation and difference of different statistical techniques**

For the LSE method that generally used to fit the frequency density histogram for deconvolution analysis, it is known to depend on the bin size. The correlation and difference of the LSE and MLE methods are discussed by the hardness histogram of AAFA-M1-S. The possible N-A-S-H gel phase of AAFA-M1-S starts to appear in the model with 5 components and decompose into two phases in the model with 10 components. The possible gel would exist in models with 5 to 9 components. However, as displayed in Figure 5.10, any model could match the histogram if suitable bin size is set for the histogram. If the bin size is more than 0.28, it is hard to obtain the hardness of N-A-S-H gel (the green peak in Figures. 5.10(b) and (c)) by LSE, as there is no corresponding peak in the histogram. The large green peak in Figure 5.10(a) would be misidentified as the N-A-S-H. Generally, the bin size set in exiting studies is more than 0.28 and the number of components adopted is 4. In that case, the final results should be from a mixed phase instead of N-A-S-H gel. When the bin size is small to around 0.12, as can be clearly observed from Figure 5.10(c) and (d), the model with 10 components can even better match the histogram than the model with 9 components. Consequently, the properties of N-A-S-H would be erroneously derived from the 10 components model.

For the GMM estimated by the MLE method, reasonably increasing the number of components enables the model to reflect more details of the distribution of the collected data. Bin size plays a similar role in the histogram. Smaller bin size contributes to revealing more information on the collected data. Therefore, for the models with increased phases, there are histograms with decreased bin sizes that can match them. However, for both of the number of components and bin size, the inappropriate parameters would lead to either mixed phase (k=4) or sub-phases (k=10). For the MLE method adopted, the gel phase could be determined by empirical knowledge of multiple

parameters within a few models with a different number of components. For LSE method, the bin size is hard to set reasonably, since it is a continuous number with an infinite range of values. Besides, the suitable bin size would be affected by lots of factors, such as features of the sample and the number of test data. For the same bin size, a small number of test data would be no more able to form a neat and identifiable histogram for fitting.

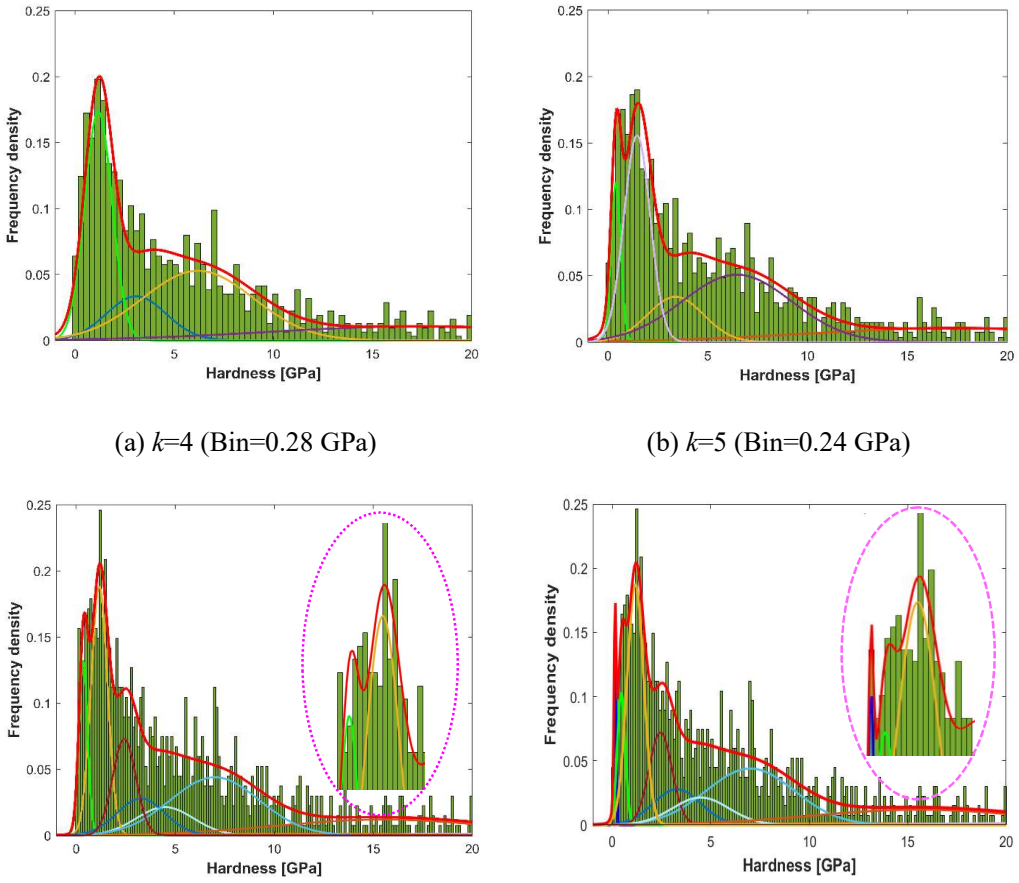

(a) k=4 (Bin=0.28 GPa)

(b) k=5 (Bin=0.24 GPa)

(c) k=9 (Bin=0.12 GPa)

(d) k=10 (Bin=0.12 GPa)

Figure 5.10 Comparison of PDF with hardness frequency histogram for AAFA-M1-S

5.5.4 **Nano/micromechanical properties of N-A-S-H gel in geopolymers**

The properties of the gel phases in this study are summarized in Table 5.6. It is obvious that the AAFA-M1-H sample has the highest micromechanical properties while the AAFA-M0-H has the lowest one. The properties of the AAFA-M1-S are just slightly

higher than the AAFA-M0-H and modestly lower than the AAFA-M1.5-H. As estimated above, the possible errors for elastic modulus and hardness are around 0.68 and 0.13 GPa, respectively. Even in the most unfavourable situation, where the larger one has been overestimated and the smaller one has been underestimated (deviation of 1.36 and 0.26 GPa), one still can point that the elastic modulus of AAFA-M1-H is larger than the AAFA-M0-H and AAFA-M1-S, and AAFA-M1.5-H is larger than AAFA-M0-H. In chapter 4, higher elastic modulus and hardness of 15.46 and 0.73 GPa than AAFA-M1-H were obtained for geopolymer with similar mix design but higher alkali concentration of 10%. Thus, the statistical nanoindentation results suggest that the micromechanical properties of N-A-S-H gel should vary with the samples, but just in a very small range. The variation range of the elastic modulus obtained here is smaller than that of other studies by the LSE method (Lee, Vimonsatit & Chindaprasirt 2016; Ma, Ye & Hu 2017).

Table 5.6 Properties of N-A-S-H in geopolymers with different silica modulus under different curing conditions

Samples	k	M [GPa]	H [GPa]	f	C		
					$C11$	$C12=C21$	$C22$
AAFA-M1-S	Ave_5-7	11.05	0.40	7.24%	12.63	0.57	0.06
AAFA-M0-H	Ave_3-5	10.50	0.41	14.66%	15.42	0.76	0.05
AAFA-M1-H	Ave_12_ 3-5	14.30	0.57	6.16%	17.86	0.79	0.04
AAFA-M1.5-H	Ave_4-6	12.21	0.45	17.57%	16.23	0.46	0.04

5.5.5 **Mechanism analysis of the variable nano/micromechanical properties of N-A-S-H gel**

The micromechanical properties of N-A-S-H gels obtained in this study are similar but slightly lower than that of LD C-S-H gel (Hu & Li 2015b). Besides, the proportion of it is also lower than reported for both N-A-S-H (Das et al. 2015; Němeček, Šmilauer & Kopecký 2011) and LD C-S-H (Constantinides & Ulm 2007). In fact, there is an important factor that would influence the test results but hasn't been considered in existing nanomechanical test research of N-A-S-H gel, namely, the presence of crystals. Although the study by the XRD shown in Figure 5.11 doesn't detect any new crystals when compared with raw material fly ash, it can't eliminate the possibility that the crystals significantly affect the results.

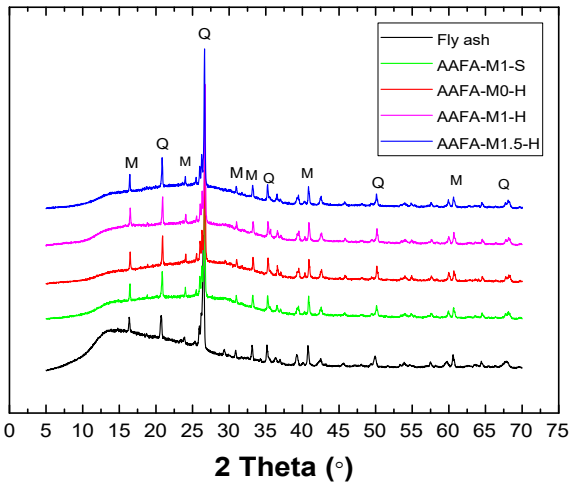

Figure 5.11 X-ray diffraction patterns of geopolymer paste

In the activation process, crystals from fly ash are hard to react which would then be surrounded by the generated gel. Evidence can be found by the micro to nanoscale observation of N-A-S-H gel displayed in Figure 5.12. Slender crystals can be observed clearly in Figure 5.12 (a). Additionally, for the gel near the clustered crystals, the magnified photo in Figure 5.12(b) indicates that there are also lots of crystals in the gel.

Higher magnification observations were conducted at lots of other locations of the sample. Although there is gel without recognizable crystal, as shown in Figure 5.12(c), nano to sub-micron crystals can be found to embed in gel in some other locations. The presence of crystals in the involved range of nanoindentation would significantly enhance the mechanical properties and then identified as the mixed phase in deconvolution analysis. It should be the main reason responsible for the low proportion of the gel obtained.

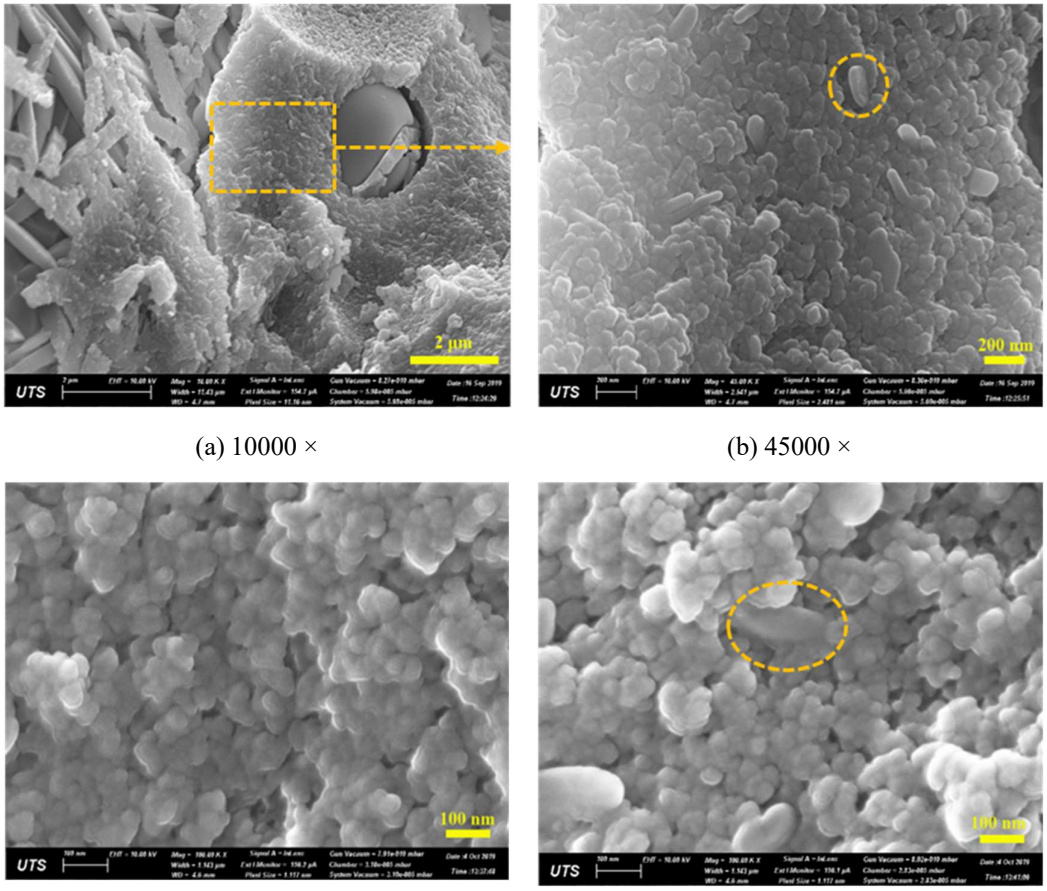

(a) 10000 ×　　(b) 45000 ×

(c) 100000 ×　　(d) 100000 ×

Figure 5.12 Microstructure of N-A-S-H gel in AAFA

For almost all of the samples, there is a phase with elastic modulus slightly more than 20 GPa and hardness slightly more than 1 GPa. It can be typically found in Figure 5.3(f) for AAFA-M1-S (yellow phase), Figure 5.4(b) for AAFA-M0-H (yellow phase), and Figure 5.6(b) for AAFA-M1.5-H (blue phase, 21.43 GPa, 1.52 GPa). For AAFA-M0-H based on

18 grids, the majority of the new test points from the additional nanoindentation grids are intentionally not put on unreacted fly ash. Hence, the test data would concentrate on the region with smaller micromechanical properties. The part of this mixed phase with large mechanical properties would be lost in the deconvolution due to the small proportion, resulting in the slightly smaller of the mechanical properties of it. The same consideration could possibly also be applied for AAFA-M1.5-H. The maximum proportion of it may be ascribed to the grids. Some of them happen to be in gel-rich areas. This mixed phase also shows small properties when k is large.

The final N-A-S-H gel phase is separated from the part of this kind of mixed phase where it has the lowest mechanical properties. This phase may be mainly a mixture of crystals and gels, and just have a small fraction of other inclusions. Firstly, the "big phase" can be found in all samples with similar properties which mean it may be a stable phase that exists in AAFA rather than a mixture of gel phase with random inclusions. Besides, the micromechanical properties of this kind of mixed phase are close and a bit lower than the agglomeration of C-S-H and CH crystal identified in Portland cement paste (Davydov, Jirásek & Kopecký 2011), which is plausible to be the mixture of crystals and N-A-S-H as N-A-S-H's modulus and hardness are also slightly lower than that of LD C-S-H. This kind of mixed phase has lower mechanical properties than other phases. This may be caused by the small scale of the crystals and different mechanical properties of it compared with other unreacted particles that come from fly ash.

As shown in Figure 5.12, the microstructure of N-A-S-H is found to be looser than that normally known for C-S-H gel, which may be the reason for lower micromechanical properties of N-A-S-H gel, and then the generally lower macro performance of fly ash-based geopolymer. In terms of the micromechanical properties in different geopolymers, the variation may be affected by both the mechanical properties of the gel particles and

the nanoscale pores. For the study of C-S-H in Portland cement paste, Jennings (Jennings 2000) proposed a simplified model to represent the microstructure of C-S-H. Basic spherical blocks with size about 2 nm cluster together to form globules and then the globules pack together to form LD and HD C-S-H structures. This model is further modified as a packing structure with the ~5 nm globules as the basic unit (Jennings et al. 2007) to help the understanding of the microstructural changes associated with drying and heat curing. The globules are considered to have intrinsic parking density. The geopolymer gel is also formed by the packing of primary globular polymeric entities of several nanometres (Duxson et al. 2005), which can't be observed in Figure 5.12 due to the limited resolution of SEM. The globular polymeric entities form gel particles with the sizes of dozens of nanometres, while the gel particles are not always tightly integrated as shown in Figures. 5.12(c) and (d). The defects and pores between gel particles would be a factor affecting the micromechanical properties detected. The gel particles are governed by the globular polymeric entities and their parking density, while the stiffness of polymeric entities may be affected at least by its maturity and chemical structure.

The different maturity, and the different composition and chemical structure of the N-A-S-H gel are considered by Ma, Ye & Hu (2017) as the main reasons that account for the constant elastic's modulus in the study by Němeček, Šmilauer & Kopecký (2011) but varied elastic modulus in the study by Ma, Ye & Hu (2017). The polymerization process of AAFA is very slow and heat curing is usually used to accelerate it. For ambient cured AAFA and heat cured AAFA with different curing temperature, the difference between their 28-day compressive strength and longer time compressive strength is quite different (De Vargas et al. 2011; Singh & Subramaniam 2019; Sun & Vollpracht 2019) and larger than the difference in the Portland cement paste, which means that at 28 days, the samples have significantly different reaction degree under different curing conditions. The

different maturity would induce different stiffness of polymeric entities, the gel particles and then the micromechanical properties of the N-A-S-H gel. It is considered as the dominant reason for the significantly smaller properties of AAFA-M1-S than AAFA-M1-H. As for the influence of the composition and chemical structure of the gel phase, Constantinides & Ulm (2004b) found that the C-S-H decalcification would cause remarkable degradation of elastic modulus of C-S-H gel. Additionally, the indentation modulus and hardness of the synthetic C-S-H would change with the Ca/Si molar ratio (Pelisser, Gleize & Mikowski 2012). For geopolymer, within a suitable range, the increase of silica content may result in the increase of the fully condensed tetrahedral aluminosilicate network structures and then the strength of the geopolymer due to the higher strength of Si-O-Si bonds than the Si-O-Al bonds (Duxson et al. 2005). These results or theoretical basis indicate that the globular polymeric entities themselves may have different stiffness when chemical structure changed significantly. NaOH activated fly ash normally has lower macro strength than the alkali-silicate activated fly ash with similar mixture and condition. Provis, Lukey & van Deventer (2005) proposed that larger crystals in NaOH activated fly ash are hard to pack densely within the binder phase, which could be one of the reasons for its low macro strength. The lowest nanoindentation results for AAFA-M0-H can provide another reason that the N-A-S-H gel in NaOH activated fly ash would have lower micro-strength than others. These two factors work together to make the lower macro strength of NaOH activated fly ash sample.

5.6 Conclusions

The micromechanical properties of N-A-S-H gel in AAFA with different silica modulus and under different curing conditions are investigated in this study by deconvolution of

grid nanoindentation data with maximum likelihood estimation method. The following conclusions can be drawn up:

(1) Mixed phases and sub-phases are typical spurious phases in geopolymer. It is virtually impossible to reconcile these two kinds of spurious phases to obtain the accurate micromechanical properties of all real component by statistical nanoindentation. A compromise approach was proposed, which ensures the accuracy of the gel phase by intentionally introducing spurious phases for other components.

(2) The errors generated from the analytical technique itself were estimated from the two aspects of the average method adopted, and the number of the experimental data. The average deviation of elastic modulus and hardness introduced by the average method are 0.44 GPa, 0.04 GPa, respectively. Correspondingly, the number of test data would bring the errors of -0.24 GPa and 0.09 GPa.

(3) For the GMM estimated by MLE method, reasonably increasing the number of components enables the model to reflect more details of the distribution of the collected data. Bin size plays a similar role in the histogram. When increasing the number of phases in the model, there are histograms with decreased bin sizes that can match them. Different from the MLE method where multiple parameters could be referenced to determine the gel in a few models, the appropriate bin size is practically impossible to be determined from the infinite range of values.

(4) The micromechanical properties obtained for geopolymers vary in a minor range of 10.50 to 14.30 GPa for elastic modulus and 0.40 to 0.57 GPa for hardness. The highest micromechanical properties were achieved by AAFA-M1-H. Both AAFA-M0-H and AAFA-M1-S show significantly smaller properties. The variation may be affected by both the mechanical properties of the gel particles and the nanoscale

pores between them. The formal one would be determined at least by its maturity and chemical structure.

(5) The intermixing of crystals with gel was observed under high-resolution SEM. The interaction of them in the involved range results in a mixed phase in deconvolution, which largely decreased the proportion of N-A-S-H gel obtained. Compared to C-S-H, the looser structure of N-A-S-H should be one of the reasons for its inferior micromechanical properties.

(6) The properties of gel in different geopolymer samples should be more variable than that of C-S-H in different Portland cement paste samples. Cement grains can easily react with water, while fly ash needs to be activated by alkali solution. If under the extreme condition that the alkali solution is like water, it can be inferred that the 'gel' would undoubtedly have low properties than other geopolymers.

CHAPTER 6. NANOPARTICLES REINFORCING OF GEOPOLYMER AND MECHANISM ANALYSIS

6.1 Introduction

The optimal design of geopolymer is generally realized by adjusting alkali solution, source materials, admixtures, related ratio and curing conditions (Khale & Chaudhary 2007), which results in differences in the gel structure, reaction products, degree of polycondensation, etc., and then different properties of geopolymer. In addition to conventional methods, one of the very noticeable progress in the reinforcement of cement-based materials is the nanoscale modification (Monteiro et al. 2019; Sanchez & Sobolev 2010). There are extensive studies using nanomaterials to modify Portland cement matrix (Li, Huang, et al. 2016; Li et al. 2017; Monteiro et al. 2019). Positive effects such as filler effect and nucleation effect of nanomaterials on the performance of concrete have been found (Kawashima et al. 2013; Sobolev et al. 2009).

The application of nanomaterials in geopolymers is of great significance. In addition to improve the strength and durability of geopolymer concrete, the addition of nanoparticles is a promising strategy to avoid the inconvenient heat curing process (Adak, Sarkar & Mandal 2017). The filler effects of nanoparticles could lead to a dense microstructure and decreased sorptivity. Thus, using nanoparticles is also a potential solution to control alkali leaching and subsequent issues such as efflorescence. In this study, nano/microscale characterization was conducted on the nano-SiO_2 (NS)/nano-TiO_2 (NT) reinforced geopolymers to reveal the effects of nanoparticles on microstructure, gel proportion and gel micromechanical properties to promote the understanding of the macro-strength

reinforcement mechanism. Besides, the results obtained from different techniques were compared and discussed.

6.2 Experimental and analysis methods

6.2.1 Sample preparation

Alkali solutions and fly ash were mixed based on a silica modulus (SiO_2/Na_2O) of 1, Na_2O to ash ratio of 10%, and water to solid ratio of 0.32. The morphology and properties of NS and anatase NT are shown in Figure 6.1 and Table 6.1.

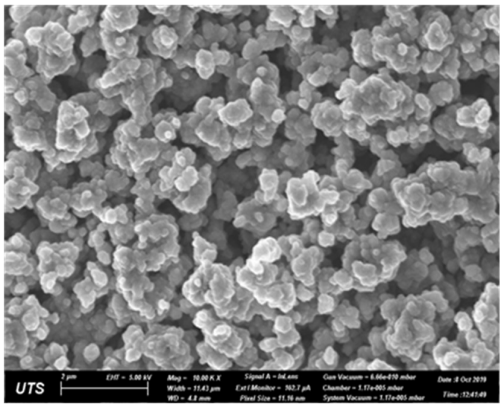

(a) NT particles (10000 ×)

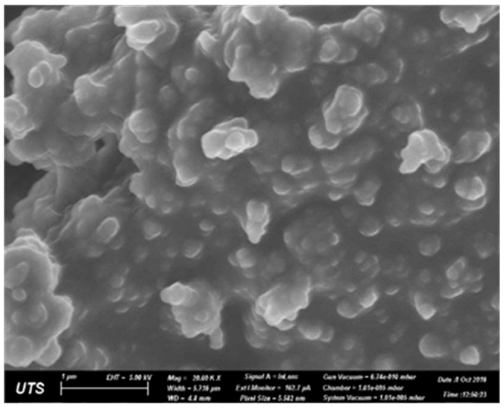

(a) NT particles (20000 ×)

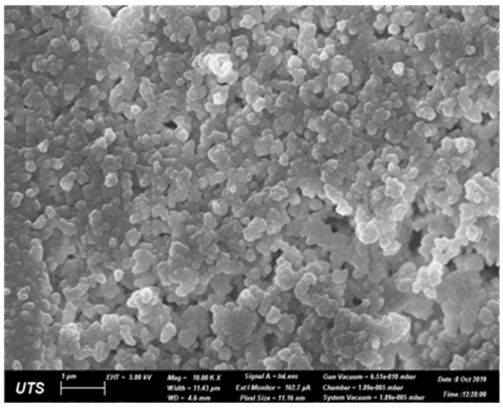

(b) NS particles (10000 ×)

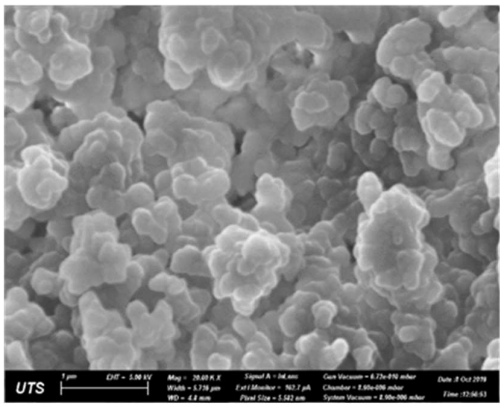

(b) NS particles (20000 ×)

Figure 6.1 Morphology of nanoparticles

NS and NT have the same average particle size of 20 nm. Nanoparticles were incorporated by the way of replacing 2% of fly ash while other factors were kept the same as the reference sample. Nanoparticles are easy to combine with each other owing to the high van der Waals force (Li, Luo, et al. 2016). In this research, 0.5% of Polycarboxylate superplasticizer was incorporated into the alkali solution (also for the reference sample) to help disperse nanoparticles. After adding nanoparticles to the alkali solutions, the suspensions was manually stirred for 3 min and then dispersed in an ultrasonic bath (120W, 40 kHz) for 2 hrs. In order to avoid the heat generated in the dispersion process, the water in the bath was replaced every 3 min in the first 1.5 hr, every 2 min in the following 20 min and every 1 min in the last 10 min. Alkali solution for the reference sample was also sonicated in the bath. A typical appearance change of the alkali-NS suspension is shown in Figure 6.2.

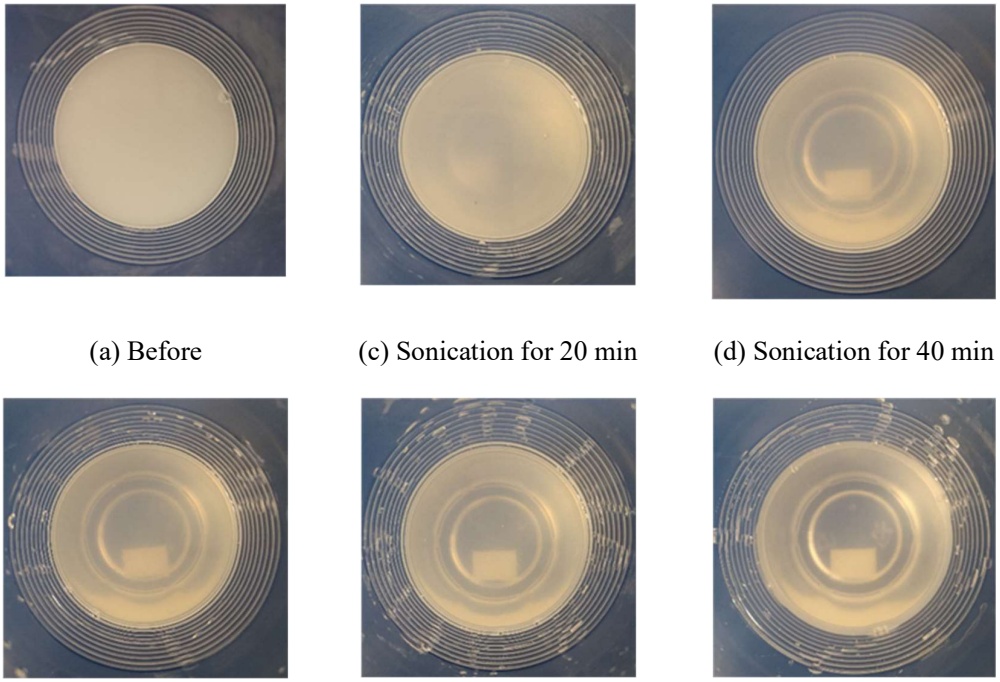

(a) Before (c) Sonication for 20 min (d) Sonication for 40 min

(e) Sonication for 60 min (f) Sonication for 90 min (g) Sonication for 120 min

Figure 6.2 Appearance changes of the alkali-NS suspension

Table 6.1 Basic properties of nanoparticles

Material	Appearance	Average particle size (nm)	Purity (%)	Type
Nano-TiO_2	White powder	20	99.9%	Anatase
Nano-SiO_2	White powder	20	99.9%	Amorphous

Geopolymer paste and mortar were mixed by Hobart mixer and cast in 50 mm ×50 mm ×50 mm cubic plastic moulds. Expect for 2 times of sand by weight of fly ash, the mortar samples had the same mix proportions as paste samples. After vibrated for 3 min, samples were sealed by plastic film and cured in a 65 °C oven for 48 hrs, followed by standard curing until 28 days. Then, small samples with a size of about 10 mm ×10 mm ×5 mm were cut from the core part of geopolymer pastes and embedded in epoxy resin. They were ground by 320, 600 and 1200 grits abrasive papers with each grade lasted for 10 minutes and polished with a small force by 0.3 μm alumina (20 min) and 0.05 μm cerium oxide slurry (20 min) to achieve a satisfactory surface. The polished samples were used for the nanoindentation test and BSE image analysis. Besides, paste samples were ground into powders for XRD and TGA analysis. Thereafter, samples were soaked in isopropanol for 3 days and then put in 50 °C vacuum oven drying for 3 days. Prepared samples were stored in a vacuum desiccator.

6.2.2 **Testing and characterization techniques**

The BSE images were taken at the low magnification of 500× to balance the requirement between details and overall information of samples (Diamond 2001; Scrivener 2004). A total of twenty figures were taken for statistical analysis of each sample. BSE was operated under the accelerating voltage of 15 kV on Zeiss EVO LS15, while Zeiss Supra 55VP was adopted for scanning electron (SE) image observation of geopolymer paste

samples to the nanoscale. The voltage for SE observation was 5 or 10 kV. The heat of reaction test, TGA test, XRD test, compressive test and workability test are conducted as stated in Chapter 3. Nine of 10 × 10 grids with a grid spacing of 15 μm were performed on samples. In an individual nanoindentation point test, the maximum force was set as 1.5 mN. The loading and unloading time (unloading to 10% of peak force) was 7.5 s. When reaching the maximum force, it was maintained for 5 s to remove creep. Constant Poisson's ratio of 0.2 was set. After deleting abnormal test points, the data were subjected to deconvolution analysis as Chapter 4 and 5.

6.3 Results and discussions

6.3.1 **Compressive strength and fresh properties**

The 28-day compressive strength of the reference sample, Geo-NS (geopolymer incorporated with NS) and Geo-NT (geopolymer incorporated with NT) are 30.5 ± 1.31 MPa, 35.8 ± 1.12 MPa and 33.7 ± 0.83 MPa, respectively, based on three duplicate samples. It means that both NS and NT particles have enhanced the strength of geopolymers, with an improvement of 17.38% and 10.49% for Geo-NS and Geo-NT samples, respectively. The addition of nanoparticles shows a slightly adverse effect on the workability, owing to the high specific area of fine particles. The flow diameter for the reference sample was 152.3 mm, while a smaller diameter of 148.4 mm and 145.7 mm were observed for Geo-NS and Geo-NT mortar samples. Due to the use of superplasticizer, the nano-geopolymers still have good workability.

6.3.2 **Heat of reaction**

The heat of reaction of samples during the first 48 hr is given in Figure 6.3. As presented in Figure 6.3(a), the heat flow curves are similar for these three samples. When compared with Portland cement paste (Lothenbach, Scrivener & Hooton 2011), much higher heat

flow is found for the heat cured geopolymers in the initial stage, and no peak was obtained in the later stage. The detailed figure in Figure 6.3(a) indicates that the highest heat release rate occurs at a similar time for samples. The nanomodified samples show significantly higher heat flow than the reference sample in the initial 2000 s, with the highest value achieved by Geo-NS. It indicates that NT and especially NS have accelerated the reaction rate, quite similar to the phenomenon observed in Portland cement paste (Björnström et al. 2004; Chen, Kou & Poon 2012; Monteiro et al. 2019). It would be attributed to increased interparticle space (Berodier & Scrivener 2014), as well as the possible nucleation effect from the ultra-small size of particles (Chen, Kou & Poon 2012; García-Taengua et al. 2015; Lee & Kurtis 2010; Rees et al. 2008). Increased thermal conductivity could also contribute to the acceleration of reaction. However, considering the fact that NT with high thermal conductivity than NS brings a less significant increase in the heat flow of geopolymer, this factor should be less dominant than others in the initial stage. In terms of the cumulative heat generated, similar values were achieved for Geo-NS (193.56 J) and Geo-NT (193.95 J) samples, all larger than the reference sample (186.64 J). The higher cumulative heat in the nanomodified samples implies the higher reaction degree promoted by both nanoparticles during the first 48 hr. A previous study for nano-Al_2O_3 indicated that it can avoid the induction period in NaOH activated fly ash, generating gel much earlier (Rees et al. 2008). The results here for NS and NT again reveal the potential of nanoparticles for improving the early performance of geopolymer, which is in agreement with macro-mechanical results (Deb, Sarker & Barbhuiya 2015; Duan et al. 2016).

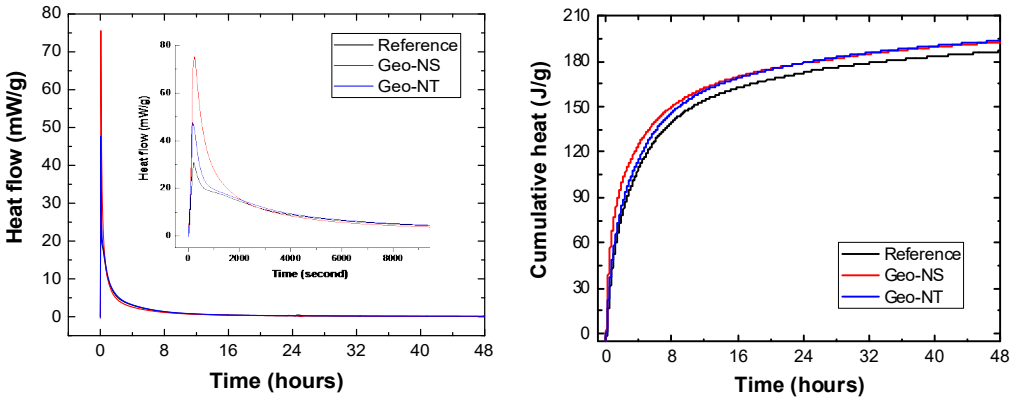

(a) Heat flow over time (b) Cumulative heat over time

Figure 6.3 Heat of reaction during the first 48 hrs

6.3.3 **Micro and nanoscale structure of nanoparticles reinforced geopolymer**

The micro and nanoscale structure of nanoparticles reinforced geopolymers is shown in Figure 6.4. At the magnification of 5000 ×, Figure 6.4 (a) shows that geopolymer is mainly composed of residual fly ash and matrix. Defects such as pores and cracks are found to present in both fly ash and matrix. At the higher magnification of 10000 ×, the local microstructure observation of matrix in Figure 6.4 (b) indicates that in addition to the main reacted product of N-A-S-H gel, sometimes there are also microcrystals. At this magnification, the image starts to show the feature that the matrix generated has a looser microstructure than the raw materials fly ash.

The nanoscale's images can more clearly reveal the difference. In Figure 6.4(c), the N-A-S-H gel in matrix is found to be a loose structure packed by different particles, while the appearance of the fly ash (upper right corner) is still smooth and dense at this magnification. Nanoscale's details of the matrix are displayed in Figure 6.4(d). The particles pile up and entangle with each other. Most of them display in the granular form. Some typical particles displayed are found to have a size of slightly more than 30 nm. As mentioned previously, these particles actually consist of smaller globules as the basic unit. Due to the resolution limitation of SEM techniques, the smaller globules of a size of

around 5 nm (Provis, Lukey & van Deventer 2005) can be just seen faintly in the enlarged picture of 300000 ×.

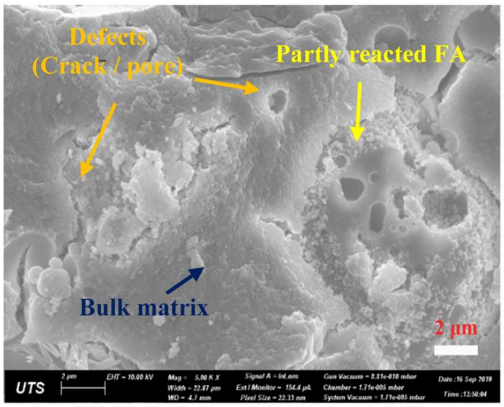

(a) Microscale of geopolymer (5000 ×)

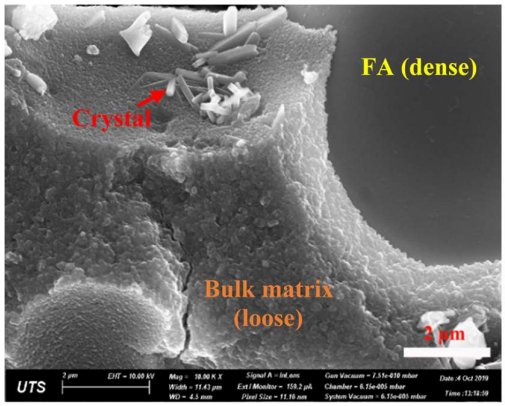

(b) Microscale of geopolymer (10000 ×)

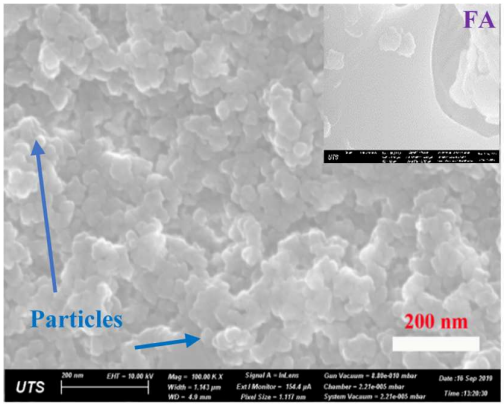

(c) Nanoscale of N-A-S-H gel (100000 ×)

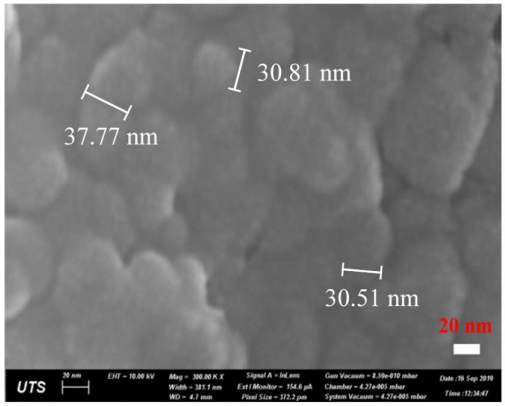

(d) Nanoscale of N-A-S-H gel (300000 ×)

Figure 6.4 Microstructure observation of nanoparticles reinforced geopolymer paste

6.3.4 **Crystals in geopolymer**

The crystals detected by XRD are presented in Figure 6.5. Quartz and Mullite are the main crystals in geopolymer. Compared with the raw material fly ash, it shows that there is no new kind of crystal generated in the activated system, which is in line with some previous studies (Provis, Lukey & van Deventer 2005). The geopolymer aluminosilicate gel has been proposed to be related to the precursor gel for the formation of zeolite (Provis, Lukey & van Deventer 2005). The new zeolite phase Na-F was formed in the nano-Al_2O_3

seeded geopolymer (Rees et al. 2008). However, a previous study for geopolymer incorporated with Zirconia showed that it is not able to act as a nucleation germ for zeolite formation (Phair, Van Deventer & Smith 2000). The XRD analysis in this research reveals that the NS and NT also fail to promote the evolution of the zeolite phase.

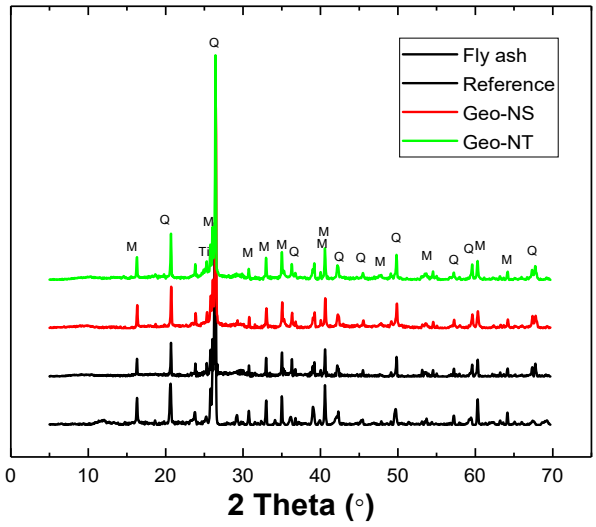

Figure 6.5 XRD results of nanoparticles reinforced geopolymer paste

6.3.5 **Micromechanical properties and proportion of nanoparticles reinforced N-A-S-H gel**

6.3.5.1 Micromechanical properties of nanoparticles reinforced N-A-S-H gel

The deconvolution process is briefly illustrated based on the case of Geo-NT. As shown in Table 6.2 and Figure 6.6, for the model of Geo-NT with 3 phases, it is the sand brown phase that has the minimum micromechanical properties, with the modulus of 19.25 GPa, hardness of 1.15 GPa and covariance matrix of (C_{11}=31.31, C_{12}=C_{21}=1.53, C_{22}=0.14), respectively. When increasing the number of phases to 4 and 5, there is no significant change for the sand brown phase. For this phase, it has high micromechanical properties and especially large variance, which does not conform to the characteristics of the gel phase in the literature (Davydov, Jirasek & Kopecký 2011; Hu & Li 2015b), and in

chapters 4 and 5. The N-A-S-H gel phase with small micromechanical properties (M=15.44 GPa, H=0.90 GPa) and small covariance matrix (C_{11}=11.43 C_{12}=C_{21}=0.49 C_{22}=0.06) appears when the number of phases was set as 6, which changes just slightly with the increase in the number of phases. The decomposition of the above sand brown phase to the new smaller sand brown phase (N-A-S-H) can be observed clearly in Figures. 6.6 (b) to (c) and (e) to (f). The micromechanical properties of N-A-S-H are determined by the average value of the N-A-S-H phase in the first three models as shown in Table 6.2. The elastic modulus, hardness and proportion of N-A-S-H gel in Geo-NT are 15.17 GPa, 0.89 GPa and 22.74%, respectively.

Table 6.2 Micromechanical properties of Geo-NT

k	M [GPa]	H [GPa]	f	BIC	C		
					$C11$	$C12$=$C21$	$C22$
3	19.25	1.15	47.42%	9151.100	31.31	1.53	0.14
4	19.30	1.15	47.76%	9094.102	31.77	1.54	0.14
5	18.73	1.13	44.78%	9055.36	27.58	1.37	0.13
6	15.44	0.90	24.67%	9029.64	11.43	0.49	0.06
7	14.68	0.86	18.93%	9026.98	9.33	0.41	0.05
8	15.39	0.90	24.63%	9019.36	11.20	0.48	0.06
Average 6-8	15.17	0.89	22.74%	-	10.65	0.46	0.06

Note: Geo-NT is 2% NT modified geopolymer with 65 °C heat curing of 48 hr. k is the number of phases. "M" and "H" refer to mean value of elastic modulus and hardness, respectively. f is the proportion of the phase. $C11$ is the variance of elastic modulus, $C22$ is the variance of hardness and $C12$ is the covariance of modulus and hardness.

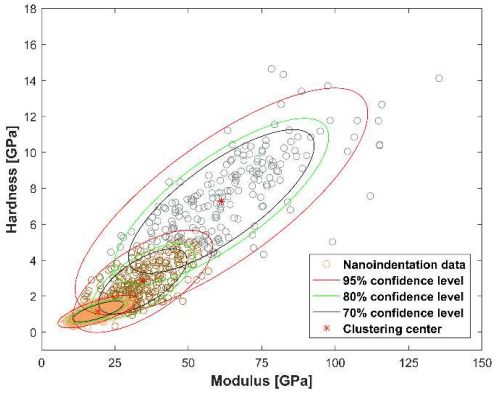

(a) k=3

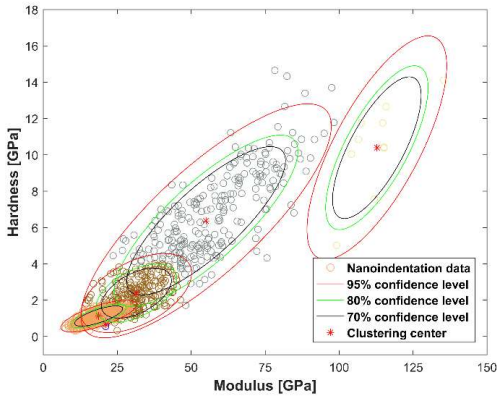

(b) k=5 (blue dots also represent a phase)

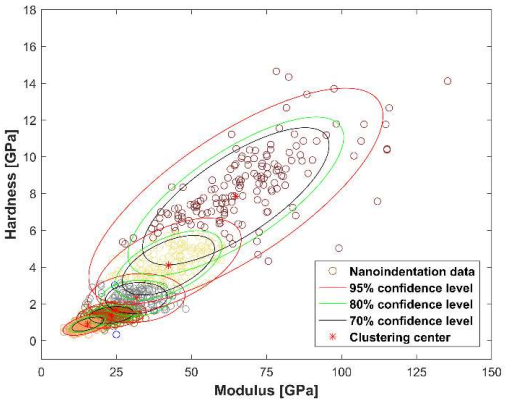

(c) k=6 (blue dots also represent a phase)

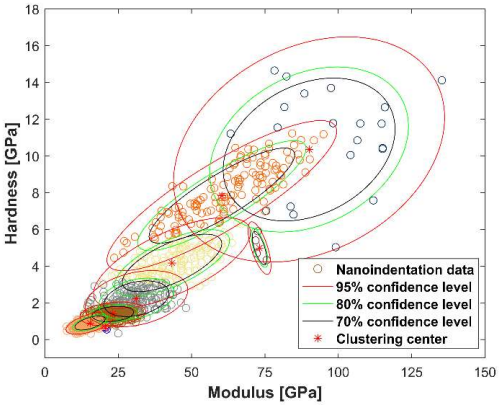

(d) k=8 (blue dots also represent a phase)

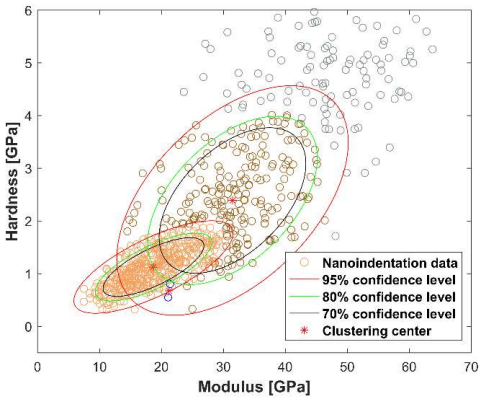

(e) k=5_local detail

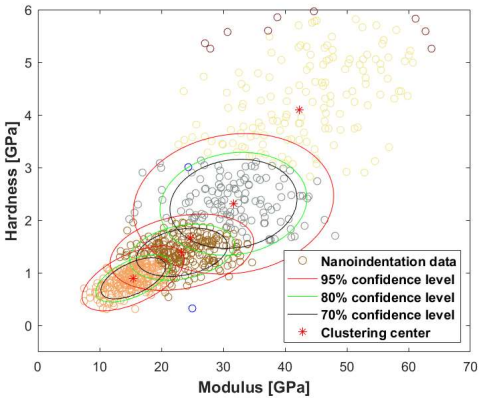

(f) k=6_local detail

Figure 6.6 Statistical nanoindentation results for Geo-NT

For reference and Geo-NS sample, the N-A-S-H gel appears in model with 4 components, and behaviours as a stable phase with the increase in the number of components. The model and SNT results for Geo-NS and reference with 4 and 6 components are shown in Figure 6.7 as well as Tables 6.3 and 6.4, respectively. The average elastic modulus, hardness and proportion of N-A-S-H gel in Geo-NS are 13.30 GPa, 0.75 GPa and 23.78%, respectively. The corresponding values in the reference sample are 11.03 GPa, 0.64 GPa and 12.16%, respectively.

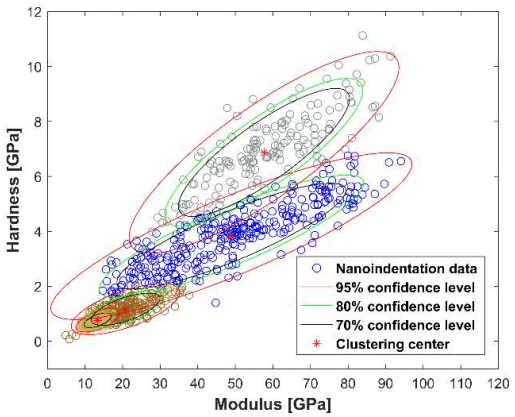

(a) Geo-NS, k=4

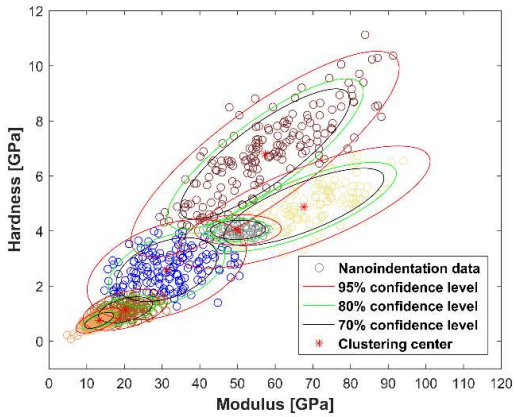

(b) Geo-NS, k=6

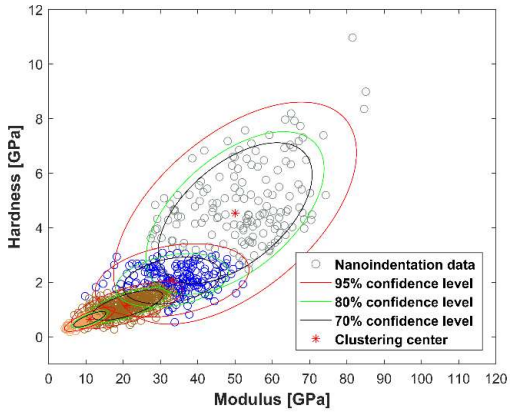

(c) Reference, k=4

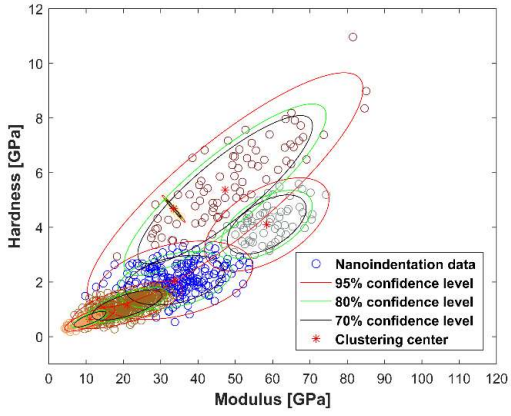

(d) Reference, k=6

Figure 6.7 Statistical nanoindentation results for Geo-NS and reference sample

Table 6.3 Micromechanical properties of Geo-NS

k	M [GPa]	H [GPa]	f	BIC	C		
					$C11$	$C12=C21$	$C22$
4	13.38	0.76	22.80%	9051.71	5.47	0.25	0.03
5	13.27	0.75	24.36%	9020.92	6.27	0.31	0.04
6	13.26	0.75	24.19%	9001.09	6.23	0.3	0.04
Average	13.30	0.75	23.78%	-	5.99	0.29	0.04

Table 6.4 Micromechanical properties of the reference sample

k	M [GPa]	H [GPa]	f	BIC	C		
					$C11$	$C12=C21$	$C22$
4	11.04	0.64	12.20%	8341.59	7.78	0.40	0.03
5	11.02	0.64	12.15%	8297.51	7.74	0.40	0.03
6	11.02	0.64	12.13%	8278.39	7.74	0.40	0.03
Average	11.03	0.64	12.16%	-	7.75	0.40	0.03

6.3.5.2 Repeatability and validity of gel proportion and micromechanical properties

According to the above results, it is clear that the nanoparticles would increase the micromechanical properties of the gel, and the Geo-NT achieves the highest value. Besides, the proportion of gel for the reference sample is just about 50% of the Geo-NT and Geo-NS samples. Before using the above results to analyze the micro mechanism of the macro properties, verification was conducted to understand the repeatability and validity of the results.

Since the reference sample has the lowest gel proportion, SNT test was conducted on the sample again to investigate if the results were affected by limited test points and also the repeatability of SNT results. For the above results of reference, Geo-NT and Geo-NS, they were based on the random principle of the SNT, namely, each grid was selected

randomly. Since the research focusing on the gel phase only, grids nanoindentation were performed on gel rich areas to provide richer test data and more accurate test results for gel. In the repeated test procedure, six locations (150 points each) were selected randomly under a microscope and then grids were intentionally set on the gel rich area within the field of vision. The result is provided in Figure 6.8 and Table 6.5. Regarding the verification of proportion, BSE images were taken. These images were segmented into three phases of pores/cracks, gel and unreacted fly ash as shown in Figure 6.9. The proportion of gel determined by BSE and nanoindentation are summarized in Table 6.6.

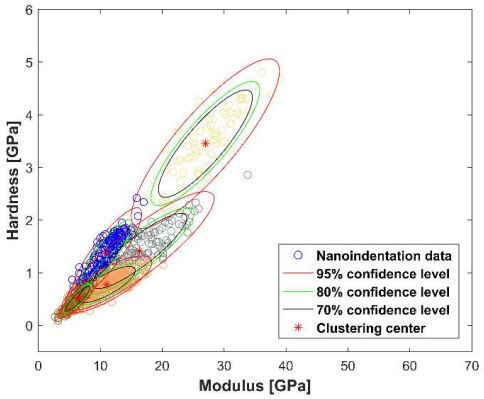

(d) k=5

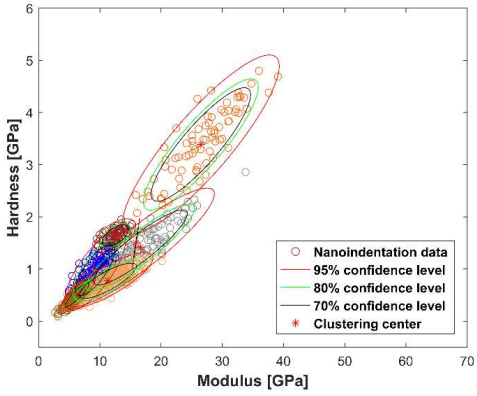

(d) k=7

Figure 6.8 Statistical nanoindentation results for Reference-repeated

Table 6.5 Micromechanical properties of reference sample-repeated

k	M [GPa]	H [GPa]	f	BIC	C		
					$C11$	$C12$=$C21$	$C22$
5	11.07	0.78	33.42%	4991.91	8.88	0.52	0.05
6	11.30	0.77	29.89%	4972.91	9.03	0.54	0.05
7	11.32	0.77	29.71%	4960.76	9.10	0.54	0.05
Average	11.23	0.77	31.01%	-	9.00	0.53	0.05

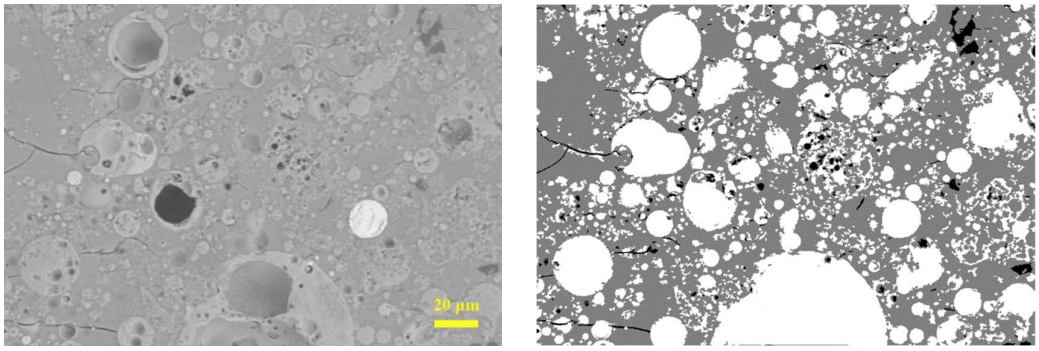

(a) BSE image (500 ×) (b) Segmented image

Figure 6.9 Segment of phases based on the grey value of BSE image (Pores caused by fly ash falling off during polishing are counted as fly ash or pores to ensure the accuracy of gel content)

Table 6.6 Summary of results from SNT and BSE

Samples	Modulus (GPa)	Hardness (GPa)	Proportion from SNT	Proportion from BSE
Geo-NT	15.17	0.89	22.74%	54.02%
Geo-NS	13.30	0.75	23.78%	55.69%
Reference	11.03 (11.23)	0.64 (0.77)	12.16% (31.01%)	49.16%

Note: Samples were heat cured at 65 °C for 48 hr. The results in brackets are from the repeated test on the reference sample where some grids are intentionally set on gel rich area.

As shown in Table 6.6, the SNT results based on 12.16% gel and 31.01% gel data set in different tests are quite similar to each other. It means that the accuracy of the test method would not be a significant obstacle for the comparison of micromechanical properties. However, the gel proportion obtained by statistical nanoindentation is obviously different from that obtained by the generally used BSE technique. In this study, epoxy resin was not used to impregnate the surface to avoid its effect on micromechanical testing. Thus, crystals are basically dropped, making the gel proportion obtained by BSE greater than the true value. However, since crystals in matrix may be mainly from raw material fly

ash, the interference would not impact the relative trend of gel proportion significantly. BSE would still be a more accurate method than SNT on phase proportion evaluation as analyzed in the next subsection. Based on the result of BSE, and considering that nanoparticles are added in the way of replacing FA, the difference of gel content in samples should be small.

6.3.6 **Microscale mechanism of macro performance**

As opposed to the phenomenon at the macro scale where Geo-NS displays better performance than others, it is the gel in Geo-NT that has the highest modulus and hardness. Besides, for random nanoindentation results, the reference sample presents only 12.16% of gel while Geo-NT and Geo-NS have 22.74% and 23.78% gel, respectively. If based on the SNT results solely, it is easy to consider that the nanoparticles have increased the content of the gel/reaction degree and then better macro performance. In fact, the number of nanoindentation test points is very few when compared with pixels in BSE images, which is hard to accurately reflect the overall information of the highly heterogeneous geopolymer. Besides, the interaction of gel with other phases in the involved volume would also decrease the proportion of gel detected by deconvolution analysis. Therefore, the proportion obtained from SNT should be less reliable than that from BSE. Another evidence is from the TGA result as shown in Figure 6.10. The remaining weights for reference, Geo-NS and Geo-NT are 88.55%, 88.98% and 88.82%, respectively. The weight loss between 25 to 300 °C is the free water and loosely bound water, while the weight loss in the later period is caused by the loss of structure water and carbonaceous substances (Zhang et al. 2014). When the influence of free water is eliminated, the TGA results are almost the same for all the specimens, indicating that there would be no significant difference between the content of the gel phase.

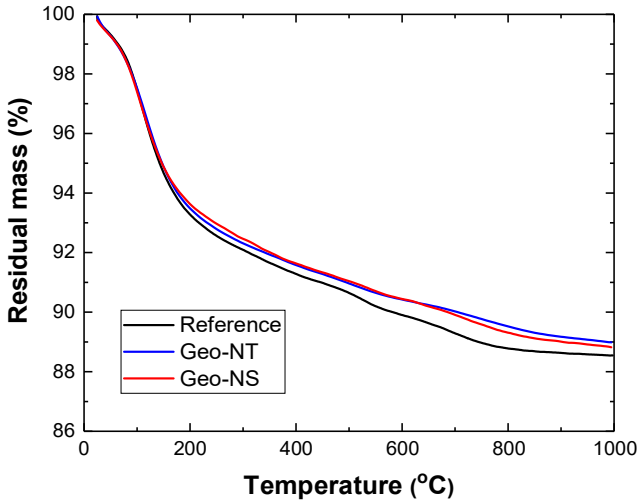

Figure 6.10 Thermogravimetric analysis of geopolymer paste

As analyzed through the heat of reaction, the nanoparticles have an accelerating effect in the early stage. It would lead to a higher amount of gel in nano-geopolymers, which plays a significant role in the early performance of geopolymer. In fact, both NT and NS particles in this study could be treated as unreactive particles due to the limited solubility of NS in the sodium silicate solution. These particles promote the growth of gel in a more physical way, just as the interparticle distance is demonstrated as the most important parameter for the mineral additions to accelerate the clinker hydration (Berodier & Scrivener 2014). Therefore, the relative difference of gel content (not the absolute difference) between geopolymer and nanomodified geopolymer would narrow over time. For the later stage, instead of the gel proportion, the differences in macro-mechanical properties between samples would be more related to the strength of the gel, as well as the coordination (e.g. bonding) between gel and other phases.

For nano-geopolymer, the nanoparticles could act as filler which contributes to the formation of a denser gel structure and then improved macro behaviour. However, the NS would be more compatible with both sodium silicate solution and N-A-S-H gel particles since they have similar chemical composition. The NS may achieve better dispersion and

also integrate with the gel particles better, resulting in more prominent macro mechanical properties. For micromechanical properties, the denser gel structure would also result in higher modulus and hardness. However, there is another factor that would influence the micromechanical results significantly.

In the nanoindentation test, the involved depth is usually considered as 3 to 4 times of the indentation depth (Chen et al. 2010a), reaching around 1 micron on N-A-S-H gel. When the nanoparticles are well dispersed (single particle, very small aggregations), they have a similar size to the gel particles shown in Figure 6.4(d), and works together with the gel particles as a composite. Owing to the large involved range, the well-dispersed nanoparticles are able to be detected by the nanoindentation test. The micromechanical properties of N-A-S-H in nano-geopolymers come from the interaction of gel particles and nanoparticles. Single nanosilica is reported to have elastic modulus and hardness of 68.9±9.6 GPa and 2.8 ±0.4 GPa, respectively in nanoindentation test (Zou & Yang 2006). For nano-titania (anatase), the modulus and hardness are as high as around 170 GPa and 8 GPa, respectively (Gheewala, Smith & Kenny 2008; Zywitzki et al. 2004). N-A-S-H gel is actually similar to the counterpart LD C-S-H gel. Both are reported to consist of globules of about 5 nm (Jennings et al. 2007; Provis, Lukey & van Deventer 2005). The nanoindentation results for them are also quite close. The globules of C-S-H are reported to have an elastic modulus of 59.7±1.9 GPa (Constantinides & Ulm 2007). Therefore, the N-A-S-H gel particles with a size larger than 30 nm would have a smaller elastic modulus because of the existence of nano pores between the packed globules. The higher mechanical properties of NS and especially NT particles than gel particles contribute to the high micromechanical properties of nano-reinforced gel detected. Meanwhile, due to the small size and small proportion of the nanoparticles in each test point, the SNT results of the nano-reinforced gel would be improved but within a small range. For some of the

nanoparticles that happen to present densely in the nanoindentation test points (poor dispersion), these test points with significantly high mechanical properties would not be identified and clustered to the gel phase in the deconvolution process. The above reasons lead to the results in Table 6.6 for the gel particles-nanoparticles composites where Geo-NT and reference sample achieve the highest and the lowest value, respectively. Thus, the properties of the particles themselves cause the different reinforcement effect of NS and NT on macro compressive strength and micro modulus and hardness.

6.4 Conclusions

The effect of the nanosilica (NS) and nano titanium dioxide (NT) particles on the microscale properties of geopolymer, especially the most important component N-A-S-H gel, was investigated to promote the understanding of the reinforcement mechanism of different nanoparticles. Conclusions can be drawn up as follows:

(1) The addition of 2% nano-SiO_2 and nano-TiO_2 particles helps the geopolymers gain 17.38% and 10.49% in strength at 28 days but leads to a slight decrease in workability.

(2) The content of the N-A-S-H gels obtained by SNT vary significantly for samples and are less than around 50% of the BSE results. SNT results due to the limited test points on the highly heterogeneous geopolymer are considered less reliable than the results from BSE. Besides, the multiple phase interaction would be responsible for the significantly lower amount of gel detected by SNT.

(3) The presence of both nano-SiO_2 and nano-TiO_2 particles increase the early reaction rate in geopolymer, while the reaction degree of different samples in the later age is not vastly different. The contents of gel in 28 days geopolymer and nano-geopolymers vary in a small range of 49.16% to 54.02%.

(4) Gel particles packed by around 5 nm globules are typically observed to have a size

of more than 30 nm, similar to the size of well-dispersed nanoparticles. Nanoparticles integrate with gel particles to form a composite with higher mechanical properties. The elastic modulus of N-A-S-H gel is 11.03 GPa, 13.30 GPa and 15.17 GPa, respectively, for reference, Geo-NS and Geo-NT sample.

(5) Nanoparticles have higher mechanical properties (highest for NT) but a much lower proportion than the gel particles, leading to slightly higher micromechanical properties of gel in nano-geopolymers obtained by SNT. Nano-SiO_2 is more compatible with sodium silicate solution and gel particles, resulting in better dispersion and bonding, then a higher macro strength of Geo-NS than Geo-NT.

CHAPTER 7. COMPARISON OF ITZS IN GEOPOLYMER AND PORTLAND CEMENT CONCRETES BASED ON MODELLED ITZS

7.1 Introduction

In addition to matrix, the ITZ between matrix and aggregate is also a critical part of concrete. The ITZ in Portland cement (PC) concrete is well known as the weakest link that predominantly responsible for the initial development of microcracks under loading. In addition to mechanical properties, the ITZ also has an important impact on transport properties and durability. It is therefore considered to be the key to develop concrete with high performance (Scrivener, Crumbie & Laugesen 2004). The knowledge of ITZ in PC concrete cannot be applied directly to geopolymer concrete. It is necessary to conduct microstructural observations and quantitative investigations such as nanomechanical testing for a better understanding of ITZ in geopolymer. The research would be more meaningful if it is based on a comparison with PC concrete. The features and differences of this crucial region of these two materials would be clearly presented, while the mechanism analysis could be a source of inspiration for properties improvement of the weaker ITZ. The current grid nanoindentation and comparative study of ITZs are almost all based on real concrete. As stated in Chapter 2, the local ITZ properties randomly chose for investigation would be highly variable. In this study, two types of modelled ITZs were prepared to decrease the high heterogeneity that interferes with the comparative study of ITZs. The modelled ITZs have important significance for precise nanomechanical testing of ITZ as well.

7.2 Experimental and analysis methods

7.2.1 Significance of modelled ITZ

The modelled interface approach is revealed in Figure 7.1. Any modelled experiment with simplified conditions would sacrifice some real factors and may not be as precise as tests under the real condition. For instance, the bonding strength would decrease for a smooth surface. However, there are at least the following reasons for conducting the simplified modelled experiment. Due to the irregular shape of aggregates, as shown in Figure 7.2(a), the statistical results of each column of the grid would not be related to the pure properties of ITZ, incorporating results from both aggregate and paste. Even if the test results in a column that belongs to the aggregate are eliminated, the substantial reduction of the number of test points in some columns would affect the statistical results. More importantly, the indent points in each column for statistical analysis actually have different distances from the boundary of the aggregate, which thus brings test errors to reveal the real variation of ITZs with the increased distance from the aggregate surfaces. In the penetration direction as shown in Figure 7.2(b), the irregular shape of aggregates is also a factor that possibly affects the test result. Therefore, there are challenges to effectively investigate the properties of real ITZs through the grid nanoindentation analysis.

In addition, as clarified in subsection 2.2.2, ITZ is highly heterogeneous in concrete. The properties of ITZ would vary with many factors such as the location of ITZ chosen from an aggregate particle, the size of the aggregate and local mixture condition. The random selection of several test objects for comparison would make the results unreliable. Besides, it is almost impossible to do so many tests that can obtain a reliable result to represent the overall ITZ properties of real concrete for comparative study.

Until now, the high workload statistical comparison between ITZ in real concretes is hard to find. In this study, two types of modelled samples were considered to provide some insights for the basic understanding and comparison of ITZ in geopolymer and PC concrete. The modelled sample I is shown in Figure 7.1(a). An aggregate with a polished surface was embedded in the mortar. Figure 7.1(b) displays the cross section of the specimen. The magnified details of the interface are shown in Figure 7.2(c). Obviously, the modelled interface allows for avoiding the issues showed in Figures. 7.2(a) and (b) for the grid nanoindentation test relating to uneven interface. In addition, the interference resulting from factors such as different types, shapes, size, relative positions and relative mix condition of aggregates, as well as different locations in ITZ from an aggregate can be avoided, enabling more accurate comparison of ITZ with an acceptable statistical workload. The modelled interface is also convenient for tests like energy dispersive X-ray spectroscopy (EDS) mapping of the pure ITZ. Modelled sample II is given in Figure 7.1(c), which can be traced back to some early studies, such as the XRD study of ITZ (Detwiler et al. 1988; Scrivener, Crumbie & Laugesen 2004). Compared with the cross section ITZ in Figures. 7.2(a) and (c), Modelled sample II can void the damage on phases from cutting process. Besides, it can reveal more abundant information than when considering only one cross-section. The origin of ITZ is mainly ascribed to the “wall effect” (Scrivener, Crumbie & Laugesen 2004). Considering this mechanism, the modelled interface would not have a significant difference to the real, well-formed ITZ, but is just not able to reflect the heterogeneity and complexity in the real concrete.

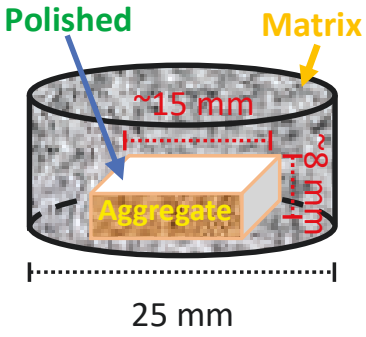

(a) Modelled sample I

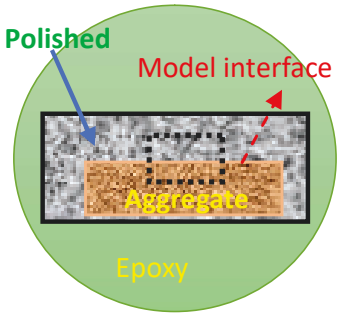

(b) Surface for testing

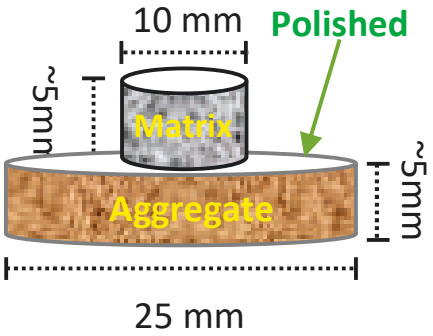

(c) Modelled sample II

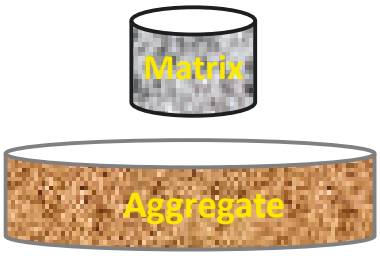

(d) Separated surface

Figure 7.1 Schematic diagram of the modelled interfaces

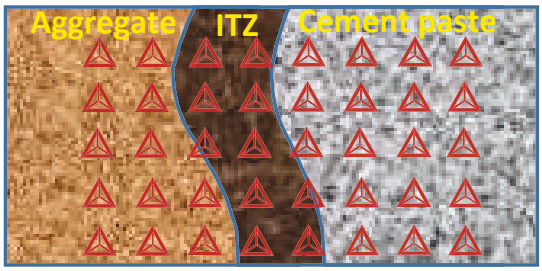

(a) The real interface in concrete

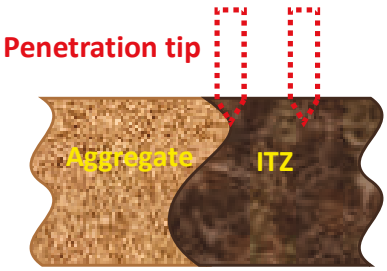

(b) Penetration in ITZ

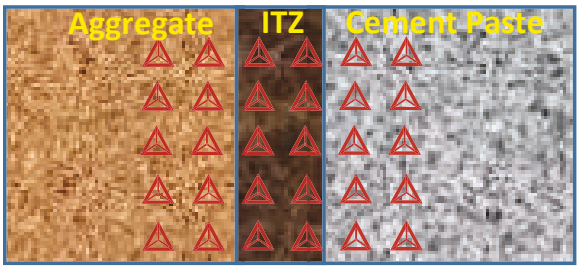

(c) Test on the modelled interface

Figure 7.2 Nanomechanical tests on different types of ITZs

7.2.2 **Sample preparation**

The raw materials such as fly ash and General Purpose Portland cement are still the same as introduced in Chapter 3. One side of the ϕ 25 mm aggregate slices was manually ground by using 320, 600 and 1200 grits of abrasive paper and polished by using 1 μm alumina for 20 min to achieve a smooth surface.

For geopolymer and PC, a representative comparison is difficult to conduct since the raw materials and mix design parameters are very different. When one mix design parameter or property of PC and geopolymer is controlled to be the same, others are still variable and may lead to different comparison results. Therefore, comparative studies can only reveal the differences under specific conditions to enrich the understanding of the two binders. In this study, instead of mix ratio parameters as in existing studies (Khedmati, Kim & Turner 2019; Khedmati et al. 2018), the companion is based on the equivalent flowability. The similar flowability is assumed to create interfaces with similar mix and cast condition and then allows to experimental investigation to reveal the interface properties differences caused by the different nature of cementitious materials. Both paste and mortar have been tried for investigation. Paste is ideal for minimizing interference but found to cause significant microcracking in ITZ due to shrinkage. As a result, mortars by weight the sand to fly ash/Portland cement ratio of two were prepared to make modelled sample I for BSE, EDS and nanoindentation test. The w/c of PC was 0.42. The according solution/fly ash, Na_2O/fly ash, and silica modulus were 0.53, 0.08 and 1.00 for geopolymer, respectively. A similar flow table test value of 168 mm was achieved by PC and geopolymer mortars according to ASTM C1437 (Standard Test Method for Flow of Hydraulic Cement Mortar). For modelled sample II, mortar presented the same phenomena and conclusions in separation test as paste. However, the very strong bond of geopolymer mortar to aggregate produces abundant residual paste and no aggregate

surface for ITZ observation. Thus, paste samples with the same mix ratio as corresponding mortar samples were used to cast modelled sample II for the SEM observation ITZ of PC and geopolymer.

For the first type of modelled sample, the sides of the circle slice aggregate (Φ25) were ground to a rectangle shape of around 15 × 10 mm. A Φ25 mould was oiled, and then a layer of cling film was sticked to the mould. The rectangle aggregate was then put inside the mould and geopolymer or PC mortar was poured to form the modelled sample I. For the modelled sample II, the 10 mm diameter clear vinyl tubing was cut into short tubes with a height of around 5 mm. One side of the tubes was polished to flat, and pasted to the circle slice aggregates (SSD) using super glue. The mixed geopolymer and PC paste were cast into the tubes as described in Figure 7.1(c). After two minutes of vibration, the geopolymer samples were covered with cling film and cured under a temperature of 65 °C for 24 hrs in an oven. Afterward, there were subjected to standard curing like PC samples until 28 days.

Modelled sample I was cast with an interface condition similar to that in real concrete. Besides, the cling film applied between the modelled concrete and the mould could avoid restrain on matrix deformation caused by bonding, and minimize damage of interface from the demoulding process. After demoulding, samples were put into a Φ35 mould and coated by using epoxy resin to preventing damage during the surface preparation procedures. The sample as shown in Figure 7.1(a) was cut from top to bottom to expose a surface as displayed in Figure 7.1(b). This surface with very neat interface in both the horizontal direction and the penetration direction was polished by using 320, 600 and 1200 grits of abrasive paper and by alumina of 1 μm and 0.3 μm. The well prepared surface was used for the following microstructure and nanomechanical study. The

modelled sample II was manually separated into two parts of matrix and aggregate for interface observation as shown in Figure 7.1(d).

7.2.3 **Structure characterization techniques**

SEM, Zeiss Supra 55VP was used for interfacial microstructure observation at high magnification, where the accelerating voltage was set as 10 kV. The distribution and width of the ITZ were determined by the statistical of forty BSE images at a magnification of 500×. In each image, 17 of 5 μm-width bands were taken successively from the surface of the aggregate to paste. Representative EDS mapping was conducted to reveal the detailed element distribution of ITZ. BSE and EDS analysis were performed using a Zeiss EVO LS15 with an accelerating voltage of 15 kV.

7.2.4 **Grid nanoindentation**

Microindentation test normally requires measuring the residual indent impression, while impression less than 20 μm is susceptible to imprecision according to ASTM E384-17 (Standard Test Method for Microindentation Hardness of Materials). With the advance in testing techniques, depth-sensing nanoindentation with nanoscale indenter has been widely used in material characterization in recent years. The contact area in the test can be obtained by combining the depth detected and the geometry of the indenter, allowing much shallower indentation tests. In this study, the BSE results indicated that the width of ITZ in PC and geopolymer was around 20 and 30 μm, respectively. Thus, nanoindentation has advantages over the microindentation for investigation.

For the previous studies shown in review paper (Luo et al. 2018), the grid nanoindentation investigations of ITZ are almost all at a small force such as 1200 μN and 2000 μN. The average value of each column of the test results was used to reveal the variation of micromechanical properties from ITZ to paste. Small force makes it possible to conduct

dense testing with small spacing to reveal more abundant mechanical information of ITZ. However, very shallower indentation makes the results specific to each single phase. For pores and cracks under small force test, they either do not return a value during the test, or cause significantly abnormal nanoindentation test curves. Those test points are generally omitted. Calcium hydroxide (CH) crystal is detrimental to the performance of ITZ owing to the loose bonding between CH and C-S-H gel, but reported to have higher micromechanical properties than the gel phase (Chen et al. 2010d; Hu & Li 2015a). On the one hand, the loose bonding makes it easy to drop off from the polished surface. The shallow test would detect a lower fraction of crystals than in real situation. On the other hand, the shallow test points on CH phase just capture its high mechanical properties, but not the poor bonding properties. The larger size and amount of pores, cracks, and CH with weak bonding are indicators of the inferior properties of ITZ in PC concrete, but these adverse effects could not be well reflected in small force test. Higher force with large penetration depth that results in the interaction of multiple phases would be more appropriate to reveal the relative properties of ITZ to paste as the phenomenon at the macro scale. However, to ensure the accuracy of the result, the involved range should not exceed the thickness of ITZ. Moreover, the interference from adjacent test points as well as the restraint effect of aggregate should be avoided. The activated depth in nanoindentation test is considered as 3-4 times the indentation depth (Chen et al. 2010d). In ASTM E384-17 (Standard Test Method for Microindentation Hardness of Materials), the minimum recommended spacing for Knoop and Vickers indentations are 2 or 2.5 times of the diagonal. In order to make the involved range more controllable, the nanoindentation test was conducted with constant penetration depth. The above two criteria were referenced to determine the indentation depth.

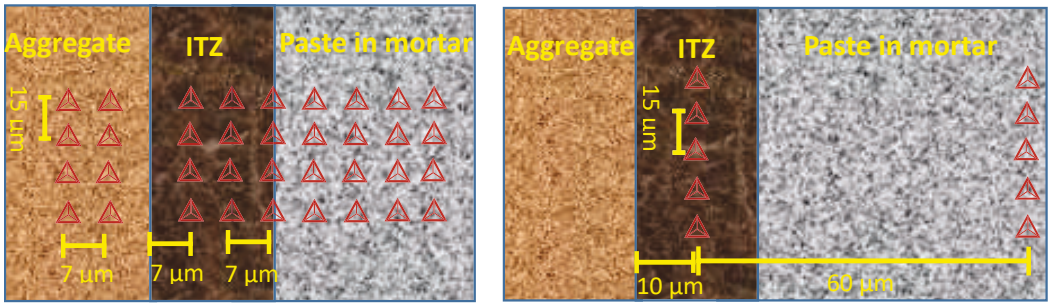

(a) Two columns of test indents on ITZ (b) One column of test indents on ITZ

Figure 7.3 Grid nanoindentation on ITZ region

Two types of large depth tests with different numbers of nanoindentation columns on ITZ were conducted as shown in Figure 7.3. In the first type, two columns of nanoindentation test points were set on the ITZ. Considering a smaller ITZ width of around 20 μm, the horizontal grid spacing and the distance between the surface of aggregate and nearest test points were set as 7 μm. The vertical grid spacing was 15 μm. A total of ten 4 × 9 grids were conducted on both geopolymer and PC to reveal the variation in mechanical properties with increased distance to the surface of aggregate. The corresponding nanoindentation depth was determined as 850 nm. The second type of test was conducted at a larger scale to compare the properties of ITZ with paste. As shown in Figure 7.3(b), just one column of test data was set on ITZ, which allows the test to achieve the maximum feasible interaction range within ITZ. The properties of paste were tested simultaneously by one column of test points at the distance of 70 μm to the surface of aggregate. After several trial tests, the nanoindentation depth of 1200 nm was adopted. Total 25 of these 5 × 2 grids were randomly selected along the modelled interface for investigation. The locations close to sand grains were avoided.

7.3 Results and discussion

7.3.1 Microstructures of separated surfaces

Appearance of the aggregates after being separated from modelled samples II is shown in Figure 7.4. In Figure 7.4(a), a circular area (PC area) was less bright than its surrounding areas, which was identified as the location of PC before separation. The details in Figure 7.4(b) indicate that after separated, no remarkable PC paste is left on aggregate. In contrast, as displayed in Figure 7.4(c), a significant amount of residual geopolymer can be observed on the aggregate surface. Additionally, separation of geopolymer sample was more difficult than for PC sample. Indeed, the PC paste sample was very easily removed while considerable force was still required for geopolymer paste sample. The above phenomena clearly mean that geopolymer bond to the surface of the aggregate is better than that of PC.

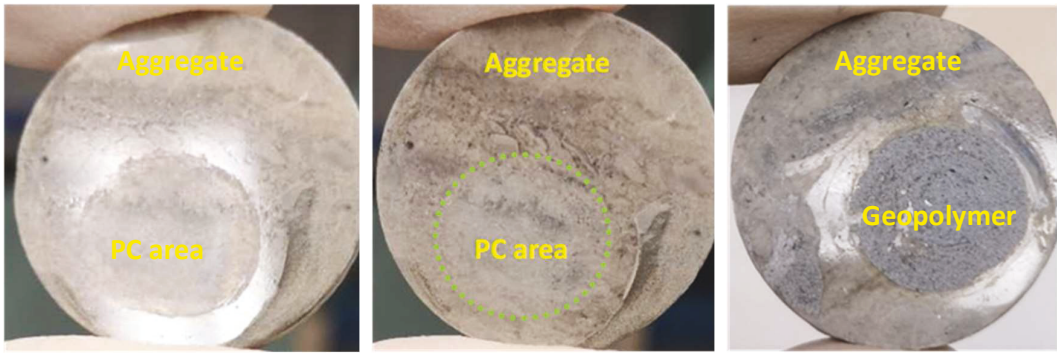

(a) PC (b) PC (C) Geopolymer

Figure 7.4 Surface of aggregates after removing geopolymer or PC matrix

Within the circular area, the interfacial appearance of geopolymer was observed at high magnifications based on attached paste. As shown in Figure 7.5(a), the geopolymer itself is highly heterogeneous, but a layer of paste rich in gel is found to adhere to the surface of aggregate, which should be caused by the wall effect and also slight bleeding. This

layer of paste has a very dense and uniform structure even observed at high magnifications 20000 ×, which implies a well-formed interface.

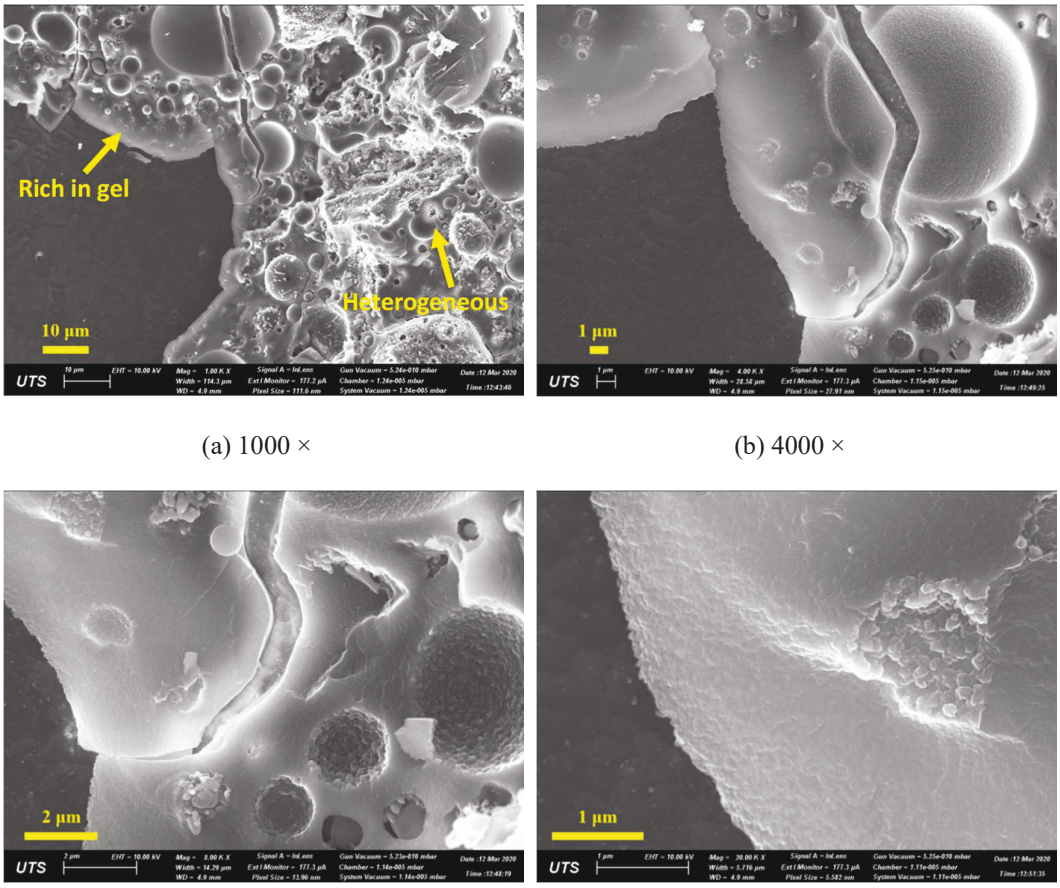

(a) 1000 ×

(b) 4000 ×

(c) 8000 ×

(d) details 20000 ×

Figure 7.5 Residual geopolymer on aggregate

For the PC modelled sample, since there was no significant residual paste attached to aggregate, the surface of the bulk paste after separation could also be within the range of ITZ. Therefore, both the separated aggregate and paste were observed as exhibited in Figures. 7.6 and 7.7. In Figure 7.6(a), the residual PC paste has a small size, thin thickness, and heterogeneous characteristics. At the magnification of 8000 ×, it is clear that abundant crystals can be found on paste very close to the surface of the aggregate. Details can be observed at 20000 ×.

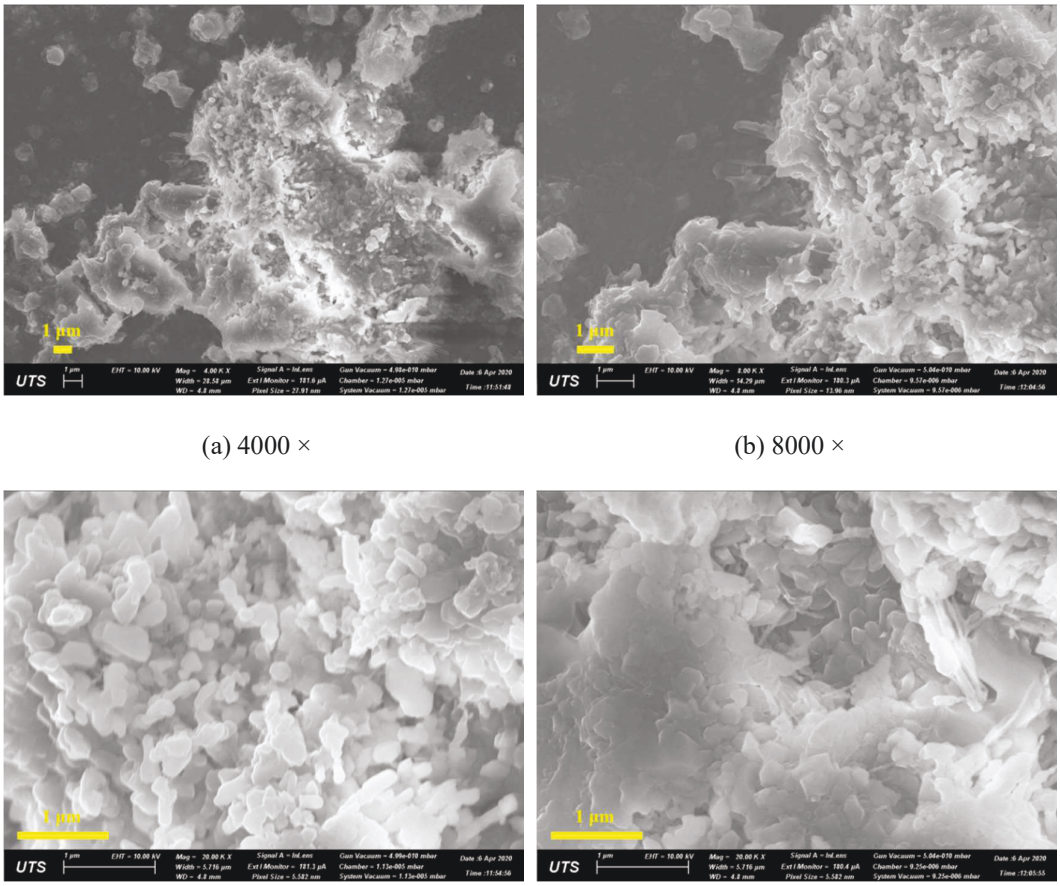

(a) 4000 ×　　(b) 8000 ×

(c) details 20000 ×　　(d) details 20000 ×

Figure 7.6 Residual PC on aggregate

Moreover, some locations of the bulk paste shown in Figure 7.7 are also found to be rich in calcium hydroxide and ettringite crystals. Crystals such as calcium hydroxide and ettringite generated from cement hydration, are able to develop into large size due to the high water to cement ratio (water films) in ITZ (Mehta & Monteiro 2017). High porosity and weak bond between crystals and C-S-H gel induce a loose structure leading to the poor performance of ITZ in the PC sample. For geopolymer, the study by Provis, Lukey & van Deventer (2005) indicated that there are generally no newly formed crystals that can be detected by XRD. This phenomenon can also be found in Figure 5.11 and Figure 6.5. Except for the possible zeolite at the ultra-fine size of several nanometres (Provis,

Lukey & van Deventer 2005), a lot of the crystals existing in geopolymer would be introduced by the raw material fly ash.

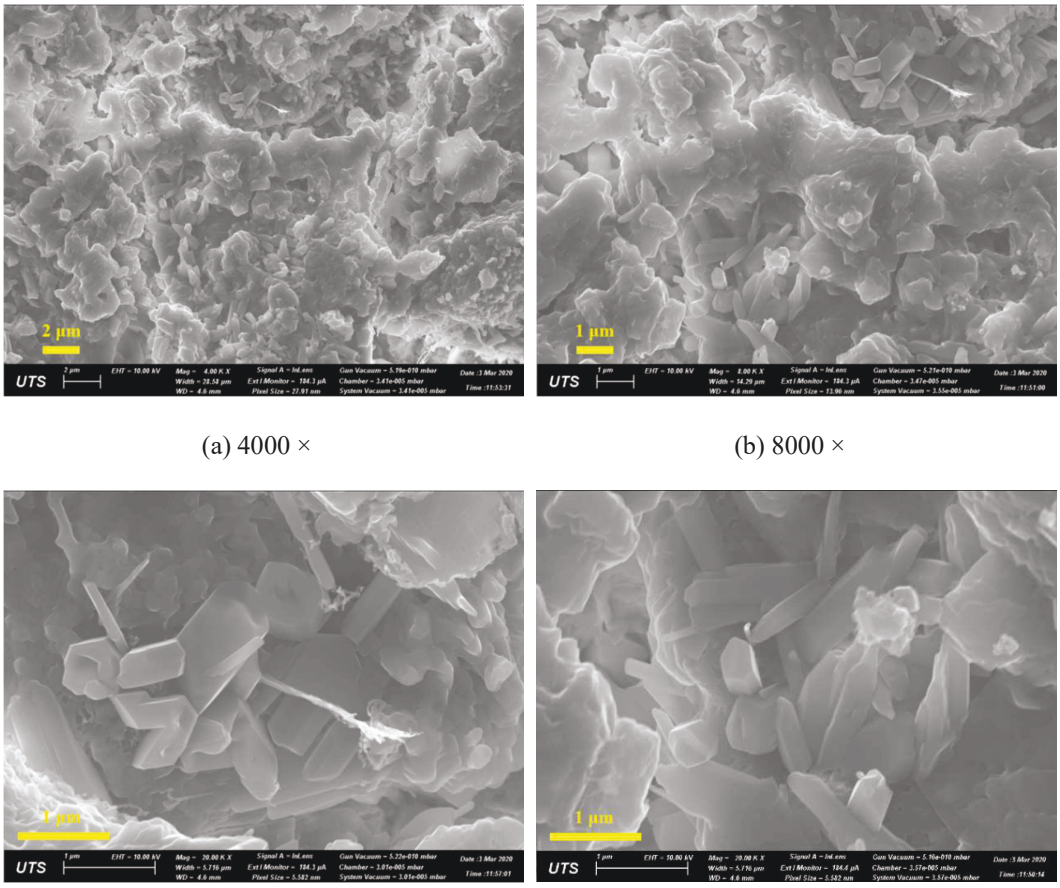

(a) 4000 ×　　(b) 8000 ×

(c) details 20000 ×　　(d) details 20000 ×

Figure 7.7 The surface of bulk PC after removing of aggregate

Due to the wall effect, the content of fly ash and its crystals can be assumed to be low in the vicinity of the aggregate. In addition, although the liquid to fly ash ratio can be expected to be high in the area near to aggregate, transformation of the possible nanoscale zeolite into harmful large scale crystals is not possible. Water content, temperature, and soluble silicate are important factors that govern the formation of large size zeolites (Provis, Lukey & van Deventer 2005). Water just accounts for a small proportion of the solution. The increase in water to fly ash ratio is lower than that of liquid to fly ash ratio in ITZ. Thus, the increase in water content is small and would not be able to overcome

the inhibition of crystallization from the soluble silicate in the sodium silicate solution. The above mechanism indicates that crystals and even porosity would not be the dominant factors affecting ITZ in geopolymer. Besides, the sodium silicate solution has adhesive properties by nature, which could contribute to achieving better bonding in geopolymer than the PC. When reactive aggregate is used, the benefits of alkali solution on ITZ would be further manifested by improved bonding due to chemical reaction (Hajimohammadi et al. 2019; Hajimohammadi, Ngo & Vongsvivut 2019).

7.3.2 Constituents distribution of ITZ

The distribution of constituents at different distances to the surface of the aggregate was investigated by statistical analysis of segmented BSE images. As shown in Figure 7.8, image segmentation was conducted based on the different grey values of the BSE image. Thereafter, the percentage of unreacted FA, reacted products and defects (e.g. pore, cracks) in each strip of geopolymer samples were obtained. Similar operations were also conducted on PC as shown in Figure 7.9. The average distribution of the constituents in PC and geopolymer based on the statistic of BSE images is provided in Figure 7.10. Wall effect can be clearly observed. The content of both FA and clinker is substantially low at the area near to aggregate and then increases to an almost stable value. The zone before the stable stage is around 20 μm and 30 μm in the PC and geopolymer samples, respectively. Those regions were identified as the ITZ. The thickness of ITZ in the modelled PC sample of this study is in agreement with results obtained in real PC concrete (Brough & Atkinson 2000; Scrivener 2004), which validates that this artificial interface is feasible for ITZ research. The average volume of reacted products in ITZ is similar for geopolymer and PC, 66.32% in the first 20 μm of PC and 65.78% in the first 30 μm of geopolymer. Although the ITZ in geopolymer is larger than in PC, the high gel content instead of crystalline phases in the reacted products enables to achieve better performance.

Due to the difference in shrinkage and elastic modulus of aggregate and paste, microcracks are likely to form in ITZ, as observed in both geopolymer and PC samples. However, microcracks in PC are generally larger and more developed than in geopolymer, which is in line with observation at macroscope (Figure 7.4). In addition to different gel shrinkage, higher microcracking in PC could also be partially explained by the crystals rich and large pores in ITZ of PC. Interfacial debonding was observed in real PC samples by Khedmati et al. (Khedmati, Kim & Turner 2019; Khedmati et al. 2018) and Diamond (2001). The width of interfacial debonding was measured as 15 to 50 μm (Khedmati et al. 2018) by laser scanning microscopy, which was larger than the few microns cracks observed in this study.

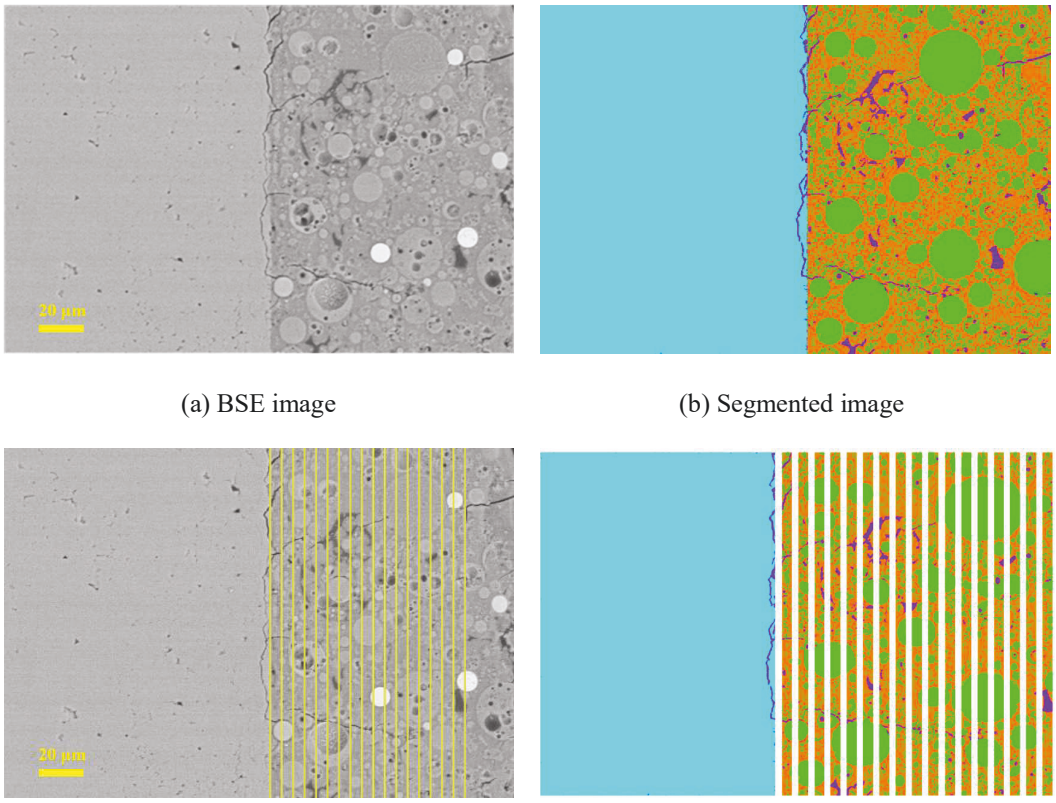

(a) BSE image

(b) Segmented image

(c) Taking strips from ITZ to paste

(d) Statistic of strips

Figure 7.8 Statistical analysis of ITZ in modelled geopolymer concrete

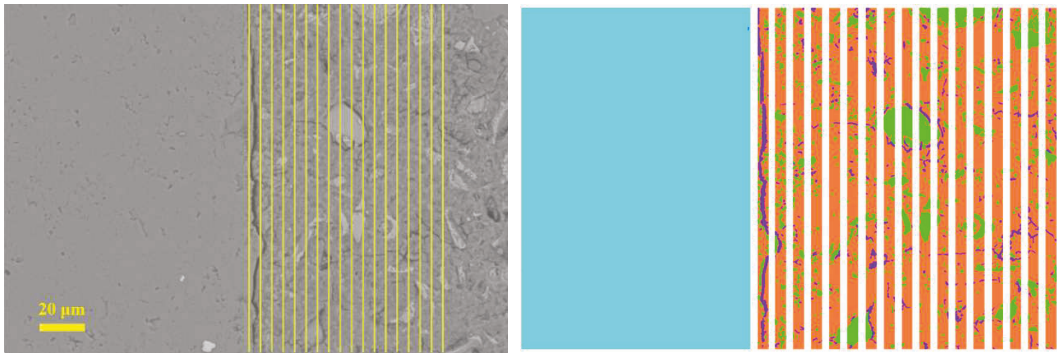

(a) Taking strips from ITZ to paste (b) Statistic of strips

Figure 7.9 Statistical analysis of ITZ in the modelled PC concrete

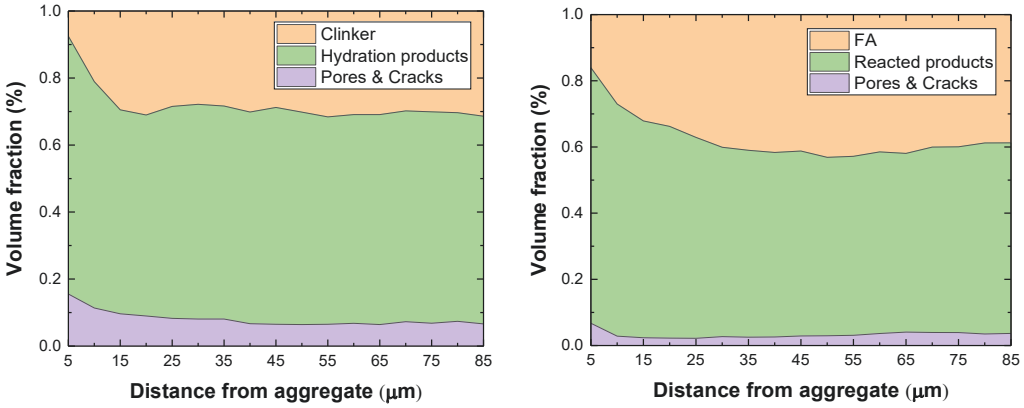

(a) ITZ in PC concrete (b) ITZ in geopolymer concrete

Figure 7.10 Volume fraction of microstructural constituents in ITZs

7.3.3 **Element distribution of ITZ**

EDS mapping and line scans were conducted for interfaces in geopolymer and PC samples to reveal the details of element distribution in ITZ. As shown in Figures. 7.11 and 7.12, the boundary of aggregate and ITZ can be distinctly identified according to the element distributions. Calcium is the dominant element in rock, which is far less in the alkali-activated low calcium fly ash geopolymer. The distribution of Al, Si, and Na can be found in paste, indicating N-A-S-H gel. Besides, different kinds of fly ash which are composed of different elements can be visibly identified. Figures. 7.13 and 7.14 reveal the element distribution of ITZ in the PC sample. This area is found to be rich in Ca and

Si, which are the elements in the main hydration products such as C-S-H gel and CH. Elements of Fe and Al were also identified in some phases.

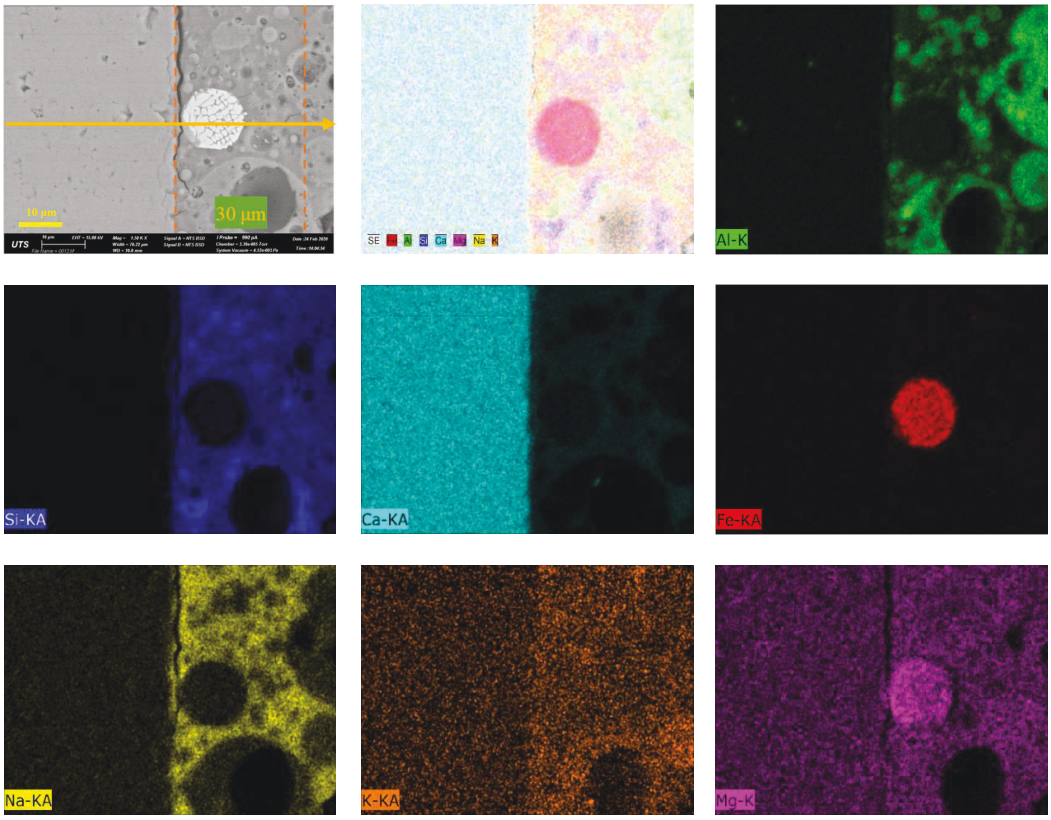

Figure 7.11 EDS element mapping of geopolymer ITZ

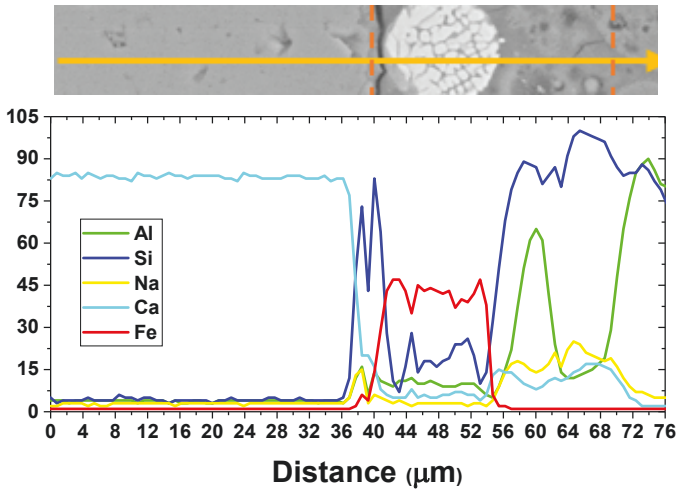

Figure 7.12 EDS section line scanning of the geopolymer ITZ

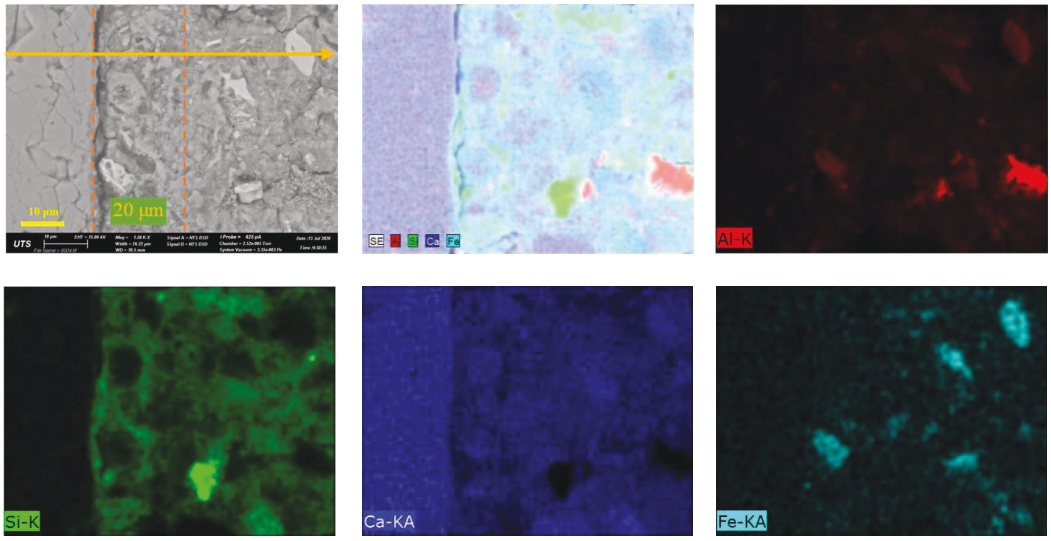

Figure 7.13 EDS mapping of the PC ITZ

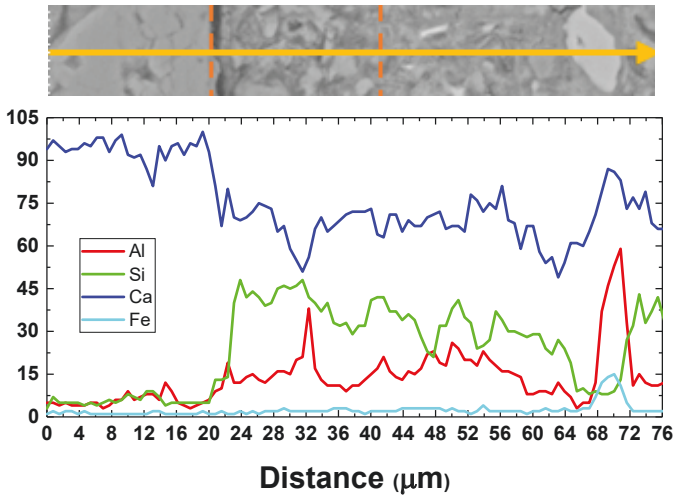

Figure 7.14 EDS section line scan of the PC ITZ

7.3.4 **Nanoindentation on ITZ**

The residual indent impressions after the test are displayed in Figure 7.15. After the test with a penetration depth of 850 nm, four rows of residual indent impressions can be observed on aggregate in Figure 7.15(a). Figure 7.15(b) shows that the residual impressions on paste are smaller than that on aggregate. More clearly residual impressions are shown in Figures. 7.15(c) and (d), which are from a test with the penetration depth of 1200 nm.

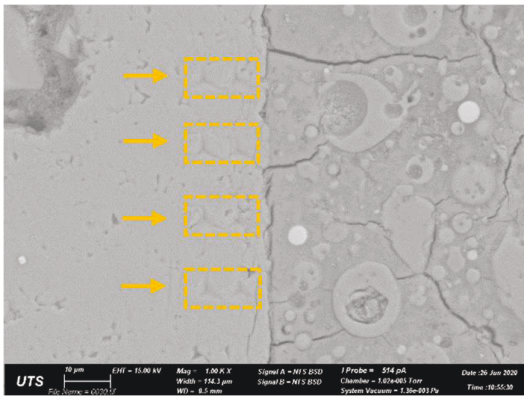

(a) Penetration depth of 850 nm (1000 ×)

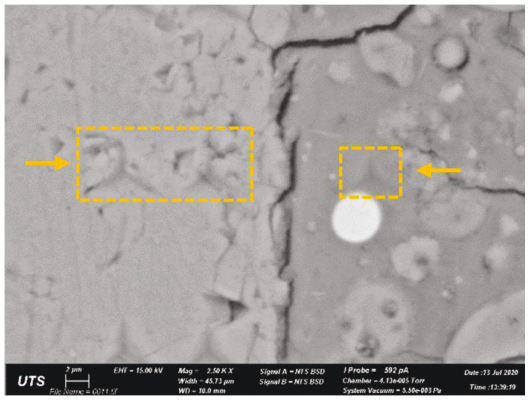

(b) Penetration depth of 850 nm (2500 ×)

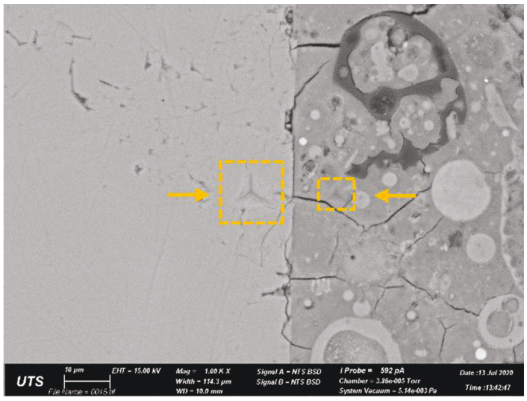

(c) Penetration depth of 1200 nm (1000 ×)

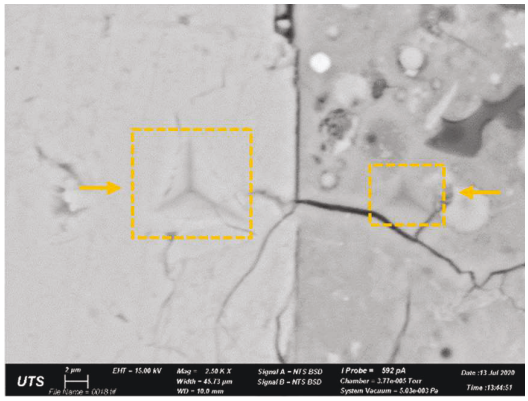

(d) Penetration depth of 1200 nm (2500 ×)

Figure 7.15 Residual indent impression after nanoindentation

The nanoindentation test results for geopolymer and PC are presented in Figures. 7.16 to 7.19 and summarized in Table 7.1. Figures. 7.16 and 7.17 provide the test results for geopolymer and PC under a penetration depth of 850 nm. The ITZ in geopolymer is found to have a very similar micromechanical properties distribution to that of bulk paste. The average elastic modulus values of the nanoindentation test points within ITZ and bulk paste are 25.70 GPa and 26.38 GPa, respectively. The elastic modulus ratio of ITZ to bulk paste is 0.97. The corresponding average hardness values are 1.87 GPa and 1.93 GPa, with a hardness ratio of 0.97. Even in PC concrete, there is still no distinct difference between the distributions of elastic modulus in ITZ and bulk paste. The average elastic modulus for ITZ and bulk paste is 28.34 GPa and 29.37 GPa, respectively. The

identifiable inferior property on ITZ compared to paste is only revealed in the hardness distribution histogram of PC. The average hardness is 0.98 GPa for ITZ, while a larger value of 1.20 is obtained for paste. The average elastic modulus ratio and hardness ratio of ITZ to paste is 0.96 and 0.82, respectively. Thus, except for hardness in PC, the micromechanical properties distribution of both materials does not show significant weakness in ITZ. Geopolymer has a slightly lower elastic modulus but an evidently higher hardness compared to PC. In terms of aggregate, it is noted that the second column of test data on the aggregate in geopolymer has obviously lower mechanical properties than the first column of data. This is not observed in the PC sample. It should be partly attributed to the better bonding of geopolymer with aggregate. Figure 7.4 shows that geopolymer adheres tightly to aggregate. The shrinkage of the geopolymer is restrained by this strong bond, which sometimes leads to cracking of this brittle aggregate as typically shown in Figure 7.8.

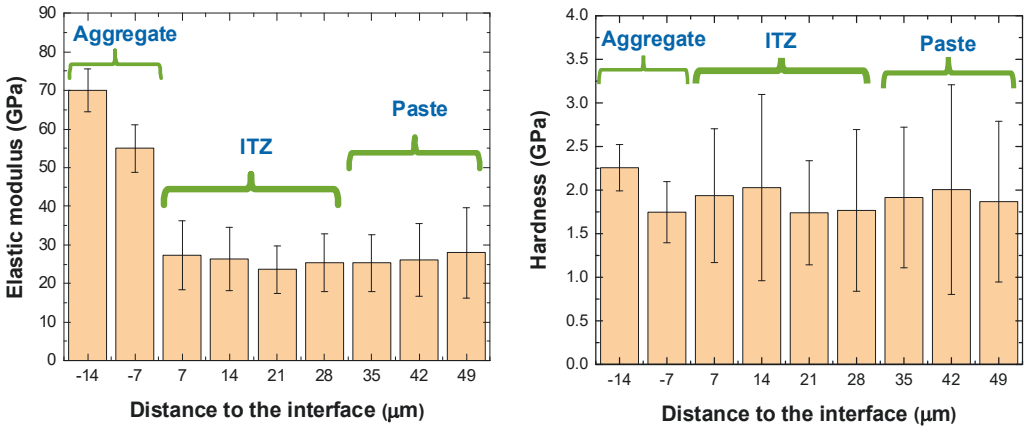

(a) Elastic modulus (b) Hardness

Figure 7.16 Micromechanical properties of geopolymer matrix from aggregate to paste (850 nm)

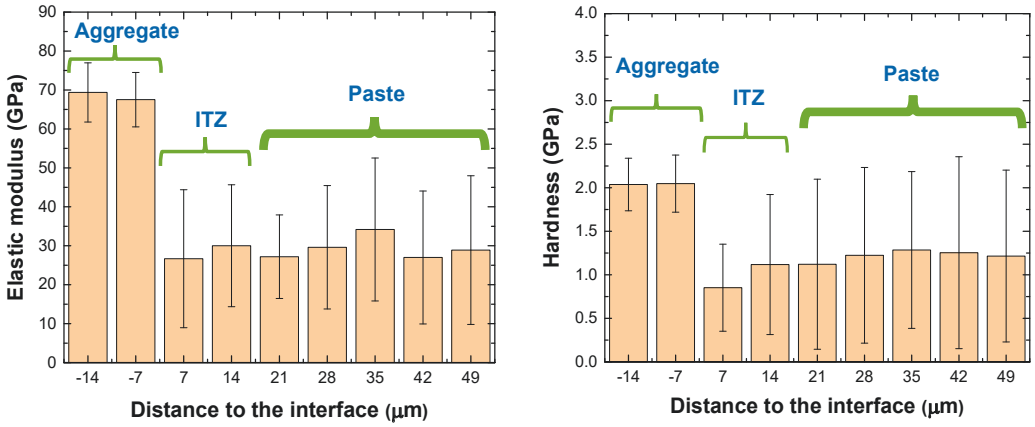

(a) Elastic modulus (b) Hardness

Figure 7.17 Micromechanical properties of PC matrix from aggregate to paste (850 nm)

Table 7.1 Results for geopolymer and PC from penetration depth of 850 nm and 1200 nm

Objects	Test depth	M [GPa]	H [GPa]	σ_M	σ_H	M_{ITZ}/M_{Paste}	H_{ITZ}/H_{Paste}
Geo-ITZ	850 nm	25.70	1.87	7.84	0.86	0.97	0.97
Geo-Paste	850 nm	26.38	1.93	9.58	0.99		
PC-ITZ	850 nm	28.34	0.98	16.69	0.65	0.96	0.82
PC-Paste	850 nm	29.37	1.20	16.22	1.01		
Geo-ITZ	1200 nm	23.08	1.61	6.22	0.60	1.21	1.18
Geo-Paste	1200 nm	19.15	1.36	7.02	0.74		
PC-ITZ	1200 nm	23.46	0.69	13.11	0.50	1.07	0.91
PC-Paste	1200 nm	21.96	0.76	11.62	0.71		

Note: M is the average elastic modulus and H is the average hardness. σ_M and σ_H are the standard deviation of elastic modulus and hardness, respectively. For the test with the penetration depth of 850 nm, the test data belong to ITZ or paste are determined as shown in Figures. 16 and 17. Then, M, H, σ_M and σ_H of ITZ or paste are obtained based on all of the test data within them. M_{ITZ}/M_{Paste} is the ratio of the average elastic modulus of ITZ to that of paste. H_{ITZ}/H_{Paste} is the corresponding ratio for hardness.

The results for geopolymer and PC under a larger penetration depth of 1200 nm are provided in Figures. 7.18 and 7.19. For this test with a larger involved range, the results for geopolymer are different compared to the results obtained under smaller penetration depth of 850 nm. Both the elastic modulus and hardness of ITZ in Figure 7.18 are found to be larger than paste. The elastic modulus of ITZ and paste are 23.08 GPa and 19.15 GPa, respectively. Correspondingly, the hardness of ITZ and paste is 1.61 GPa and 1.36 GPa, respectively. The elastic modulus of ITZ is 1.21 times that of the paste and the hardness is 1.18 times that of the paste. In terms of the PC sample, the elastic modulus of ITZ and paste is 23.46 GPa and 21.96 GPa, respectively, and the hardness is 0.69 GPa and 0.76 GPa, respectively, for ITZ and paste. The hardness ratio of ITZ to paste is 0.91 GPa, which still indicates the low hardness of ITZ compared to paste. However, the difference is reduced when compared with the ratio of 0.82 obtained under the smaller penetration depth of 850 nm. Additionally, the elastic modulus ratio of ITZ to paste is even slightly greater than 1, reaching the value of 1.07.

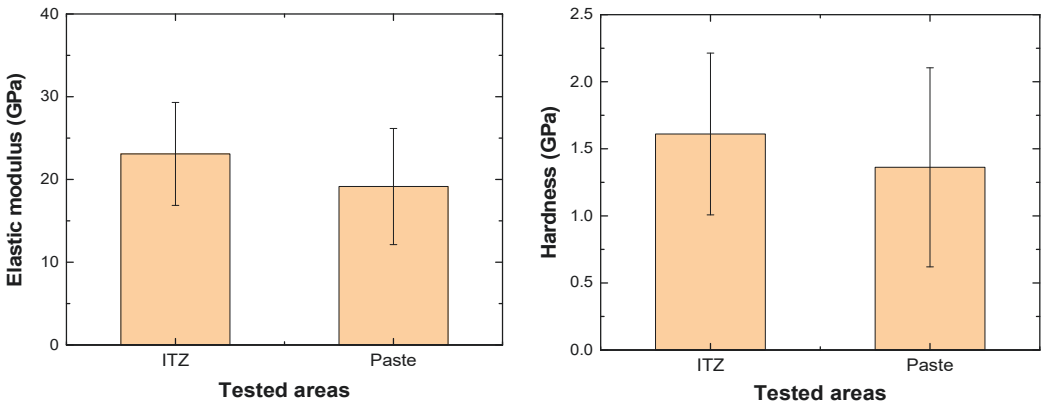

(a) Elastic modulus (b) Hardness

Figure 7.18 Comparison on micromechanical properties of ITZ with paste in geopolymer (1200 nm)

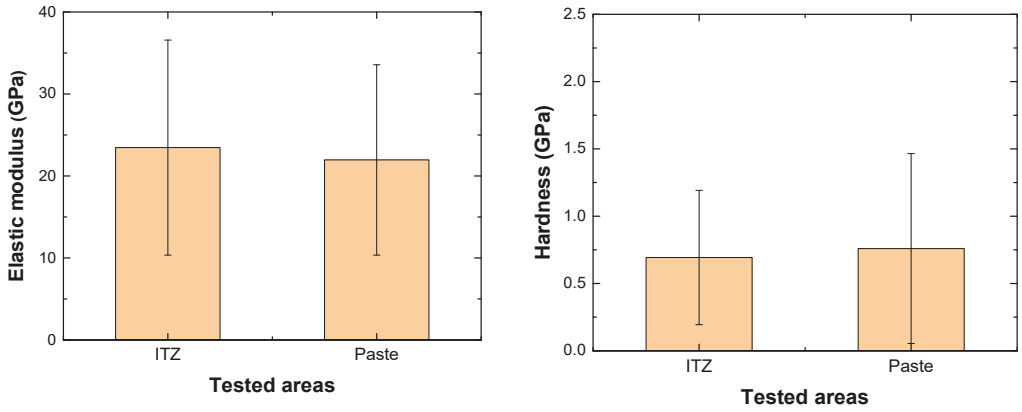

(a) Elastic modulus (b) Hardness

Figure 7.19 Comparison on micromechanical properties of ITZ with paste in PC (1200 nm)

For both geopolymer and PC, as shown in Table 7.1, both elastic modulus and hardness decrease when the penetration depth is increased from 850 nm to 1200 nm, especially for the elastic modulus of PC. This shows that the micromechanical properties are lower when a larger extent of multiple phase interaction is involved. Even under the depth of 1200 nm, the micromechanical properties obtained are still found to be larger than the corresponding gel phase in materials, N-A-S-H gel (chapters 4 and 5) and LD C-S-H gel (Hu & Li 2015b; Jennings et al. 2007; Kim, Foley & Taha 2013). In addition to micromechanical properties, the standard deviation also decreased, indicating more homogeneous results obtained under larger penetration depth test. However, due to the limitation of ITZ width on the maximum test depth of nanoindentation, the materials are still heterogeneous at the test scale. The distinct difference between micromechanical properties of phases governs the intrinsic large standard deviation of this type of test, which cannot be reduced by increasing the number of test data.

For both the test result from 850 nm and 1200 nm, it is obvious that PC has slightly higher elastic modulus but significantly lower hardness than geopolymer. The hardness of PC is just 0.52~0.62 times (850nm) and 0.43~0.56 times (1200nm) of the hardness of

geopolymer. Moreover, the standard deviation of PC elastic modulus is always significantly higher than for geopolymer, indicating more heterogeneous modulus properties in PC, which is not consistent with test results reported in another study involving smaller penetration depth (Khedmati et al. 2018).

As illustrated previously, tests with a larger involved range should be more appropriate to reflect the micromechanical properties of ITZ. Based on the result from the maximum allowed depth of 1200 nm, the interface of alkali-activated low calcium fly ash geopolymer is found to have higher micromechanical properties than its paste. This phenomenon is not observed when considering smaller depth tests as reported in both this study and other studies (Khedmati et al. 2018). The ITZ of geopolymer does not have many crystals and pores. The higher micromechanical properties could be attributed to the layer of dense paste rich in gel product shown in Figure 7.5. The strong paste and low content of harmful large crystalline phase and pores contribute to the strong interface in geopolymer, which is consistent with the macro phenomenon revealed in Figure 7.4. The layer of geopolymer paste remaining on the surface of aggregate after separation indicates that the ITZ should be stronger than the bulk paste. Thus, the large width of ITZ in geopolymer is a favourable factor for its performance.

In terms of the PC sample, ITZ elastic modulus is slightly higher and hardness is slightly lower than paste, which seems to conflict with the conventional concept that the ITZ is a significant weak part of PC concrete. In fact, the high micromechanical properties tested for ITZ are not groundless. As shown in Figures. 7.6 and 7.7, there is a large amount of CH in ITZ, which greatly enhances the micromechanical properties of ITZ. Hardness is related to strength (Vandamme, Ulm & Fonollosa 2010), which means that ITZ is still inferior to paste in some aspects. The macro behaviour of ITZ is determined by many factors. The existence of a large crack at the surface of aggregate due to shrinkage as

typically displayed in Figure 7.9 should be a more influencing factor explaining the weak feature of ITZ. Besides, the large content and large size of CH with loose bonding make ITZ easy to crack under loading. This kind of property is not effectively captured in the micromechanical test. Thus, ITZ of PC should be a weak region, which can be verified by the observation in Figures. 7.4 (a) and (b). Nevertheless, the "weak features" of ITZ do not affect its micro-elastic modulus and micro-hardness dramatically, which are close to the corresponding properties in the paste.

7.4 Conclusions

In this study, an idealized method of using modelled concrete was developed to understand the property differences in ITZs between geopolymer concrete and Portland cement (PC) concrete. The properties of ITZs in both the geopolymer and PC concretes depend largely on the material composition, mix design and so on. The comparisons were conducted based on a specified situation that geopolymer and PC samples exhibited the equivalent flowability. The main conclusions are drawn up as follows:

(1) For the comparative study of ITZs, the interferences caused by factors such as different types, shapes, size and relative positions of the aggregates, as well as different locations of ITZ taken from an aggregate can be effectively avoided by using modelled interface. Besides, the clear interfaces could eliminate the effects of the irregular shape of aggregate on the nanomechanical results of the ITZ.

(2) After removing geopolymer from aggregate, residual paste was observed on the surfaces of the polished aggregate. However, no obvious residual PC paste was found to adhere to the aggregate. Besides, the force needed to remove geopolymer was much higher than that for PC. It indicates that geopolymer has stronger bonding than that of PC to aggregate surface.

(3) The statistical analysis of BSE images indicates that the widths of ITZ in PC and geopolymer are around 20 and 30 μm, respectively. Morphology features showed that a layer of dense gel-rich paste formed on the initial interfacial zone of geopolymer, while a large amount of CH crystals were found on the ITZ of PC. A larger ITZ may lead to inferior performance of PC concrete and better performance of geopolymer concrete.

(4) Grid nanoindentation under the indent depth of 850 nm shows that the elastic modulus ratio and hardness ratio of ITZ to bulk paste are both around 0.97 in geopolymer. The corresponding ratios for PC are around 0.96 and 0.82, respectively. Thus, compared with paste, only the hardness of ITZ in PC reveals significantly lower properties at this indent scale.

(5) Grid nanoindentation indent under the depth of 1200 nm revealed more homogeneous properties. The elastic modulus and hardness of ITZ in geopolymer are around 1.21 and 1.18 times that of the bulk paste. The corresponding ratios are around 1.07 and 0.91 for PC, respectively.

(6) The higher micromechanical properties of ITZs in geopolymer can be attributed to the dense and uniform gel-rich paste on the surface of aggregate, which contributes to the strong interfacial bonding properties. In PC, the micro-elastic modulus and micro-hardness properties of ITZ are enhanced by the CH crystals, making it not as low as expected for this weak region.

CHAPTER 8. STATISTICAL NANOSCRATCH TECHNIQUE FOR THE QUICK MICROMECHANICAL PROPERTIES INVESTIGATION OF MODELLED ITZS

8.1 Introduction

In chapter 7, the alkali silicate solution is identified as an important factor leading to the better ITZ properties in geopolymer than PC concrete. The effects of silica modulus of the solution on the relative micromechanical properties of paste and ITZ were further investigated in this chapter. For comparative study, the heterogeneity of ITZ was largely decreased in chapter 7 by using modelled ITZ samples. Considering the neat ITZ boundary provided in the modelled samples, scratch technique with the advantages of fast testing a long range was introduced to improve the testing efficiency further. Abundant scratch data were analyzed in the form of histograms and Gaussian mixture models to compare the properties of ITZ and paste.

8.2 Experimental and analysis methods

8.2.1 Sample preparation

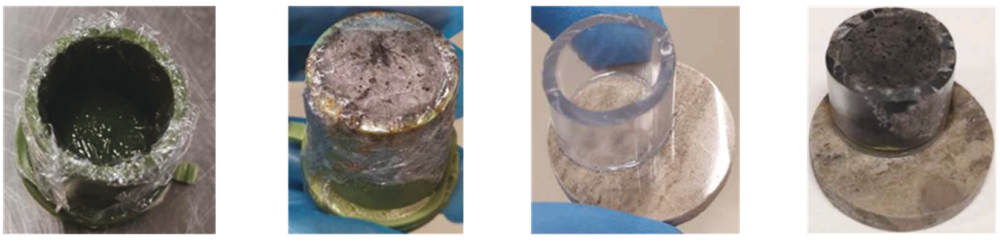

(a) Mould I (b) Modelled sample I (c) Mould II (d) Modelled sample II

Figure 8.1 Preparation of model samples for nanoscratch tests

The raw materials are the same as in chapter 7. The two types of modelled ITZ samples prepared can be observed in Figure 8.1. The silica modulus (SiO_2/Na_2O) of the samples

in this study is 1 and 1.5, respectively. For geopolymer samples with different silica modulus, they have the same Na_2O/fly ash of 8%, water/solid ratio of 0.33. A sand/fly ash ratio of 2 was used to prepare mortar samples.

8.2.2 **Characterization techniques**

The width of ITZ in geopolymer samples was determined by grey-level threshold segmentation of backscattered electron (BSE) images (Scrivener 2004). The magnification of BSE images was determined as 500× (Diamond 2001; Wu et al. 2016). For a segmented image, fourteen consecutive 5 μm strips cover ITZ and partial paste were taken starting at the boundary of aggregate. A total of forty such BSE images were adopted for statistic the average proportion of components in strips. BSE was operated under an accelerating voltage of 15 kV by using Zeiss EVO LS15. SEM observation of ITZ in modelled sample II was conducted by Zeiss Supra 55VP with an accelerating voltage of 10 kV.

8.2.3 **Scratch technique**

Scratch test was performed on Agilent G200 Nano Indenter by using a hemispherically-tipped, conical stylus. The radius and apex angle of this tip is 5 μm and 120°, respectively. It has the same apex angle but a far small radius compared with the representative tip (radius of 200 ± 10 μm) in ASTM G171-03 (Standard Test Method for Scratch Hardness of Materials Using a Diamond Stylus) to facilitate the test on ITZ. For a real interface at the microscopic scale, due to the irregular shape of aggregate, the starting point of ITZ is likely to be a curved surface rather than a straight plane. In this study, as shown in Figure 8.2(a), the neat aggregate boundary provided by modelled sample allows scratch to precisely test on “pure ITZ” to collect rich test data without incorporating properties results from aggregate and paste. According to the statistical results of BSE, the scratch tests on ITZ were set at 15 μm away from the boundary of aggregate. Tests were set on

paste for comparison, which were 65 μm away from the boundary of aggregate. The accompanied setting of ITZ and paste shown in Figure 8.2(a) can decrease the effects of local condition on the comparison of them. For the first several ITZ tests, scratches with the same distance of 15 μm to the boundary were conducted on aggregate to help locate and observe scratch impression. The scratch paths were adjusted under a microscope to ensure that they were parallel to the aggregate boundary and started at the same level. The properties of ITZ and paste were both determined by twelve effective 100 μm scratches. In addition to the scratch test scheme I, parallel to the boundary of aggregate, as in Figure 8.2(a) on individual objects, thirty three scratches based on the traditional scratch scheme II, perpendicular to the boundary, as given in Figure 8.2(b) were conducted on geopolymer with a silica modulus of 1.5 to compare the test results.

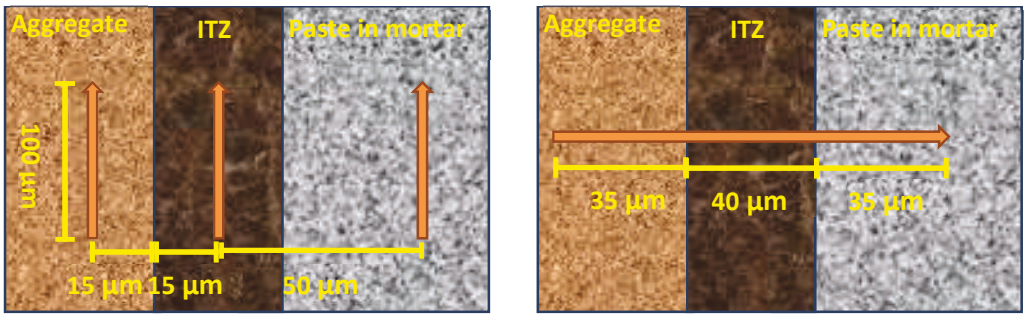

(a) Scratch scheme I (b) Scratch scheme II

Figure 8.2 Scratch schemes for the ITZs

To ensure the accuracy of the test, the normal load used should be moderately large. However, for the research here, an important factor limiting the normal load is the small width of the ITZ. The constraint effects of aggregate could possibly enhance the properties of ITZ significantly when the penetration depth is large. After a trial on a series of load levels, the final load for the scratch study of ITZ and paste was determined as 4 mN by referring to both ASTM G171-03 and the involved range of indentation test (Chen et al. 2010c). 2 mN and 8 mN scratch results on the more homogeneous modelled

aggregate were also provided to help understand the effects of load levels. The tests on aggregate with different load levels were conducted at the location around 1500 μm away from the boundary of aggregate, which had the same scratch length and number as ITZ and paste tests. For all scratch tests, a constant scratch speed of 4 μm/s was applied. Prescratch and postscratch scan were always performed at a small profiling load of 20 μN. The data acquisition rate is one point per micron.

$$HS_p = \frac{8P}{\pi w^2} \tag{8.1}$$

$$\mu = \frac{F_{scr}}{p} \tag{8.2}$$

$$d_{gt} = r(1-\sin(\frac{\alpha}{2})) \tag{8.3}$$

$$w = \begin{cases} 2\sqrt{r^2-(r-d)^2} & d \le d_{gt} \\ w_{gt} + 2\tan(\frac{\alpha}{2}) \times (d - d_{gt}) & d > d_{gt} \end{cases} \tag{8.4}$$

where the value of α and r is 120° and 5 μm, respectively, representing the apex angle of the conical portion and the radius of the hemispherical portion of the tip adopted.

According to ASTM G171-03, the scratch hardness HS_p based on this kind of tip can be determined by Equation (8.1). Scratch friction coefficient μ was obtained by Equation (8.2), based on scratch lateral force F_{scr} and normal force P. The geometric transition depth d_{gt} provided in Equation (8.3) means a critical depth. When the test depth is larger than this value, the test would involve the conical portion of the indenter tip. In this study, d_{gt} was calculated as 669.87 nm. For the test with depth-sensing technique, similar to a previous study (Akono, Chen & Kaewunruen 2018), the scratch width w was obtained based on the geometry of the indenter and the depth acquired as given in Equation (8.4).

The scratch width w_{gt} under geometric transition depth was calculated as 5 μm, equal to the tip radius.

8.3 Results and discussion

8.3.1 **Determining of ITZ by BSE**

BSE images were segmented into three components of reacted products, fly ash and pores/cracks. Pores on unreacted fly ash are sometimes unable to be precisely captured by grey values and incur inaccuracy when classified as pores manually. Therefore, they are still counted as fly ash in the part of BSE analysis. The ITZ in concrete is considered to be caused by the "wall" effect (Scrivener 2004). It means that the amount of unreacted fly ash would decrease, whereas the solution to ash ratio would increase in ITZ due to the presence of aggregate as a wall. This phenomenon is clearly presented in the statistical results of BSE images as shown in Figure 8.3, in which the proportion of constituents were plotted in the middle of the position of each strip. For geopolymer with different silica modulus, the distribution of constituents generally shows a similar trend. However, the "wall" effect is less significant in geopolymer with a higher silica modulus of 1.5. Besides, geopolymer with a silica modulus of 1 presents more pores/cracks and unreacted fly ash, but fewer reacted products than the sample with a higher silica modulus of 1.5.

For geopolymer with silica modulus of 1, the most significant part of ITZ was the first six strips, which corresponds to a width of around 30 μm. The increase of fly ash in geopolymer with silica modulus of 1.5 is less apparent. Nevertheless, it was identified that the increasing trend sustained until to 40 μm. Based on the results, the scratch test of ITZ was conducted at a distance of 15 μm to the boundary of aggregate.

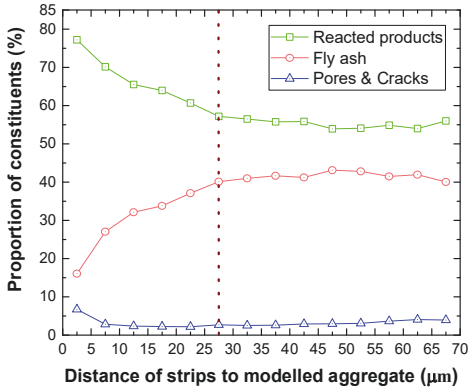

(a) Geo-Ms1

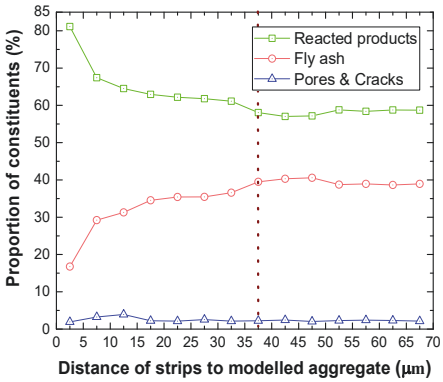

(b) Geo-Ms1.5

Figure 8.3 Variation of constituents with increased distance to modelled aggregate (the dashed lines indicate the boundary of ITZ and paste determined by BSE analysis)

8.3.2 **Microstructural observation of ITZ**

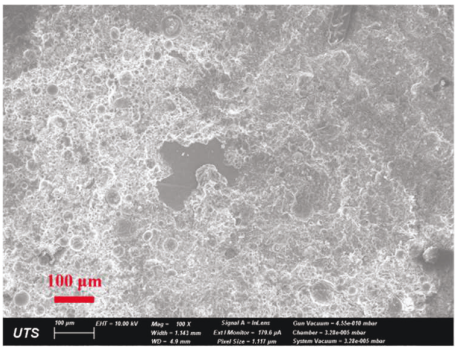

(a) 100 ×

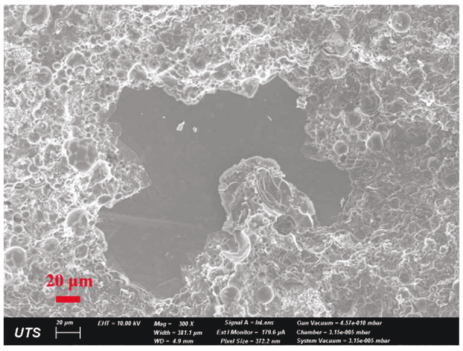

(b) 300 ×

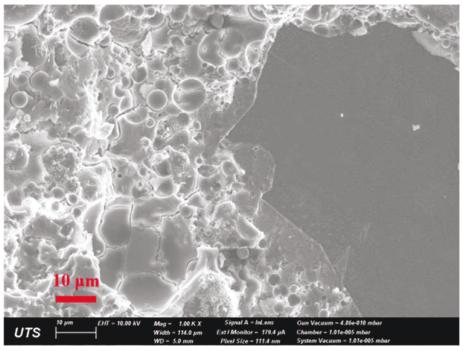

(c) 1000 ×

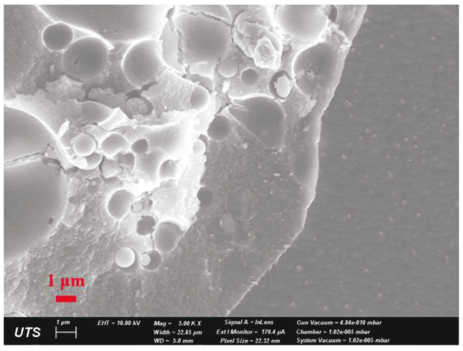

(d) 5000 ×

Figure 8.4 SEM observation of ITZ in geopolymer with silica modulus of 1.5 on the aggregate surface

After separating bulk paste and aggregate of modelled sample II, abundant residual geopolymer paste was observed on the surface of aggregate as typically shown in Figures. 8.4 (a) and (b). The detail of the boundary was revealed in Figures. 8.4(c) and (d). The slight inner bleeding helps to show the layer of matrix adhered to the aggregate, which has a dense and homogeneous appearance. The change in silica modulus in this study did not bring significant differences for the observed results.

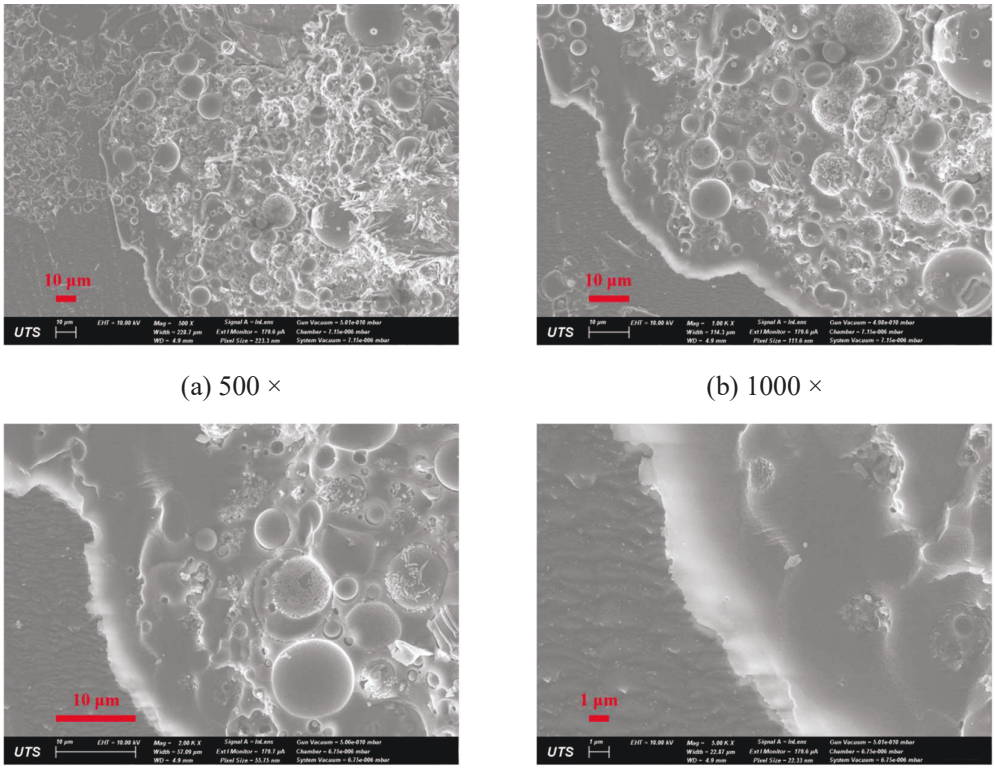

(a) 500 ×　　(b) 1000 ×

(c) 2000 ×　　(d) 5000 ×

Figure 8.5 SEM observation of ITZ in geopolymer with silica modulus of 1.0 on the aggregate surface

For geopolymer with silica modulus of 1.0, similar phenomenon is typically displayed in Figure 8.5. The high amount of residual geopolymer observed on aggregate actually indicates that geopolymer bonded tightly to aggregate. The interface would be sometimes stronger than the highly heterogeneous geopolymer bulk paste, which contains different types of fly ash and microscale crystals embedded in the gel phase. For the modelled

sample prepared, the bond between geopolymer and polished aggregate is weaker than that of geopolymer and field aggregate which has rough surface. Thus, the same phenomenon of a good bond of geopolymer to aggregate should also occur in real geopolymer concrete.

8.3.3 **Scratch test results**

8.3.3.1 Basis of Scratch test

The direct scratch results acquired are shown in Figure 8.6, which consists of prescratch, formal scratch and postscratch. The meaning of these scratch curves has been widely illustrated in many papers (Liu, Zeng & Xu 2020; Luo et al. 2018; Wang et al. 2019) and also subsection 2.4.1. The typical SEM images after scratch tests are shown in Figure 8.7. Owing to the small normal force adopted in this study, the scratch impression is not obvious even at high magnification, especially for matrix with high elastic recovery. A clearer scratch impression can be found in Figure 8.7 (b), which was generated from a scratch test using a normal force of 8 mN. The large residual scratch width actually implies the large involved range under scratch test, which is not suitable for the study of ITZ.

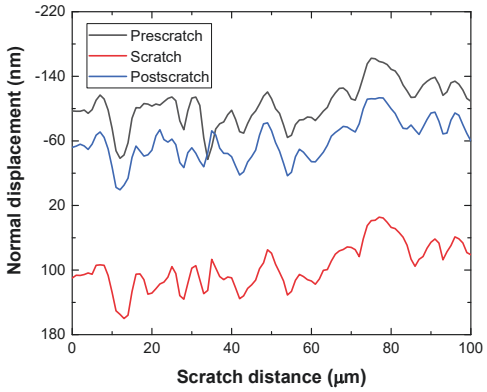

Figure 8.6 Scratch profiling curves at three different test stages

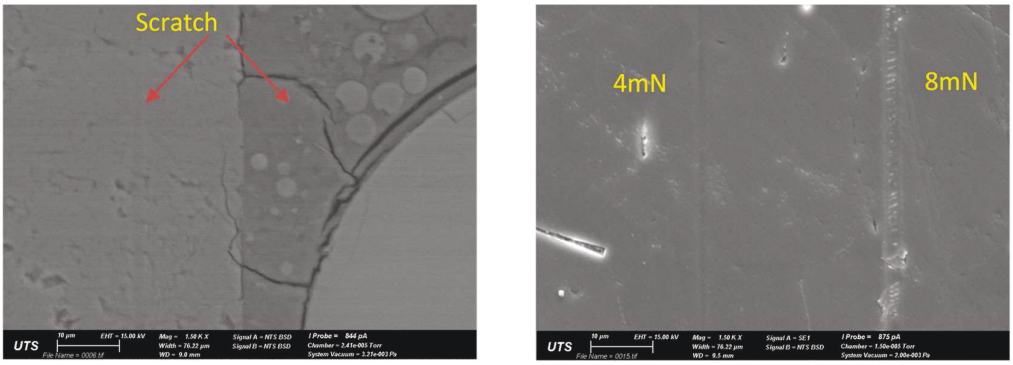

(a) ITZ (b) Aggregate

Figure 8.7 Scratch impression mark on the surface (1500 ×)

8.3.3.2 Effects of load level

The 2 mN, 4mN and 8 mN scratch loads were applied on the modelled aggregate. The obtained results for hardness and friction coefficient were presented in the form of frequency density histogram as displayed in Figure 8.8 and Figure 8.9. Although chapters 4 and 5 illustrated that histogram varies with its bin size and it is difficult to find an appropriate bin size, the same bin size specified for all samples would be still feasible for the comparison purpose. In addition to histograms, the properties distribution was described as Gaussian mixture models, with the parameters determined by maximum likelihood estimation. The number of components for models was increased until it can match the histogram well. Then, the models were used to represent the frequency density histograms and plotted in the same figure to facilitate comparison. As revealed in Figure 8.8(d) and Figure 8.9(d). The results clearly indicate that both hardness HS_p and friction coefficient μ increased with load level P. The average value and standard deviation of test result data are given in Table 8.1. Friction coefficients are very small values in the range of 0.12 to 0.35, while hardness is around one order of magnitude greater than the friction coefficient, which varies between 1.95 GPa to 2.64 GPa.

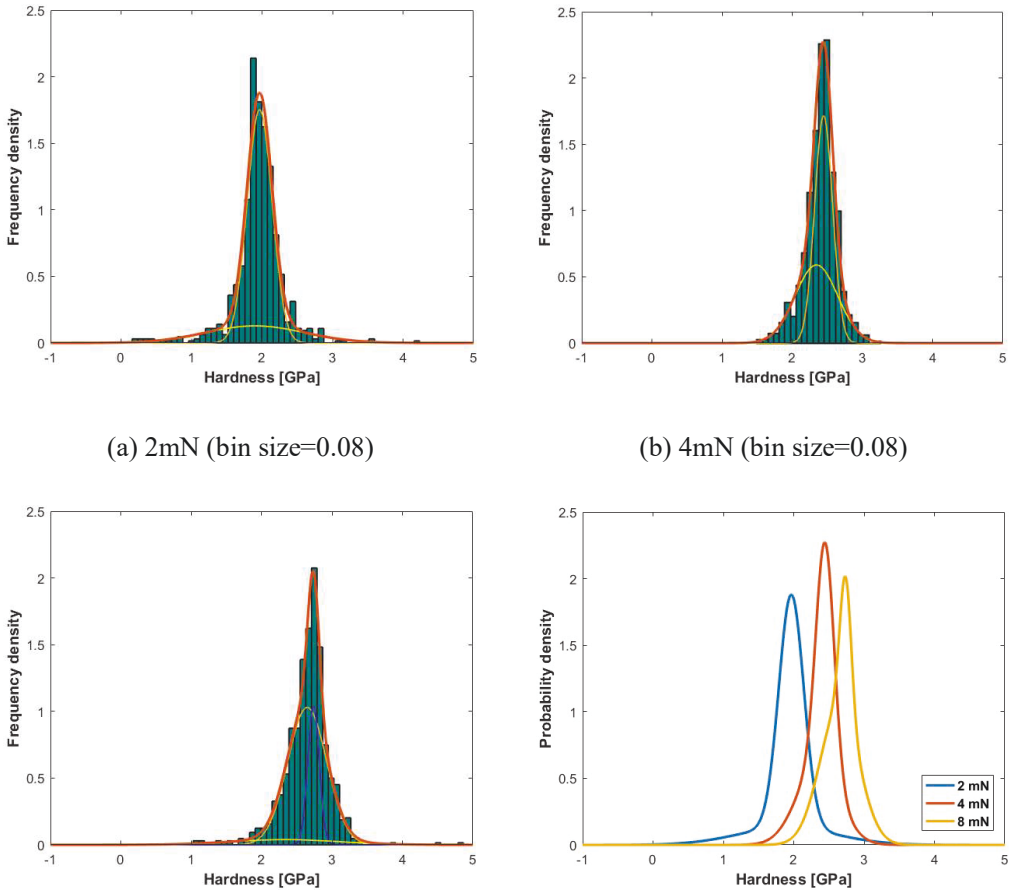

(a) 2mN (bin size=0.08)

(b) 4mN (bin size=0.08)

(c) 8mN (bin size=0.08)

(d) Comparison on load levels

Figure 8.8 Scratch hardness of aggregate under different load levels

Although both hardness and friction coefficient increased with the increase of normal load, their increasing trends are different. When the normal load was increased from 2 mN to 4 mN, the hardness and friction coefficient were increased by 23.08% and 41.67%, respectively. The corresponding increase from 4 mN to 8 mN is 10.00% and 105.88%, respectively. The load level is obviously more influential on the friction coefficient and causes less change in hardness. It could be attributed to the effects of surface defects under small load tests, which is especially significant for friction coefficient that governed by the topology of the contacted surface (Akono, Chen & Kaewunruen 2018). Since properties are dependent on test factors, the same scratch load and speed are set for the test of ITZ and paste.

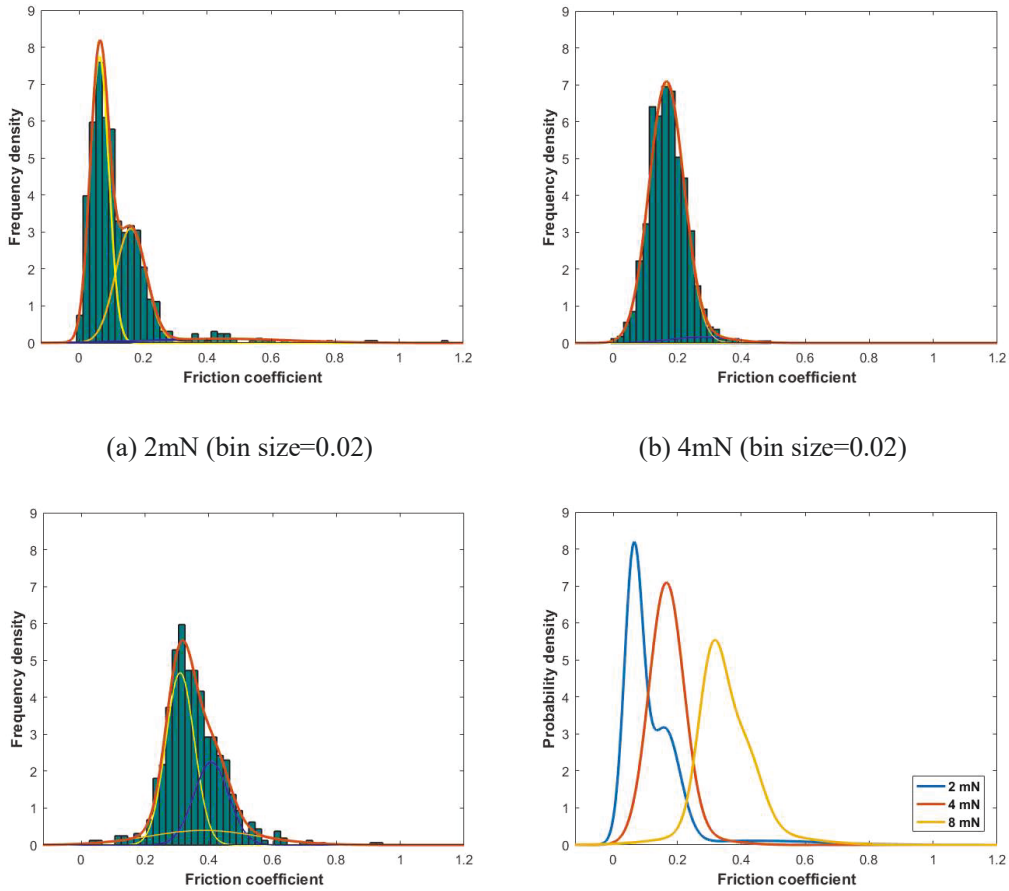

(a) 2mN (bin size=0.02)

(b) 4mN (bin size=0.02)

(c) 8mN (bin size=0.02)

(d) Comparison on load levels

Figure 8.9 Scratch friction coefficient of aggregate under different load levels

Table 8.1 Scratch hardness and scratch friction coefficient of aggregate under different load levels

Load level	Scratch hardness (GPa)	Scratch friction coefficient
2 mN	1.95 ± 0.37	0.12 ± 0.11
4 mN	2.40 ± 0.23	0.17 ±0.06
8 mN	2.64 ± 0.33	0.35 ± 0.09

8.3.3.3 Properties comparison of ITZ and paste

Based on the constant load of 4 mN under test scheme I, the average value and standard deviation of hardness and friction coefficient results of ITZ and paste are obtained as

listed in Table 8.2. ITZ and paste are found to have lower hardness but higher friction coefficient and standard deviation than that of aggregate when the same scratch load and speed were applied. The high standard deviation is caused by distinct hardness of different constituents. For geopolymer with different silica modulus, results reveal that ITZ of Geo-Ms1.5 sample has almost the same hardness and friction coefficient as its paste, whereas a significant properties discrepancy is presented between ITZ and paste of Geo-Ms1. In Geo-Ms1, its ITZ shows distinctly higher hardness but lower friction coefficient than paste. The hardness and friction coefficient of Geo-Ms1 are all larger than that of Geo-Ms1.5. Obvious differences are found for the hardness of ITZ and friction coefficient of paste. In fact, the comparison of heterogeneous samples cannot be just based on the average value. The largest hardness tested for ITZ and paste of Geo-Ms1 is 52.49 GPa and 35.40 GPa, respectively, significantly larger than the values of around 10 GPa in Geo-Ms1.5. It should be caused by the less important component fly ash. Although the number of mechanical test data on ITZ is more than most studies, they should still not be able to reflect the proportion of constituent very accurately. To further understand the properties of ITZ and paste in geopolymer samples, the properties data were presented by histograms and analyzed as below.

Table 8.2 Scratch hardness and friction coefficient of ITZ and paste with difference silica modulus

Samples	Scratch hardness (GPa)	Scratch friction coefficient
Geo-Ms1.5-ITZ	1.38 ± 0.75	*0.31* ±0.30
Geo-Ms1.5-paste	1.39 ± 0.83	*0.31* ± 0.27
Geo-Ms1-ITZ	1.72 ± 1.42	*0.32* ± 0.29
Geo-Ms1-paste	1.49 ± 1.46	*0.42* ± 0.37

Note: for Geo-MsXX-XX, Ms1.5/Ms1 means the silica modulus of the sample is 1.5 or 1, while ITZ or paste means the object investigated is ITZ or paste.

8.3.3.4 Scratch hardness of ITZ and paste

The scratch hardness of ITZ and paste in geopolymer samples with different silica modulus are displayed in Figure 8.10. It can be observed that the Gaussian mixture models with 3 components match with corresponding frequency distribution histograms. To clearly identify differences, the probability density distribution curves are summarized in Figure 8.11. For geopolymer with silica modulus of 1.5, it can be found in Figure 8.11 that the hardness of ITZ and paste has very close probability density distribution. However, obviously deviated hardness probability density distribution is found for ITZ and paste of geopolymer with silica modulus of 1.

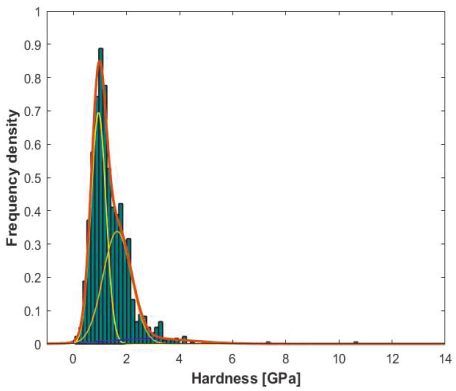

(a) Geo-Ms1.5-ITZ (Bin size=0.15 GPa)

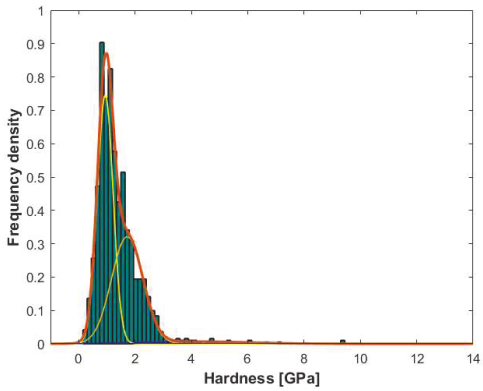

(b) Geo-Ms1.5-paste (Bin size=0.15 GPa)

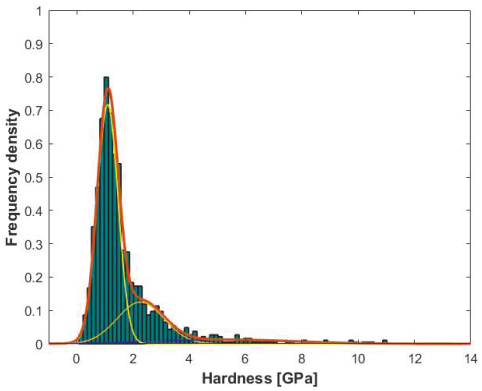

(c) Geo-Ms1-ITZ (Bin size=0.15 GPa)

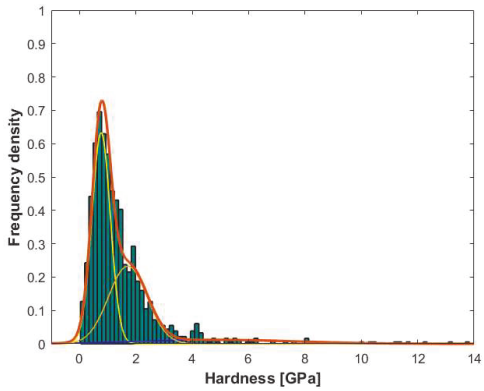

(d) Geo-Ms1-paste (Bin size=0.15 GPa)

Figure 8.10 Scratch hardness of ITZ and paste in geopolymer samples

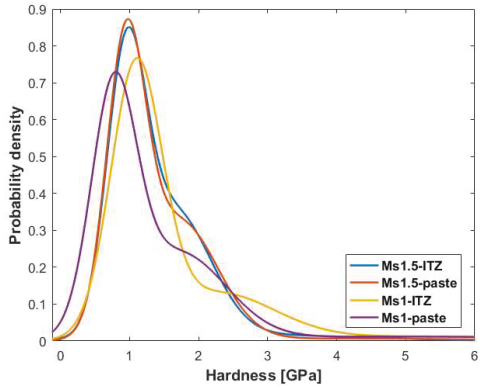

Figure 8.11 Summary of the probability density distribution of scratch hardness

Table 8.3 Deconvolution results for hardness probability density distribution

Samples	Components	Hardness (GPa)	Proportion	Standard deviation
	1	0.95	49.05%	0.28
Geo-Ms1.5-ITZ	2	1.65	45.01%	0.53
	3	2.93	5.94%	1.50
	1	0.94	52.17%	0.28
Geo-Ms1.5-paste	2	1.72	44.64%	0.56
	3	4.11	3.19%	1.89
	1	1.10	66.48%	0.37
Geo-Ms1-ITZ	2	2.27	26.09%	0.83
	3	5.34	7.43%	2.40
	1	0.77	51.80%	0.33
Geo-Ms1-paste	2	1.71	39.87%	0.68
	3	4.88	8.33%	2.81
	1	0.58	30.37%	0.23
	2	1.06	32.01%	0.32
Geo-Ms1-paste	3	1.81	25.80%	0.52
	4	3.30	9.20%	1.09
	5	7.82	2.61%	2.95

Geopolymer is highly heterogeneous, mainly composed of unreacted fly ash, N-A-S-H gel phase, crystals and defects (pores and cracks). Histograms in Figure 8.10 show that Geo-Ms1 has more large hardness data than Geo-Ms1.5 sample, which can be typically observed by the part of hardness larger than 4 GPa. This phenomenon is in line with the statistical results for BSE images. There is a higher content of uncreated fly ash in Geo-Ms1 than Geo-Ms1.5. To figure out if the higher average hardness of Geo-Ms1 than Geo-Ms1.5 is just caused by fly ash, deconvolution analysis was conducted. Due to the large indenter tip adopted in this study for scratch and the small characteristic size of real phases, the deconvolution study is not expected to generate individual pure phases. However, the three components obtained by decomposition of Gaussian mixture models are still useful for the analysis of mechanisms. The deconvolution results revealed in Figure 8.10 for hardness are listed in Table 8.3.

For the deconvolution results, the third component with maximum hardness should be from fly ash particles. The first component with minimum hardness corresponds to the mixed phase containing mainly defects, N-A-S-H gel and also some crystals/fly ash, which shows larger hardness than 0.45 GPa~0.73 GPa obtained for N-A-S-H gel by statistical nanoindentation at smaller scales in chapters 4 and 5. Compared with nanoscale indentation, scratch doesn't eliminate defects, and would have far larger multiple phase interaction due to the large tip. The deconvolution results for ITZ and paste of Geo-Ms1.5 sample are quite similar to each other. The hardness of the gel phase in ITZ may not be significantly different from that in the paste. Compared with a similar value of around 0.94 GPa in Geo-Ms1.5, the minimum hardness of ITZ and paste of Geo-Ms1 showed discrepancy, which was 1.10 GPa and 0.77 GPa, respectively. The summarized distributions provided in Figure 8.11 also clearly display this difference.

In this study, 3 components were set for the convenience of comparison. In fact, for these figures, Geo-Ms1-paste is slightly less match with the histogram in the region around the highest peak. Further increasing the number of components is accompanied by a better match of probability density curve with frequency density histogram. When the number of components increased to 5, as shown in Figure 8.12, the component with hardness of 0.77 was decomposed into two components with hardness of 0.58 GPa and 1.06 GPa, respectively. The deconvolution results for 5 component model provided in Table 8.3 show that in addition to the small proportion, the second newly decomposed component with hardness of 1.06 GPa is similar to the minimum component in other test objects. The lowest hardness of 0.77 GPa obtained in 3 component models for Geo-Ms1-paste should be caused by the first newly decomposed component with a small hardness of 0.58. This component should have a considerable amount of defects related test points. Defects such as some capillary pores in gel are not large enough to be detected by BSE analysis at the magnification of 500 ×, but would still affect scratch properties significantly. Table 8.4 presents the percentage of test data from typical large scratch widths of larger than 5 μm and 4 μm. The range of hardness values was provided accordingly in brackets. For hardness data less than 0.407 GPa and 0.637 GPa in Geo-Ms1-paste, the proportion of data from the defects related phase (H=0.58) can be estimated based on Equation (5) and deconvolution results in Table 8.3, which is obtained as 89.56% and 84.27%, respectively. Thus, the data of scratch width larger than 5 μm and 4 μm in Geo-Ms1-paste are primarily from the defects related phase. Results in Table 8.4 indicate that the percentage of test data of scratch width larger than 5 μm and 4 μm are very close for Geo-Ms1.5-ITZ, Geo-Ms1.5-paste and Geo-Ms1-ITZ, which vary in the range of 1.66% to 1.94% and 7.46% to 8.65%, respectively. Lager proportions of 8.45% and 21.21% are found for Geo-Ms1-paste. In fact, the points in the defects related phase with the average hardness of 0.58

GPa should not be entirely defects related points and some of which are normal gel. Besides, the real differences in the proportion of defects between Geo-Ms1-paste and others may be less significant as manifested in the Table 8.4. After all, the contact area of nanoscratch test is very large, and the distance between adjacent test points is only 1 μm. Although the real proportion difference would be smaller, it still can be pointed that the defects are more in Geo-Ms1-paste.

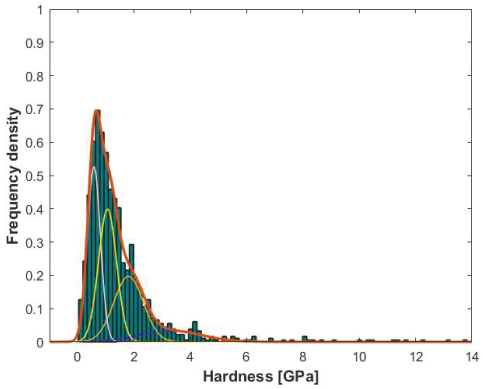

Figure 8.12 Matching histograms of Geo-Ms1-paste by Gaussian mixture models with 5 components

Table 8.4 Percentage of test data from large scratch widths

Samples	w>5 μm (H<0.407 GPa), %	w>4 μm (H<0.637 GPa), %
Geo-Ms1.5-ITZ	1.66	8.65
Geo-Ms1.5-paste	1.82	7.88
Geo-Ms1-ITZ	1.94	7.46
Geo-Ms1-paste	8.45	21.21

Although the average hardness of Geo-Ms1-paste is large than Geo-Ms1.5-paste, as revealed in Table 8.3, it should be caused by the third component with hardness of 4.88/4.11 GPa, which is the fly ash related phase. By using clustering technology, the

data that belong to the third component with the maximum hardness in the three component models were removed. Then, the average hardness for Geo-Ms1-paste and Geo-Ms1.5-paste is obtained as 1.19 ± 0.70 GPa and 1.31 ± 0.58 GPa, respectively. In fact, the properties comparison should more depend on the gel-related phase, namely the first component, instead of the average value of all data. After all, fly ash by nature results in a high scratch hardness, but is not a key factor as defects and gel that govern the macro failure of sample.

Based on the scratch hardness results and SEM observation above, it can be found that the ITZ in the both geopolymer samples studied are not the weakest phase in the concrete. Besides, the silica modulus of 1.5 used makes the difference between ITZ and paste less significant, enabling to make better use of both parts. The benefits brought by silica modulus on ITZ coincide with previous studies using siliceous aggregates (Lee & Van Deventer 2004, 2007).

$$f = \pi_1 \Phi\left(\frac{m-\mu_1}{\sigma_1}\right) / \sum_{i=1}^{5} \pi_i \Phi\left(\frac{m-\mu_i}{\sigma_i}\right) \quad (5)$$

where f is the proportion of data from the defect related phase shown by the purple phase in Figure 8.12(a). The m is the hardness value of 0.407 GPa or 0.637 GPa provided in Table 8.4. π_i, μ_i and σ_i are the proportion, average value and standard deviation of the i th component of the five components model.

8.3.3.5 Scratch friction coefficient of ITZ and paste

The frequency density of scratch friction coefficient distribution is shown in Figure 8.13. Compared with hardness, the distribution of friction coefficient is more concentrated, which mainly varies in the range of 0 to 1.5. The more concentrated distribution enables small bin size to reveal more details. The 3-component models are unable to reflect the

data well. Thus, the number of components is all increased to 5, which leads to an excellent match of models with histograms. These probability distribution curves are summarized for comparison in Figure 8.14.

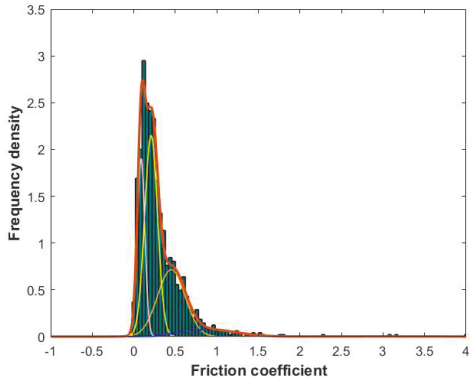

Geo-Ms1.5-ITZ (Bin size=0.04 GPa)

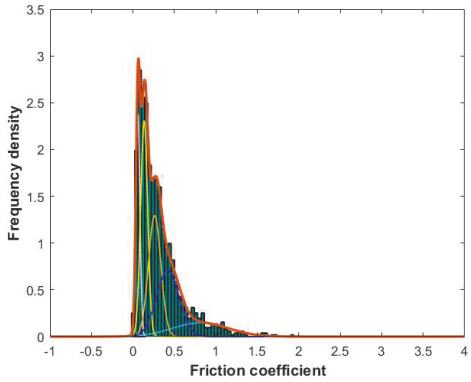

Geo-Ms1.5-paste (Bin size=0.04 GPa)

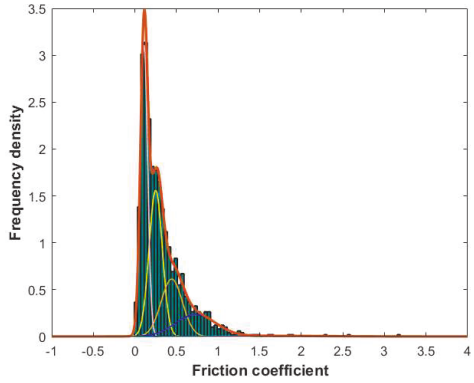

Geo-Ms1-ITZ (Bin size=0.04 GPa)

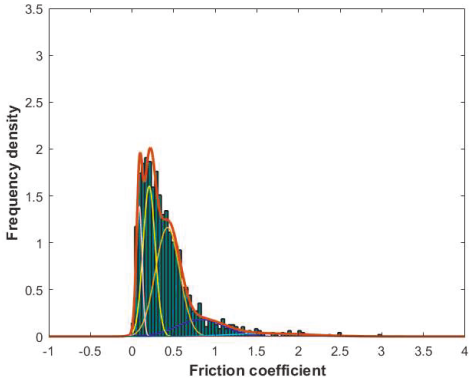

Geo-Ms1-paste (Bin size=0.04 GPa)

Figure 8.13 Scratch friction coefficient of ITZ and paste in geopolymer samples

The distribution of friction coefficient does not show strong consistency with scratch hardness. Compared with others, Ms1-paste in Figure 8.11 was found to have a substantial amount of low hardness data. The same phenomenon is not observed for its friction coefficient distribution. The results listed in Table 8.2 indicate that only Geo-Ms1-paste displays a significantly different average scratch friction coefficient, which shows larger values than others and even larger than Geo-Ms1-ITZ that has the maximum hardness. As analyzed previously by 5 components model, the distinct hardness probability

distribution of Ms1-paste should be caused by the defects related component, which has an average hardness of 0.58 GPa. After clustering, hardness data belonging to this component were collected. For each of hardness, by tracking the raw test data, the corresponding friction coefficient that tested at the same scratch location can be obtained. The hardness and friction coefficient data are combined presented by scatter points in Figure 8.15.

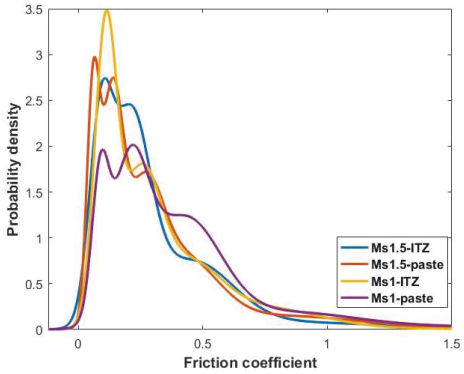

Figure 8.14 Summary of the probability density distribution of scratch friction coefficient

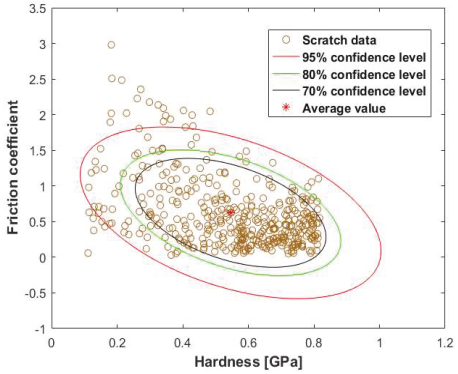

Figure 8.15 Clustered hardness data and corresponding friction coefficient for the component with average hardness of 0.58 GPa

For the clustered data, the hardness is 0.55 ± 0.19 GPa, while the friction coefficient is 0.62 ± 0.49. The hardness result indicates that although there is a slight deviation, the clustered data can still reflect the component with hardness of 0.58 GPa. The corresponding friction coefficient is found to have a very high average value and standard

deviation. After removing the friction coefficient corresponding to defects related points, the average value and standard deviation of remaining friction coefficient data are 0.31 and 0.22, respectively, which achieve similar values as other results in Table 8.2. Thus, the abnormally high friction coefficient of the Geo-Ms1-paste should be caused by the defects related component. A two-dimensional Gaussian distribution model was calculated based on these data. Since just one component is used, the model provided a perfect evaluation of average value but deviation on variance/covariance. Nevertheless, according to the confidence ellipses, it is not questionable to know that there is a negative correlation coefficient between hardness and friction coefficient. This phenomenon is in line with scratch results on different individual micro-constituents (Akono, Chen & Kaewunruen 2018), where harder constituent has a lower friction coefficient. It is attributed to different mechanisms behind the tested properties (Akono, Chen & Kaewunruen 2018): hardness is governed by composition and morphology, while fiction is affected by the topology of the contacted surface. The defects related component is destined to have a large friction coefficient. Thus, defects that have a negative impact on macro performance has been identified by scratch technique via both scratch hardness displayed in Figure 8.11 and scratch friction coefficient given in Table 8.2.

8.3.3.6 Effects of scratch direction

The results of the scratch test across aggregate, ITZ and paste of geopolymer with silica modulus of 1.5 are shown in Figure 8.16. The result in Figure 8.16(a) shows that there is a significant difference between the hardness of aggregate and matrix. When the scratch test reaches ITZ, the hardness value decreases rapidly and then increases. Scratch hardness in the boundary of ITZ and paste also shows low value. The average hardness of aggregate, ITZ and paste are 2.08 ± 0.73 GPa, 1.43 ± 0.92 GPa and 1.51 ± 1.15 GPa, respectively, which all show a larger standard deviation than the results collected from

test scheme I. There is also a difference between the average values obtained by these two different test schemes.

For this test, it was set to have a similar number of test points on each object as the scratch test parallel to ITZ (scheme I). However, the wall effect leads to properties that change gradually with increased distance to aggregate. Compared with results all collected from a constant distance to the boundary of aggregate, the average results from this kind of test would be undoubtedly more variable. The around 33 test points at each distance make the results hard to overcome the heterogeneous features and hard to be used for deconvolution analysis. The typical evidence is the different hardness of ITZ and paste on the same locations as that in scratch scheme I, which are obtained as 1.28 ± 0.60 GPa and 1.53 ± 1.05 GPa, respectively, in scheme II for scratch tests 15 μm and 65 μm away from aggregate. There are some reasons such as interfacial cracks and very low content of unreacted particles that may be able to support the low hardness of ITZ at the location near to aggregate. Different from the first boundary, the low hardness at the boundary of ITZ and paste does not indicate a successful identification of boundary by scratch test, which would be mainly attributed to the unstable results from limited test points at each given distance. After all, the term 'transition zone' means gradually changing properties. Boundary defined between 'ITZ' and 'paste' is from the location where properties tend to be stable. Thus, the properties around this boundary are expected to be close. In addition to unstable results, another inaccuracy in scratch test II is the constraint effect, which would enhance the properties of the part of ITZ that near to aggregate. Hence, although the average of all hardness data on each object doesn’t show a significant difference as that in test scheme I, the average results from scheme II should also be more instability.

The friction coefficient along scratch is shown in Figure 8.16(b), which are 0.29 ± 0.21, 0.48 ± 0.34 and 0.58 ± 0.42 respectively for aggregate, ITZ and paste. The average value

and standard deviation obtained are all larger than that in the test scheme I. For aggregate, it may be caused by a high amount of defects at the location near to boundary resulted from polish. Compared with 0.31 in scratch scheme I, the friction coefficient of ITZ and paste tested at the distance of 15 μm and 65 μm to the surface of aggregate in scratch scheme II are larger values of 0.38 ± 0.25 and 0.56 ± 0.44, respectively. Although different directions may sometimes affect the friction coefficient even in the same location, the nearly one times of difference in the same paste still indicates the errors caused by the number of test data.

Thus, based on the same number of test points, scratch scheme I could provide a more reliable result for a comparison of ITZ with paste. Scratch scheme II with increased distance to aggregate has the potential to reveal the variation trend of properties, but requires much more tests to eliminate the inaccuracy caused by insufficient test data on each given scratch distance. The number of test points should increase further if a smaller tip as shown in studies (Yan et al. 2019; Zhou, Jiang & Sui 2019) is adopted to obtain valid data without affected by constraint effect on the part of ITZ very close to aggregate.

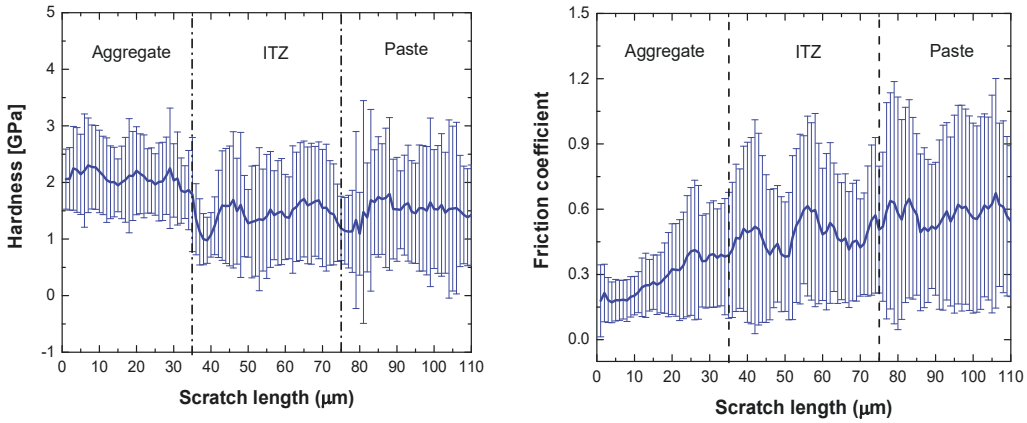

(a) Hardness (b) Friction coefficient

Figure 8.16 Scratch test perpendicular to the boundary of modelled aggregate

8.4 Conclusions

Based on modelled aggregate with a neat interface, nanoscratch technique was conducted on ITZ to understand mechanical properties of ITZ in geopolymer composites with the same water to solid ratio but different silica modulus of 1 and 1.5. The main conclusions can be drawn as below:

(1) ITZ caused by wall effect is more distinct in geopolymer composites with silica modulus of 1. Based on the ranges in fly ash content, the size of ITZ was determined as around 30 μm and 40 μm for Geo-Ms1 and Geo-Ms1.5, respectively. The ITZ in the modelled geopolymer concrete exhibited dense microstructures and is more uniform than geopolymer paste.

(2) Scratch hardness and scratch friction coefficient depended on the normal load applied. When slightly increases the normal load from 2 mN to 4 mN and 8 mN, the hardness was increased by 23.08% and 10.00%, respectively, while the friction coefficient was increased by 41.67% and 105.88%, respectively.

(3) ITZ and paste of Geo-Ms1.5 showed very close scratch hardness and scratch friction coefficient. The scratch friction coefficient of ITZ and paste were 0.31 ±0.30 and 0.31 ± 0.27, respectively. In addition to a similar overall hardness value, the scratch hardness of the first component has a similar value of around 0.95 GPa for ITZ and paste. Thus, a suitable silica modulus can reduce the difference between ITZ and paste, making them more compatible to each other.

(4) For Geo-Ms1, the scratch friction coefficient is 0.32 ± 0.29 for ITZ and 0.42 ± 0.37 for paste. In the three component model, the scratch hardness of the first component is 1.10 GPa and 0.77 GPa, respectively for ITZ and paste. Compared with ITZ, the significantly lower hardness of the first component but higher overall friction

coefficient of paste was caused by defects related points.

(5) Compared to the scratch test parallel to the aggregate boundary, perpendicular scratch that continuously crosses aggregate, ITZ and paste presented the potential to reveal the detailed variation of properties with increased distance to aggregate. However, based on a similar number of test points, the properties results obtained from perpendicular scratch are less stable and reliable. Parallel scratch uniquely applicable to the modelled interface can quickly provide useful information to reflect mechanical properties of ITZ.

CHAPTER 9. THE COMPLICATED NATURE OF ITZ: PROPERTIES INVESTIGATION AND TEST STRATEGY

9.1 Introduction

For Portland cement concrete, studies (Diamond 2001; Scrivener, Crumbie & Laugesen 2004) report that the properties of ITZ are highly inhomogeneous in concrete and also heterogeneous around the same aggregate. It is important to figure out if such inhomogeneity is also significant in geopolymer. On the one hand, the extent of inhomogeneity is a very meaningful aspect to reflect the interfacial quality of concrete. On the other hand, if the ITZ is highly inhomogeneous, the ITZ properties comparison between samples as usually conducted should consider the interference caused by the random selection of test objects. This chapter categorized the heterogeneity of ITZ into three levels. Modelled samples in chapters 7 and 8 are mainly for the comparative study of different samples, which reduced the heterogeneity to level one and partial II to realize a quick examination of ITZ/paste difference caused by the different nature of the cementitious materials used. In this chapter, the heterogeneity was increased to investigate the ITZ properties at different locations of an aggregate particle (level 2) to promote a deeper understanding of ITZ in geopolymer. It could benefit the understanding of crack development of concrete and establishing more reasonable concrete numerical model. In addition, a test strategy was provided for the investigation of ITZs with a higher level of heterogeneity.

9.2 Experimental and analysis methods

9.2.1 Sample preparation

The ϕ25 slices were long time ground by 120 grit abrasive paper until become cuboids with a size of around 15 × 10 × 8 mm. The cuboids were further polished by 320, 600 and 1200 grits abrasive papers and 1 micron alumina to achieve smooth surfaces. The geopolymer mortar was prepared with a Na_2O/fly ash of 8%, solution/powder ratio of 0.57, SiO_2/Na_2O of 1.3 and sand/fly ash of 2. After 5 minutes of mixture, fresh geopolymer mortar was poured into moulds shown in Figure 8.1 (a) and (b). When the mortar reaches half the height of the mould, the polished modelled aggregate was placed on the centre part prior to proceeding with the casting. After casting, the samples were vibrated on a vibration table for 1.5 minutes and then sealed by plastic film. The curing regime applied was heat curing under 65 °C for 24 hrs, followed by 22 °C curing to 28 days. Afterwards, the samples were demoulded and cut from top to bottom to expose the modelled aggregate and interfaces as shown in Figure 9.1 (a). A specimen with only slightly inclined aggregate was subjected to polish and used for the test. The surface was ground by 320, 600 and 1200 grit abrasive paper to flat and then polished by 1 micron and 0.3 micron alumina for 20 minutes each.

The properties of ITZ at the top, bottom and left/right side of the modelled aggregate were investigated in to reveal the properties difference caused by locations. The left/right side means the tests are about half for each side. As shown in Figure 9.1 (b), it is difficult to strictly distinguish the top surface and the side surfaces for nature aggregate with an irregular shape. Besides, it is difficult to accurately conduct scratch and indentation tests on the ITZs surrounding nature aggregate. The simplified mix condition also leads to more even binders at each side and hence ensure the accuracy of limited tests.

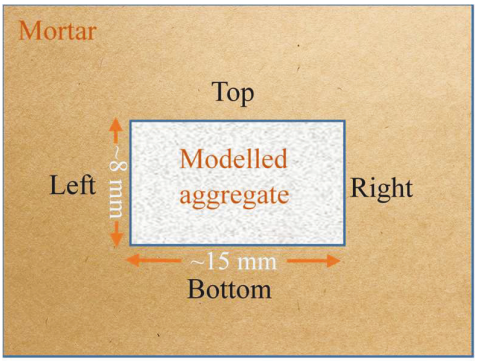

(a) Modelled aggregate embedded in mortar

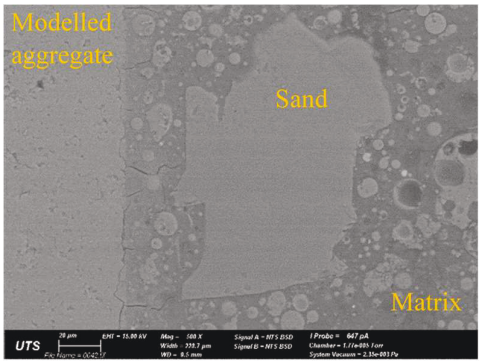

(b) Comparison of different interfaces

Figure 9.1 Characteristics of the interface around natural aggregate and modelled aggregate

9.2.2 **Image analysis**

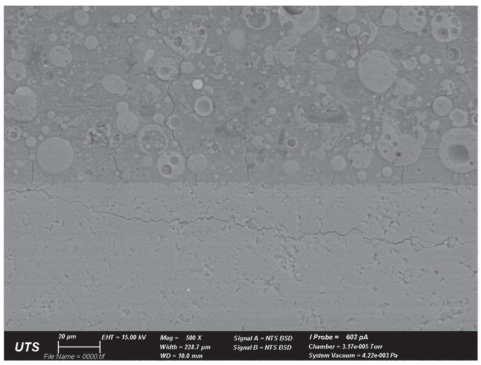

(a) Top

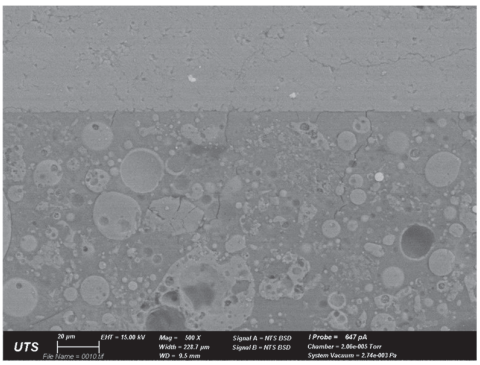

(c) Bottom

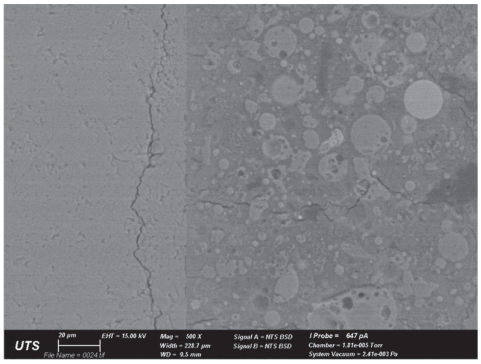

(c) Right side

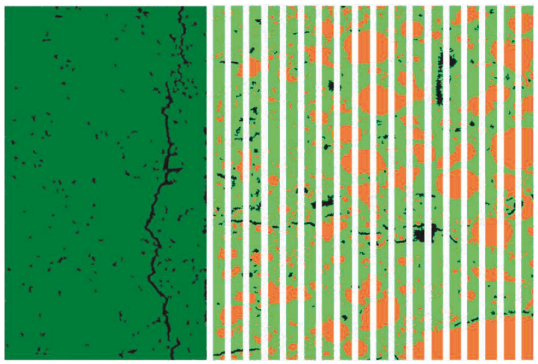

(d) Segmented image based on grey value

Figure 9.2 BSE image at different locations

BSE were operated under accelerating voltage of 15 kV and magnification of 500×. The top, bottom, left ITZ were rotated to the right side for taking BSE image, which can ensure the same length of bands for the following image analysis. The constituents of

geopolymer were identified and classified in images by grey values threshold segmentation technique. The initial 90 μm matrix adhered to modelled aggregate was divided into eighteen small bands of 5 microns. After averaging the results from fifty 500× BSE images, the proportion variation trend of constituents in consecutive bands with increased distance to aggregate was presented.

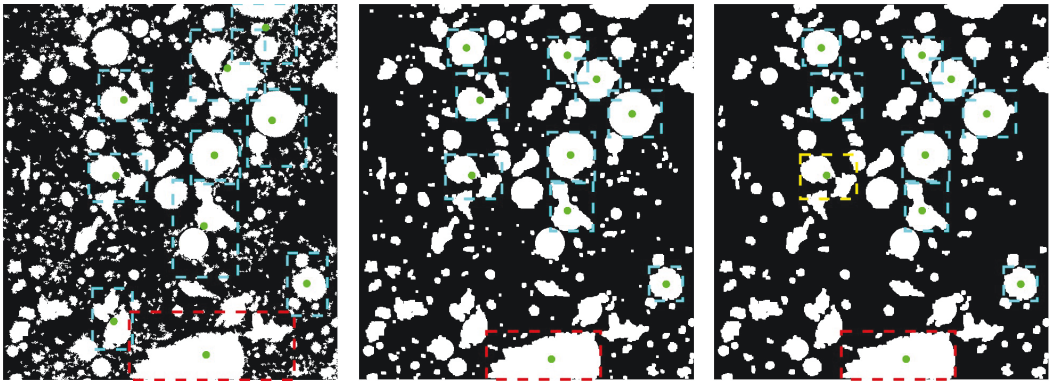

(a) Binary image (b) Morphologically open (c) Delete small areas

Figure 9.3 Image analysis of the number and diameter of fly ash

(a) Original (b) After disconnection

Figure 9.4 Disconnection of special objects

In addition, the BSE images were further processed to statistic the diameter and number of fly ash particles as shown in Figure 9.3 to Figure 9.5. The dotted rectangle is the minimum rectangle that contains the object identified and the solid dot is the centroid of the object. The largest object was marked by a red rectangle. The fly ash particles were assigned to a band according to their centroid. The properties distribution were studied in the form of 10 μm ×9 bands and 30 μm ×3 bands. The final number and equivalent diameter presented are the results based on the average of fifty images. The possible significant impact from large particles on the average results are investigated and analyzed. It shall be mentioned that the equivalent diameter of the section would underestimate the actual diameter of the three-dimensional particles (Scrivener 2004).

Thus, the results are mainly for comparison purpose. The details for the analysis and discussion of the method can be found in the author's journal paper.

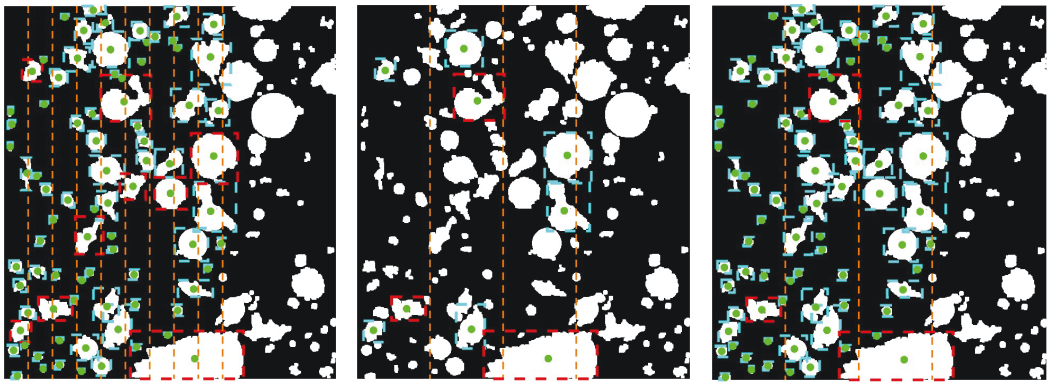

(a) 10 μm ×9 bands (b) 30 μm ×3 bands (c) 30 μm ×3 bands

Figure 9.5 Statistical of number and diameter of fly ash based on bands

9.2.3 **Nanoscratch and nanoindentation technique**

Scratch and indentation tests were performed by using the same instrument, but different tips. A Berkovich tip is used for nanoindentation test, while a hemispherically-tipped, conical stylus is adopted for scratch test to avoid errors caused by the orientation of tip. The tip radius is 20 nm and 5 μm, respectively, for nanoindentation and scratch. A comparison of these two test techniques can be found in Figure 9.6.

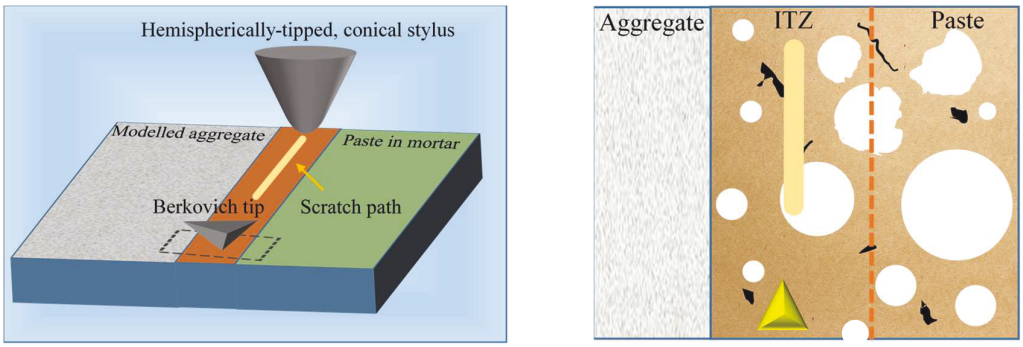

(a) Scratch and nanoindentation test on ITZ (b) Enlarged dotted area

Figure 9.6 Micromechanical properties test of ITZ in geopolymer concrete

Scratch tests were conducted under the normal force of 4 mN and scratch speed of 4 μm/s. Eighteen 100 μm scratches were randomly set along each specific type of ITZ at 15 μm away from the aggregate, while increased number of twenty-four scratches were set for

more heterogeneous bulk paste far away from ITZ at the regions without abundant large particles. The nanoindentation test is 10 μm away from the aggregate and performed under a constant depth of 1200 nm. At least 125 effective indentation data are tested from the gel zone of each test object, where large particles are intentionally avoid. Indentation tests were also performed on gel rich areas of paste far away from ITZ for comparison.

9.3 Results and discussion

9.3.1 Results from image analysis

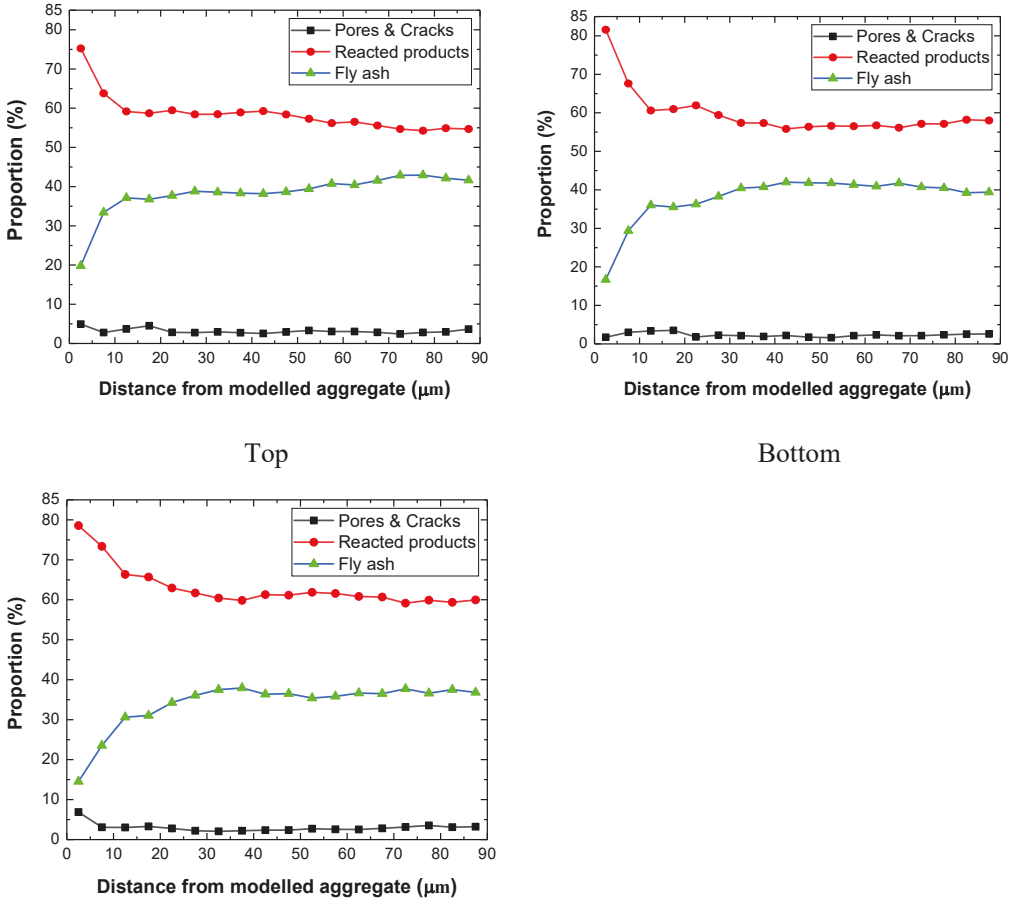

Figure 9.7 Variation in the proportion of constituents from ITZ to paste

The BSE results shown in Figure 9.7 indicate that the distribution of constituents is not the same for ITZs at different locations of the same aggregate. The proportion of fly ash

in the initial part of ITZ is higher in top-ITZ and bottom-ITZ than the left/right side-ITZ. Besides, the effects of the aggregate wall on the proportion distribution of constituents are less significant for the bottom and especially the top side ITZ.

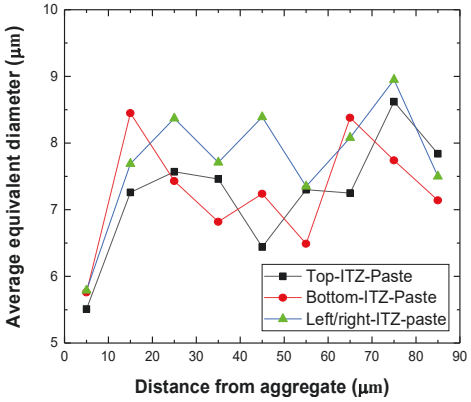

(a) All fly ash particles in each band

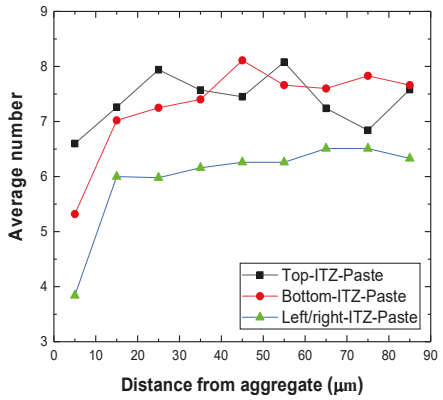

(b) All fly ash particles in each band

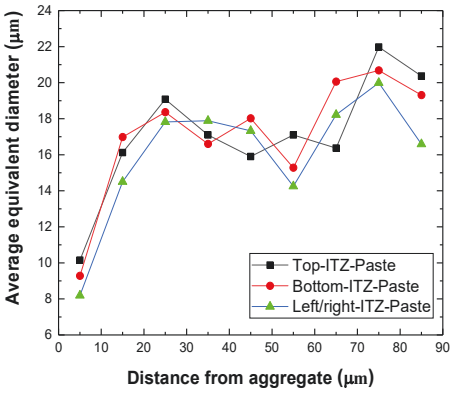

(c) The largest fly ash particle in each band

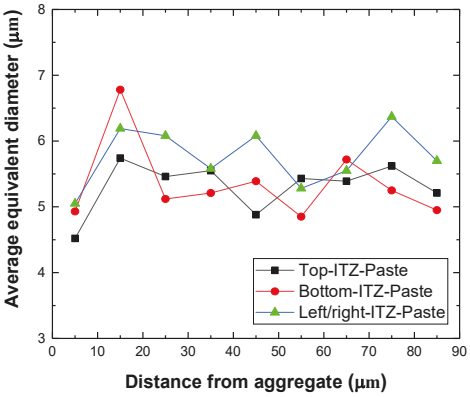

(d) After removing the largest fly ash in each band

Figure 9.8 The average equivalent diameter and number of fly ash particles in each band (10 μm × 9 bands)

The variation in number and equivalent diameter of fly ash from ITZ to paste can be found in Figure 9.8 to Figure 9.9. The small band of 10 μm is used to understand the detailed distribution, whereas it would obtain less stable results than that of 30 μm bands. As shown in Figure 9.8 (a), the results fluctuate significantly for the average equivalent diameter of all fly ash particles in each band. However, it still indicates that, after around 20 μm, the average diameter of fly ash is relatively larger in the left/right side ITZ-paste

than that of the top and bottom side ITZ-paste. A more apparent difference between samples is observed for the number of particles. The left/right side ITZ-paste always shows fewer fly ash particles than that of the top and bottom side, especially for the first band with the distance of 0 to 10 μm away from aggregate. For all these ITZ-pastes at different sides, the significantly lower diameter and number values are generally just found for the first band, although there are sometimes still increasing trends for later bands. The average diameter is around 5.51 μm to 5.79 μm in the first band and increased to the range of 6.44 μm to 8.95 μm for the later bands. Similarly, the average number of fly ash particles in the first band is 3.84 to 6.60, where the left/right side ITZ has obviously fewer particles than the top side ITZ. The average number increased to 5.98–8.11 for later bands, with the average number difference between samples at each band less than 2.

In addition to all particles, Figure 9.8 (c) and (d) show the average diameter of the largest particle and average diameter of remaining particles after removing the largest particle in each band. Compared with Figure 9.8 (a), Figure 9.8 (c) presents a more remarkable increase in the diameter of fly ash with distance. Besides the first band, the second band also has average diameters generally smaller than later bands. Both the first and second band of the left/right side ITZs show smaller diameter when compared with the top and bottom side ITZ. The above results do not mean that there are no large particles involved in this initial ITZs. The first band of Figure 9.8 (c) is generally not lower than the later bands of Figure 9.8 (a). Before averaging the results from multiple figures for Figure 9.8 (c), the largest diameter appeared is 18.97 μm, 15.27 μm, 17.06 μm in the first band and 30.23 μm, 34.59 μm, 25.67 μm in the second band for the top, bottom and left/right side ITZ, respectively. In addition, it is possible that part of the large particles is in the initial ITZ but their centroid is outside of the first several bands. The diameter/number analysis in the initial band would be more sensitive to wall effect than the proportion analysis

when the particles size is significantly larger than the band size. If the largest fly ash particle is excluded as provided in Figure 9.8 (d), the results display a less significant difference between the first and later bands than in Figure 9.8 (a).

Figure 9.9 provides the statistical results from 30 μm bands. Figure 9.9 (a) and (b) manifest that there are more fly ash particles in the top and bottom side ITZ-paste, but their average diameter is smaller than the left/right side ITZ-paste. The average diameter of fly ash in the three bands is in the range of 6.71 – 7.44 μm, 6.87 – 7.61 μm, and 7.55 – 8.09 μm, respectively for the ITZ-paste tested from different sides of aggregate. The corresponding number of fly ash ranges from 15.81 to 21.81, 18.67 to 23.17, and 19.35 to 23.09, respectively, in these bands. For the results tested from different sides of aggregate, there is a general increasing trend for both average diameter and number with the increased distance to aggregate, although deviations are also observed. The details presented in Figure 9.9 (c) and (d) indicate that the smaller average diameter of the top and bottom ITZ-paste is not caused by several large particles. Instead, the average diameter of the three largest fly ash particles of them is significantly larger than that of left/right ITZ. For fly ash in all these sides, the diameter of the three largest fly ash particles increases remarkably with the distance to aggregate, resulting in the increased average diameter in Figure 9.9 (a). Despite that the binary image for the number and diameter analysis was further filled compared with the image for area analysis, the results still reveal some similar phenomenon and can be analyzed relevantly. For the larger proportion of fly ash and less significant wall effect in the top and bottom side shown in Figure 9.7, the dominant reason should be the increased number of particles as presented in Figure 9.8 (b) and Figure 9.9 (b).

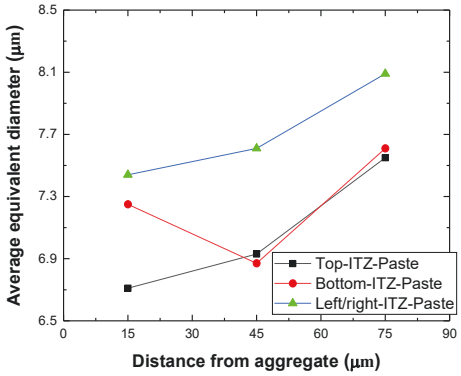

(a) All fly ash particles in each band

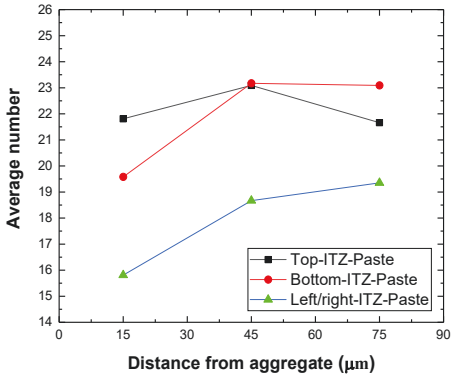

(b) All fly ash particles in each band

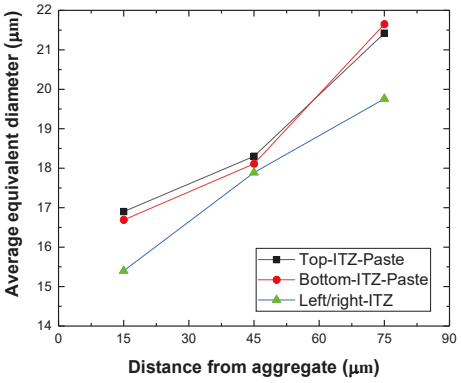

(c) The three largest fly ash particle in each band

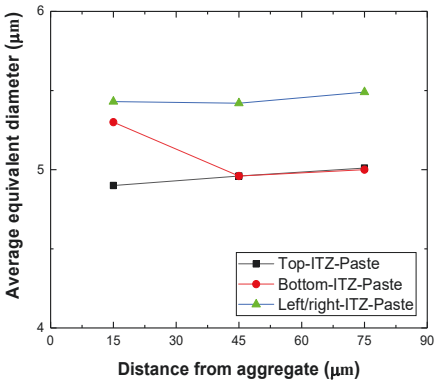

(d) After removing the three largest fly ash in each band

Figure 9.9 The average equivalent diameter and number of fly ash particles in each band (30 μm × 3 bands)

9.3.2 **Scratch results**

The scratch hardness of the paste and different ITZs based on the same small bin size of 0.15 is shown in Figure 9.10. A small number of components can facilitate comparison. However, the ITZs in the same sample may have small differences. Thus, the large number of component of 5 was used, which can match histograms well and further increase of number generally leads to spurious phases. Before analysis, hardness data more than 14 GPa are deleted. Deleting these several data does not change the results for the first several components and can decrease spurious phases as well as the effects of large value on the comparison of average value. The hardness probability density distributions were summarized in Figure 9.11. It is clear that the initial part of left/right

side-ITZ and paste curves are coincident, while bottom-ITZ and especially top-ITZ shows low probability density at this low hardness value part. The end part of the curves indicates that the top-ITZ has the highest proportion of large hardness components, while the left/right side-ITZ has the lowest proportion. These results agree well with the BSE results. The top-ITZ has more fly ash particles than others, and the ITZs from different aggregate locations have different properties.

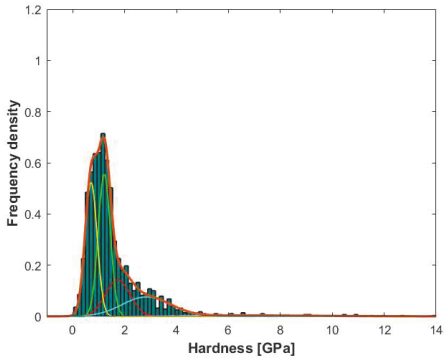

(a) Top-ITZ (mean: 1.59 ± 1.33)

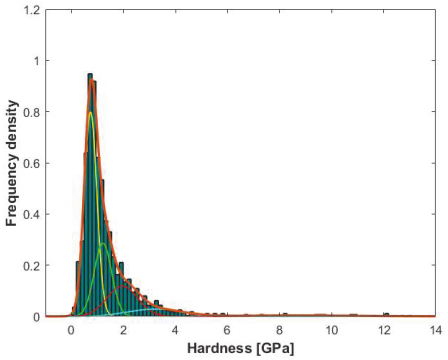

(b) Bottom-ITZ (mean: 1.44 ± 1.45)

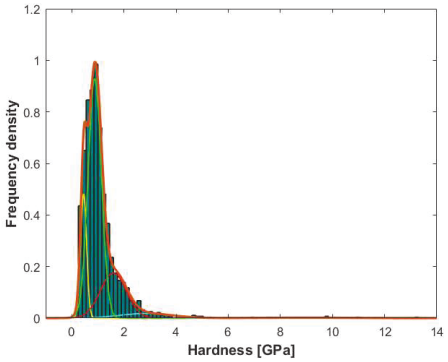

(c) Left/right-ITZ (mean: 1.13 ± 0.94)

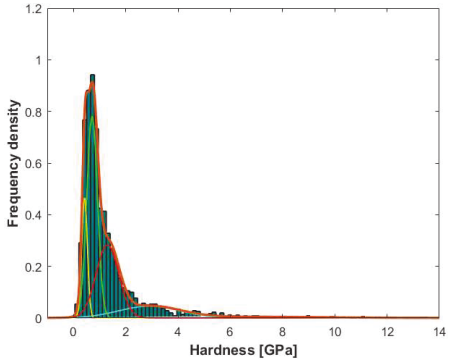

(d) Paste (mean: 1.36 ± 1.48)

Figure 9.10 Scratch hardness of different ITZs and paste

It shall be noted that paste result in Figure 9.10 (d) is not the optimal model with the maximum log-likelihood function value but the one with the second maximum value. The optimal model as displays in Figure 9.12 (a) actually match with the histogram better at the region where the hardness is larger than 2 but worse at the most prominent peak region. After increasing the number of components to 6, the model matches both regions well

with the deconvolution results at the regions similar to the corresponding better matched 5 component model as displayed in Figure 9.12 and Table 9.2.

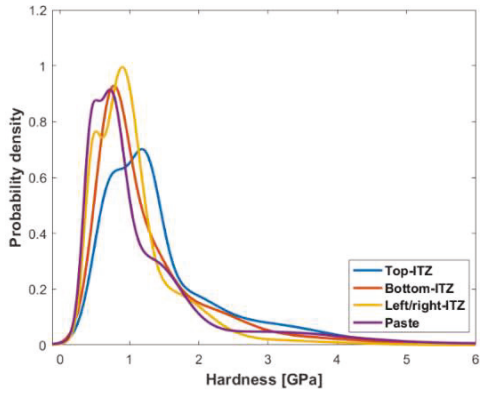

Figure 9.11 Summary of the probability density distribution of scratch hardness

Considering that other samples are all based on 5 component model and 6 components generally lead to spurious phases with a small proportion for them, the comparison study is mainly based on the 5 component model of paste that can match the peak well. The deconvolution results in Table 9.1 indicate that k_1 and k_2 are similar for the top and bottom ITZ, but just have a different proportion. Compared with the top and bottom ITZ, in addition to the component of around 0.7 GPa, the left/right-ITZ and paste show a significant component with a small hardness of around 0.4 GPa. This small hardness phase exists merely in paste and the left/right ITZ should be formed by test points on low strength products, for instance, porosity gel. There is a component with an average hardness of around 0.7 GPa for all samples as provided in Table 9.1, which is within the big peak of histogram as shown in Figure 9.10. It may correspond to the mixed phase that is primarily reacted product gel. The later components would be more and more affected by crystals and fly ash. It shall be noted that abnormal points in the previous nanoscale indentation study of geopolymer matrix has been removed. That is why only near 800 valid test points were mentioned is a test before. The scratch data here still contains defects related points. Beside, for the scratch test with a tip of several microns, the smaller

hardness value means larger test depth, which is inevitably accompanied by increased interactions. Thus, the smallest hardness should not be from purer gel phase as that of nanoscale indentation study.

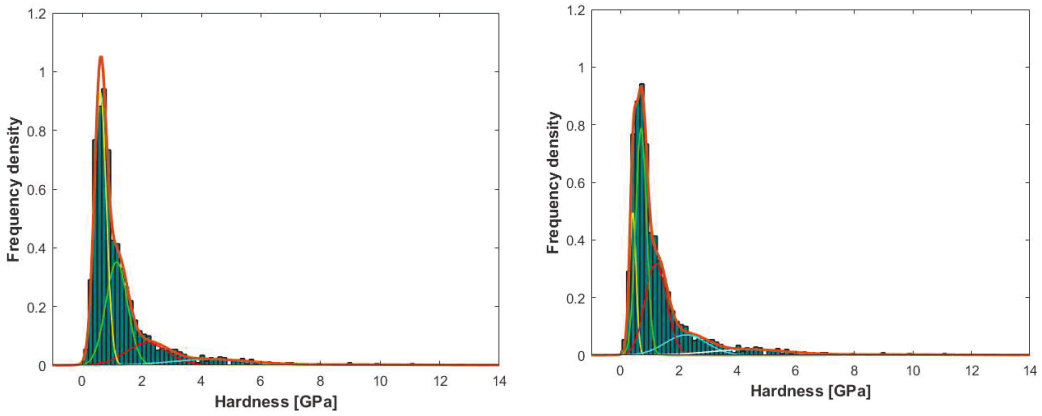

(a) k is 5 (b) k is 6

Figure 9.12 The optimal model for paste with 5 and 6 components

Table 9.1 Deconvolution results for hardness probability density distribution

Test objects		k_1	k_2	k_3	k_4	k_5
	$\mu \pm \sigma$	0.71 ± 0.23	1.22 ± 0.23	1.74 ± 0.47	2.83 ± 0.93	6.91 ± 2.88
Top-ITZ	f	30.34%	32.54%	16.84%	17.58%	2.70%
Bottom-ITZ	$\mu \pm \sigma$	0.73 ± 0.24	1.21 ± 0.34	1.96 ± 0.59	3.21 ± 1.04	8.64 ± 2.49
	f	48.58%	24.08%	17.53%	7.42%	2.38%
Left/right-ITZ	$\mu \pm \sigma$	0.46 ± 0.11	0.88 ± 0.25	1.59 ± 0.50	2.84 ± 1.00	8.93 ± 1.83
	f	13.80%	59.21%	21.78%	4.48%	0.73%
paste	$\mu \pm \sigma$	0.43 ± 0.11	0.71 ± 0.20	1.30 ± 0.43	2.89 ± 1.17	6.61 ± 2.98
	f	12.47%	39.89%	30.65%	13.36%	3.64%

Table 9.2 Optimal results for GMM models with increased number of components

Test objects		k_1	k_2	k_3	k_4	k_5	k_6
Paste_5	$\mu \pm \sigma$	0.61 ± 0.20	1.16 ± 0.36	2.18 ± 0.70	4.28 ± 1.33	8.82 ± 2.81	–
	f	46.67%	32.01%	13.14%	6.60%	1.59%	–
Paste_6	$\mu \pm \sigma$	0.42 ± 0.11	0.70 ± 0.19	1.21 ± 0.37	2.24 ±0.71	4.34 ± 1.31	8.84 ± 2.80
	f	13.74%	36.70%	29.23%	12.42%	6.33%	1.58%

9.3.3 **Nanoindentation results**

The nanoindentation test aims to provide test results for both hardness and elastic modulus. Large indentation depth is adopted to activate large involved range and more homogeneous properties of ITZ. The fly ash particles are intentionally avoided in test to decrease interference from these large hardness components. The results presented in Figure 9.13 represent the properties of mixed phase containing gel and small size fly ash particles/crystals, which should correspond to the gel-related phase in the deconvolution analysis of scratch. It is obvious that these two techniques indicate similar conclusion although the values are not close due to the different indenter and degree of involvement of other phases. The top and bottom ITZ have similar k_1 but just different proportions in the scratch test. It should be the reason for the close elastic modulus and hardness value obtained by nanoindentation as presented in Table 9.3. Different from the top and bottom ITZ, scratch results indicate that the left/right ITZs and paste have a considerable amount of a small hardness phase. The nanoindentation at large penetration depth would detect them and hence result in low average micromechanical properties. Both investigations

indicate that the properties of ITZ are different at different locations surrounding the aggregate, and all ITZs are not inferior to the bulk paste.

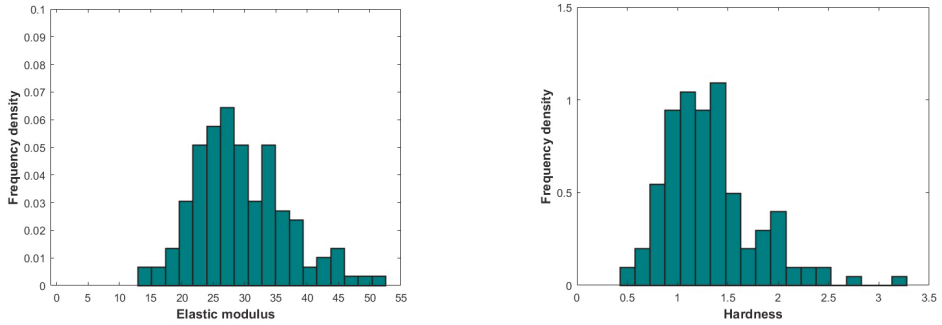

(a) Top

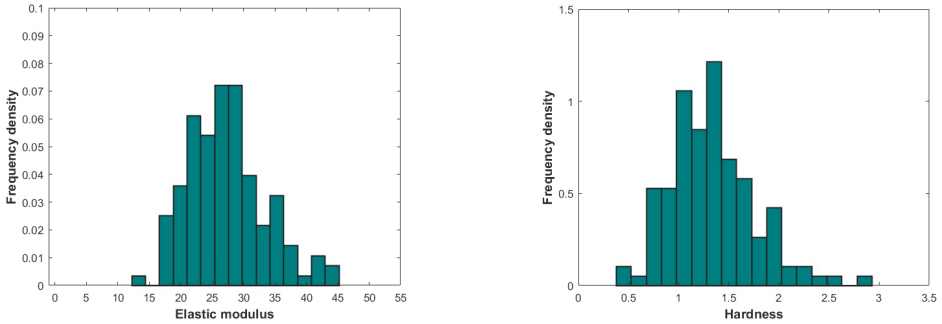

(b) Bottom

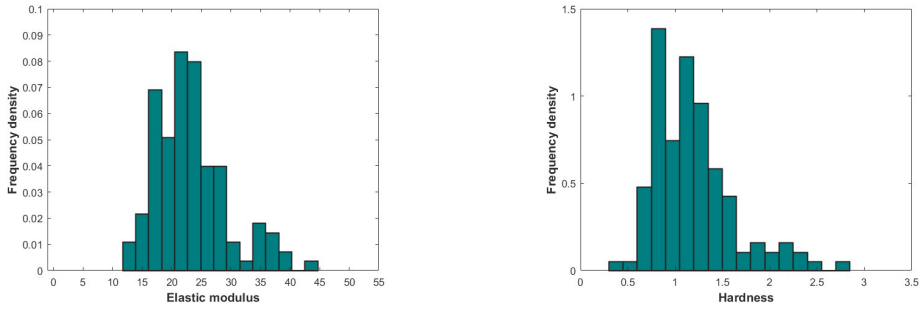

(c) Left/right side

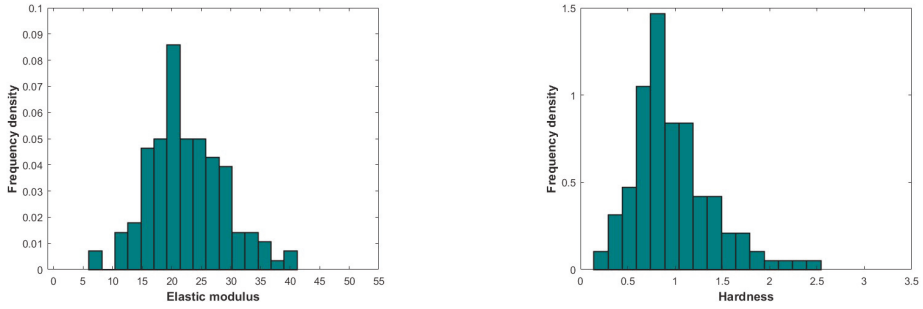

(d) Paste

Figure 9.13 Elastic modulus and hardness of ITZs investigated by nanoindentation

Table 9.3 Nanoindentation test results for ITZs and paste

Test objects	*M* (GPa)	*H* (GPa)
Top-ITZ	29.39 ± 7.35	1.32 ± 0.46
Bottom-ITZ	27.31 ± 6.13	1.33 ± 0.43
Left/right-ITZ	23.24 ± 6.02	1.19 ± 0.43
Paste	22.55 ± 6.40	0.98 ± 0.42

9.3.4 **Mechanisms of different properties of ITZs surrounding aggregate**

There is sometimes internal bleeding in Portland cement concrete. Water is separated from the water-cement-aggregate mixture and accumulates under aggregate particles. In this case, the especially high water content would make the bottom ITZ of aggregate in Portland cement concrete has relatively low properties (Mehta & Monteiro 2017). Owing to the high viscosity of alkali-silicate solution, the same situation would be harder to occur in the geopolymer concrete. However, the slight segregation of alkali-silicate solution and fly ash caused by their different flowability and density would be still able to cause the microscale difference of ITZ around the "wall" provided by aggregate particle. As shown in Figure 9.14, during the vibration process, the aggregate due to large gravity would drop at least at microscale and squeeze the matrix below it, which drains more proportion of flowable alkali solution and left more fly ash particles at the bottom ITZ. Because of the general followed heat curing and the resulting quick setting, the viscous alkali-silicate solution would be hard to gather to the bottom side again. Besides, the matrix above the aggregate would also drop correspondingly and contact closely with the aggregate as a result of gravity. The continuous vibration would make the solids like fly ash accumulate on top of the aggregate. Therefore, fly ash particles in both the top and bottom side ITZ and paste near ITZ become close to the aggregate after vibration. It is manifested in the

increased proportion shown in Figure 9.7 and the increased number of fly ash particles shown in Figure 9.8 (b) and Figure 9.9 (b) compared with the left/right ITZ and paste.

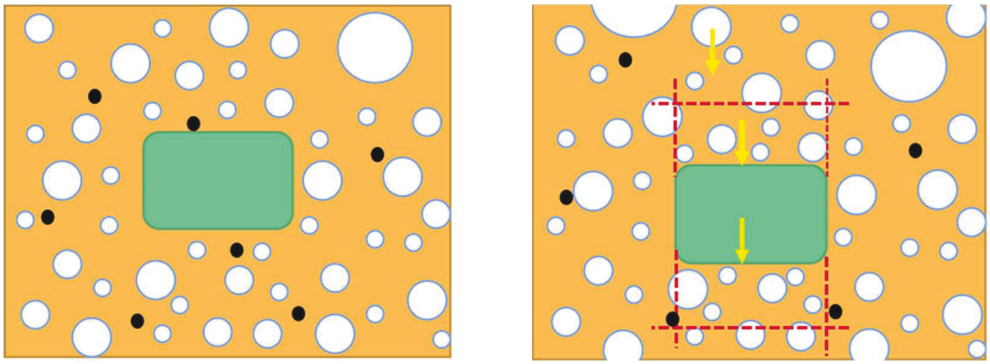

(a) Before vibration (b) After vibration

Figure 9.14 Accumulation of particles and intensified structure at the top and bottom side

Despite the high solution to solid ratio in ITZ of geopolymer, the sodium silicate-based alkali solution would not greatly evaporate like water. Besides, due to the gravity and falling of aggregate and binder above aggregate, the vibration process would contribute to the compaction of binder near the bottom and top of the aggregate. The local compaction may be able to remove some bubbles and lead to intensified structure for the top and bottom ITZ, while the bubbles of the viscous mixture may be harder to be eliminated in the bulk paste via vibration. Therefore, it could lead to a higher strength of top and bottom ITZ than the bulk paste and left/right ITZ. In addition, the results in Fig. 9.8 (b) indicate that besides the first 10 μm of bottom ITZ, the number of particles in the top and bottom ITZ is more than the left/right paste, where the left/right paste far from aggregate should be similar to bulk paste. In fact, the experiment results do not reflect reacted small particles. Besides, the section method would underestimate the number of small particles due to less change to meet them (Scrivener 2004). Even assuming that the original small particles are uniformly distributed in the ITZ and paste, the accumulation of fly ash on the top and bottom side ITZ due to vibration should still make the

corresponding ITZ have a higher amount of small size particles than bulk paste. The more small particles with higher activity in top and bottom ITZ may lead to a higher reactive degree. In bulk paste, the growth of products is limited by unreacted particles. In ITZ, the results from the section method shown in Figure 9.7 indicate that the top ITZ and bottom ITZ with a distance of more than 10 μm from aggregate already have a similar or larger amount of unreacted particles compared with the left/right paste far from aggregate, namely, bulk paste. In addition to particles, the stiff aggregate wall would restrict the growth of products in ITZ. Thus, for these ITZs already subjected to local compaction, the possible high degree of reaction in limited space may further densify the structure. In terms of the left/right side ITZ, the results in Figure 9.8 (a) and (d) indicate that the smaller average diameter of the first band than later bands may be more affected by the large particles. The average number of fly ash in the first several bands of left/right ITZ shown in Figure 9.8 (b) is also lower than in later bands. Thus, the left/right side ITZ may not have a significantly higher amount of small size particles than bulk paste. At least, it would not be significant as that in the top and bottom ITZ. The above two mechanisms may work together and lead to the higher mechanical properties of the gel related phase in the top and bottom ITZ than the left/right side ITZs and bulk paste as revealed by both scratch and indentation tests.

It is a fact that if the test is on the ITZ of an aggregate particle in real concrete, the conclusion would vary with the particle used for testing. Besides, there are sometimes test biases hard to avoid for nature aggregate as will illustrate in the next section. Thus, this investigation is based on a simplified condition with only one coarse aggregate embedded in the mortar matrix to obtain a representative result. For the phenomenon and possible mechanisms obtained in this study, they should still exist in the real concrete, but the degree would depend on many factors. Real concrete contains more aggregate

particles, which have diverse orientations, shapes and sizes. Typically, the phenomenon should be more significant when the surface of some crushed stone particles that most tends to be flat or concave is on the top side instead of the left/right side. The different vibration method, and different flowability and viscosity of the matrix should also be significant influential factors.

9.3.5 Nano/micromechanical testing strategies for complex ITZ

The ITZ in real concrete has a three dimensional and complex structure. Nano/micromechanical testing needs to be conducted on polished section sample. Even in this case, the ITZ is still highly heterogeneous. The heterogeneity of ITZ in a section concrete sample could be simply understood from three increased levels where the higher level contains the lower level. Firstly, for a local region, ITZ consists of different micro-constituents. The properties of each type of micro-constituent could also be variable. Then, for an aggregate particle, the properties of surrounded ITZ are different between different local regions. In terms of the polished regular aggregate in this research, it can be understood from the two aspects of the difference of ITZ in different sides of the aggregate such as top, bottom, etc., and the inner difference of ITZ in a specified side. Finally, the different aggregate particles in the same concrete sample would have different ITZs. In an investigation, it is challenging to conduct as many tests that can overcome the level three heterogeneities and obtain the overall ITZ properties in a concrete sample. Owing to the small test scale, micro to nanoscale tests would even be significantly affected by the level one heterogeneity. The limited test on the inhomogeneous object would make the results only local properties, which sometimes may be highly variable and lead to unreliable conclusions. Depending on the research purpose, a feasible investigation can be realized by strategies such as decreasing the complexity of the tested concrete system and improving existing test efficiency.

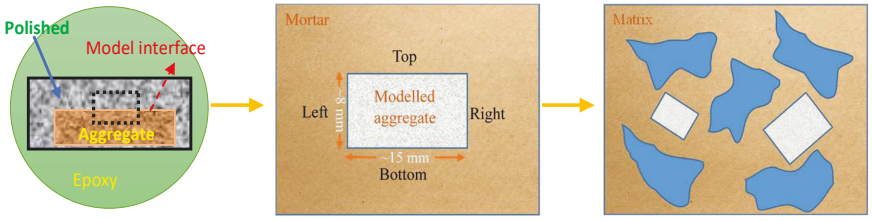

(a) Level I and partial II (b) Level II (c) Level II

Figure 9.15 Different heterogeneity of ITZ provided by modelled samples

The heterogeneity for modelled ITZ samples in chapter 7 and 8 can be treated as level one and partial II. The low complexity system allows a quick comparison of ITZs formed by different cementitious materials. It is especially meaningful when the test techniques are impossible to overcome the high heterogeneity that would significantly interfere with the comparison results. However, the simplified sample just provides basic ITZ information. In this study, the heterogeneity was increased to level two, which reveals that the top, bottom and left/right side ITZ have different properties. Above this level, the ITZ surrounding different aggregate particles after mixing would be highly complex since it is affected by far more factors such as the difference in local mix state, aggregate characteristics (shape, size, etc.), and distance between aggregates.

The nanoindentation test in conventional instrument takes several minutes for a single point. Despite faster tests, the test by modulus mapping and PeakForce QNM are limited to very small test areas. When aims to deeply understand the properties of complex ITZ in concrete or wants to incorporate more ITZ information for comparison, it is necessary to find more efficient testing strategies to cope with the largely increased workload. The modelled aggregate has a regular linear boundary, making it possible to apply the line scan technique, nanoscratch to test the ITZ. Nanoscratch is able to obtain massive test points from a long range in a very short time. For the investigation of a given long range of ITZ, the total time (testing, data analysis/image segment and statistic, etc.) needed for

scratch technique is even lower than BSE. Thus, scratch technique combined with regular polished aggregate is a potential method to provide information for evaluating more complex ITZ with acceptable time-consuming. Meanwhile, nanoindentation can be used to investigate the relatively important regions of the same sample or a more simplified modelled sample with the same binder for both hardness and modulus. Nanoindentation and mechanical mapping techniques above can verify the results of critical individual phases provided by scratch and provide richer and more accurate information.

The relatively complicated ITZ systems can be constructed with some real aggregate particles and a certain proportion of polished aggregate particles. They can be mixed like normal concrete. The polished aggregate within the system can be used as test objects for quick mechanical information acquisition of ITZ. It shall be noted that the orientation of aggregate would change after mixing. Compared with the modelled aggregate perpendicular to the exposed test surface, the inclined modelled aggregate would be closer to the test surface on one side, which may result in constraint effect for the micromechanical penetration test. In addition, the section method for inclined aggregate would overestimate the actual width of ITZ because the apparent ITZ obtained is not from the planes perpendicular to the aggregate (Zhu & Chen 2017). Correspondingly, the micromechanical test location on apparent ITZ surrounding the inclined modelled aggregate would correspond to the real ITZ that has a closer distance to aggregate, as revealed in Figure 9.16. In addition, the involved ITZ in the penetration direction will have a continuously changed distance to aggregate. Small force and depth as that in scratch can decrease the negative impact, but not all. For natural aggregate, the complex shape would cause or exacerbate similar test biases, making them almost unavoidable. For regular modelled aggregate, the biases can be removed by testing aggregates with only small inclinations. A typical method is to use non-destructive three-dimensional

imaging techniques such as X-ray computed tomography (CT) (Liu et al. 2017). Based on the known distribution of aggregate, another cutting may be applied to find a test surface with more qualified aggregate particles. It may also be feasible to identify the orientation based on multiple cuts and the variation of section size of regular aggregate with known size. For the nanoscratch in a complex system, it must have many scratches even in a given side to cover the heterogeneity, especially when wants to reflect the difference in the proportion of constituent (e.g. fly ash) between samples.

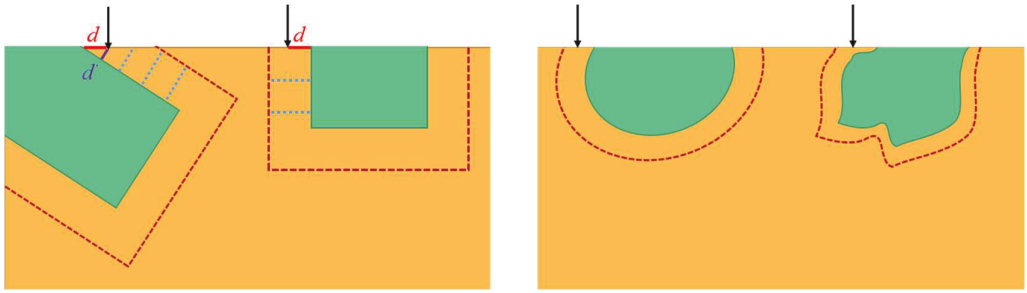

(a) Modelled aggregate (b) Natural aggregate

Figure 9.16 Test biases for significantly inclined modelled aggregate and natural aggregate (Side view)

The polished aggregate would be different from natural aggregate, although it does not violate the specifications for using aggregate. Given that the current nano/micromechanical testing techniques are generally not even able to efficiently evaluate the ITZ around a single real coarse aggregate particle, this method could be at least used to overcome the high heterogeneity and provide some useful information for complex ITZ. Especially that, most of the research is to compare ITZ formed by different binders. The surface of the tested aggregate is equally simplified in both samples, which may not significantly affect the comparison conclusion and would have higher accuracy than the comparison based on insufficient local properties. In addition to nanoscratch, the polished surface also facilitates other research such as the BSE image segmentation

analysis, EDS line scan and grid nanoindentation test of ITZ. The complexity of the tested ITZ can be controlled by adjusting the amount of aggregate and variable parameters given to modelled aggregate such as size, shape, etc. In a more complicated case, the natural aggregate with few small polished surfaces may be tried for testing.

9.4 Conclusions

In this chapter, the properties differences of ITZs at different locations of aggregate and the related mechanism are investigated and analyzed. Besides, the test biases and test strategies for more complex ITZ are discussed. The properties of ITZs surrounding aggregate should depend on many factors such as the matrix used, the main conclusions based on the given sample are drawn up as follows:

(1) The top and bottom side ITZ-paste present a higher proportion and number of fly ash than the left/right side ITZ-paste, which makes the disrupted distribution of fly ash particles caused by aggregate become less obvious. Besides top ITZ-paste, the average number of fly ash particles generally presents an increasing trend with the increased distance to aggregate, while the left/right side paste around 90 μm away from aggregate still has fewer particles than even the initial 0-10 μm of top ITZ and 10-20 μm of bottom ITZ.

(2) For all ITZs, the average diameter of fly ash particles is significantly low in the initial 0-10 μm ITZ. The average diameter is around 5.51 μm to 5.79 μm in the first 10 μm band and increased to the range of 6.44 μm to 8.95 μm for the later bands. The results from 30 μm bands show that the left/right side ITZ has a higher average diameter of all fly ash particles but a lower average diameter of the three largest fly ash particles than the top and bottom ITZs. The increase of diameter with distance from aggregate is primarily caused by the several largest fly ash particles.

(3) Compared with the top and bottom ITZs, the deconvolution of scratch results indicate a significant low hardness component in the left/right side ITZ and bulk paste. The nanoindentation tests obtain similar results that the top and bottom ITZ have higher elastic modulus and hardness than the left/right side ITZ and bulk paste. The indentation elastic modulus and hardness range from 22.55 to 29.39 GPa and 0.98 to 1.32 GPa, respectively, where the top ITZ achieves the highest value and paste achieves the lowest value. The micromechanical properties of the left/right side ITZ are close to and slightly larger than that of bulk paste.

(4) The alkali-silicate solution would have a low degree of evaporation and hence may not lead to a particular high porosity in ITZ. Aggregate and fly ash have a larger density than the solution. The vibration would result in the drop of large size aggregate, which squeezes the binder below it. The binder above aggregate would drop correspondingly. The vibration process leads to local compaction and intensified structure for the top and bottom side binder. This process is also accompanied by the accumulation of fly ash, while the increased small size particles with high activity is also a possible reason for enhanced micromechanical properties at the top and bottom ITZ.

(5) For the micromechanical investigation of ITZ and especially comparison study of ITZs between samples, insufficient test points on highly heterogeneous ITZ may sometimes lead to less reliable results. In addition, there are sometimes biases for micromechanical test on ITZ. The heterogeneity of ITZ in a section sample that would interfere with studies was simply classified into three increased levels. A strategy proposed is to control the complexity of ITZ and use more efficient testing techniques such as the combination of polished aggregate and fast scratch technique.

CHAPTER 10. CONCLUSIONS AND RECOMMENDATIONS

10.1 Summary and conclusions

The fundamental aspects of geopolymer concrete are investigated in this thesis via nano/micromechanical related multiple characterization techniques such as nanoindentation, nanoscratch, SEM (SE; BSE; EDS), etc. In addition to understanding the properties and mechanisms of geopolymer concrete, the significance of this study is expanded by the novel research methods proposed for the nano/micromechanical investigation of highly heterogeneous materials as well as the suggestions and enlightenments for the selection of testing techniques in different types of research.

Based on the study of geopolymer paste by SNT, the main conclusions can be drawn as follows:

(1) The MLE method has significant advantages over the LSE method for deconvolution analysis. When using the MLE method, the process of separating stable N-A-S-H gel from mixed phases can be intuitively observed. Moreover, nanoindentation data can be clustered to corresponding components with a good match, which allows for further analysis. Compared with the LSE method, the MLE method is independent of distribution histogram, less sensitive to the number of test points, and able to determine the component numbers more reasonably. For some phases (e.g. N-A-S-H gel) in highly heterogeneous materials, they do not always show as a distinct peak in the histogram and are easy to be mixed into identifiable large peaks, which means that even if the bin size used is small enough their properties are still hard to be obtained by the LSE method.

(2) The MLE method can be related to the LSE method by histogram. When increasing

the number of phases in the Gaussian mixture model, there are frequency distribution histograms with decreased bin sizes that can match them. Increasing the number of components enables the model to reflect more details of the distribution of the collected data, while bin size plays a similar role in the histogram. Different from the MLE method where multiple parameters could be referenced to determine the gel phase in a few models, the appropriate bin size is practically impossible to be determined from the infinite range of values for the LSE analysis.

(3) Mixed phases and sub-phases are typical spurious phases in the deconvolution of highly heterogeneous materials, which are caused by the nature of the sample, the test factors and the deconvolution parameters (number of components for MLE). It is virtually impossible to reconcile these two kinds of spurious phases to obtain the accurate micromechanical properties of all real component in geopolymer by statistical nanoindentation. Thus, a compromise approach is proposed. It generates stable deconvolution results for gel nano/micromechanical properties with very small errors. However, the SNT technique is found to have low accuracy for volume evaluation of phases owing to a small number of test points and exclusion of multiply phase interaction data during deconvolution.

(4) The elastic modulus and hardness of N-A-S-H gel in geopolymers with different design parameters studied are in the range of 10.50 ~ 15.46 GPa and 0.40 ~ 0.73 GPa, respectively. The lowest values were from the NaOH activated sample (heat curing 24 hrs) with the Na_2O/fly ash ratio of 8% and water to solid ratio of 0.338, while the highest values were from the Na_2SiO_3 activated sample (heat curing 24 hrs) with the silica modulus of 1, Na_2O/fly ash ratio of 10% and water to solid ratio of 0.338. The gel in the geopolymer sample without heat curing also shows low mechanical properties close to that in the NaOH activated sample.

(5) The variation of nano/micromechanical properties of gel would be affected by both the gel particles' mechanical properties and the nanoscale pores between them. The formal one would be determined at least by its maturity and chemical structure. Owing to the intermixing of unreacted particles and micro to nanoscale crystalline phases such as mullite and quartz with gel, the N-A-S-H gel obtained by deconvolution generally has a small proportion. Compared to C-S-H, the looser structure of N-A-S-H should be one of the reasons for its inferior micromechanical properties.

(6) The presence of both nano-SiO_2 and nano-TiO_2 particles increase the early reaction rate in geopolymer, while the reaction degree of different samples in the later age is not vastly different. The gel contents in 28 days geopolymer and nano-geopolymers vary in a small range of 49.16% to 54.02%. With the addition of both types of nanoparticles, the compressive strength of geopolymer and the micromechanical properties of N-A-S-H gel were increased. NS exhibited higher reinforcement effect than NT on macro-strength. However, NT more significantly enhanced gel micromechanical properties.

(7) Gel particles packed by around 5 nm globules are typically observed to have a size of more than 30 nm, similar to the size of well-dispersed nanoparticles. Nanoparticles integrate with gel particles to form a composite with higher mechanical properties. Nanoparticles have higher mechanical properties (highest for NT) but a much lower proportion than the gel particles, leading to slightly higher micromechanical properties of gel in nano-geopolymers obtained by SNT. Nano-SiO_2 is more compatible with sodium silicate solution and gel particles, resulting in better dispersion and bonding, then a higher macro strength of Geo-NS than Geo-NT.

Based on the study of ITZ between geopolymer paste and aggregate by nanoscratch, nanoindentation and microstructure characterization techniques, the main conclusions can be drawn as follows:

(1) ITZ is highly heterogeneous in concrete. The conventional method of randomly selecting several small ITZ test areas in concrete just reflects local properties, which could be highly variable. In addition, the workload for massive nanoindentation tests to obtain the overall ITZ properties of a concrete sample is too heavy to complete. Modelled ITZs prepared can greatly reduce the heterogeneity of ITZ for comparative study and can provide neat boundaries to ensure the precise nanomechanical testing of ITZ.

(2) The heterogeneity of ITZ in a section concrete can be categorized into three levels, namely, the local region heterogeneity, the heterogeneity of ITZ surrounding an aggregate particle and the heterogeneity of ITZ surrounding different aggregates. Depending on the research purpose, modelled aggregate can control the heterogeneity to different levels for investigation. To understand ITZ properties in a complex system, quick nanoscratch combined with statistical techniques and polished modelled aggregate particles is a promising method to overcome the high heterogeneity with acceptable time-consuming.

(3) At the macro scale, geopolymer shows better bonding to aggregate than PC by abundant residual paste on aggregate surface and significantly large bonding force. At the micro scale, nanoindentation test with a depth of 1200 nm indicates that the elastic modulus and hardness of ITZ in geopolymer are 1.21 and 1.18 times that of the bulk paste. These ratios are 1.07 and 0.91 for PC. The width of ITZ in geopolymer is found to be slightly larger than ITZ in paste. Geopolymer at the indentation test scale has a slightly lower elastic modulus but an evidently higher hardness compared to PC.

(4) Both macro bonding and nanoindentation tests indicate that the ITZ is not a weak region of geopolymer. SEM observations show that there is a large amount of CH crystal on the ITZ of PC, while a layer of dense gel-rich paste formed on the initial interfacial zone of geopolymer. For geopolymer, except for the possible zeolite at the ultra-fine size of several nanometres, its crystals are not newly formed, but from the raw material fly ash. Wall effect decreases fly ash particles and their crystals in the vicinity of the aggregate. In addition, water just accounts for a small proportion of the solution. The increase in water content in ITZ is small and would not be able to overcome the inhibition of crystallization from the soluble silicate in the sodium silicate solution. The mechanism analysis indicates that crystals and even porosity are not the dominant factors affecting the ITZ properties of geopolymer concrete as that in PC concrete.

(5) Mix ratios parameters such as silica modulus have important effects on the relative properties of ITZ to paste. BSE image statistical analysis indicates that ITZ caused by wall effect is more distinct in geopolymer composite with silica modulus of 1 than the geopolymer with silica modulus of 1.5. ITZ in both samples exhibits dense microstructures and is more uniform than geopolymer paste. ITZ and paste of geopolymer with silica modulus of 1.5 show very close scratch hardness of around 0.95 GPa for the gel related phase. For geopolymer with silica modulus of 1, defects make the paste has significant lower scratch hardness but higher scratch friction coefficient than ITZ. Thus, both BSE and nanoscratch results indicate that high silica modulus 1.5 could make the geopolymer achieve more uniform properties.

(6) The properties of ITZ surrounding an aggregate particle vary with the locations. For the geopolymer sample studied, top and bottom ITZ show less significant wall effect than the left/right side. In addition, both the top and bottom ITZ have higher micromechanical properties than the left/right side ITZ and paste. Compared with water in PC concrete, the

viscous alkali-silicate solution in geopolymer is relatively harder to separate from reactive particles (fly ash) and accumulate under aggregate particles. The vibration process would lead to the consolidation of the contact between the aggregate and matrix at the top and bottom side and the accumulation of fly ash particles. The left/right side matrix is less affected by the wall provided by aggregate during vibration. Thus, it presents a different interfacial constituent distribution. Instead of the bottom side, the left/right side is the weakest ITZ region of an aggregate particle in geopolymer. Even for the weakest ITZ, its properties are still not lower than the paste.

10.2 Recommendations for future work

The current understanding of nano/microscale mechanical properties and structure of geopolymer is still far from sufficient. The advantages of advanced nanomechanical testing techniques also have not been fully utilized in the research of materials. To promote the above two aspects, a key point lies in the proper application of nanomechanical testing techniques with the consideration of the characteristics of material microstructure. As a matter of fact, there is no solid foundation for the use of nanomechanical testing techniques in cement-based materials. Even for the most used nanoindentation technique, there are still issues to be solved. Great efforts are still needed in some basic aspects, which are recommended as follows:

(1) The interaction range is reported as 3-4 times of the penetration depth, which is the basis of the 1 μm^3 involved volume adopted in the virtual nanoindentation experiment to examine the validity of SNT. However, the 3-4 times relationship is obtained from FE simulations with very simple conditions. A more precise investigation could be conducted by using image-based simulation. High-resolution SEM image could reflect the micro to nanoscale structure of gel, which is sometimes embedded with particles/crystals. The

mechanical properties of the gel globules and crystals could be obtained by atomistic simulations and atom force microscope. By giving the properties to the SEM image and upgrading the image to 3D for nanoindentation simulation, the results can examine if it is possible that the presence of a small number of small inclusions within the 1 μm strain energy density field range of the gel phase does not significantly change the mechanical properties detected by nanoindentation. The result can reveal whether there are excessive concerns about using SNT in cement-based materials.

(2) Establish criteria and theoretical foundation for nanomechanical testing techniques in cement-based material research and further explore their novel application. Typically, for the ITZ research of geopolymer, the initial part of ITZ is of great significance. PeakForce quantitative nanomechanical mapping and modulus mapping with small penetration depth show great advantages. They can be used to test the part of ITZ less than 1 μm from the aggregate surface. However, for applying these techniques, it is necessary to specify the criteria for specimen preparation and testing. By considering size effect, strain rate effect, etc., the relationship of results obtained by different nanomechanical testing techniques are expected to be established.

(3) Raw materials of alkali-activated materials are sometimes industry by-products such as fly ash and slag, which have significantly different chemical components in different factories. In addition, there are more mix design parameters for alkali-activated materials than Portland cement materials. Alkali-activated fly ash geopolymer generally needs heat curing, which is also a changing factor in different studies that would lead to distinct performance. Thus, the macro and nano/microscale properties of geopolymer concrete would be more variable than Portland cement concrete. More studies are necessary to extend the understanding of geopolymers under various conditions.

(4) The nanoscale packing density of N-A-S-H gel can be investigated in the future based on atomistic simulations and micromechanical models. In addition, further studies can be conducted to obtain the precise mechanical properties of various crystals and fly ash particles. Micromechanical models can then be established to predict the macroscopic homogenized properties such as modulus according to the mechanical properties of individual constituents. The model would guide the design of raw materials and mixing ratio to form microconstituents that corresponds to concrete with high performance.

REFERENCES

Abbasi, S.M., Ahmadi, H., Khalaj, G. & Ghasemi, B. 2016, 'Microstructure and mechanical properties of a metakaolinite-based geopolymer nanocomposite reinforced with carbon nanotubes', *Ceramics International*, vol. 42, no. 14, pp. 15171-6.

Adak, D., Sarkar, M. & Mandal, S. 2017, 'Structural performance of nano-silica modified fly-ash based geopolymer concrete', *Construction and Building Materials*, vol. 135, pp. 430-9.

Akono, A.-T. 2016, 'Energetic size effect law at the microscopic scale: application to progressive-load scratch testing', *Journal of Nanomechanics and Micromechanics*, vol. 6, no. 2, p. 04016001.

Akono, A.-T., Chen, J. & Kaewunruen, S. 2018, 'Friction and fracture characteristics of engineered crumb-rubber concrete at microscopic lengthscale', *Construction and Building Materials*, vol. 175, pp. 735-45.

Akono, A.-T., Reis, P.M. & Ulm, F.J. 2011, 'Scratching as a fracture process: From butter to steel', *Physical review letters*, vol. 106, no. 20, p. 204302.

Allison, P.G., Weiss Jr, C., Moser, R.D., Diaz, A., Rivera, O.G. & Holton, S.S. 2015, 'Nanoindentation and SEM/EDX characterization of the geopolymer-to-steel interfacial transition zone for a reactive porcelain enamel coating', *Composites Part B: Engineering*, vol. 78, pp. 131-7.

Alomayri, T. 2019, 'Experimental study of the microstructural and mechanical properties of geopolymer paste with nano material (Al_2O_3)', *Journal of Building Engineering*, vol. 25, p. 100788.

Andrew, R.M. 2019, 'Global CO2 emissions from cement production, 1928–2018', *Earth System Science Data*, vol. 11, no. 4.

Asgari, H., Ramezanianpour, A. & Butt, H.-J. 2016, 'Effect of water and nano-silica solution on the early stages cement hydration', *Construction and Building Materials*, vol. 129, pp. 11-24.

Assaedi, H., Shaikh, F. & Low, I.M. 2016, 'Characterizations of flax fabric reinforced nanoclay-geopolymer composites', *Composites Part B: Engineering*, vol. 95, pp. 412-22.

ASTM 2015, 'C1437−15: Standard test method for flow of hydraulic cement mortar', *West Conshohoken, PA, USA: American Society for Testing and Materials International*.

ASTM 2016, 'C109/C109M-16a: Standard test method for compressive strength of hydraulic cement mortars', *West Conshohoken, PA, USA: American Society for Testing and Materials International*.

Balooch, G., Marshall, G., Marshall, S., Warren, O., Asif, S.S. & Balooch, M. 2004, 'Evaluation of a new modulus mapping technique to investigate microstructural features of human teeth', *Journal of biomechanics*, vol. 37, no. 8, pp. 1223-32.

Barbhuiya, S. & Chow, P. 2017, 'Nanoscaled mechanical properties of cement composites reinforced with carbon nanofibers', *Materials*, vol. 10, no. 6, p. 662.

Barthel, E. & Perriot, A. 2004, 'Elastic contact to a coated half-space-Effective elastic modulus and real penetration', *Journal of Materials Research*, vol. 19, pp. 600–8.

Beake, B., Harris, A. & Liskiewicz, T. 2013, 'Review of recent progress in nanoscratch testing', *Tribology-Materials, Surfaces & Interfaces*, vol. 7, no. 2, pp. 87-96.

Bernard, O., Ulm, F.-J. & Lemarchand, E. 2003, 'A multiscale micromechanics-hydration model for the early-age elastic properties of cement-based materials', *Cement and Concrete Research*, vol. 33, no. 9, pp. 1293-309.

Berodier, E. & Scrivener, K. 2014, 'Understanding the Filler Effect on the Nucleation and Growth of C-S-H', *Journal of the American Ceramic Society*, vol. 97, no. 12, pp. 3764-73.

Bhatt, A., Priyadarshini, S., Mohanakrishnan, A.A., Abri, A., Sattler, M. & Techapaphawit, S. 2019, 'Physical, chemical, and geotechnical properties of coal fly ash: a global review', *Case Studies in Construction Materials*, vol. 11, p. e00263.

Bhutta, A., Farooq, M., Zanotti, C. & Banthia, N. 2017, 'Pull-out behavior of different fibers in geopolymer mortars: effects of alkaline solution concentration and curing', *Materials and Structures*, vol. 50, no. 1, p. 80.

Bishop, C.M. 2006, *Pattern recognition and machine learning*, Springer.

Björnström, J., Martinelli, A., Matic, A., Börjesson, L. & Panas, I. 2004, 'Accelerating effects of colloidal nano-silica for beneficial calcium–silicate–hydrate formation in cement', *Chemical Physics Letters*, vol. 392, no. 1-3, pp. 242-8.

Brough, A. & Atkinson, A. 2000, 'Automated identification of the aggregate–paste interfacial transition zone in mortars of silica sand with Portland or alkali-activated slag cement paste', *Cement and Concrete Research*, vol. 30, no. 6, pp. 849-54.

Brown, L., Allison, P.G. & Sanchez, F. 2018, 'Use of nanoindentation phase characterization and homogenization to estimate the elastic modulus of heterogeneously decalcified cement pastes', *Materials & Design*, vol. 142, pp. 308-18.

Çevik, A., Alzeebaree, R., Humur, G., Niş, A. & Gülşan, M.E. 2018, 'Effect of nano-silica on the chemical durability and mechanical performance of fly ash based geopolymer concrete', *Ceramics International*, vol. 44, no. 11, pp. 12253-64.

Chanda, D.K., Chowdhury, S.R., Bhattacharya, M., Mandal, A.K., Dey, N. & Mukhopadhyay, A.K. 2018, 'Intelligently designed fly-ash based hybrid composites with very high hardness and Young's modulus', *Construction and Building Materials*, vol. 158, pp. 516-34.

Chatterjee, S., Gadad, S.S. & Kundu, T.K. 2010, 'Atomic force microscopy', *Resonance*, vol. 15, no. 7, pp. 622-42.

Chawla, K.K. & Meyers, M. 1999, *Mechanical behavior of materials*, Prentice Hall Upper Saddle River.

Chen, J., Kou, S.-c. & Poon, C.-s. 2012, 'Hydration and properties of nano-TiO_2 blended cement composites', *Cement and Concrete Composites*, vol. 34, no. 5, pp. 642-9.

Chen, J.J., Sorelli, L., Vandamme, M., Ulm, F.J. & Chanvillard, G. 2010a, 'A Coupled nanoindentation/SEM-EDS study on low water/cement ratio Portland cement paste: evidence for C-S-H/Ca $(OH)_2$ nanocomposites', *Journal of the American Ceramic Society*, vol. 93, no. 5, pp. 1484-93.

Chen, J.J., Sorelli, L., Vandamme, M., Ulm, F.J. & Chanvillard, G. 2010b, 'A coupled nanoindentation/SEM-EDS study on low water/cement ratio Portland cement paste: Evidence for C-S-H/$Ca(OH)_2$ nanocomposites', *Journal of the American Ceramic Society*, vol. 93, no. 5, pp. 1484-93.

Chen, J.J., Sorelli, L., Vandamme, M., Ulm, F.J. & Chanvillard, G. 2010c, 'A Coupled nanoindentation/SEM ‐ EDS study on low water/cement ratio Portland cement paste: evidence for C ‐ S ‐ H/Ca (OH) 2 nanocomposites', *Journal of the American Ceramic Society*, vol. 93, no. 5, pp. 1484-93.

Chen, J.J., Sorelli, L., Vandamme, M., Ulm, F.J. & Chanvillard, G. 2010d, 'A Coupled nanoindentation/SEM ‐ EDS study on low water/cement ratio Portland cement paste: evidence for C ‐ S ‐ H/$Ca(OH)_2$ nanocomposites', *Journal of the American Ceramic Society*, vol. 93, no. 5, pp. 1484-93.

Chen, S.J., Duan, W.H., Li, Z.J. & Sui, T.B. 2015, 'New approach for characterisation of mechanical properties of cement paste at micrometre scale', *Materials & Design*, vol. 87, pp. 992-5.

Chen, X. & Vlassak, J.J. 2001, 'Numerical study on the measurement of thin film mechanical properties by means of nanoindentation', *Journal of Materials Research*, vol. 16, no. 10, pp. 2974-82.

Constantinides, G., Chandran, K.R., Ulm, F.-J. & Van Vliet, K. 2006, 'Grid indentation analysis of composite microstructure and mechanics: Principles and validation', *Materials Science and Engineering: A*, vol. 430, no. 1-2, pp. 189-202.

Constantinides, G. & Ulm, F.-J. 2004a, 'The effect of two types of C-S-H on the elasticity of cement-based materials: Results from nanoindentation and micromechanical modeling', *Cement and Concrete Research*, vol. 34, no. 1, pp. 67-80.

Constantinides, G. & Ulm, F.-J. 2004b, 'The effect of two types of CSH on the elasticity of cement-based materials: Results from nanoindentation and micromechanical modeling', *Cement and Concrete Research*, vol. 34, no. 1, pp. 67-80.

Constantinides, G. & Ulm, F.-J. 2007, 'The nanogranular nature of C–S–H', *Journal of the Mechanics and Physics of Solids*, vol. 55, no. 1, pp. 64-90.

COOPER, R. 2007, 'Tl-900 TriboIndenter User Manual', Hysitron Incorporated, Minneapolis.

Das, S., Yang, P., Singh, S.S., Mertens, J.C., Xiao, X., Chawla, N. & Neithalath, N. 2015, 'Effective properties of a fly ash geopolymer: Synergistic application of X-ray

synchrotron tomography, nanoindentation, and homogenization models', *Cement and Concrete Research*, vol. 78, pp. 252-62.

Davidovits, J. 2002, '30 years of successes and failures in geopolymer applications. Market trends and potential breakthroughs', *Geopolymer 2002 Conference*, vol. 28, Geopolymer Institute Saint ‐ Quentin, France; Melbourne, Australia, p. 29.

Davydov, D., Jirasek, M. & Kopecký, L. 2011, 'Critical aspects of nano-indentation technique in application to hardened cement paste', *Cement and Concrete Research*, vol. 41, no. 1, pp. 20-9.

Davydov, D., Jirásek, M. & Kopecký, L. 2011, 'Critical aspects of nano-indentation technique in application to hardened cement paste', *Cement and Concrete Research*, vol. 41, no. 1, pp. 20-9.

De Vargas, A.S., Dal Molin, D.C., Vilela, A.C., Da Silva, F.J., Pavao, B. & Veit, H. 2011, 'The effects of Na2O/SiO2 molar ratio, curing temperature and age on compressive strength, morphology and microstructure of alkali-activated fly ash-based geopolymers', *Cement and Concrete Composites*, vol. 33, no. 6, pp. 653-60.

Deb, P.S., Sarker, P.K. & Barbhuiya, S. 2015, 'Effects of nano-silica on the strength development of geopolymer cured at room temperature', *Construction and building materials*, vol. 101, pp. 675-83.

Deb, P.S., Sarker, P.K. & Barbhuiya, S. 2016, 'Sorptivity and acid resistance of ambient-cured geopolymer mortars containing nano-silica', *Cement and Concrete Composites*, vol. 72, pp. 235-45.

DeJong, M.J. & Ulm, F.-J. 2007, 'The nanogranular behavior of CSH at elevated temperatures (up to 700 C)', *Cement and Concrete Research*, vol. 37, no. 1, pp. 1-12.

Detwiler, R.J., Monteiro, P.J., Wenk, H.-R. & Zhong, Z. 1988, 'Texture of calcium hydroxide near the cement paste-aggregate interface', *Cement and Concrete Research*, vol. 18, no. 5, pp. 823-9.

Dhoble, Y.N. & Ahmed, S. 2018, 'Review on the innovative uses of steel slag for waste minimization', *Journal of Material Cycles and Waste Management*, vol. 20, no. 3, pp. 1373-82.

Diamond, S. 2001, 'Considerations in image analysis as applied to investigations of the ITZ in concrete', *Cement and Concrete Composites*, vol. 23, no. 2-3, pp. 171-8.

Ding, Y., Dai, J.-G. & Shi, C.-J. 2018, 'Fracture properties of alkali-activated slag and ordinary Portland cement concrete and mortar', *Construction and Building Materials*, vol. 165, pp. 310-20.

Dolado, J.S. & Van Breugel, K. 2011, 'Recent advances in modeling for cementitious materials', *Cement and concrete research*, vol. 41, no. 7, pp. 711-26.

Drouin, D., Couture, A.R., Joly, D., Tastet, X., Aimez, V. & Gauvin, R. 2007, 'CASINO V2. 42—a fast and easy‐to‐use modeling tool for scanning electron microscopy and microanalysis users', *Scanning: The Journal of Scanning Microscopies*, vol. 29, no. 3, pp. 92-101.

Duan, P., Yan, C., Luo, W. & Zhou, W. 2016, 'Effects of adding nano-TiO_2 on compressive strength, drying shrinkage, carbonation and microstructure of fluidized bed fly ash based geopolymer paste', *Construction and Building Materials*, vol. 106, pp. 115-25.

Duxson, P., Provis, J.L., Lukey, G.C., Mallicoat, S.W., Kriven, W.M. & Van Deventer, J.S. 2005, 'Understanding the relationship between geopolymer composition, microstructure and mechanical properties', *Colloids and Surfaces A: Physicochemical and Engineering Aspects*, vol. 269, no. 1-3, pp. 47-58.

Elsharief, A., Cohen, M.D. & Olek, J. 2003, 'Influence of aggregate size, water cement ratio and age on the microstructure of the interfacial transition zone', *Cement and concrete research*, vol. 33, no. 11, pp. 1837-49.

Feynman, R.P. 1959, 'There's plenty of room at the bottom', *Engineering and science*, vol. 23.

Gao, D., Wang, F.-P., Wang, Y.-T. & Zeng, Y.-N. 2020, 'Sustainable Utilization of Steel Slag from Traditional Industry and Agriculture to Catalysis', *Sustainability*, vol. 12, no. 21, p. 9295.

Gao, X., Wei, Y. & Huang, W. 2017a, 'Critical aspects of scanning probe microscopy mapping when applied to cement pastes', *Advances in Cement Research*, pp. 1-12.

Gao, X., Wei, Y. & Huang, W. 2017b, 'Effect of individual phases on multiscale modeling mechanical properties of hardened cement paste', *Construction and Building Materials*, vol. 153, pp. 25-35.

Gao, X., Wei, Y. & Huang, W. 2018, 'Critical aspects of scanning probe microscopy mapping when applied to cement pastes', *Advances in Cement Research*, vol. 30, no. 7, pp. 293-304.

García-Taengua, E., Sonebi, M., Hossain, K., Lachemi, M. & Khatib, J. 2015, 'Effects of the addition of nanosilica on the rheology, hydration and development of the compressive strength of cement mortars', *Composites Part B: Engineering*, vol. 81, pp. 120-9.

Gautham, S., Sindu, B. & Sasmal, S. 2017, 'Evaluation of the phase properties of hydrating cement composite using simulated nanoindentation technique', *Modelling and Simulation in Materials Science and Engineering*, vol. 25, no. 7, p. 075012.

Geetha, D., Sophia, P.J., Radhika, R. & Arivuoli, D. 2017, 'Evaluation of nanoindentation and nanoscratch characteristics of GaN/InGaN epilayers', *Materials Science and Engineering: A*, vol. 683, pp. 64-9.

Gheewala, I., Smith, R. & Kenny, S. 2008, 'Nanoindentation and nanoscratching of rutile and anatase TiO_2 studied using molecular dynamics simulations', *Journal of Physics: Condensed Matter*, vol. 20, no. 35, p. 354010.

Gholampour, A. & Ozbakkaloglu, T. 2017, 'Performance of sustainable concretes containing very high volume Class-F fly ash and ground granulated blast furnace slag', *Journal of Cleaner Production*, vol. 162, pp. 1407-17.

Giessibl, F.J. & Quate, C.F. 2006, 'Exploring the nanoworld with atomic force microscopy', *Physics Today*, vol. 59, no. 12, p. 44.

Guo, J., Legum, B., Anasori, B., Wang, K., Lelyukh, P., Gogotsi, Y. & Randall, C.A. 2018, 'Cold sintered ceramic nanocomposites of 2D MXene and zinc oxide', *Advanced Materials*, p. 1801846.

Hajimohammadi, A., Ngo, T., Provis, J.L., Kim, T. & Vongsvivut, J. 2019, 'High strength/density ratio in a syntactic foam made from one-part mix geopolymer and cenospheres', *Composites Part B: Engineering*, vol. 173, p. 106908.

Hajimohammadi, A., Ngo, T. & Vongsvivut, J. 2019, 'Interfacial chemistry of a fly ash geopolymer and aggregates', *Journal of cleaner production*, vol. 231, pp. 980-9.

Hemalatha, T. & Ramaswamy, A. 2017, 'A review on fly ash characteristics–Towards promoting high volume utilization in developing sustainable concrete', *Journal of cleaner production*, vol. 147, pp. 546-59.

Herath, C., Gunasekara, C., Law, D.W. & Setunge, S. 2020, 'Performance of high volume fly ash concrete incorporating additives: A systematic literature review', *Construction and Building Materials*, vol. 258, p. 120606.

Hintsala, E., Risan, J., Dietrich, R. & Nay, R. 2017, 'Correlated EBSD and high speed nanoindentation mapping', *Microscopy and Microanalysis*, vol. 23, no. S1, pp. 780-1.

Hintsala, E.D., Hangen, U. & Stauffer, D.D. 2018, 'High-throughput nanoindentation for statistical and spatial property determination', *JOM*, vol. 70, no. 4, pp. 494-503.

Horszczaruk, E., Mijowska, E., Kalenczuk, R.J., Aleksandrzak, M. & Mijowska, S. 2015, 'Nanocomposite of cement/graphene oxide – Impact on hydration kinetics and Young's modulus', *Construction and Building Materials*, vol. 78, pp. 234-42.

Howind, T., Hughes, J. & Zhu, W. 2014, 'Mapping of mechanical properties of cement-based materials at micro/nano-scale', *Journal of Innovative Engineering*, vol. 2, no. 1, p. 2.

Hrbek, V., Petráňová, V. & Němeček, J. 2017, 'Early stage microstructure development of cement paste modified by crystalline admixture', *Key Engineering Materials*, vol. 722, Trans Tech Publ, pp. 92-9.

Hu, C. 2014, 'Microstructure and mechanical properties of fly ash blended cement pastes', *Construction and Building Materials*, vol. 73, pp. 618-25.

Hu, C., Gao, Y., Zhang, Y. & Li, Z. 2016, 'Statistical nanoindentation technique in application to hardened cement pastes: Influences of material microstructure and analysis method', *Construction and Building Materials*, vol. 113, pp. 306-16.

Hu, C., Han, Y., Gao, Y., Zhang, Y. & Li, Z. 2014, 'Property investigation of calcium–silicate–hydrate (C–S–H) gel in cementitious composites', *Materials Characterization*, vol. 95, pp. 129-39.

Hu, C., Hou, D. & Li, Z. 2017, 'Micro-mechanical properties of calcium sulfoaluminate cement and the correlation with microstructures', *Cement and Concrete Composites*, vol. 80, pp. 10-6.

Hu, C. & Li, Z. 2015a, 'Property investigation of individual phases in cementitious composites containing silica fume and fly ash', *Cement and Concrete Composites*, vol. 57, pp. 17-26.

Hu, C. & Li, Z. 2015b, 'A review on the mechanical properties of cement-based materials measured by nanoindentation', *Construction and Building Materials*, vol. 90, pp. 80-90.

Huajian, G., Cheng-Hsin, C. & Jin, L. 1992, 'Elastic contact versus indentation modeling of multi-layered materials', *International journal of Solids and Structures*, vol. 29, no. 20, pp. 2471-92.

Hughes, J.J. & Trtik, P. 2004, 'Micro-mechanical properties of cement paste measured by depth-sensing nanoindentation: a preliminary correlation of physical properties with phase type', *Materials Characterization*, vol. 53, no. 2-4, pp. 223-31.

Ishitani, T. & Kaga, H. 1995, 'Calculation of local temperature rise in focused-ion-beam sample preparation', *Microscopy*, vol. 44, no. 5, pp. 331-6.

Jennings, H.M. 2000, 'A model for the microstructure of calcium silicate hydrate in cement paste', *Cement and Concrete Research*, vol. 30, no. 1, pp. 101-16.

Jennings, H.M., Thomas, J.J., Gevrenov, J.S., Constantinides, G. & Ulm, F.-J. 2007, 'A multi-technique investigation of the nanoporosity of cement paste', *Cement and Concrete Research*, vol. 37, no. 3, pp. 329-36.

Ji, T., Gao, Q., Zheng, W., Lin, X. & Wu, H.-C. 2017, 'Interfacial Transition Zone of Alkali-Activated Slag Concrete', *ACI Materials Journal*, vol. 114, no. 3.

Jingjing, Z., Qing, Z., Dan, H. & Feng, S. 2015, 'A peridynamic approach for the simulation of calcium silicate hydrate nanoindentation', *Advances in Cement Research*, vol. 28, no. 2, pp. 84-91.

Johnson, C.V., Chen, J., Hasparyk, N.P., Monteiro, P.J. & Akono, A.T. 2017, 'Fracture properties of the alkali silicate gel using microscopic scratch testing', *Cement and Concrete Composites*, vol. 79, pp. 71-5.

Jones, C.A. & Grasley, Z.C. 2011, 'Short-term creep of cement paste during nanoindentation', *Cement and Concrete Composites*, vol. 33, no. 1, pp. 12-8.

Juenger, M.C. & Siddique, R. 2015, 'Recent advances in understanding the role of supplementary cementitious materials in concrete', *Cement and Concrete Research*, vol. 78, pp. 71-80.

Kawashima, S., Hou, P., Corr, D.J. & Shah, S.P. 2013, 'Modification of cement-based materials with nanoparticles', *Cement and Concrete Composites*, vol. 36, pp. 8-15.

Khale, D. & Chaudhary, R. 2007, 'Mechanism of geopolymerization and factors influencing its development: a review', *Journal of Materials Science*, vol. 42, no. 3, pp. 729-46.

Khedmati, M., Kim, Y.-R. & Turner, J.A. 2019, 'Investigation of the interphase between recycled aggregates and cementitious binding materials using integrated microstructural-nanomechanical-chemical characterization', *Composites Part B: Engineering*, vol. 158, pp. 218-29.

Khedmati, M., Kim, Y.-R., Turner, J.A., Alanazi, H. & Nguyen, C. 2018, 'An integrated microstructural-nanomechanical-chemical approach to examine material-specific characteristics of cementitious interphase regions', *Materials Characterization*, vol. 138, pp. 154-64.

Kim, J.J., Foley, E.M. & Taha, M.M.R. 2013, 'Nano-mechanical characterization of synthetic calcium–silicate–hydrate (C–S–H) with varying CaO/SiO_2 mixture ratios', *Cement and Concrete Composites*, vol. 36, pp. 65-70.

Lee, B.Y. & Kurtis, K.E. 2010, 'Influence of TiO_2 nanoparticles on early C_3S hydration', *Journal of the American Ceramic Society*, vol. 93, no. 10, pp. 3399-405.

Lee, H., Vimonsatit, V. & Chindaprasirt, P. 2016, 'Mechanical and micromechanical properties of alkali activated fly-ash cement based on nano-indentation', *Construction and Building Materials*, vol. 107, pp. 95-102.

Lee, H., Vimonsatit, V., Chindaprasirt, P., Ngo, T. & Mendis, P. 2018, 'Creep properties of cement and alkali activated fly ash materials using nanoindentation technique', *Construction and Building Materials*, vol. 168, pp. 547-55.

Lee, W., Lee, H., Lee, G. & Yoon, D.S. 2016, 'Advances in AFM imaging applications for characterizing the biophysical properties of amyloid fibrils', *Exploring new findings on amyloidosis*, InTech, pp. 99-125.

Lee, W. & Van Deventer, J. 2004, 'The interface between natural siliceous aggregates and geopolymers', *Cement and Concrete Research*, vol. 34, no. 2, pp. 195-206.

Lee, W. & Van Deventer, J. 2007, 'Chemical interactions between siliceous aggregates and low-Ca alkali-activated cements', *Cement and Concrete Research*, vol. 37, no. 6, pp. 844-55.

Li, W., Huang, Z., Zu, T., Shi, C., Duan, W.H. & Shah, S.P. 2016, 'Influence of nanolimestone on the hydration, mechanical strength, and autogenous shrinkage of ultrahigh-performance concrete', *Journal of Materials in Civil Engineering*, vol. 28, no. 1, p. 04015068.

Li, W., Kawashima, S., Xiao, J., Corr, D.J., Shi, C. & Shah, S.P. 2016, 'Comparative investigation on nanomechanical properties of hardened cement paste', *Materials and Structures*, vol. 49, no. 5, pp. 1591-604.

Li, W., Li, X., Chen, S.J., Long, G., Liu, Y.M. & Duan, W.H. 2017, 'Effects of nanoalumina and graphene oxide on early-age hydration and mechanical

properties of cement paste', *Journal of Materials in Civil Engineering*, vol. 29, no. 9, p. 04017087.

Li, W., Luo, Z., Long, C., Wu, C., Duan, W.H. & Shah, S.P. 2016, 'Effects of nanoparticle on the dynamic behaviors of recycled aggregate concrete under impact loading', *Materials & Design*, vol. 112, pp. 58-66.

Li, W., Xiao, J., Kawashima, S., Shekhawat, G.S. & Shah, S.P. 2015a, 'Experimental investigation on quantitative nanomechanical properties of cement paste'.

Li, W., Xiao, J., Kawashima, S., Shekhawat, G.S. & Shah, S.P. 2015b, 'Experimental investigation on quantitative nanomechanical properties of cement paste', *ACI Materials Journal*, vol. 112, no. 2, pp. 229-38.

Li, Y., Wang, P. & Wang, Z. 2017, 'Evaluation of elastic modulus of cement paste corroded in bring solution with advanced homogenization method', *Construction and Building Materials*, vol. 157, pp. 600-9.

Li, Y., Zhang, G., Wang, Z., Wang, P. & Guan, Z. 2018, 'Integrated experimental-computational approach for evaluating elastic modulus of cement paste corroded in brine solution on microscale', *Construction and Building Materials*, vol. 162, pp. 459-69.

Ling, Y., Wang, K., Li, W., Shi, G. & Lu, P. 2019, 'Effect of slag on the mechanical properties and bond strength of fly ash-based engineered geopolymer composites', *Composites Part B: Engineering*, vol. 164, pp. 747-57.

Liu, J., Jiang, R., Sun, J., Shi, P. & Yang, Y. 2017, 'Concrete damage evolution and three-dimensional reconstruction by integrating CT test and fractal theory', *Journal of Materials in Civil Engineering*, vol. 29, no. 9, p. 04017122.

Liu, J., Zeng, Q. & Xu, S. 2020, 'The state-of-art in characterizing the micro/nano-structure and mechanical properties of cement-based materials via scratch test', *Construction and Building Materials*, vol. 254, p. 119255.

Liu, Z., Cai, C., Peng, H. & Fan, F. 2016, 'Experimental study of the geopolymeric recycled aggregate concrete', *Journal of Materials in Civil Engineering*, vol. 28, no. 9, p. 04016077.

Lloyd, R.R., Provis, J.L., Smeaton, K.J. & van Deventer, J.S. 2009, 'Spatial distribution of pores in fly ash-based inorganic polymer gels visualised by Wood's metal intrusion', *Microporous and Mesoporous Materials*, vol. 126, no. 1-2, pp. 32-9.

Lloyd, R.R., Provis, J.L. & van Deventer, J.S. 2009, 'Microscopy and microanalysis of inorganic polymer cements. 1: remnant fly ash particles', *Journal of materials science*, vol. 44, no. 2, pp. 608-19.

Long, W., Xiao, B., Gu, Y. & Xing, F. 2018, 'Micro-and macro-scale characterization of nano-SiO_2 reinforced alkali activated slag composites', *Materials Characterization*, vol. 136, pp. 111-21.

Lothenbach, B., Scrivener, K. & Hooton, R. 2011, 'Supplementary cementitious materials', *Cement and concrete research*, vol. 41, no. 12, pp. 1244-56.

Luković, M., Schlangen, E. & Ye, G. 2015, 'Combined experimental and numerical study of fracture behaviour of cement paste at the microlevel', *Cement and Concrete Research*, vol. 73, pp. 123-35.

Luo, Z., Li, W., Wang, K. & Shah, S.P. 2018, 'Research progress in advanced nanomechanical characterization of cement-based materials', *Cement and Concrete Composites*, vol. 94, pp. 277-95.

Lura, P., Trtik, P. & Münch, B. 2011, 'Validity of recent approaches for statistical nanoindentation of cement pastes', *Cement and Concrete Composites*, vol. 33, no. 4, pp. 457-65.

Lyngdoh, G.A., Nayak, S., Krishnan, N.A. & Das, S. 2020, 'Fracture toughness of fly ash-based geopolymer gels: Evaluations using nanoindentation experiment and molecular dynamics simulation', *Construction and Building Materials*, vol. 262, p. 120797.

Ma, Y., Ye, G. & Hu, J. 2017, 'Micro-mechanical properties of alkali-activated fly ash evaluated by nanoindentation', *Construction and Building Materials*, vol. 147, pp. 407-16.

Mallikarjunachari, G. & Ghosh, P. 2016, 'Analysis of strength and response of polymer nano thin film interfaces applying nanoindentation and nanoscratch techniques', *Polymer*, vol. 90, pp. 53-66.

Mao, Y., Yao, W. & Xu, J. 2013, 'Study on the unhydrated cement grain/C-S-H gel interface in cement paste by use of nano-scratch technique', *Key Engineering Materials*, vol. 539, pp. 84-8.

Mehta, P.K. & Monteiro, P.J. 2017, *Concrete Microstructure, Properties and Materials*.

Miller, M., Bobko, C., Vandamme, M. & Ulm, F.-J. 2008, 'Surface roughness criteria for cement paste nanoindentation', *Cement and Concrete Research*, vol. 38, no. 4, pp. 467-76.

Millington, B. 2019, 'Coal ash has become one of Australia's biggest waste problems — and a solution is being ignored', *ABC NEWS*, Newcastle.

Mondal, P., Shah, S. & Marks, L. 2009, 'Nanomechanical properties of interfacial transition zone in concrete', *Nanotechnology in Construction 3*, Springer, pp. 315-20.

Monteiro, P.J., Geng, G., Marchon, D., Li, J., Alapati, P., Kurtis, K.E. & Qomi, M.J.A. 2019, 'Advances in characterizing and understanding the microstructure of cementitious materials', *Cement and Concrete Research*, vol. 124, p. 105806.

Nedeljković, M., Šavija, B., Zuo, Y., Luković, M. & Ye, G. 2018, 'Effect of natural carbonation on the pore structure and elastic modulus of the alkali-activated fly ash and slag pastes', *Construction and Building Materials*, vol. 161, pp. 687-704.

Němeček, J., Králík, V., Šmilauer, V., Polívka, L. & Jäger, A. 2016, 'Tensile strength of hydrated cement paste phases assessed by micro-bending tests and nanoindentation', *Cement and Concrete Composites*, vol. 73, pp. 164-73.

Němeček, J. & Lukeš, J. 2020, 'High-speed mechanical mapping of blended cement pastes and its comparison with standard modes of nanoindentation', *Materials Today Communications*, vol. 23, p. 100806.

Němeček, J., Šmilauer, V. & Kopecký, L. 2011, 'Nanoindentation characteristics of alkali-activated aluminosilicate materials', *Cement and Concrete Composites*, vol. 33, no. 2, pp. 163-70.

North, L., Labonte, D., Oyen, M., Coleman, M., Caliskan, H. & Johnston, R. 2017, 'Interrelated chemical-microstructural-nanomechanical variations in the structural units of the cuttlebone of Sepia officinalis', *APL Materials*, vol. 5, no. 11, p. 116103.

Oliver, W.C. & Pharr, G.M. 1992, 'An improved technique for determining hardness and elastic modulus using load and displacement sensing indentation experiments', *Journal of Materials Research*, vol. 7, no. 6, pp. 1564-83.

Palin, D., Thijssen, A., Wiktor, V., Jonkers, H. & Schlangen, H. 2015, 'ESEM-BSE coupled with rapid nano-scratching for micro-physicochemical analysis of marine exposed concrete', *EMABM 2015: Proceedings of the 15th Euroseminar on*

Microscopy Applied to Building Materials, Delft, The Netherlands, 17-19 June 2015.

Pelisser, F., Gleize, P.J.P. & Mikowski, A. 2012, 'Effect of the Ca/Si molar ratio on the micro/nanomechanical properties of synthetic CSH measured by nanoindentation', *The Journal of Physical Chemistry C*, vol. 116, no. 32, pp. 17219-27.

Peng, H., Cui, C., Cai, C., Liu, Y. & Liu, Z. 2019, 'Microstructure and microhardness property of the interface between a metakaolin/GGBFS-based geopolymer paste and granite aggregate', *Construction and Building Materials*, vol. 221, pp. 263-73.

Phair, J.W., Van Deventer, J. & Smith, J. 2000, 'Mechanism of polysialation in the incorporation of zirconia into fly ash-based geopolymers', *Industrial & engineering chemistry research*, vol. 39, no. 8, pp. 2925-34.

Pittenger, B., Erina, N. & Su, C. 2010, 'Quantitative mechanical property mapping at the nanoscale with PeakForce QNM', *Application Note Veeco Instruments Inc*, pp. 1-12.

Provis, J.L. & Bernal, S.A. 2014, 'Geopolymers and related alkali-activated materials', *Annual Review of Materials Research*, vol. 44, pp. 299-327.

Provis, J.L., Lukey, G.C. & van Deventer, J.S. 2005, 'Do geopolymers actually contain nanocrystalline zeolites? A reexamination of existing results', *Chemistry of Materials*, vol. 17, no. 12, pp. 3075-85.

Provis, J.L., Myers, R.J., White, C.E., Rose, V. & Van Deventer, J.S. 2012, 'X-ray microtomography shows pore structure and tortuosity in alkali-activated binders', *Cement and Concrete Research*, vol. 42, no. 6, pp. 855-64.

Provis, J.L., Palomo, A. & Shi, C. 2015, 'Advances in understanding alkali-activated materials', *Cement and Concrete Research*, vol. 78, pp. 110-25.

Provis, J.L. & Van Deventer, J.S. 2013, *Alkali activated materials: state-of-the-art report, RILEM TC 224-AAM*, vol. 13, Springer Science & Business Media.

Rashad, A.M. 2014, 'A comprehensive overview about the influence of different admixtures and additives on the properties of alkali-activated fly ash', *Materials & Design*, vol. 53, pp. 1005-25.

Rashad, A.M. 2015, 'A brief on high-volume Class F fly ash as cement replacement–A guide for Civil Engineer', *International Journal of Sustainable Built Environment*, vol. 4, no. 2, pp. 278-306.

Reddy, M.S., Dinakar, P. & Rao, B.H. 2016, 'A review of the influence of source material's oxide composition on the compressive strength of geopolymer concrete', *Microporous and Mesoporous Materials*, vol. 234, pp. 12-23.

Rees, C.A., Provis, J.L., Lukey, G.C. & Van Deventer, J.S. 2008, 'The mechanism of geopolymer gel formation investigated through seeded nucleation', *Colloids and Surfaces A: Physicochemical and Engineering Aspects*, vol. 318, no. 1-3, pp. 97-105.

Riahi, S. & Nazari, A. 2012, 'The effects of nanoparticles on early age compressive strength of ash-based geopolymers', *Ceramics International*, vol. 38, no. 6, pp. 4467-76.

Roa, J., Jimenez-Pique, E., Verge, C., Tarragó, J., Mateo, A., Fair, J. & Llanes, L. 2015, 'Intrinsic hardness of constitutive phases in WC–Co composites: Nanoindentation testing, statistical analysis, WC crystal orientation effects and flow stress for the constrained metallic binder', *Journal of the european ceramic society*, vol. 35, no. 13, pp. 3419-25.

San Nicolas, R., Bernal, S.A., de Gutiérrez, R.M., van Deventer, J.S. & Provis, J.L. 2014, 'Distinctive microstructural features of aged sodium silicate-activated slag concretes', *Cement and Concrete Research*, vol. 65, pp. 41-51.

Sanchez, F. & Sobolev, K. 2010, 'Nanotechnology in concrete–a review', *Construction and building materials*, vol. 24, no. 11, pp. 2060-71.

Schwarz, G. 1978, 'Estimating the dimension of a model', *The annals of statistics*, vol. 6, no. 2, pp. 461-4.

Scrivener, K.L. 2004, 'Backscattered electron imaging of cementitious microstructures: understanding and quantification', *Cement and Concrete Composites*, vol. 26, no. 8, pp. 935-45.

Scrivener, K.L., Crumbie, A.K. & Laugesen, P. 2004, 'The interfacial transition zone (ITZ) between cement paste and aggregate in concrete', *Interface science*, vol. 12, no. 4, pp. 411-21.

Scrivener, K.L., Juilland, P. & Monteiro, P.J. 2015, 'Advances in understanding hydration of Portland cement', *Cement and Concrete Research*, vol. 78, pp. 38-56.

Sebastiani, M., Moscatelli, R., Ridi, F., Baglioni, P. & Carassiti, F. 2016, 'High-resolution high-speed nanoindentation mapping of cement pastes: Unravelling the effect of microstructure on the mechanical properties of hydrated phases', *Materials & Design*, vol. 97, pp. 372-80.

Shaikh, F.U., Supit, S.W. & Barbhuiya, S. 2017, 'Microstructure and nanoscaled characterization of HVFA cement paste containing nano-SiO_2 and nano-$CaCO_3$', *Journal of Materials in Civil Engineering*, vol. 29, no. 8, p. 04017063.

Shen, Q., Pan, G. & Zhan, H. 2017, 'Effect of interfacial transition zone on the carbonation of cement-based materials', *Journal of Materials in Civil Engineering*, vol. 29, no. 7, p. 04017020.

Shi, C., Roy, D. & Krivenko, P. 2003, *Alkali-activated cements and concretes*, CRC press.

Shi, C. & Xie, P. 1998, 'Interface between cement paste and quartz sand in alkali-activated slag mortars', *Cement and Concrete Research*, vol. 28, no. 6, pp. 887-96.

Singh, G.B. & Subramaniam, K.V. 2019, 'Influence of processing temperature on the reaction product and strength gain in alkali-activated fly ash', *Cement and Concrete Composites*, vol. 95, pp. 10-8.

Škvára, F., Kopecký, L., Šmilauer, V. & Bittnar, Z. 2009, 'Material and structural characterization of alkali activated low-calcium brown coal fly ash', *Journal of Hazardous Materials*, vol. 168, no. 2-3, pp. 711-20.

Smolyakov, G., Pruvost, S., Cardoso, L., Alonso, B., Belamie, E. & Duchet-Rumeau, J. 2016, 'AFM PeakForce QNM mode: Evidencing nanometre-scale mechanical properties of chitin-silica hybrid nanocomposites', *Carbohydrate Polymers*, vol. 151, pp. 373-80.

Sobolev, K., Flores, I., Torres-Martinez, L., Valdez, P., Zarazua, E. & Cuellar, E. 2009, 'Engineering of SiO_2 nanoparticles for optimal performance in nano cement-based materials', *NICOM3*, Springer, pp. 139-48.

Soliman, E.M., Aboubakr, S.H. & Taha, M.M.R. 2017, 'Estimating fracture toughness of C–S–H using nanoindentation and the extended finite element method', *International Journal of Advances in Engineering Sciences and Applied Mathematics*, vol. 9, no. 3, pp. 154-68.

Sorelli, L., Constantinides, G., Ulm, F.-J. & Toutlemonde, F. 2008, 'The nano-mechanical signature of ultra high performance concrete by statistical nanoindentation techniques', *Cement and Concrete Research*, vol. 38, no. 12, pp. 1447-56.

Stynoski, P.B. 2015, *Quantification of bond strength between cementitious materials and microbially-induced calcium carbonate precipitates*, University of Illinois at Urbana-Champaign

Sun, Z. & Vollpracht, A. 2019, 'One year geopolymerisation of sodium silicate activated fly ash and metakaolin geopolymers', *Cement and Concrete Composites*, vol. 95, pp. 98-110.

Tang, Z., Li, W., Hu, Y., Zhou, J.L. & Tam, V.W. 2019, 'Review on designs and properties of multifunctional alkali-activated materials (AAMs)', *Construction and Building Materials*, vol. 200, pp. 474-89.

Thomas, R., Gebregziabiher, B.S., Giffin, A. & Peethamparan, S. 2018, 'Micromechanical properties of alkali-activated slag cement binders', *Cement and Concrete Composites*, vol. 90, pp. 241-56.

Trtik, P., Dual, J., Muench, B. & Holzer, L. 2008, 'Limitation in obtainable surface roughness of hardened cement paste:‘virtual’topographic experiment based on focussed ion beam nanotomography datasets', *Journal of microscopy*, vol. 232, no. 2, pp. 200-6.

Trtik, P., Kaufmann, J. & Volz, U. 2012, 'On the use of peak-force tapping atomic force microscopy for quantification of the local elastic modulus in hardened cement paste', *Cement and Concrete Research*, vol. 42, no. 1, pp. 215-21.

Trtik, P., Münch, B. & Lura, P. 2009, 'A critical examination of statistical nanoindentation on model materials and hardened cement pastes based on virtual experiments', *Cement and Concrete Composites*, vol. 31, no. 10, pp. 705-14.

Ulm, F.-J. & James, S. 2011, 'The scratch test for strength and fracture toughness determination of oil well cements cured at high temperature and pressure', *Cement and Concrete Research*, vol. 41, no. 9, pp. 942-6.

Ulm, F.-J., Vandamme, M., Jennings, H.M., Vanzo, J., Bentivegna, M., Krakowiak, K.J., Constantinides, G., Bobko, C.P. & Van Vliet, K.J. 2010, 'Does microstructure matter for statistical nanoindentation techniques?', *Cement and Concrete Composites*, vol. 32, no. 1, pp. 92-9.

Ulm, F.J., Vandamme, M., Bobko, C., Alberto Ortega, J., Tai, K. & Ortiz, C. 2007, 'Statistical indentation techniques for hydrated nanocomposites: concrete, bone, and shale', *Journal of the American Ceramic Society*, vol. 90, no. 9, pp. 2677-92.

Vandamme, M. & Ulm, F.-J. 2013, 'Nanoindentation investigation of creep properties of calcium silicate hydrates', *Cement and Concrete Research*, vol. 52, pp. 38-52.

Vandamme, M., Ulm, F.-J. & Fonollosa, P. 2010, 'Nanogranular packing of C–S–H at substochiometric conditions', *Cement and Concrete Research*, vol. 40, no. 1, pp. 14-26.

Voss, A., Dietz, C., Stocker, A. & Stark, R.W. 2015, 'Quantitative measurement of the mechanical properties of human antibodies with sub-10-nm resolution in a liquid environment', *Nano research*, vol. 8, no. 6, pp. 1987-96.

Wang, L., Zhang, S., Zheng, D., Yang, H., Cui, H., Tang, W. & Li, D. 2017, 'Effect of graphene oxide (GO) on the morphology and microstructure of cement hydration products', *Nanomaterials*, vol. 7, no. 12, p. 429.

Wang, M. & Liu, L. 2017, 'Investigation of microscale aging behavior of asphalt binders using atomic force microscopy', *Construction and Building Materials*, vol. 135, pp. 411-9.

Wang, X., Xu, P., Han, R., Ren, J., Li, L., Han, N., Xing, F. & Zhu, J. 2019, 'A review on the mechanical properties for thin film and block structure characterised by using nanoscratch test', *Nanotechnology Reviews*, vol. 8, no. 1, pp. 628-44.

Wei, Y., Gao, X. & Liang, S. 2018a, 'A combined SPM/NI/EDS method to quantify properties of inner and outer C-S-H in OPC and slag-blended cement pastes', *Cement and Concrete Composites*, vol. 85, pp. 56-66.

Wei, Y., Gao, X. & Liang, S. 2018b, 'A combined SPM/NI/EDS method to quantify properties of inner and outer CSH in OPC and slag-blended cement pastes', *Cement and Concrete Composites*, vol. 85, pp. 56-66.

Wei, Y., Liang, S. & Gao, X. 2017, 'Phase quantification in cementitious materials by dynamic modulus mapping', *Materials Characterization*, vol. 127, pp. 348-56.

Wilson, W., Rivera-Torres, J., Sorelli, L., Durán-Herrera, A. & Tagnit-Hamou, A. 2017, 'The micromechanical signature of high-volume natural pozzolan concrete by combined statistical nanoindentation and SEM-EDS analyses', *Cement and Concrete Research*, vol. 91, pp. 1-12.

Wu, K., Shi, H., Xu, L., Ye, G. & De Schutter, G. 2016, 'Microstructural characterization of ITZ in blended cement concretes and its relation to transport properties', *Cement and Concrete Research*, vol. 79, pp. 243-56.

Xiao, J., Li, W., Corr, D.J. & Shah, S.P. 2012, 'Simulation study on the stress distribution in modeled recycled aggregate concrete under uniaxial compression', *Journal of Materials in Civil Engineering*, vol. 25, no. 4, pp. 504-18.

Xiao, J., Li, W., Corr, D.J. & Shah, S.P. 2013, 'Effects of interfacial transition zones on the stress–strain behavior of modeled recycled aggregate concrete', *Cement and Concrete Research*, vol. 52, pp. 82-99.

Xu, J., Corr, D.J. & Shah, S.P. 2015a, 'Nanomechanical investigation of the effects of nanoSiO2 on C–S–H gel/cement grain interfaces', *Cement and Concrete Composites*, vol. 61, pp. 7-17.

Xu, J., Corr, D.J. & Shah, S.P. 2015b, 'Nanomechanical properties of C-S-H gel/cement grain interface by using nanoindentation and modulus mapping', *Journal of Zhejiang University-SCIENCE A*, vol. 16, no. 1, pp. 38-46.

Xu, J., Corr, D.J. & Shah, S.P. 2015c, 'Nanomechanical properties of CSH gel/cement grain interface by using nanoindentation and modulus mapping', *Journal of Zhejiang University-Science A*, vol. 16, no. 1, pp. 38-46.

Xu, J., Corr, D.J. & Shah, S.P. 2017, 'Nanoscratch study of the modification effects of nanoSiO_2 on C—S—H gel/cement grain interfaces', *Journal of Materials in Civil Engineering*, vol. 29, no. 9, p. 04017093.

Xu, J. & Yao, W. 2011, 'Nano-scratch as a new tool for assessing the nano-tribological behavior of cement composite', *Materials and Structures*, vol. 44, no. 9, pp. 1703-11.

Xu, J. & Yao, W. 2012, 'An experimental study of the nano-scratch behavior of cement composite material', *Key Engineering Materials*, vol. 492, Trans Tech Publ, pp. 47-54.

Yan, K., Guo, Y., Ma, Z., Zhao, Z. & Cheng, F. 2018, 'Quantitative analysis of crystalline and amorphous phases in pulverized coal fly ash based on the Rietveld method', *Journal of Non-Crystalline Solids*, vol. 483, pp. 37-42.

Yan, Y., Chang, S., Wang, T. & Geng, Y. 2019, 'Scratch on Polymer Materials Using AFM Tip-Based Approach: A Review', *Polymers*, vol. 11, no. 10, p. 1590.

Zhai, C., Gan, Y., Hanaor, D., Proust, G. & Retraint, D. 2016, 'The role of surface structure in normal contact stiffness', *Experimental Mechanics*, vol. 56, no. 3, pp. 359-68.

Zhang, H., Šavija, B., Chaves Figueiredo, S., Lukovic, M. & Schlangen, E. 2016, 'Microscale testing and modelling of cement paste as basis for multi-scale modelling', *Materials*, vol. 9, no. 11, p. 907.

Zhang, W., Patel, K. & Ren, S. 2017, 'Exfoliated BN shell-based high-frequency magnetic core–shell materials', *Nanoscale*, vol. 9, no. 35, pp. 13203-8.

Zhang, Z., Provis, J.L., Reid, A. & Wang, H. 2014, 'Fly ash-based geopolymers: the relationship between composition, pore structure and efflorescence', *Cement and concrete research*, vol. 64, pp. 30-41.

Zhao, P., Liu, X., De La Torre, A.G., Lu, L. & Sobolev, K. 2017, 'Assessment of the quantitative accuracy of Rietveld/XRD analysis of crystalline and amorphous phases in fly ash', *Analytical Methods*, vol. 9, no. 16, pp. 2415-24.

Zhao, S., Van Dam, E., Lange, D. & Sun, W. 2016, 'Abrasion resistance and nanoscratch behavior of an ultra-high performance concrete', *Journal of Materials in Civil Engineering*, vol. 29, no. 2, p. 04016212.

Zhou, M., Jiang, Y. & Sui, Y. 2019, 'Microstructure and properties of interfacial transition zone in ZTA particle–reinforced iron composites', *Applied Physics A*, vol. 125, no. 2, p. 110.

Zhu, X., Gao, Y., Dai, Z., Corr, D.J. & Shah, S.P. 2018, 'Effect of interfacial transition zone on the Young's modulus of carbon nanofiber reinforced cement concrete', *Cement and Concrete Research*, vol. 107, pp. 49-63.

Zhu, X., Yuan, Y., Li, L., Du, Y. & Li, F. 2017, 'Identification of interfacial transition zone in asphalt concrete based on nano-scale metrology techniques', *Materials & Design*, vol. 129, pp. 91-102.

Zhu, Z. & Chen, H. 2017, 'Aggregate shape effect on the overestimation of interface thickness for spheroidal particles', *Powder Technology*, vol. 313, pp. 218-30.

Zhuang, X.Y., Chen, L., Komarneni, S., Zhou, C.H., Tong, D.S., Yang, H.M., Yu, W.H. & Wang, H. 2016, 'Fly ash-based geopolymer: clean production, properties and applications', *Journal of Cleaner Production*, vol. 125, pp. 253-67.

Zlotnikov, I., Zolotoyabko, E. & Fratzl, P. 2017, 'Nano-scale modulus mapping of biological composite materials: Theory and practice', *Progress in Materials Science*, vol. 87, pp. 292-320.

Zou, M. & Yang, D. 2006, 'Nanoindentation of silica nanoparticles attached to a silicon substrate', *Tribology letters*, vol. 22, no. 2, pp. 189-96.

Zywitzki, O., Modes, T., Sahm, H., Frach, P., Goedicke, K. & Glöß, D. 2004, 'Structure and properties of crystalline titanium oxide layers deposited by reactive pulse magnetron sputtering', *Surface and coatings technology*, vol. 180, pp. 538-43.